UNIVERSITÉ LIBRE DE BRUXELLES ULB

Retrieval of the horizontal distributions of NO_2, HCHO, and aerosols from urban MAX-DOAS measurements in support to air quality satellite validation

Thesis submitted by Ermioni DIMITROPOULOU
in fulfilment of the requirements of the PhD Degree in Sciences (ULB - "Docteur en Sciences")
Academic year 2021-2022

Supervisor: Prof. Dr. Pierre-François COHEUR
Spectroscopy, Quantum Chemistry and Atmospheric Remote Sensing (SQUARES)/ULB
Co-supervisor: Dr. François HENDRICK
Royal Belgian Institute for Space Aeronomy/BIRA-IASB

Thesis jury:
Prof. Dr. Nadine MATTIELLI (Université libre de Bruxelles/ULB, Chair)
Dr. Lieven CLARISSE (Université libre de Bruxelles/ULB, Secretary)
PD Dr. Andreas RICHTER (Institute of Environmental Physics, University of Bremen/IUP-Bremen)
Dr. Ankie PITERS (Royal Netherlands Meteorological Institute/KNMI)

"If at first you don't succeed try, try and try again."
Robert the Bruce, king of Scotland

Acknowledgments

When I first came to Brussels to start my Ph.D., its end seemed so far away. However, here we are, finalizing this thesis, which is a result of a lot of work and help from many people, to whom I would like to express my gratefulness.

First, I would like to thank Francois Hendrick, who has supervised my work at the Belgian Institute for Space Aeronomy (BIRA-IASB). His scientific expertise, help, and patience during these four years of research were essential to me. He has always been there more than just a supervisor, especially during the challenging periods of my thesis. I am grateful that I worked with you during my Ph.D. and that you accompanied me on this exciting but sometimes difficult journey.

I would like to say special thanks to Michel Van Roozendael for his scientific expertise, for sharing his knowledge with me, and for always giving me useful and relevant advices on my work. I would also like to thank him for his financial support during these four years.

I want to express my gratefulness to my supervisor at ULB, Pierre-Francois Coheur, for supporting me and giving me valuable advices. It was always a pleasure to talk with him about my work.

I could not forget to thank Lieven Clarisse and Jean Vander Auwera for following and monitoring my work progress every year. Their presence as members of my Ph.D. committee was crucial to improving myself.

All the members of the UV/visible DOAS group did not stop helping me during my research. They were always open to sharing their knowledge. I would like to thank Caroline Fayt, Gaia Pinardi, Christian Hermans, Martina Friedrich, Nicolas Theys, Hugues Brenot, Isabelle De Smedt, Nathalie Kalb, Christophe Lerot, Jeroen van Gent, Jonas Vlietinck, and Huan Yu for helping me scientifically and personally. Special thanks to Alexis Merlaud for allowing me to come to BIRA-IASB before my Ph.D. and for participating to the CINDI-2 campaign. Thanks to him, doing a Ph.D. became more a reality than a dream. Finally, I could not finish my acknowledgments without expressing my great gratitude to my colleague and dear friend Frederik Tack for sharing his office with me and always being there in good and bad moments.

Apart from my UV/visible DOAS colleagues and friends, I had the chance to meet incredible people at BIRA-IASB, who became my close friends, and I am so happy to share lovely moments with them. But also, thank you for listening to my complaints and always giving me your support and love. I am referring to my super scientist friends Miriam Cisneros, Daniele Minganti, Justin Erwin, Shohei Aoki, Catalina Poraicu, Sieglinde Callewaert and Lucie Lamort.

I would like to express my gratitude to Jenny Stavrakou, who was always there for me as a friend and scientist. Her office was always open to help me with all my struggles during these four years. Additionally, I would like to thank Jean-Francois Muller for his interest and support.

I should express my great gratitude to my family, who always believed in me and supported me for almost 30 years in everything that I do. The unconditional support of my mother, father, little brother, and grandparents helped me believe in myself and stick to my goals. Furthermore, I feel fortunate to have in my life my Greek friends who always helped me remotely but constantly during my thesis. Special thanks to my dear friends Konstantina, Vivi, Vaggelis, Foteini, Antonia, and Ilias for always being there. Also, I made friends in Brussels who were always there for me, listening to my concerns during my Ph.D. journey: my dear Christina, Marion, Tristan, Nina, and Lucas.

Last but not least, I could not finish my acknowledgments without talking about you, Simon. A lifetime would not be enough to thank you for your support. You didn't understand the complexity of living together with a Ph.D. student, but you helped me every day with your presence, even if you think that you did not. Without you, I could not arrive at this moment.

Following the private defense, I would also like to thank the members of the Thesis Jury, Prof. Dr. Nadine Mattielli (Chair), Dr. Lieven Clarisse (Secretary), PD Dr. Andreas Richter, and Dr. Ankie Piters, for making the private defense a fascinating discussion, for providing valuable feedback and contributing to expanding my knowledge.

Thank you all for being there and making these four years an unforgettable journey.

Abstract

The Earth's atmosphere has always been attracting human attention. Its study, i.e. understanding its characteristics and processes, its response to natural and anthropogenic activities, and its evolution over the years, is one of the most fascinating and complicated research domains. When focusing on the lowest part of the Earth's atmosphere, anthropogenic emissions become highly important by changing the atmosphere's composition and influencing the climate. In urban regions, one of the most critical pollutants emitted by anthropogenic activities, such as traffic, industrial activity, domestic heating, and power plants is nitrogen dioxide (NO_2). NO_2 is considered a proxy for air pollution. Another important tropospheric pollutant is formaldehyde (HCHO), which is emitted in the troposphere from natural, anthropogenic, and pyrogenic sources, and it is often used to monitor the biogenic and anthropogenic emissions of hydrocarbons. Finally, aerosols are crucial in the troposphere in terms of air quality and climate.

The purpose of this work is the retrieval of the horizontal distributions of NO_2, HCHO, and aerosols from MAX-DOAS measurements in urban conditions to support the validation of air quality satellite observations. To achieve that, dual-scan ground-based Multi-AXis Differential Optical Absorption Spectroscopy (MAX-DOAS) measurements of tropospheric NO_2, HCHO and aerosols have been carried out in Uccle (50.8^{o}N, 4.35^{o}E; Brussels region, Belgium) for two years, from March 2018 to February 2020. The MAX-DOAS instrument has been operating in both UV and Visible wavelength ranges in a dual-scan configuration consisting of two sub-modes: (1) an elevation scan in a fixed viewing azimuthal direction (the so-called main azimuthal direction) pointing to the northeast and (2) an azimuthal scan in a fixed low elevation angle (2^o). By applying a vertical profile inversion algorithm in the main azimuthal direction and a parameterization technique in the other azimuthal directions, near-surface NO_2 and HCHO volume mixing ratios (VMRs) and vertical column densities (VCDs) and near-surface aerosol extinction were retrieved in ten different azimuthal directions.

In a first step, the multi-azimuthal MAX-DOAS dataset is used to characterize the NO_2 and HCHO horizontal distributions around the measurement site. We show that the horizontal distributions of NO_2 and HCHO differ per season as expected. Maximum NO_2 values are retrieved during cold seasons and towards the Brussels city center, while maximum HCHO values are observed during warmer seasons and towards a large forested area in the Brussels region. Additionally, we demonstrate that measuring the tropospheric NO_2 and HCHO VCDs in multiple azimuthal directions improves the spatial colocation with measurements from the TROPOMI/ S5P, leading to improved satellite validation results. Although there is a better agreement between both datasets, we show that the observed systematic underestimation of the tropospheric NO_2 columns by TROPOMI/ S5P is rising from inadequate a priori NO_2 profiles shape data in the satellite retrieval.

In a second step, a new Optimal-Estimation-based inversion approach is developed by exploiting the O_4 and NO_2 dSCDs measured at six different wavelength intervals to retrieve the horizontal distribution of the NO_2 near-surface concentrations and vertical column densities (VCDs) and the aerosols near-surface extinction coefficient along every azimuthal direction. For the first time, seasonal tropospheric NO_2 column maps are constructed from MAX-DOAS observations, enabling the identification of the main NO_2 hotspots in the Brussels area at a horizontal resolution of about 3km. Correlative comparisons of the retrieved horizontal NO_2 distribution have been conducted with airborne, mobile, and satellite datasets collected during the S5P validation campaign over Belgium (S5PVAL-BE), and overall a good agreement is found. Furthermore, we show that this new way of characterizing the tropospheric NO_2 VCD horizontal distribution from MAX-DOAS measurements, the appropriate sampling of TROPOMI pixels, and again an adequate a priori NO_2 profile shape in TROPOMI retrievals lead to a significantly better agreement between satellite and ground-based datasets.

List of acronyms

AK Averaging Kernel
AMF Air Mass Factor
AOD Aerosol Optical Depth
APEX Airborne Prism EXperiment
BIRA-IASB koninklijk Belgisch Instituut voor Ruimte-Aeronomie - Institut royal d'Aéronomie Spatiale de Belgique
CAMS Copernicus Atmospheric Monitoring Service
CCD Charged Coupled Device
CINDI-2 Cabauw Intercomparison Campaign of Nitrogen Dioxide - 2
CTM Climate Transport Model
DLR-IMF Deutschen Zentrums für Luft- und Raumfahrt - Institut für Methodik der Fernerkundung
DOFS Degree Of Freedom for Signal
DSCD Differential Slant Column Density
EEA European Environmental Agency
EGU European Geosciences Union
ERS-2 European Remote-Sensing Satellite-2
ESA/ESRIN European Space Agency/European Space Research Institute
ETHZ Eidgenössische Technische Hochschule Zürich (Swiss Federal Institute of Technology, Zurich)
EU European Union
FOV Field Of View
GHG GreenHouse Gas
GOME Global Ozone Monitoring Experiment
FRESCO Fast REtrieval Scheme for Clouds from the Oxygen A-band
IGARSS International Symposium on Geoscience and Remote Sensing
IPCC Intergovernmental Panel on Climate Change
IR InfraRed
KNMI Koninklijk Nederlands Meteorologisch Instituut
MAP Maximum A Posteriori
MAX-DOAS Multi-AXis Differential Optical Absorption Spectroscopy
McArtim Monte Carlo Atmospheric Radiative Transfer Inversion Model
MLH Mixing Layer Height
MMF Mexican MAX-DOAS Fit
NOAA National Oceanic and Atmospheric Administration
OEM Optimal Estimation Method
OMI Ozone Monitoring Instrument
PBL Planetary Boundary Layer
PM Particulate Matter
RMI Royal Meteorological Institute of Belgium
RMS Root-Mean-Square
RSAA Relative Solar Azimuthal Angle
RTE Radiative Transfer Equation
RTM Radiative Transfer Modeling
S5P/TROPOMI Sentinel-5 Precursor/TROPOspheric Monitoring Instrument
SCIAMACHY SCanning Imaging Absorption spectroMeter for Atmospheric CartograpHY
SCIATRAN Radiative Transfer Model for SCIAMACHY
SOA Secondary Organic Aerosols
SOLSPEC SOLar SPECtrum

SOSP SOlar SPectrum
SSA Single Scattering Angle
SZA Solar Zenith Angle
TM5 Tracer Model version 5
TNO The Netherlands Organization
TRACY-2 Trace gas RAdiative Transfer Monte Carlo Y(I)implementation - 2
UTC Coordinated Universal Time
UV UltraViolet
VCD Vertical Column Density
Vis Visible
VLIDORT Vectors LInearized Discrete Ordinate Radiative Transfer
VMR Volume Mixing Ratio
VOC Volatile Organic Compound
WF Weighting Function
WS WorkShop

List of publications

- Kreher, K., Van Roozendael, M., Hendrick, F., Apituley, A., **Dimitropoulou, E.**, Friess, U., Richter, A., Wagner, T., Lampel, J., Abuhassan, N., Ang, L., Anguas, M., Bais, A., Benavent, N., Bosch, T., Bognar, K., Borovski, A., Bruchkouski, I., Cede, A., Chan, K. L., Donner, S., Drosoglou, T., Fayt, C., Finkenzeller, H., Garcia-Nieto, D., Gielen, C., Gomez-Martin, L., Hao, N., Henzing, B., Herman, J. R., Hermans, C., Hoque, S., Irie, H., Jin, J., Johnston, P., Khayyam Butt, J., Khokhar, F., Koenig, T. K., Kuhn, J., Kumar, V., Liu, C., Ma, J., Merlaud, A., Mishra, A. K., MÃ¼ller, M., Navarro-Comas, M., Ostendorf, M., Pazmino, A., Peters, E., Pinardi, G., Pinharanda, M., Piters, A., Platt, U., Postylyakov, O., Prados-Roman, C., Puentedura, O., Querel, R., Saiz-Lopez, A., Schonhardt, A., Schreier, S. F., Seyler, A., Sinha, V., Spinei, E., Strong, K., Tack, F., Tian, X., Tiefengraber, M., Tirpitz, J.-L., van Gent, J., Volkamer, R., Vrekoussis, M., Wang, S., Wang, Z., Wenig, M., Wittrock, F., Xie, P. H., Xu, J., Yela, M., Zhang, C., and Zhao, X.: Intercomparison of NO_2, O_4, O_3 and HCHO slant column measurements by MAX–DOAS and zenith–sky UV–visible spectrometers during CINDI–2, Atmos. Meas. Tech., 13, 2169–2208, https://doi.org/10.5194/amt–13–2169–2020, 2020.

- **Dimitropoulou, E.**, Hendrick, F., Pinardi, G., Friedrich, M. M., Merlaud, A., Tack, F., De Longueville, H., Fayt, C., Hermans, C., Laffineur, Q., Fierens, F., and Van Roozendael, M.: Validation of TROPOMI tropospheric NO_2 columns using dual– scan multi–axis differential optical absorption spectroscopy (MAX–DOAS) measurements in Uccle, Brussels, Atmos. Meas. Tech., 13, 5165–5191, https://doi.org/10.5194/amt–13–5165–2020, 2020.

- Tack, F., Merlaud, A., Iordache, M.–D., Pinardi, G., **Dimitropoulou, E.**, Eskes, H., Bomans, B., Veefkind, P., and Van Roozendael, M.: Assessment of the TROPOMI tropospheric NO_2 product based on airborne APEX observations, Atmos. Meas. Tech., 14, 615–646, https://doi.org/10.5194/amt–14–615–2021, 2021.

- **Dimitropoulou, E**., Hendrick, F., Friedrich, M. M., Tack, F., Pinardi, G., Merlaud, A., Fayt, C., Hermans, C., and Van Roozendael, M. (2021, July). Improved TROPOMI HCHO Column Validation Using Dual-Scan MAX-DOAS Retrievals. In 2021 IEEE International Geoscience and Remote Sensing Symposium IGARSS (pp. 8026-8029). IEEE.

- **Dimitropoulou, E.**, Hendrick, F., Friedrich, M. M., Tack, F., Pinardi, G., Merlaud, A., Fayt, C., Hermans, C., Fierens, F., and Van Roozendael, M.: Horizontal distribution of tropospheric NO2 and aerosols derived by dual-scan multi-wavelength MAX-DOAS measurements in Uccle, Belgium, Atmos. Meas. Tech. Discuss. [preprint], https://doi.org/10.5194/amt-2021-308, in review, 2021.

Selected oral presentations

- **Dimitropoulou, E.**, Van Roozendael, M., Hendrick, F., Merlaud, A., Tack, F., Friedrich, M., Fayt, C., Hermans, C., Pinardi, G., De Longueville, H., Laffineur, Q., and Fierens, F.: One year of 2–D MAX-DOAS tropospheric measurements over Brussels. Presented at the 3rd CINDI–2 Workshop, ESA/ESRIN, Frascati, Italy, February 2019

- **Dimitropoulou, E.**, Van Roozendael, M., Hendrick, F., Merlaud, A., Tack, F., Friedrich, M., Fayt, C., Hermans, C., Pinardi, G., De Longueville, H., Laffineur, Q., and Fierens, F.: 2–D MAX–DOAS tropospheric measurements over Brussels. Presented at the EGU General Assembly, Vienna, Austria, April 2019

- **Dimitropoulou, E.**, Van Roozendael, M., Hendrick, F., Friedrich, M. M., Tack, F., Pinardi, G.,Merlaud, A., Fayt, C., Hermans, C. and Fierens, F.: Horizontal distribution of tropospheric aerosols and NO_2 derived by dual–scan multi– wavelength MAX–DOAS measurements in Uccle, Belgium. Presented at the MAX–DOAS WS conference, Online conference, May 2021

Selected poster presentations

- **Dimitropoulou, E.**, Van Roozendael, M., Hendrick, F., Merlaud, A., Tack, F., Fayt, C., Hermans, C., Pinardi, G., Pereira, N., Fierens, F., and Laffineur, Q.: Investigation of the vertical distributions of in Brussels area using MAX–DOAS measurements. Presented at the EGU General Assembly, Vienna, Austria, April 2018

- **Dimitropoulou, E.**, Van Roozendael, M., Hendrick, F., De Longueville, H., Merlaud, A., Pinardi, G., Tack, F., Fayt, C., and Hermans, C.: Validation of TROPOMI tropospheric using 3–D MAX–DOAS measurements in the Brussels area. Presented at the ATMOS conference, Salzburg, Austria, November 2018

- **Dimitropoulou, E.**, Hendrick, F., Pinardi, G., Friedrich, M. M., Merlaud, A., Tack, F., H., Fayt, C., Hermans, C. and Van Roozendael, M.: Tropospheric NO_2 and HCHO derived from dual–scan MAX–DOAS measurements in Uccle (Belgium) and application to S5P/TROPOMI validation. Presented at the EGU General Assembly, Vienna, Austria, May 2020

- **Dimitropoulou, E.**, Hendrick, F., Pinardi, G., Friedrich, M. M., Merlaud, A., Tack, F., H., Fayt, C., Hermans, C. and Van Roozendael, M.: Horizontal distribution of tropospheric NO_2 derived from dual–scan multi–wavelength MAX– DOAS measurements in Uccle (Belgium). Presented at the DOAS workshop, Utrecht, The Netherlands, July 2020

- **Dimitropoulou, E**., Van Roozendael, M., Hendrick, F., Friedrich, M. M., Tack, F., Pinardi, G.,Merlaud, A., Fayt, C., Hermans, C. and Fierens, F.: Improved TROPOMI HCHO column validation using dual–scan MAX-DOAS retrievals. Presented at the IGARSS conference, Brussels, Belgium, July 2021

Contents

List of Figures

List of Tables

General Introduction and objectives

The Earth's atmosphere is a thin layer of gases, which surrounds our planet. Its presence is crucial for life by e.g. allowing liquid water to exist on the Earth's surface, raising the surface temperature through the greenhouse effect, and protecting the living organisms from harmful UV radiation via the stratospheric ozone layer. Therefore, understanding the Earth's atmosphere (i.e. its characteristics and processes, its response to natural and anthropogenic activities, and its evolution over the years) is vital.

It is a fact that anthropogenic activities change the atmosphere's composition and influence the climate (IPCC, 2021). Even if the concentration of harmful anthropogenic pollutants such as ozone (O_3) and nitrogen dioxide (NO_2) is low compared to the total mass of the atmosphere, their influence on humans, ecosystems, and the climate is highly damaging.

When focusing on the troposphere, one of the most critical anthropogenic pollutants is NO_2. Mainly emitted by combustion processes associated with traffic, industrial activity, domestic heating, and power plants, NO_2 is considered as a proxy for air pollution. Its high concentrations are often associated with high concentrations of other pollutants such as tropospheric O_3 and aerosols. Depending on the NO_x ($NO_x = NO_2 + NO$), O_3 and volatile organic compound (VOC) concentration levels in the troposphere, two regimes can be distinguished: the NO_x-limited and the VOC-limited regimes. In the NO_x-limited regime, an increase in NO_x concentrations leads to an O_3 increase, while in the VOC-limited (or NO_x-saturated) regime, the tropospheric O_3 increases when the VOC concentration levels increase. In the boundary layer, the lifetime of NO_2 is short (typically a few hours close to the surface), and therefore its concentrations can vary rapidly in time and space.

Another important tropospheric atmospheric constituent is formaldehyde (HCHO). It is mainly produced from the photochemical oxidation of methane (CH_4) and non-methane volatile organic compounds (NMVOCs). HCHO is emitted in the atmosphere from natural (vegetation), anthropogenic (industrial activities), and pyrogenic (biomass burning) sources. HCHO is therefore often used as an indicator of biogenic and anthropogenic emissions of hydrocarbons. Additionally, HCHO is produced with the formation of peroxy radicals (RO_2) and is referred to as secondary HCHO. HCHO plays a critical role in tropospheric chemistry by influencing the formation of tropospheric O_3 and secondary organic aerosols (SOA). Aerosols are tiny particles that can considerably influence the Earth's climate system by changing its radiation budget by scattering and absorbing sunlight. As a result, they can affect cloud formation and, consequently, the Earth's albedo.

NO_2, HCHO, and aerosols directly impact human health, causing headaches, fatigue, and eye and throat irritation. Therefore, monitoring the global and regional distributions of these pollutants is of high importance.

The daily global monitoring of a great number of air pollutants, such as NO_2 and HCHO, but also sulfur dioxide (SO_2) and glyoxal (CHOCHO), can be performed by satellite nadir air-quality measurements of atmospheric back-scattered sunlight in the UV-visible range. This type of space-borne observations started in 1995 with the ERS-2/GOME (Global Ozone Monitoring Experiment) instrument (Burrows et al., 1999), followed in chronological order by ENVISAT/SCIAMACHY (SCanning Imaging Absorption spectroMeter for Atmospheric CHartographY) in 2002 (Bovensmann et al., 1999), AURA/OMI (Ozone Monitoring Experiment) in 2004 (Levelt et al., 2006), MetOpA/GOME-2A in 2006, MetOp-B/GOME-2B in 2012 and MetOp-C/GOME-2C in 2018 (Munro et al., 2016). It is worth mentioning that the pixel size of those instruments showed a significant reduction from 40x320 km^2 for

GOME to 13x24 km^2 for OMI.

More recently, the TROPOspheric Monitoring Instrument (TROPOMI) sensor launched onboard the Sentinel-5p Precursor (S5P) platform in October 2017 reached an even finer resolution of 7x3.5 km^2 and which has been further improved to 3.5x5.5 km^2 from 6 August 2019 onward. S5P is the first mission of the EU Copernicus Program dedicated to atmospheric measurements with a high spatio-temporal resolution. The improved spatial resolution of TROPOMI offers new opportunities for air quality monitoring compared to previous satellite instruments, but it also introduces additional challenges about the validation of such high spatial resolution measurements. Ground-based instruments and associated trace gas retrieval methods should be therefore developed driven by the necessity of validating these air quality satellite missions.

For about 2 decades, the Multi-AXis Differential Optical Absorption Spectroscopy (MAX-DOAS) technique has been widely used for retrieving the vertical distribution of trace gases and aerosols in the troposphere (e.g. Platt and Stutz, 2008). MAX-DOAS instruments perform observations of scattered sunlight in the visible and ultraviolet (UV) spectral ranges at multiple elevation angles towards the horizon, leading to increased sensitivity to absorbers situated close to the surface (Hönninger et al., 2004). NO_2, HCHO, CHOCHO, SO_2, bromine monoxide (BrO), water vapor (H_2O), nitrous acid (HONO) and tropospheric O_3 are some of the tropospheric species that can be measured by those instruments (Wittrock et al., 2004; Sinreich et al., 2007; Irie et al., 2008; Pinardi et al., 2008; Clémer et al., 2010; Irie et al., 2011; Wagner et al., 2011; Pinardi et al., 2013; Hendrick et al., 2014). Because of their ability to retrieve vertical column and profile information with a horizontal representativeness similar to the air quality space-borne sensors, MAX-DOAS observations provide an adequate source of reference data for the validation of satellite nadir trace gas measurements (Irie et al., 2008; Peters et al., 2012; Wang et al., 2017). In the case of NO_2, studies published so far (e.g. Celarier et al., 2008; Kramer et al., 2008; Irie et al., 2012; Ma et al., 2013; Pinardi et al., 2020) indicate that satellite sensors tend to underestimate tropospheric NO_2 columns, especially over large cities.

During the last years, MAX-DOAS instruments operating in more than one azimuthal direction have been emerging (Sinreich et al., 2013; Wang et al., 2014; Ortega et al., 2015). These multi-azimuthal (or dual-scan) measurements allow to retrieve the horizontal distribution of trace gases and aerosols together with the vertical profile. In urban regions, deploying multi-azimuthal MAX-DOAS measurements is essential because the NO_2 horizontal distribution can be highly heterogeneous, with maximum NO_2 concentrations observed close to urban hotspots and decreasing as moving away from those sources. Multi-azimuthal MAX-DOAS measurements offer therefore many possibilities for air-quality monitoring, such as a better characterization of the NO_2 near-surface concentration and tropospheric column horizontal fields around the measurement site. This makes that these ground-based datasets can be highly valuable for validating high horizontal resolution space-borne nadir sensors over urban and suburban areas.

The present thesis aims at developing new ground-based MAX-DOAS approaches to retrieve and characterize the NO_2, HCHO, and aerosols horizontal and vertical distributions over urban regions and investigating how these new data sets can improve the validation of air quality satellite observations. For this purpose, we use the MAX-DOAS instrument operated at the Space Pole in Uccle (Belgium) by the UV/visible DOAS group of the Royal Belgian Institute for Space Aeronomy (BIRA-IASB). Brussels-Capital Region is the most densely populated area in Belgium, where pollutant concentrations, such as NO_2, are among the highest in Europe due to high anthropogenic activities. More precisely, the main objectives of this thesis are the following:

- the optimization of the Uccle MAX-DOAS instrument's operation mode to enable the retrieval of both vertical and horizontal distributions of NO_2, HCHO, and aerosols around the measurement site in a time resolution representative of these trace gases' and aerosols' natural variabilities.
- the development of new strategies for retrieving vertical and horizontal NO_2 and HCHO near-surface concentrations and tropospheric vertical columns from the collected ground-based multi-azimuthal MAX-DOAS measurements at various wavelengths.
- the validation of the retrieved NO_2 concentration and column horizontal fields by comparing them with collected ancillary data, such as in-situ, airborne, and car-doas observations.

- the use of the ground-based multi-azimuthal MAX-DOAS retrieval results to validate the TROPOMI/S5P observations over the Brussels-Capital region. In particular, we investigate how these new MAX-DOAS data sets can potentially improve the validation of the satellite observations in urban conditions.

Outline of the thesis

The present thesis is organized in five main parts, each of them consisting of multiple chapters.

Part I provides detailed theoretical background about the Earth's atmosphere (**chapter 1**), the processes that Sun's radiation undergoes when traveling into Earth's atmosphere (**chapter 2**), the main chemistry of nitrogen species, HCHO, and aerosols in the troposphere (**chapter 3**), the Differential Optical Absorption Spectroscopy (**chapter 4**), the atmospheric radiative transfer (**chapter 5**), and the inversion theory (**chapter 6**).

In **Part II**, we provide information about the Uccle measurement site and the ground-based MAX-DOAS instrument operated at this location (**chapter 7**). Satellite measurements with a particular focus on the TROPOMI/S5P instrument are presented in **chapter 8**. Airborne APEX measurements, which provide a reference data set for validating our MAX-DOAS NO_2 observations, are presented in **chapter 9**.

The main results of the thesis are presented in **Parts III** to **V**.

Part III focuses on the validation of TROPOMI tropospheric NO_2 columns using dual-scan MAX-DOAS measurements in Uccle, Belgium. After providing an abstract and the main objectives (**chapter 10**), we present the developed retrieval methods for ground-based MAX-DOAS measurements in multiple azimuthal directions (**chapter 11**). The validation of TROPOMI/S5P tropospheric NO_2 columns (**chapter 12**) in Brussels has been conducted by using the multi-azimuthal MAX-DOAS measurements during one year (March 2018 - March 2019). These results are presented in **chapter 13**. Concluding remarks are given in **chapter 14**.

In **Part IV**, after giving the main objectives (**chapter 15**), we present the multi-wavelength DOAS analysis in six different fitting windows (**chapter 16**), which is used as input to develop a new dual-scan multi-wavelength inversion approach for retrieving the horizontal distribution of tropospheric NO_2 and aerosols. This new dual-scan multi-wavelength MAX-DOAS inversion approach is described in **chapter 18**. The TROPOMI dataset used in this **Part IV** is presented in **chapter 17**, and the main retrieval results are given in **chapter 19**. Finally, conclusions are presented in **chapter 20**.

Part V focuses on the retrieval of dual-scan HCHO tropospheric columns (**chapter 21**) and its use to improve the satellite TROPOMI/S5P HCHO column validation (**chapter 22**). Brief concluding remarks are given in **chapter 23**.

Finally, the thesis closes with a summary of the newly developed methodologies and main results followed by the conclusions and recommendations for future work.

Part I

Remote sensing of tropospheric trace gases and aerosols

Chapter 1

The Earth's atmosphere

Contents

In this chapter, the main characteristics of today Earth's atmosphere and its chemical composition and vertical structure are introduced.

1.1 Chemical composition

The current Earth's atmosphere consists of:
(1) a mixture of gases that constitute the dry air,
(2) water in all three phases (gas, liquid, and solid), and
(3) solid or liquid particles, which are called aerosols.

The mixture of gases that compose the dry atmospheric air is entirely free of water and solid or liquid particles. The major components are nitrogen and oxygen, with volume mixing ratios of 78.09 % and 20.95 % (Fig. 1.1). This composition of the dry atmospheric air is stable from the surface up to 85 km, where the mixing ratio of each of these both components remains the same. This layer of the atmosphere, which is well mixed, is called the homosphere, while the layer from 85 km and upper is the heterosphere.

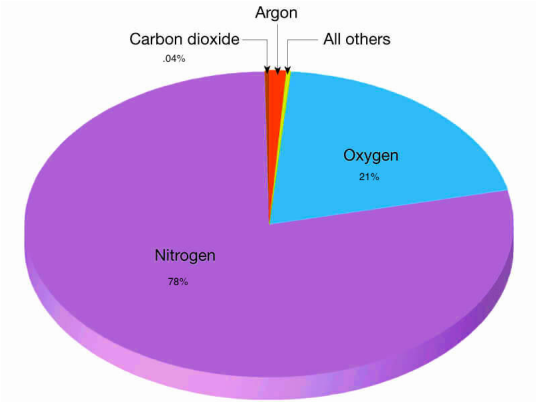

Figure 1.1: Permanent gaseous constituents of the atmosphere (Source: https://www.rajras.in/).

Except for these permanent gases, the dry air contains other gases in considerably smaller and variable quantities such as carbon dioxide (CO_2), carbon monoxide (CO), nitrogen oxides (NO_x), ozone (O_3), bromine monoxide (BrO), ammonia (NH_3), sulfur compounds, etc. These trace species are relevant for atmospheric chemistry, climate, and human health. An example is CO_2, which plays a crucial role as a climate gas with its concentrations continuously increasing due to anthropogenic activity since the start of the industrial revolution in 1750 (Dunn et al., 2020). Atmospheric CO_2 data from the National Oceanic and Atmospheric Administration (NOAA) (https://gml.noaa.gov/) and ETHZ (https://iac.ethz.ch/) show that nowadays, the amount of CO_2 in the atmosphere is 40 % higher compared to the Industrial Revolution.

The abundance of these trace gases can be expressed using different variables. Here, we present three of them that are widely used in this thesis. A first variable is the number density which is the number of gas molecules per unit volume of air (units of molecules/cm^3). The quantity of a specific gas can be also expressed as a partial or total column, which is the number of the gas molecules inside an air column, whose basis has a unit area. A partial column is calculated between two altitudes, while a total column is integrated over the full atmospheric height. Columns are expressed in units of molecules/cm^2.A third variable is the mixing ratio of a gas which is defined as the ratio of the number of trace gas molecules per unit volume divided by the number density of air (units of moles per moles). Volume mixing ratios (VMRs) are often expressed as parts per million volume (ppmv or ppm=10^{-6} mol/mol) or parts per billion volume (ppbv or ppb=10^{-9} mol/mol).

The abundance of these trace gases is highly variable and depends on their lifetime, emission sources, transport, removal processes, and temporal variability. In addition to gases, the Earth's atmosphere contains aerosols in the form of stable suspensions of solid and/or liquid particles in the air. They are emitted and produced from various sources, both natural and anthropogenic. Their presence in the atmosphere results in the condensation of vapors and the formation of clouds. They affect the intensity of solar radiation that reaches the Earth's surface through the processes of scattering and absorption (Allegre et al., 1995). Additionally, aerosols can influence the tropospheric chemistry through heterogeneous reactions (Wei, 2010).

1.2 Barometric equation

The atmosphere can be considered as a gaseous spherical layer around Earth separating the Earth's surface from the outer space. In the vertical direction, the main force affecting the atmosphere is gravity. At sea-level altitude and under standard conditions, because of the atmosphere's weight, the pressure is equal to:

$$p_0 = 1.013\text{bar} = 1\text{atm} \tag{1.1}$$

Pressure decreases with height. According to Boyle-Mariotte's law, the density is proportional to the pressure:

$$dp = -\rho g dz \tag{1.2}$$

which means that an increase dz in height results to a pressure decrease equal to dp (Fig. 1.2). Equation (1.2) is called the barometric equation.

Considering an ideal gas of 1 mole, the equation of state is:

$$pV = RT \tag{1.3}$$

The density is defined as:

$$\rho = \frac{M}{V} = \frac{Mp}{RT} \tag{1.4}$$

When inserting Eq. (1.4) to Eq. (1.2), we obtain:

$$dp = -p\frac{Mgdz}{RT} \tag{1.5}$$

The ratio between dp and dz in Eq. (1.5) gives the hydrostatic equation, which is widely used in atmospheric science.

By integrating Eq. (1.5), we obtain:

$$p(z) = p_0 \exp(-g\rho_0 z/p0) \tag{1.6}$$

where p is the pressure, M the molar mass, g the gravitational acceleration, R the universal gas constant, T the temperature, z the height, V the volume and ρ the mass density.

Equation (1.6) is called the barometric equation.

The quantity $p_0/g\rho_0$ is called scale height H and for air with temperature equal to 25°C, it is equal to 8.4 km.

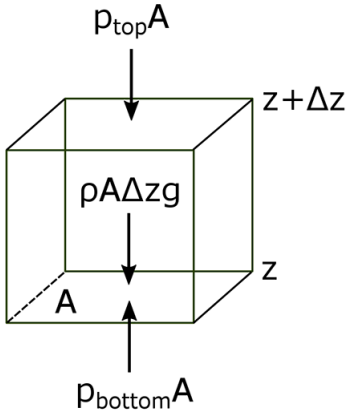

Figure 1.2: Vertical forces acting on an air volume of thickness Δz and area A (Source: https://dlpng.com/).

Contrary to air pressure, the temperature does not necessarily decrease with altitude. When the temperature decreases with height, a layer of warm air at the surface is overlain by colder air. In this case, vertical mixing occurs because of the lower density of warm air than cold air. On the other hand, when temperature increases with height, the atmosphere tends to be vertically stable.

1.3 Vertical structure

The atmosphere is separated into different regions based on the vertical distribution of temperature on them.

Three main regions can be distinguished: the lower, middle and upper atmosphere (see Fig. 1.3). The lower atmosphere extends from the Earth's surface until the top of the troposphere (around 10 km at mid-latitude), the middle atmosphere, which contains the stratosphere and the mesosphere, and the remaining upper part of the atmosphere. As also shown in Fig. 1.3, from the Earth's surface to space, the atmosphere is divided into four main layers: the troposphere, the stratosphere, the mesosphere, and the thermosphere (Seinfeld and Pandis, 2016). Those layers are described below.

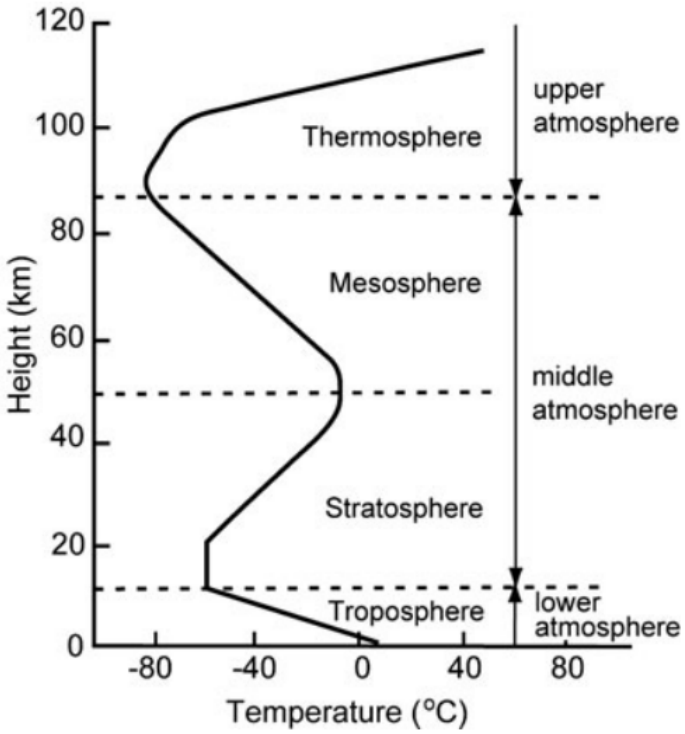

Figure 1.3: Temperature structure of the atmospheric layers (Source: Vardavas and Taylor (2007)).

1.3.1 The troposphere

The troposphere is the lowest layer of the atmosphere, extending vertically from the Earth's surface to a height varying from 10 to 15 km. It contains almost all the atmosphere's water vapor and around 80 % of the total mass of Earth's atmosphere, even though in terms of layer thickness, it is a small fraction of the total atmosphere. The troposphere includes two sub-layers: the planetary boundary layer (PBL) and the free troposphere. The PBL extends from the surface to 0.5 km-2 km height depending on the season and the meteorological conditions and is characterized by rapid vertical mixing and turbulence because of Earth's surface. The free troposphere is located above the PBL and is not directly influenced by the Earth's surface. It is the place where the long-range transport of aerosols and trace gases occurs. Because air pollution is mostly produced at the surface and is generally trapped

inside PBL due to temperature inversion, the concentrations of free-tropospheric trace gases are usually lower than the corresponding concentrations in the PBL.

The boundary between the troposphere and the stratosphere is called the tropopause. The height of the tropopause depends on the latitude, season of the year and daily changes in meteorological conditions. Higher incoming radiation and air temperature leads to more convection and consequently, to an increase of the tropopause height. For example, it is higher over the equator and during warm months than over the poles because of the higher incoming radiation and temperature (see Fig. 1.4). In the troposphere, the temperature usually decreases with altitude. The temperature decreases from the surface to the tropopause at a rate of 6.5Kkm^{-1} on average. This rate is called the lapse rate.

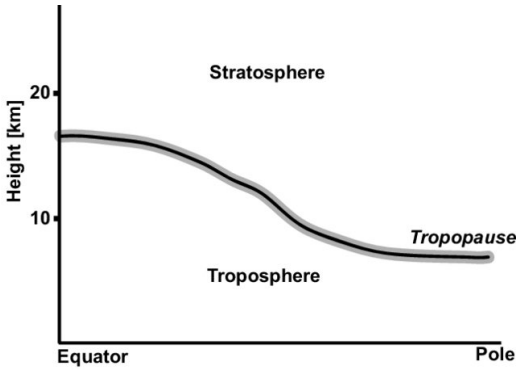

Figure 1.4: Scheme of the tropopause height as a function of latitude
(Source: `https://www.researchgate.net/profile/Renske-Timmermans`).

Under specific conditions, the temperature can increase with height in the PBL. This phenomenon is called temperature inversion and it occurs close to the surface during winter and/or nighttime. It creates a very stable near-surface atmosphere with weak vertical mixing. Consequently, it contributes to the trapping of air pollution inside this layer (Seinfeld and Pandis, 2016).

1.3.2 The stratosphere

The stratosphere extends from the tropopause up to 45-55 km altitude and the so-called stratopause. It is a dry layer because tropopause acts like a cooling trap. Low temperatures are observed in this layer. In contrast to the troposphere, the temperature is constant up to a certain height (20 km in Figure 1.3) and then, it increases with altitude. Stratosphere is surrounded by a warmer layer above and a cooler layer below, which makes it a dynamically stable layer. Because of the temperature vertical distribution, stratosphere is stratified and therefore, slow vertical mixing occurs (see section 1.3.1). In the stratosphere, one can find the ozone layer, which is located between 20 km and 30 km. The reason of the increase of temperature with height is the absorption of harmful UV radiation by O_3, which is crucial for living species. On the contrary, O_3 has toxic effects on humans when located close to the Earth's surface.

Although troposphere and stratosphere are separated layers, exchange between the two can occur through convection in the tropics, in tropopause folds and through subsidence in polar regions (Seinfeld and Pandis, 2016).

1.3.3 The mesosphere

The mesosphere is the layer extending from the stratopause to the mesopause located at 80 - 90 km altitude. The temperature decreases with altitude resulting in rapid vertical mixing. In this layer, the temperature takes its

minimum value (around 170K) at the top of the mesosphere.

1.3.4 The thermosphere

Above the mesosphere, the thermosphere is the fourth layer of the Earth's atmosphere with high temperatures because of the short-wavelength radiation absorption by N_2 and O_2. It extends to a height of around 500 km from the Earth's surface. Above 500 km, there is the outer part of the atmosphere, which is called the exosphere. There, because of the high temperature, gas molecules can escape from the Earth's gravitational attraction.

Chapter 2

Radiation in the Earth's atmosphere

Contents

The observed solar radiation at the Earth's surface gives valuable information about the atmospheric composition. In this chapter, we describe the processes that atmospheric trace gases and particles undergo in the presence of radiation in the atmosphere. First, the Sun's radiation reaching Earth's atmosphere is described, and after, the three main types of interaction between radiation and matter, which are the absorption (and emission) and scattering, are presented. Finally, the greenhouse effect is described as it plays a crucial role in Earth's radiation budget.

2.1 Solar radiation

The Sun is the central star of our solar system sending out a constant flow of charged particles (i.e. solar wind). Solar wind travels accross all the planets before being impeded by the interstellar medium forming a giant bubble around the sun and its planets, called the heliosphere. Sun supplies all bodies inside the heliosphere with different energy forms. Solar energy is categorized into four different phenomena depending on the Sun's activity: solar wind, solar flares, coronal mass ejections, and solar radiation (Güdel, 2007).

The Sun's phenomenon, which is the most important for life on Earth, is solar radiation. The outer 500 km of the Sun, called the photosphere, emits most of the radiation received on Earth. The light emitted by the Sun is in the form of electromagnetic radiation, which has particle and wave properties simultaneously. When the waves leave the Sun, they propagate through space in an area without current and charges. In this region, the electromagnetic waves propagate with their vectors of the electronic and magnetic fields perpendicular to the propagation direction. Since the two fields in this region are perpendicular to each other, the plane parallel electromagnetic wave can be connected with light speed. Additionally, the light can be explained by discrete energy quantities: the photons. For atmospheric sciences, the concept of photons explains phenomena like emission and absorption by atmospheric species.

Solar radiation heats the Earth's atmosphere in the form of electromagnetic waves. The arriving radiation is distributed across the electromagnetic spectrum and includes X-rays, gamma rays, visible light, UV light, infrared and radio waves (Figure 2.1). Even though the Sun radiates over the entire electromagnetic spectrum, most of the

energy is concentrated near the Visible portion of the spectrum (400-700 nm), as shown in Figure 2.1. A black body with a temperature of approximately 6000 K can approximate the Sun's spectrum, which arrives at the top of the atmosphere. The intensity of radiation, which is emitted by a blackbody, is given by Planck's law as follows:

$$B_\lambda(T) = \frac{2\pi hc^2\lambda^{-5}}{\exp(hc/\lambda kT) - 1} \tag{2.1}$$

where B_λ is the irradiance, λ the wavelength, T the temperature, c the speed of light, h the Planck's constant ($h = 6.626 * 10^{-34}$ J s), and k is the Boltzmann's constant ($k = 1.381 * 10^{-23}$ J K^{-1}) (Rybicki and Lightman, 2008).

Wien's law is an approximation of Planck's law for short wavelengths. Wien's displacement law (Feynman et al., 1965) gives the wavelength position of the maximum amount of radiation, which is emitted by a blackbody:

$$\lambda_{max} = \frac{b}{T} \tag{2.2}$$

where b is the Wien's constant (2897 Kμm). For a temperature of approximately 6000 K, the wavelength of the maxima of solar radiation is located at 480 nm (Figure 2.1).

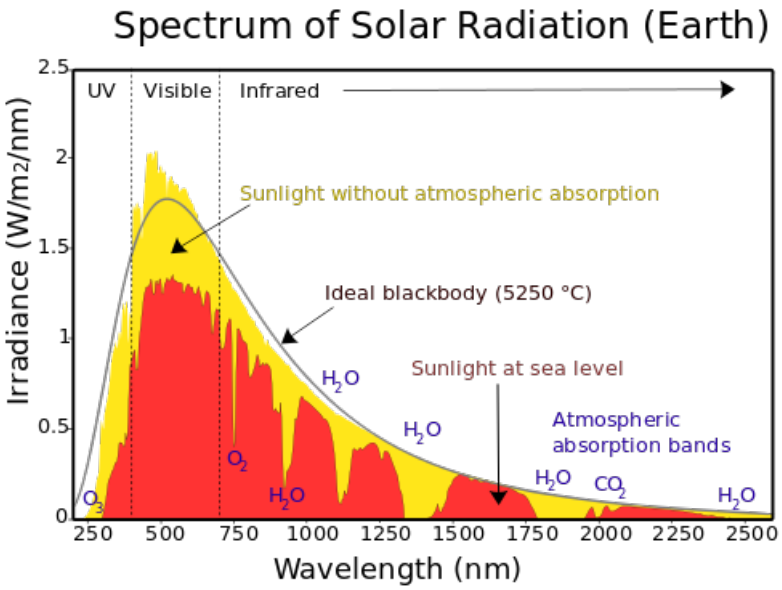

Figure 2.1: Solar spectrum and atmospheric absorbing gases from 240 nm to 2500 nm wavelengths (Source: www.e-education.psu.edu/meteo300/node/683)

.

In the Earth's atmosphere, the solar radiation is attenuated by scattering and absorption. In particular, strong absorption is associated to species such as O_3, O_2, H_2O and CO_2. Due to these effects, the solar radiation at the Earth's surface is less than the one that arrives at the top of the atmosphere and depends on many parameters such as the geometry, weather conditions, and absorbers abundancy in the atmosphere. Most of the Earth's surface encountering the highest incoming solar radiation is located in the equator.

2.2 Interaction of radiation and Earth's atmosphere

A photon emitted by the Sun undergoes various interaction processes when reaching the Earth's atmosphere (Figure 2.2). More specifically, the photon can be scattered by air molecules, aerosols, and cloud droplets, absorbed by the atmospheric constituents and/or absorbed or reflected by Earth's surface. In the following sections, we present the interaction processes of radiation in Earth's atmosphere.

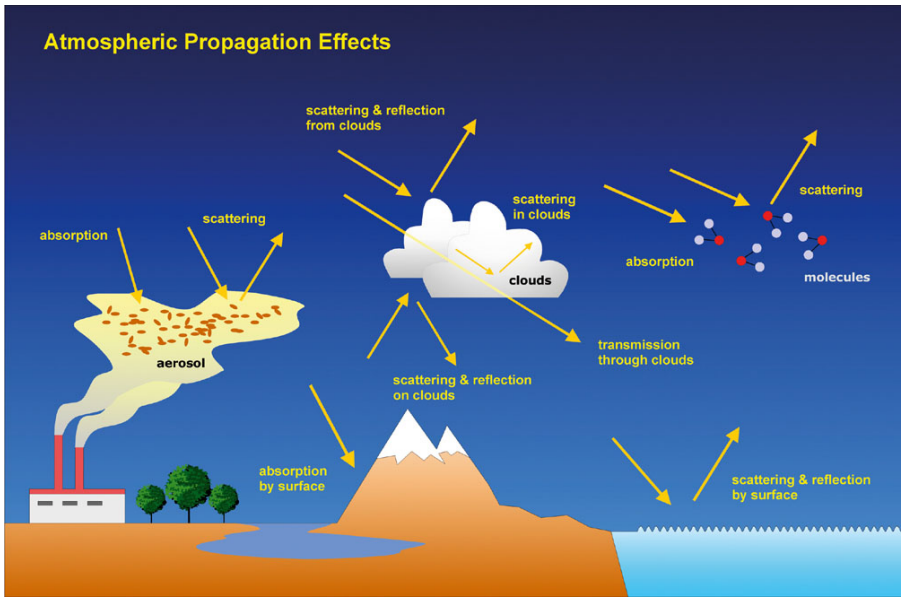

Figure 2.2: Scheme of the interactions of solar radiation with the Earth's atmosphere and surface. (Source: DLR-IMF)

.

2.2.1 Absorption and emission

The total energy of a molecule is the sum of the following four individual energies:

$$E = E_{electronic} + E_{vibrational} + E_{rotational} + E_{nuclearspin} \tag{2.3}$$

where $E_{electronic}$ is the energy of the electron shell's state, $E_{vibrational}$ is the energy of the vibrational state, $E_{rotational}$ is the energy of the rotational state and $E_{nuclearspin}$ is the nuclear spin energy. $E_{nuclearspin}$ is very small compared to the other three energies and is often neglected.

Interferences between the molecule and external electromagnetic fields (light) lead to changes of these states because of uptake or release of photons whose wavelength corresponds to the difference between the initial and final state molecule energies. The above-mentioned uptake and release of photos are called absorption or emission, respectively.

The electromagnetic spectrum consists of different wavelengths. Each wavelength has a certain energy and frequency:

$$v = \frac{c}{\lambda} = \frac{E}{h} \tag{2.4}$$

where v is the frequency, c is the speed of light, h is the Planck constant, and E is the energy.

The transition from an initial to a final state is explained as an interaction between the electromagnetic field and the molecule's dipole moment (e.g. the magnitude of the charge at either end of molecular dipole times the distance between the changes). Two cases can be distinguished:

1. The dipole moment does not change between the two states, and the transition is forbidden.

2. The dipole moment changes when a photon of the wavelength corresponding to the transition is absorbed or emitted. The photon must have the energy difference between the two states. Consequently, a sharp peak appears at the respective position in the absorption (or emission) spectrum, broadened because of natural, Doppler, and pressure broadening.

The energies are:

$$E_{electronic} > E_{vibrational} > E_{rotational} \tag{2.5}$$

A molecule in a certain state consists of the electron shell's energy levels, each having a system of vibrational levels built on them. Each vibrational level has a system of rotational levels build on it as well. Consequently, when a molecule absorbs a photon, its electronic, vibrational, and rotational states are excited (Figure 2.3).

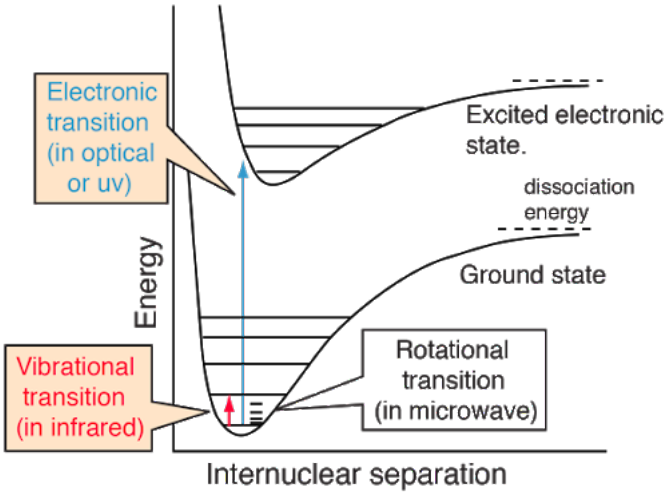

Figure 2.3: Scheme of a molecule's electronic transition, in which energy types (electronic, vibrational, and rotational) may change (Source: http://hyperphysics.phy-astr.gsu.edu/)

To conclude, each trace gas has a characteristic absorption spectrum (the so-called fingerprint), which results from inner-molecular energy levels, transitions between them, and mechanisms determining the probability of different transitions.

2.2.2 Scattering

In the atmosphere, molecules of trace gases and/or particles can scatter the incoming radiation. There are two main scattering process types:

1. The elastic scattering in which the photon energy (e.g. the wavelength) does not change because of the scattering process, but the direction of the initial photon changes. The elastic scattering depends on the ratio of the particle size to the incident radiation's wavelength and is called Rayleigh or Mie scattering.

2. The inelastic scattering in which the photon energy change due to the scattering process. It is referred to as Raman scattering by air molecules.

Scattering can be either a sink or a source of radiation. Depending on the ratio of the size of the scattering particle to the wavelength of incident light, different regimes of atmospheric scattering can be distinguished (Figure 2.4).

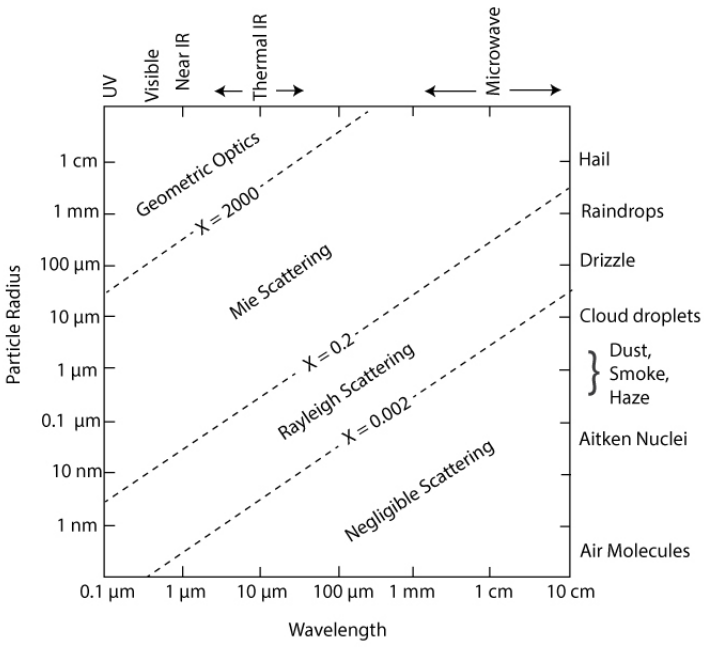

Figure 2.4: Scattering as a function of radiation wavelength and particle radius (Petty, 2006)

These scattering processes are described in more detail in the following sections.

Rayleigh scattering

Rayleigh scattering is the dominant atmospheric elastic scattering process in which the size of particle is small compared to the incident light. In the atmosphere, these particles are mostly air molecules (e.g. N_2 and O_2) and aerosol particles with a diameter smaller than 0.1 µm for the UV and Visible radiation ranges.

Particles themselves radiate as dipoles. The wavelength of incoming and outgoing radiation is the same but the angular distribution is changed. The blue sky under clear sky conditions is caused by Rayleigh scattering because shorter wavelengths are scattered more efficiently by air molecules, and consequently, most of the UV radiation is scattered before reaching the Earth's surface. The Rayleigh scattering cross-section (e.g. total amount of scattered light) is given by:

$$\sigma_{\text{Rayleigh}}(\lambda) = \frac{8\pi^3}{3\lambda^4 N_{\text{air}}^2}(n_0(\lambda)^2 - 1)^2 F_k(\lambda) \tag{2.6}$$

where $n_0(\lambda)$ is the refractive index of air, N_{air} is the air number density, and $F_k(\lambda)$ is the correction for the polarization of air molecules ($F_k(\lambda)$=1.061).

Equation 2.6 gives the wavelength dependence of the Rayleigh scattering, which is inversely proportional to the fourth power of wavelength. Therefore, Rayleigh scattering is significant for short wavelengths (UV/Vis wavelength ranges) but rapidly negligible for longer wavelengths.

The above-cited equation can be simplified for wavelength ranges of 0.2 μm $< \lambda <$ 0.55μm (Nicolet, 1984):

$$\sigma_{\text{Rayleigh}}(\lambda) \approx 4.02 \frac{10^{-28}}{\lambda^{4+x}} \tag{2.7}$$

where $x = 0.389\lambda + \frac{0.094}{\lambda} - 0.333$

Therefore, the wavelength dependence of the Rayleigh scattering is strong. The Rayleigh phase function is given by:

$$P(\cos(\vartheta)) = \frac{3}{4}(1 + \cos^2(\vartheta)) \tag{2.8}$$

where ϑ is the scattering angle.

The phase function describes the distribution of scattered light as a function of scattering angle (e.g. relative amount of light equal to P). For Rayleigh scattering, the scattered light is mainly scattered in the forward or backward direction (see Figure 2.5).

Rayleigh scattered light is strongly polarized for 90° scattering angle.

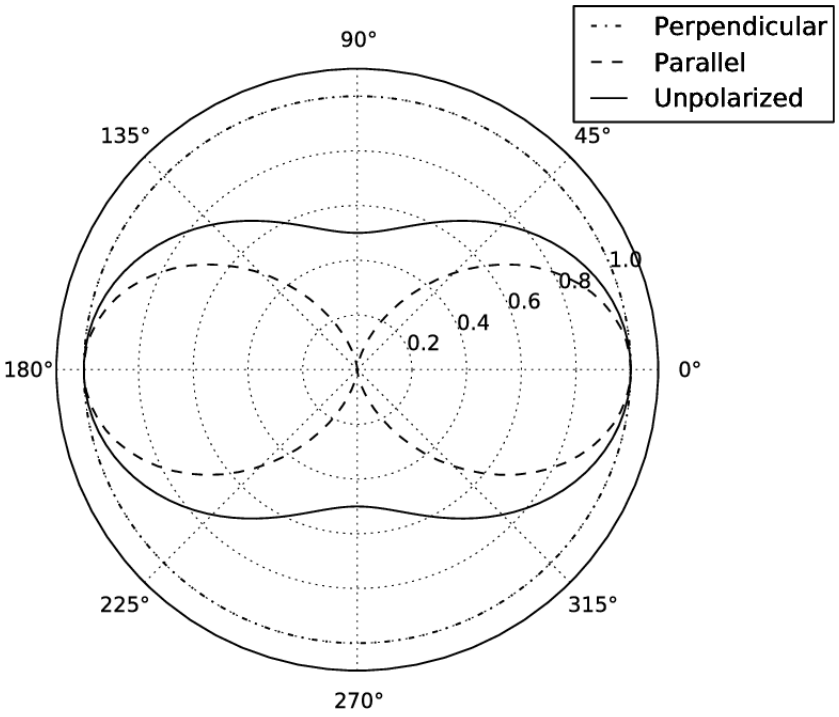

Figure 2.5: Rayleigh phase function for non-polarized light. The dotted line shows the contribution of light polarized parallel to the scattering plane, while the dot-dashed lines shows the contribution from light polarized perpendicular to the scattering plane (Haiducek, 2010)

.

Mie scattering

Mie scattering is an elastic scattering process. It occurs on particles that have a diameter comparable to or larger than the wavelength of the incident radiation (in the UV and Visible wavelength ranges). These particles are mainly aerosols and water droplets.

The Mie scattering cross-section is more complicated than for Rayleigh scattering, and a simplified relationship is given by:

$$\sigma_{\text{Mie}} \propto \lambda^{-\alpha} \tag{2.9}$$

where α is the size parameter depending on the particle size and it is calculated as:

$$\alpha = \frac{2\pi r}{\lambda} \tag{2.10}$$

For large particles, α is small. For the atmosphere, a typical value of α is 1.3. Therefore, the wavelength dependency is much weaker than for Rayleigh scattering.

The Mie phase function is given by:

$$P(\cos(\vartheta)) = \frac{1 - g^2}{4\pi(1 + g^2 - 2g\cos(\vartheta))^{\frac{3}{2}}} \tag{2.11}$$

where g is the asymmetry factor with a typical value in the range of 0.6-0.7 for tropospheric aerosols. This is the Henyey-Greenstein parameterization and the most common parameterization for the Mie phase function (Henyey and Greenstein, 1941).

For Mie scattering, the forward direction is favorized in contrast to the Rayleigh scattering (see Figure 2.6). In general, Mie scattering is not polarizing.

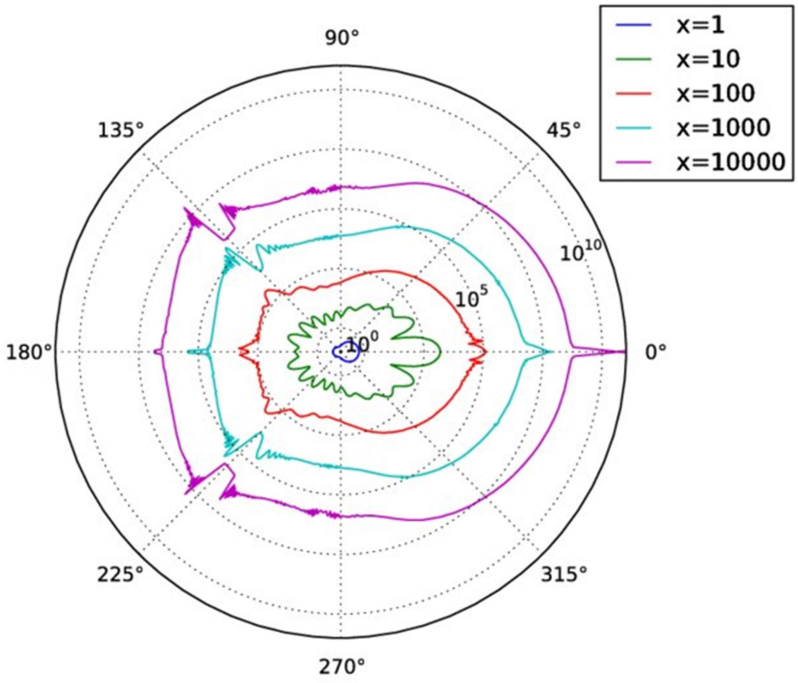

Figure 2.6: Mie phase function for different size parameters. The radial axis is a logarithmic scale and the angles are relative to the direction of propagation (Haiducek, 2010).

Aerosol scattering

Aerosols have a major impact on Earth's climate and radiation. Aerosols consist of a large group of different particles with different sizes, shapes, colors, and properties. Scattering or absorption of sunlight are the direct effects that aerosols have on Earth's radiation field. It is estimated that aerosols and clouds reflect about a quarter of the incoming Sun's radiation to space. The scattering due to the presence of aerosols is described analytically in Mie theory (see section **2.2.2**).

Additionally, depending on their color and properties, aerosols can contribute to atmospheric heating or cooling. For example, dark aerosols, such as black carbon, absorb radiation, resulting in atmospheric warming and shading of Earth's surface (Ramanathan and Carmichael, 2008). On the other hand, nitrates-based aerosols reflect the radiation resulting in atmospheric cooling. Aerosols can change the reflectivity (albedo) of the Earth's surface.

Multiple scattering

When radiation is scattered by only one scattering event, the effect is called single scattering. On the contrary, when multiple scattering events scatter more than one time the radiation, the effect is called multiple scattering. For single scattering, the scattering event's location is not known relative to the radiation path, and the single scattering can be treated as a random phenomenon. Multiple scattering is usually more stochastic. In the Earth's atmosphere, multiple scattering occurs when there is a large density of aerosols resulting in a small visual range.

The Ring effect

Rayleigh and Mie are elastic scattering processes in the Earth's atmosphere. Additionally, inelastic Raman scattering on air molecules can be present, and occurs if the scattering particle changes its state of excitation during the scattering event. If the rotational state of the scattering particle changes, the Raman scattering is called rotational. Raman scattering does not polarise. So, it slightly depolarizes the sky light.

Raman scattering moves energy from the incoming wavelengths to neighboring wavelengths and therefore, changes the spectral distribution in the scattered light.

A consequence of rotational Raman scattering in the Earth's atmosphere is the Ring effect (Grainger and Ring, 1962). The Fraunhofer lines, which are created in the solar atmosphere due to absorption by molecules and ions, have different depths between the direct and scattered light. More precisely, in spectra of scattered sunlight, the Fraunhofer lines are not so deep as expected.

So, on remote sensing observations (see chapter **4**), the Fraunhofer lines do not cancel out for scattered and direct light measurements, leading to large spectral structures that need to be corrected.

2.3 Greenhouse effect

The Greenhouse effect is a natural and crucial radiation process for Earth. Some sunlight that hits Earth is reflected back into space. The incoming solar radiation causes the warming of the Earth's surface. Then, the warm surface emits infrared radiation, which is absorbed by the greenhouse gases. So, the infrared radiation is trapped in the troposphere by the presence of these gases. It is estimated that the Greenhouse effect keeps the Earth's temperature at around 33^{o}C warmer than it would be if the Greenhouse effect did not exist.

Greenhouse gases, such as carbon dioxide, methane, nitrous oxide, and ozone, are produced in larger quantities by human activity, resulting in additional absorption of the outgoing long-wave radiation (IR). Consequently, more energy is captured inside the Earth's atmosphere and not re-emitted into space. The anthropogenic greenhouse gases (GHGs) ability to absorb Earth's outgoing radiation determines the radiative forcing. The 2021 Intergovernmental Panel on Climate Change (IPCC) report concludes that the anthropogenic influence on Earth's climate is discernible. Therefore, it is inevitable that human activities have a positive effective radiative forcing, with the total anthropogenic effective radiative forcing over the industrial era to account for 2.3 Wm^{-2}.

NO_x have both a direct and indirect effect on radiative forcing and consequently, on climate. The direct effect of NO_2 is the heating of the atmosphere as a result of absorption of UV/Vis radiation. Compared to CO_2, the global

mean contribution of NO_2 is small. NO_x affect indirectly the radiative forcing of the atmosphere through its influence on other atmospheric compounds, such as OH. For example, NO_x have a cooling effect because high NO_x levels result on high OH and consequently, low methane levels, which is an important GHG. Additionally, tropospheric NO_2 play a crucial role in the tropospheric O_3 creation process, which is an important GHG. Therefore, accurate long-term monitoring of NO_2 and aerosol abundances are also of major importance in this context of greenhouse effect.

Chapter 3

Chemistry of the troposphere

Contents

As presented in the previous chapter, tropospheric trace gases and aerosols interact with the incoming solar radiation, which is then used to measure their abundances via remote sensing techniques (see chapter 4). Additionally, trace gases and aerosols interact between each other via chemical reactions and cycles.

In this chapter, a general overview of the tropospheric chemistry is given with focus on the chemistry of nitrogen species, formaldehyde and aerosols, which are the main target species of the present work.

Over the last decades, human activities have influenced the composition of the atmosphere.

Nowadays, scientists are asked to answer various questions such as:

- What is the spatial and temporal distribution of trace gases globally but also locally?
- Which reactions are producing important atmospheric pollutants and under which atmospheric and meteorological conditions?
- What are the sources and sinks of the atmospheric species?
- How anthropogenic activities impact atmospheric chemistry?

To carefully address these questions, knowledge of the tropospheric chemistry is therefore essential.

3.1 Air pollution and mixing layer height

3.1.1 Air pollution

An important term in atmospheric studies is the term air pollution. Air pollution is defined as the presence of substances in the atmosphere at concentrations above normal levels due to emissions by anthropogenic or natural

sources. These substances, called pollutants, can influence the radiation, the air quality and the chemistry of the atmosphere. First pollution episodes have already been reported during medieval times (Brimblecombe, 1976). Serious recorded air pollution episodes are linked to industrial development and population growth during the 20^{th} century. A notoriously severe air pollution event was the Great Smog of London (Bell et al., 2004). The reason of the smog formation was the intense coal usage combined with low temperatures, the persistence of an anticyclone and windless conditions. The anticyclone caused a temperature inversion with cold, stagnant air trapped under a layer of warm air (see also section 1.3.1). As a result, a thick layer of smog stayed above the city of London during 4 days causing between 10.000 and 12.000 deaths.

Nowadays, fossil fuel combustion and agriculture are the two principal sources of atmospheric pollution. In Europe, emissions from road transport were the main NO_x source between 1950 and 1980, which resulted to a massive increase of the emissions of this important pollutant by a factor of 14. To control the NO_x emissions, European policies have been developed resulting to a decrease of these emissions by more than 30% between 1990 and 2005 (Figure 3.1). However, NO_x emissions increased in many Eastern European countries because of their recent economic situation (Vestreng et al., 2009).

Air pollution is mostly observed over large urban cities and industrialized regions and the most important pollutant are, in addition to NO_x, O_3, PM, SO_2 and VOCs, which are all harmful for the human health. To quantify the effect on air quality caused by those compounds, the knowledge of the chemical reactions and cycles in which these compounds are involved is crucial. Since this work is focusing on NO_2 and HCHO, only the NO_x and HCHO main chemical reactions are described here (see sections 3.2 and 3.3 below).

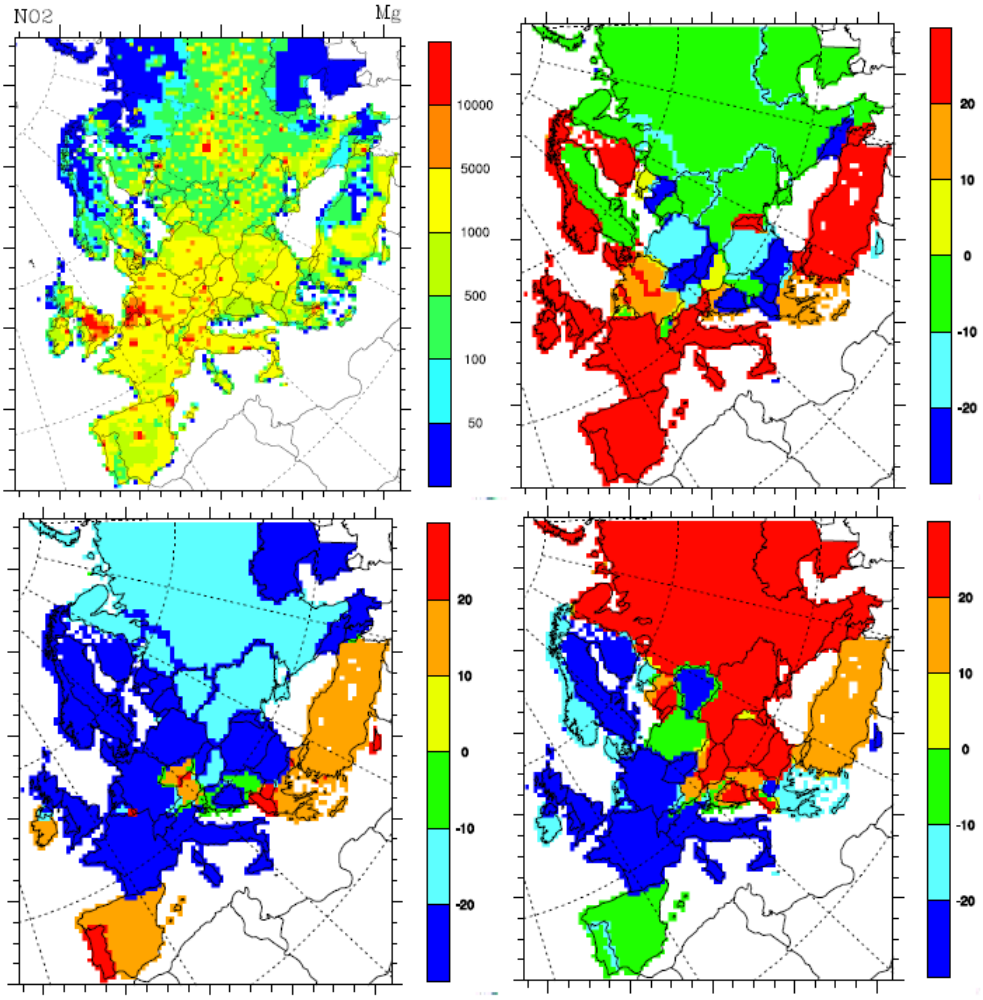

Figure 3.1: Road transport emissions of NO_x (Mg) in 2005 (top left). Difference (in %) in road transport emissions between 1980 and 1990 (top right), 1990 and 2000 (bottom left), 2000 and 2005 (bottom right) (Vestreng et al., 2009)

.

3.1.2 Mixing layer height

The Mixing Layer Height (MLH) is an important meteorological factor, which affects the horizontal and vertical distribution of atmospheric pollutants.

The Planetary Boundary Layer (PBL), which is defined as the height up to which the lower surface's influence is still detectable, has been described in section 1.3.1. The PBL should not be confused with the MLH. The latter is the height up to which atmospheric properties or substances coming from the Earth's surface or formed within this layer, are homogeneously dispersed. This dispersion originates by turbulent vertical mixing processes because of discontinuities in the temperature stratification between the lower and upper layers in the troposphere. The MLH is usually shallower than the PBL and can be determined with the aid of meteorological radiosondes, airplane surveys, and ground-based remote sensing techniques. It should be noted that for NO_2 in urban areas, the hypothesis of constant mixing ratio in the MLH is not valid, where large NO_x emissions occur (Dieudonné et al., 2013). An accurate estimate of the MLH and its diurnal variation is important to quantify the horizontal and vertical distributions of air pollutants, such as NO_2.

In the present thesis, MLH plays a crucial role in the determination of the NO_2 near-surface concentration presented in details in Parts III, IV, and V.

3.2 Nitrogen species

This section focuses on the chemistry of tropospheric NO_x, as the main purpose of the present thesis is the retrieval of tropospheric NO_2 vertical and horizontal distributions in urban conditions. It should be noted that stratospheric NO_x have a different source than tropospheric ones and they act as a catalyst for ozone loss Sillman (1999). Special focus is given on nitrous oxide (N_2O), nitric oxide (NO), nitrogen dioxide (NO_2), reactive odd nitrogen (NO_y), nitric acid (HNO_3), and ammonia (NH_3), which are the most important nitrogen-containing trace gases in the troposphere.

3.2.1 Nitrous oxide (N_2O)

N_2O is a colorless gas, which is mainly emitted by natural sources (e.g. emissions from soil and ocean due to bacteria). It is an important greenhouse gas and the dominant reactive nitrogen source (Nr) in the stratosphere. Over the last 200 years, human activities such as the expansion of agriculture resulted in a considerable increase in the N_2O mixing ratio in the troposphere (Reay et al., 2012).

3.2.2 Nitrogen oxides NO_x (NO+NO_2)

Nitrogen oxides (NOx=NO+NO_2) are essential compounds in atmospheric chemistry. They play a key role in many tropospheric chemical reactions or cycles such as the tropospheric O_3 formation, which is harmful to humans. NO_x are present in both troposphere and stratosphere. In the stratosphere, NO_x are destroying O_3 through conversion of odd to even oxygen. In the troposphere, they are key species in O_3 and HNO_3 formation.

The NO molecule is a stable free radical and a colorless gas. It reacts with other free radicals, in particular OH. NO absorbs in the UV wavelength range and more precisely, below 210 nm.

NO_2 molecule is a chemically reactive gas having a red-brownish color because it absorbs in the UV/Visible wavelength range.

Both species act directly as greenhouse gases and indirectly on climate through O_3 formation and control on the hydroxy radical (OH), and consequently, on the lifetime of other greenhouse gases like methane (CH_4). Additionally, they contribute to aerosol formation (Secondary Organic Aerosols (SOA)), acid rain and photochemical smog events.

NO is emitted by a large number of natural (e.g. lighting and microbial processes in soils) and anthropogenic (e.g. fossil fuel combustion,) sources. NO_2 is mainly produced by combustion processes (industry, vehicles, domestic heating, and power plants; along with NO) and by the oxidation of NO. The road transport sector is found to have a

large contribution to the NO_x formation, followed by energy production (Figure 3.2). More precisely, NO_x is formed when atmospheric air is heated at high temperatures in internal combustion engines through:

(1) the chemical conversion of atmospheric nitrogen and oxygen

(2) the interaction of fuel's nitrogen with atmospheric oxygen.

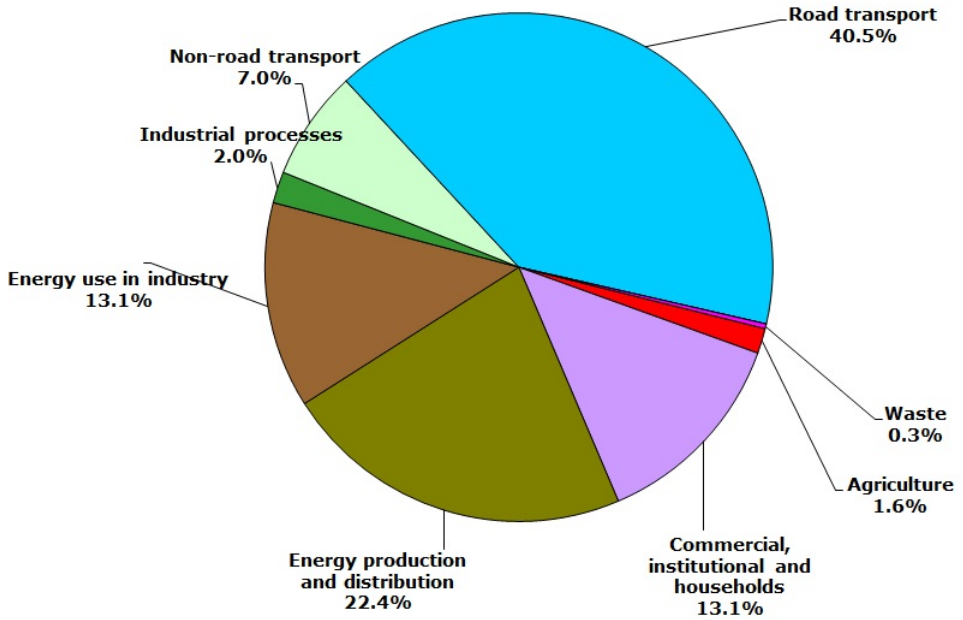

Figure 3.2: Sector share of NO_x emissions (EEA member countries; Source: eea.europe.eu).

Additionally to anthropogenic sources, NO_x are emitted by natural sources, which are mainly forest fires, microbial soil emissions, lighting and oxidation of biogenic NH_3 (Delmas et al., 1997). It should be noted that forest fires and soil emissions can be also attributed partly to anthropogenic activities (i.e. agricultural and domestic fires in addition to wild fires). Globally, anthropogenic and natural sources are equally responsible for the NO_x emissions into the atmosphere. The main difference is that worldwide, NO_x natural sources are more homogeneously distributed than anthropogenic ones (see Figure 3.3).

NO_x can also have a direct and indirect impact on aerosol formation. First, NO_x are a source of HNO_3, which in the presence of ammonia produces semi-volatile ammonium nitrate from which aerosols can be formed. An indirect effect of NO_x is the control of the oxidation capacity of the atmosphere, which influences the formation of sulfate aerosols from SO_2.

NO and NO_2 are rapidly converted into each other and are linked together as NO_x. The ratio $[NO]/[NO_x]$ is about 0.2 during daytime and at the surface but becomes larger with altitude because of the temperature dependence of the reaction between O_3 and NO. The atmospheric lifetime of NO_x is short close to the surface and during summer and increases towards higher altitudes and in winter. Satellite observations have shown that NO_x lifetime is around 4 hours during daytime at low and mid-latitudes, and 8 hours during wintertime in Moscow (Beirle et al., 2011).

Because of its short lifetime, vertical and horizontal transports of NO_x are observed on short distance, which results that NO_x components are found close to their emission sources. A map of average NO_2 tropospheric columns in June 2018 from the TROPOMI/S5P satellite instrument is shown in Figure 3.3. It should be noted that NO_2 is

a very good marker of anthropogenic activities. The highest NO_2 tropospheric columns are observed above densely populated European cities, such as Paris, Rome, and Athens, the BeNeLux countries, and close to the Italian Alpes (Pô valley).

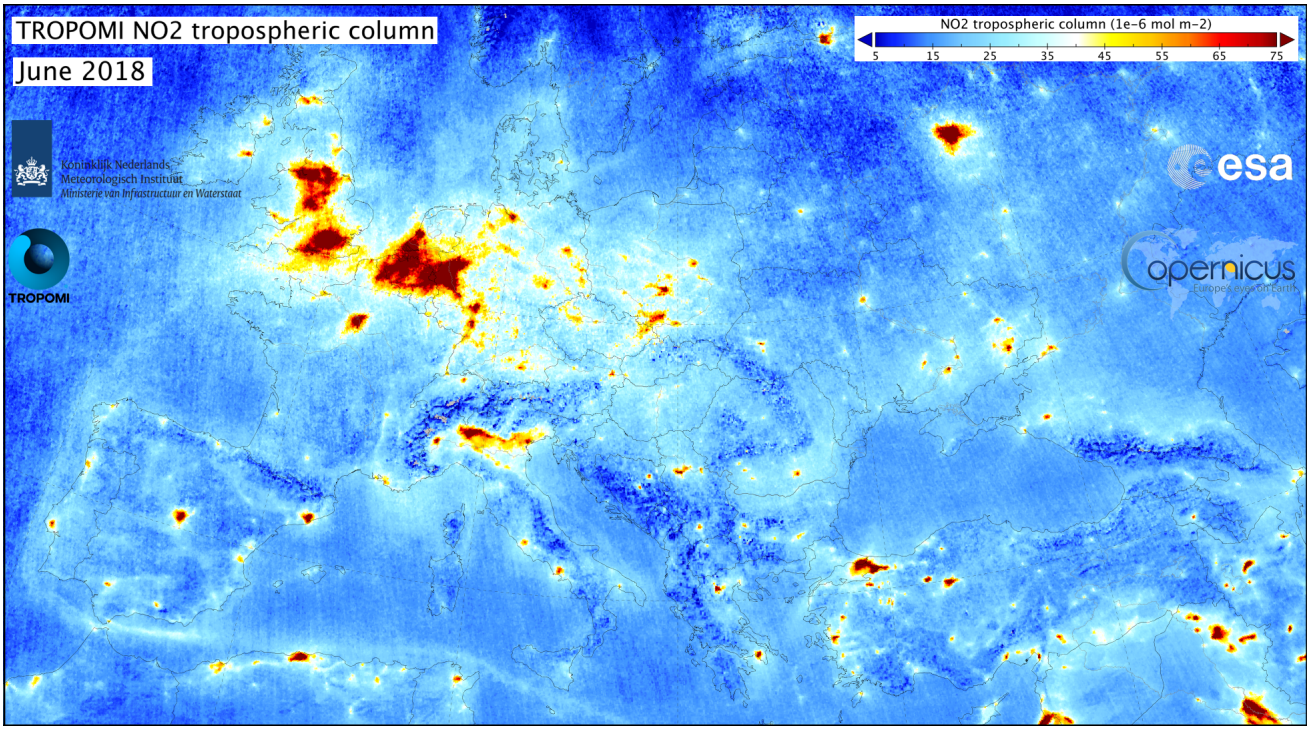

Figure 3.3: Average NO_2 vertical column distribution for June 2018 as seen from the TROPOMI/S5P satellite instrument (Source: http://www.tropomi.eu/).

The main tropospheric chemistry reactions involving NO_x are described below.
In the combustion processes (T > 2200K), the reactions that form NO are the following:

$$O_2 \longrightarrow 2O \tag{R1}$$

$$2(O + N_2 \longrightarrow NO + N) \tag{R2}$$

$$2N + 2O_2 \longrightarrow 2NO + O_2 \tag{R3}$$

After the NO emission, NO reacts rapidly with O_3 to form NO_2, as follows:

$$O_3 + NO \longrightarrow NO_2 + O_2 \tag{R4}$$

Under sunny conditions, the lifetime of NO_2 is short:

$$NO_2 + hv \longrightarrow NO + O(^3P) \tag{R5}$$

which is rapidly followed by:

$$O(^3P) + O_2 + M \longrightarrow O_3 + M \tag{R6}$$

where M is any atmospheric molecule.

As one can see, the initial formation of O_3 in the troposphere is the photolysis of NO_2 for wavelengths smaller than 420 nm.

O_3 is often rapidly oxidized by NO and reforms NO_2 through R4.

During daytime, NO and NO_2 are both present in the troposphere with their concentrations being within one order of magnitude, while during night, NO_2 is dominant. The presence of sunlight defines the different photo-stationary regimes between NO and NO_2 in which O_3 is related to the ration between the concentrations of NO and NO_2. The relationship between them is known as the Leighton relationship (Leighton, 1961):

$$\frac{[NO]}{[NO_2]} = \frac{j}{k}[O_3] \tag{3.1}$$

where j is the photolysis frequency of NO_2 and k is the rate constant for the reaction of O_3 with NO. The above-cited equilibrium is valid in the absence of other species and the reactions do not lead to a net O_3 formation.

However, if other reactions, which convert NO to NO_2 without O_3 conversion, are involved, the result is the O_3 production or destruction.

O_3 production can occur in the presence of hydroxyl (HO_x), peroxy radicals (RO_2), and NO_x. OH radicals are converted to peroxy radicals through reaction with CO or hydrocarbon (HC):

$$OH + CO + O_2 \longrightarrow CO_2 + HO_2 \tag{R7}$$

OH is a highly reactive radical (e.g. lifetime of about 1 second).

$$HO_2 + NO \longrightarrow NO_2 + OH \tag{R8}$$

$$CH_3O_2 + NO \longrightarrow NO_2 + CH_3O \tag{R9}$$

As can be seen, the final product is OH or CH_3O. NO_2 will be photolyzed again to NO.

O_3 can also react with HO_2 radicals, which lead to O_3 destruction:

$$O_3 + HO_2 \longrightarrow OH + 2O_2 \tag{R10}$$

O_3 and OH destruction or production depends on the rates of the above-cited reactions and NO concentration.

It was observed that maximum O_3 concentrations were found downwind of polluted regions, several hours after pollution peaks. Consequently, the relationship between NO_x and VOCs originated from hydrocarbons is not linear

concerning the O_3 production. In the troposphere, two main chemical regimes can be distinguished: the NO_x-limited and the VOC-limited regimes. In the NO_x-limited regime, an increase in NO_x concentrations leads to an O_3 increase, while in the VOC-limited (or NO_x-saturated) regime, the tropospheric O_3 increases when the VOC concentration levels increase.

The way that NO_x are removed from the troposphere depends on the time of the day. During the daytime, OH removes NO_2 and creates HNO_3:

$$OH + NO_2 + M \longrightarrow HNO_3 + M \tag{R11}$$

During the nighttime, O_3 and nitrate (NO_3) removes NO_2 and creates N_2O_5:

$$NO_2 + O_3 \longrightarrow NO_3 + O_2 \tag{R12}$$

$$NO_3 + NO_2 + M \longrightarrow N_2O_5 + M \tag{R13}$$

N_2O_5 may react with H_2O:

$$N_2O_5 + H_2O + \text{aerosol} \longrightarrow 2HNO_3 \tag{R14}$$

HNO_3 is considered as one of the main sinks for NO_x. HNO_3 can afterwards be removed by wet deposition, because of its high water solubility, and can contribute to acid rain. Another sink for NO_x is its reaction with carbonyls and after, the formation of peroxyacyl nitrate (PAN). PAN has a longer lifetime because it is less soluble in water.

3.2.3 Reactive odd nitrogen (NO_y)

NO_y is defined as the sum of NO_x and all NO_x oxidation products, such as HNO_3, HONO and NO_3. As mentioned above, HNO_3 is the major oxidation product of NO_x, which is rapidly deposited on the Earth's surface by rain. NO_3 is important on atmospheric composition, especially during nighttime. NO_3 is comparable to OH radical during daytime by transforming the NO_x to HNO_3. Then, HONO is an important source of OH radicals in polluted sites (Nan et al., 2017) as well as polar regions (Villena et al., 2011).

3.2.4 Ammonia (NH_3)

After N_2 and N_2O, NH_3 is the most abundant nitrogen-containing atmospheric compound. NH_3 is mainly emitted by natural sources such as livestock wastes, fertilized soils, vegetation, and the ocean. Anthropogenic sources, including industrial processes, catalytic converts in vehicles, agricultural intensification, and NH_3-based fertilizer use contribute to an NH_3 increase (Clarisse et al., 2009). NH_3 is the most abundant alkaline gas in the atmosphere. The NH_3 oxidation is a tropospheric NO_x source contributing to around 6.6 % to the global NO_x emissions (Jacob, 1999). Additionally, NH_3 plays a crucial role in atmospheric particles formation, visibility diminution and deposition of nitrogen into ecosystems.

3.3 Formaldehyde

Formaldehyde (HCHO), a colorless, flammable gas with an irritating smell, is a prominent aldehyde in the atmosphere. The main sources of HCHO are the photochemical oxidation of hydrocarbons and the direct release during

biomass burning, fossil fuel combustion, and other anthropogenic activities (e.g. fossil fuel combustion and industrial emissions).

The main precursor of HCHO in the background troposphere is CH_4 because of its significantly higher concentration compared to non-methane hydrocarbons (NMHCs). There is a considerable contribution in the HCHO production in continental areas from the oxidation of natural and anthropogenic non-methane volatile organic compounds (NMVOCs), such as isoprene. According to Stavrakou et al. (2009), 60 % of the globally produced HCHO comes from CH_4 oxidation, 30 % from the isoprene degradation, 3 % is produced directly or through oxidation of NMVOCs emitted from fire events, and the rest is linked to anthropogenic activities.

The oxidation of CH_4 with OH is as follows (Meller and Moortgat, 2000):

$$CH_4 + OH \longrightarrow CH_3 + H_2O \tag{R15}$$

$$CH_3 + O_2 + M \longrightarrow CH_3O_2 + M \tag{R16}$$

$$CH_3O_2 + NO \longrightarrow CH_3O + NO_2 \tag{R17}$$

$$CH_3O_2 + HO_2 \longrightarrow CH_3OOH + O_2 \tag{R18}$$

$$CH_3OOH + OH \longrightarrow HCHO + OH + H_2O \tag{R19}$$

$$CH_3OOH + OH \longrightarrow CH_3O_2 + H_2O \tag{R20}$$

$$CH_3OOH + hv \longrightarrow CH_3O + OH \tag{R21}$$

where the intermediate products are methyl radical (CH_3), methoxy radical (CH_3O), methyl peroxy radical (CH_3O_2), and methyl hydroperoxide (CH_3OOH). In the absence of NO, CH_3OOH decomposes directly to HCHO. Finally, CH_3O reacts directly with O_2 to form HCHO:

$$CH_3O + O_2 \longrightarrow HCHO + HO_2 \tag{R22}$$

The decomposition of HCHO by the atmosphere is either by photolysis or by reaction with OH or by wet deposition given its short-chained structure making it highly water-soluble. According to R22, this results in HO_2 production, which is an important component in the O_3 formation and in the OH and CO production, influencing therefore the atmosphere's oxidizing capacity.

3.4 Aerosols

In this section, we will focus on tropospheric aerosols. Aerosols are a suspension system of solid or liquid tiny particles in a gas. Particles, and consequently, aerosols are emitted by anthropogenic sources, such as fuel combustion, industrial processes, and natural sources such as dust, sea spray, and volcanoes. Aerosols can contain sulfate, ammonium nitrate, sodium, or other elements (Gilardoni and Fuzzi, 2017). In Europe and the United States, aerosol precursor emissions decreased back to the levels of the 1950s, while in China, they have reached a turning point in recent year. On the contrary, in India, aerosol precursor emissions still increase (Bauer et al., 2020).

Aerosols that are emitted directly in the atmosphere are called primary aerosols. Additionally, aerosols can be formed by gas-to-particle conversion processes, and in this case, they are referred as secondary aerosols. The

mechanisms that lead to organic aerosol formation are the least well-understood aspect of secondary atmospheric aerosols. SOAs are a group of aerosols which are mainly formed from the reactions of Volatile Organic Compounds (VOCs) (Kanakidou et al., 2005).

Their diameter can range from a few nanometers to 10 micrometers. It should be noted that when aerosols are in the atmosphere, they can still change in size and composition via many processes. One of them is coagulation with other particles. The removal of aerosols from the atmosphere is done via dry or wet deposition. In the troposphere, aerosols are not homogeneously distributed through the Earth's atmosphere, and their concentrations show large gradients depending on the considered geographical regions.

The aerosol vertical distribution is usually expressed as the extinction of the solar radiation caused by aerosols' presence as a function of the altitude. The aerosol optical depth (AOD) is a measure of the extinction of solar radiation caused by aerosols' presence in the atmosphere. It is defined as the vertically integrated extinction coefficient B over the altitude:

$$\mathrm{AOD} = \int \mathrm{B}\,\mathrm{dz} \tag{3.2}$$

Aerosol extinction coefficients and AODs show wavelength dependency which is expressed through the Angstrom exponent α:

$$\frac{\mathrm{AOD}(\lambda)}{\mathrm{AOD}(\lambda_0)} = \left(\frac{\lambda}{\lambda_0}\right)^{-\alpha} \tag{3.3}$$

where $\mathrm{AOD}(\lambda)$ and $\mathrm{AOD}(\lambda_0)$ are the AOD measured in two different wavelengths, λ and λ_0, respectively.

The MAX-DOAS observations used in this work are highly influenced by the presence of aerosols. Because of their ability to scatter and absorb the light, they affect the light path distribution, and consequently, they change the horizontal sensitivity of each measurement. For this reason, the aerosol vertical profile needs to be retrieved before the NO_2 vertical profile (see Part III to V).

Chapter 4

Differential Optical Absorption Spectroscopy

Contents

In the previous chapter, we highlighted the importance of measuring tropospheric trace gases and aerosols. A widely known technique for this purpose is remote sensing and more precisely, the Differential Optical Absorption Spectroscopy (DOAS) technique. In the present chapter, the principles of the absorption spectroscopy and the DOAS method are presented.

4.1 Absorption Spectroscopy

The detection of O_3 by Dobson and Harrison (1926) set the start of absorption spectroscopy in environmental sciences.

The main principle of absorption spectroscopy measurements is the use of Lambert-Beer's law, that Pierre Bouguer first presented in 1729. This law says that in a medium of uniform transparency, the light remaining in a collimated beam is an exponential function of the path's length inside the medium.

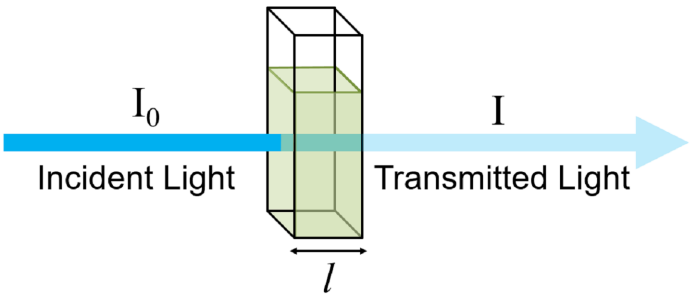

Figure 4.1: Absorption spectroscopy (Source: https://www.edinst.com/).

The Lambert-Beer's law for laboratory measurements, is expressed as follows:

$$I(\lambda) = I_0(\lambda)e^{-\sigma(\lambda)cL} \tag{4.1}$$

where $I_0(\lambda)$ is the intensity of the incident light beam, $I(\lambda)$ the intensity of the light beam after passing through the medium of thickness equal to L, c is the absorber's concentration which is located inside the medium (i.e. constant for laboratory measurements), $\sigma(\lambda)$ is the absorption cross-section as a function of wavelength (i.e. for laboratory studies, it is considered constant along the light path) and L is the length of the light path (see Figure 4.1).

The average concentration of the trace gas of interest is calculated as:

$$c = \frac{\ln\left(\frac{I_0(\lambda)}{I(\lambda)}\right)}{\sigma(\lambda)L} \tag{4.2}$$

where $\ln\left(\frac{I_0(\lambda)}{I(\lambda)}\right)$ is called optical density of a layer of a given absorber and it is dimensionless.

As can be also seen from Figure 4.2, in the atmosphere, more than one molecule may have absorption features at a given wavelength. To separate the absorption of the different species, the DOAS technique uses a continuous spectrum measured in a selected wavelength interval. This allows the separation of the different absorptions by these molecules based on the absorption cross-sections. For this reason, absorption spectra are measured at moderate spectral resolution (around 0.5 nm) in order to identify and separate the different absorbing species.

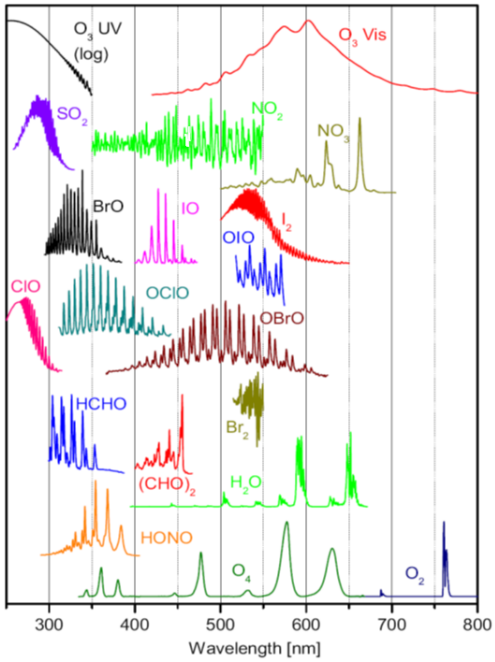

Figure 4.2: Absorption cross-sections of atmospheric species as a function of wavelength (Source: `https://earth.esa.int/eogateway/activities/uv-nadir-viewing-galleries`).

The main principle of the DOAS technique are described in next chapter.

4.2 The DOAS approach

Beer-Lambert's law application is more challenging in the open atmosphere than laboratory studies where $I(\lambda)$ and L are known quantities. In the open atmosphere, the intensity $I_0(\lambda)$ is difficult to determine because, as mentioned above, it is the light intensity that would be measured if no atmospheric absorber would be present. Additionally, more than one absorbers are present in the open atmosphere, each one them participating simultaneously to the light intensity reduction. Apart from the absorption by multiple trace gases, light intensity is also reduced because of scattering by air molecules and aerosol particles via Rayleigh and Mie scattering processes, respectively. Inelastic Raman scattering (Ring effect) influence the light extinction, as well. Assuming a single light path, the Beer-Lambert's law should be adapted as follows:

$$I(\lambda) = I_0(\lambda)A(\lambda)\exp\left(-\int_0^L \sum_{i=1}^{n} (\sigma_i(\lambda, s)c_i(s) + \varepsilon_R(\lambda, s) + \varepsilon_M(\lambda, s) + \sigma_{Ring}(\lambda, s)c_{Ring}(s))ds\right) \quad (4.3)$$

where, $I_0(\lambda)$ is the intensity emitted by a spectral broadband source in the absence of the absorbing trace gases, and $I(\lambda)$ the intensity measured at the end of the light path after passing through the atmosphere. The first term in the exponential is the same as in Eq. 4.1 but a number of absorbers equal to n is introduced because of the presence of various trace gases in the atmosphere absorbing at the selected wavelength. Every trace gas has a characteristic absorption signature which is quantified by the absorption cross-section $\sigma_i(\lambda, s)$. For most atmospheric trace gases, $\sigma_i(\lambda, s)$ vary with wavelength in a unique way. The second ($\varepsilon_R(\lambda, s)$) and third ($\varepsilon_M(\lambda, s)$) terms in the equation

account for the extinction from Rayleigh and Mie scattering processes, respectively. The Ring effect is considered as a pseudo absorber, which has a cross-section equal to $\sigma_{\mathrm{Ring}}(\lambda, \mathrm{s})$ and a density $\mathrm{c}_{\mathrm{Ring}}(\mathrm{s})$. Additionally, the $\mathrm{A}(\lambda)$ term describes the scattering efficiency. These different terms are integrated along the optical light path traveled by the measured photons in the atmosphere, i.e. between 0 (instrument location) and L (light path length in the atmosphere).

As can be seen, the Beer-Lambert law becomes more complicated for applications in the real atmosphere because of the presence of various factors, which change the light's intensity.

Assuming a constant cross-section along the light path, which is an approximation since the cross-sections are slightly temperature and pressure dependent), the optical depth of an absorber, i, is expressed as:

$$\tau_{\mathrm{i}}(\lambda) = \int_0^{\mathrm{L}} \sigma_{\mathrm{i}}(\lambda, \mathrm{s}) \mathrm{c}_{\mathrm{i}}(\mathrm{s}) \mathrm{ds} = \sigma_{\mathrm{i}}(\lambda) \int_0^{\mathrm{L}} \mathrm{c}_{\mathrm{i}}(\mathrm{s}) \mathrm{ds} \tag{4.4}$$

In Equation 4.4, the integral is referred to as slant column density of the absorber i and is defined as:

$$\mathrm{SC}_{\mathrm{i}} = \int_0^{\mathrm{L}} \mathrm{c}_{\mathrm{i}}(\mathrm{s}) \mathrm{ds} \tag{4.5}$$

SC_{i} represents the integrated concentration c_{i} along the light path s and its units are molec.cm^{-2}.

Consequently, when converting Rayleigh and Mie scattering terms to their respective optical depths and by using Equation 4.5, Equation 4.3 becomes:

$$\mathrm{I}(\lambda) = \mathrm{I}_0(\lambda) \mathrm{A}(\lambda) \exp\left(- \left(\sum_{\mathrm{i}=1}^{\mathrm{n}} \sigma_{\mathrm{i}}(\lambda) \mathrm{SC}_{\mathrm{i}}(\lambda) + \tau_{\mathrm{M}}(\lambda) + \tau_{\mathrm{R}}(\lambda) \right) \right) \tag{4.6}$$

where the Ring term is treated as an absorber with a slant column equal to SC_{i}.

DOAS method's main idea is the separation of the different light extinction components into two main categories according to their variation as a function of wavelength. First, we have the slowly-varying terms with wavelength (broad-band structures in the measured spectrum) and secondly, the rapid-varying terms with wavelength (narrow-band structures). Broad-band features are mainly coming from aerosol extinction, instrumental effects, and trace gases with smooth spectral structures and they are accounted for by a polynomial. The narrow-band features are the trace gas absorptions that the DOAS approach aims to derive (Figure 4.3).

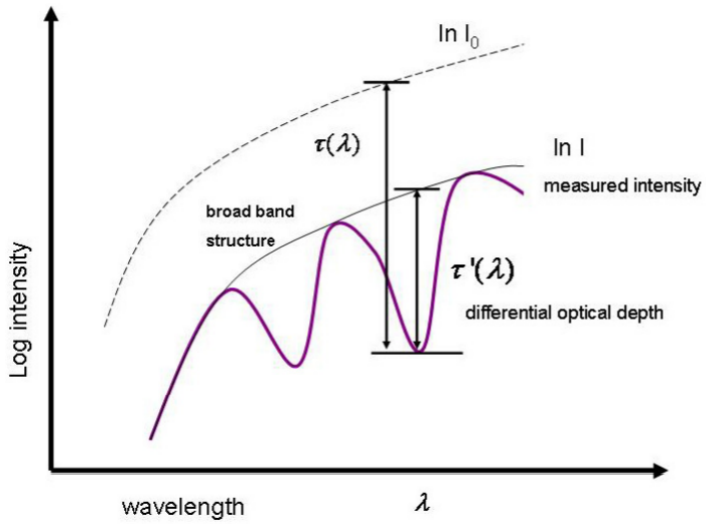

Figure 4.3: Principle of DOAS technique: the narrow and broad band parts are separated by a low-pass filtering procedure (Source: Thesis of J. Hollwedel).

Then, the broad and narrow-band are separated and Equation 4.6 can be rewritten as:

$$I(\lambda) = I_0(\lambda)A(\lambda)\exp\left(-\left(\sum_{i=1}^{n}\sigma_i'(\lambda)SC_i(\lambda) + \sum_k a_k p^k\right)\right) \tag{4.7}$$

where $\sum_k a_k p^k$ is the polynomial accounting for the broad-band structures in the measured spectra and the instrumental effects (A(λ)term which varies slowly with wavelength) and $\sigma_i'(\lambda)$ stands for rapid-varying cross-sections as a function of wavelength and is expressed as follows:

$$\sigma_i'(\lambda) = \sigma_i(\lambda) - \sigma_{i0}(\lambda) \tag{4.8}$$

where $\sigma_{i0}(\lambda)$ is the slowly varying term, and is approximated by the polynomial, which is a polynomial of low-order. $\sigma_i'(\lambda)$ is called differential cross-section.

By taking the logarithm of Equation 4.7, we have:

$$\ln(I(\lambda)) = \ln(I_0(\lambda)) - \sum_{i=1}^{n}\sigma_i'(\lambda)SC_i - \sum_k a_k p^k \tag{4.9}$$

By re-arranging Equation 4.9, we have:

$$\ln\left(\frac{I_0(\lambda)}{I(\lambda)}\right) = \sum_{i=1}^{n}\sigma_i'(\lambda)SC_i + \sum_k a_k p^k \tag{4.10}$$

The term $\ln\left(\frac{I_0(\lambda)}{I(\lambda)}\right)$ is called optical density of the absorber and we refer to as D'.

Equation 4.10 is the so-called DOAS equation.

4.3 The DOAS method in practise

In the DOAS analysis, the main goal is to retrieve trace gases slant columns, SC_i, by using Equation 4.10 in which the differential cross-sections are known from laboratory studies. For this purpose, in the present thesis, we used the software qDOAS, developed at BIRA-IASB (Fayt et al., 2011). $I_0(\lambda)$ is a reference spectrum corresponding to conditions where the absorption by the trace gas of interest is minimum.

$I(\lambda)$ and $I_0(\lambda)$, and therefore D', are measured at discrete wavelengths, λ_i. So, a measured differential optical depth , $D'_{meas}(\lambda_j)$ is calculated. After, a least squares fit is performed and a fitted differential optical depth, $D'_{fit}(\lambda_j)$, is estimated with the help of the known differential cross-sections. The degrees of the fitted polynomial should be chosen carefully to account for broadband effects and then the polynomial's coefficients, a_k, are fitted parameters.

In real measurements, the fitted differential optical depth differs from the measured ones because of noise in the measurements:

$$r_j = D'(\lambda_j) - D'_{fit}(\lambda_j) \tag{4.11}$$

where j indicates the number of the discrete wavelengths.The r_j at the respective wavelength positions λ_j is called the residual spectrum.

The aim of DOAS is to find the best fit parameters (a_k and SC_i) by minimizing r_j:

$$\sum r_j^2 \Rightarrow \text{minimum} \tag{4.12}$$

Although, the DOAS equation is linear (Equation 4.10), non-linear terms must be considered when dealing with shift, stretch, and offset (see below).

The minimization is often achieved by using a non-linear Levenberg-Marquardt fitting procedure. Therefore, the measured D' is equal to the sum of the fitted D' and the residual spectrum:

$$D'(\lambda_j) = D'_{fit}(\lambda_j) + r_j \tag{4.13}$$

Ideally, the residual should not display any systematic structure (i.e. it should be looking like noise) which indicates the presence of cross-sections misfit(s) or a missing cross-section.

From the residual, the root-mean-squared (RMS) is a quality control parameter of the fit and can be calculated:

$$RMS = \sqrt{\frac{1}{N}\sum r_j^2} \tag{4.14}$$

RMS is a measure of the combined random uncertainty of the ratio of the measured and reference spectra.

As mentioned above, this technique can be applied in certain wavelength regions, which are also called fitting windows, to separate the broad and narrow-band structures and retrieve the SC_i of the trace gase of interest successfully. For DOAS applications, the intensity is measured at 500 to 2000 individual wavelengths.

The DOAS analysis has also some specific aspects that need to be treated carefully, We give here a general overview of the most important ones (note that the DOAS applied in this thesis like wavelength intervals, cross sections sources, etc. are described in chapter III, IV, and V separately).

Instrument's response function:

In practice, the measured spectrum $I_{meas}(\lambda)$ by the detector is a convolution between the incoming radiance $I(\lambda)$ with the instrument's response function $F(\lambda)$:

$$(F * I)(\lambda) = \int F(\lambda')I(\lambda - \lambda')d\lambda' \tag{4.15}$$

$F(\lambda)$, which is often called slit function or Instrumental Spectral Response Function (ISRF), can be measured by illuminating the instrument with a monochromatic source of light (e.g. Hg-Cd lamp) and measuring its response.

$F(\lambda)$ can also be determined by analysis of the measured solar lines.

The wavelength interval:

The optimal wavelength interval to retrieve the trace gas of interest is a compromise between maximizing the sensitivity of the trace gas and minimizing interference with other absorbers. It is easy to understand that wavelength regions with high differential cross-sections of a specific trace gas show large optical depths. So, it is in these wavelength regions that the DOAS analysis should be performed.

Choosing the width of the fitting window should be driven by considering the existence of other absorbers in this spectral range. The fitting window should be large enough to decrease cross-sections correlations between existing absorbers inside the considered spectral range and small enough so that the assumption of one light path length in the fitting window is valid (i.e. the light path length depends on the wavelength; see Part IV).

The absorption cross-sections:

The absorption cross-sections are essential for the DOAS analysis. Laboratory measurements of absorption cross-sections at a spectral resolution equal or better than the instrument's resolution are needed. Note that the cross-sections have to be convolved with the instrument's slit function to be at the same resolution as the instrument.

All the absorbers who are present inside the selected fitting window should be taken into account via their corresponding cross-sections. Additionally, most cross-sections in the UV/visible spectral region are temperature dependent. So, the assumption of a constant cross-section along the light-path and consequently, inside the fitting window is not completely valid. For this reason, for certain absorbers, such as O_3 and NO_2, two absorption cross-sections measured at different temperatures are included and a linear combination of both is used in the DOAS analysis.

The reference spectrum $I_0(\lambda)$:

The selection of the reference spectrum $I_0(\lambda)$ is also an important aspect of the DOAS analysis. For ground-based DOAS measurements, there are two different options for determining $I_0(\lambda)$. First, we could use an extraterrestrial measured sun spectrum by another instrument (e.g. satellite), which contains only the Fraunhofer lines and zero light extinction caused by atmospheric absorbers. The use of such reference spectrum has some important negative aspects, which are the different resolution between $I_0(\lambda)$ and $I(\lambda)$, as they have been measured with two different instruments. This could generate artificial structures that could hide small absorption features from atmospheric trace gases.

Secondly, a reference spectrum $I_0(\lambda)$ directly measured by the same ground-based instrument could be selected. It should correspond to conditions (e.g. specific viewing geometry and measurement time) where the absorption by the absorber of interest is minimum. So the direct product of the DOAS analysis is not an absolute but a differential slant column density dSC:

$$dSC = SC - SC_{ref} \tag{4.16}$$

where SC and SC_{ref} are the slant column densities corresponding to the measured spectrum and reference spectrum, respectively.

Shift, stretch and offset

The reference spectrum $I_0(\lambda)$ is calibrated using a high-resolution Fraunhofer atlas (Kurucz, 1984), which is convolved with the instrument's slit function. To achieve the optimal match of the Fraunhofer lines, $I_0(\lambda)$ can be shifted and stretched.

Similarly, to align $I(\lambda)$ and $I_0(\lambda)$, wavelength shift and stretch is also required. Equation 4.10 takes the following form:

$$\ln\left(\frac{I_0(\lambda)}{I(\lambda+\text{shift})}\right) = \sum_{i=1}^{n} \sigma'_i(\lambda) SC_i + \sum_k a_k p^k \tag{4.17}$$

The presence of straylight due to light originated inside the spectrometer should be taken into account by fitting an offset, which will influence the optical depth:

$$\ln\left(\frac{I_0(\lambda)}{I(\lambda+\text{shift})-\text{offset}(\lambda)}\right) = \sum_{i=1}^{n} \sigma'_i(\lambda) SC_i + \sum_k a_k p^k \tag{4.18}$$

By including the offset and shift, the DOAS equation can not be solved linearly and non-linear least-square algorithms should be used to retrieve the optical depth of the absorber of interest.

The Ring effect:
As described in section 2.2.2, the difference between the depth of the Fraunhofer lines in the reference and measured spectra leads to undesired large spectral structures.
To overcome this problem, Ring effect is considered as a pseudo absorber with a specific absorption cross-section.

The solar I_0-effect:
The solar I_0-effect arises due to the different spectral resolutions and light sources used to measure the measured spectra and the laboratory cross-sections (Aliwell et al., 2002).
The solar I_0-effect can be corrected by giving a guess or a known value for the slant column of the strong absorber.

4.4 DOAS measurement type

The ground-based DOAS technique is usually separated into two categories according to the used light source (Platt and Stutz, 2008): (1) active DOAS like the long-path DOAS technique (Pöhler et al., 2010; Platt and Perner, 1980; Volkamer et al., 2005), which uses artificial light, such as xenon arc lamps or light-emitting diodes (LEDs), and (2) passive DOAS, which utilizes light coming from natural sources, like Sun, moon or stars.
Only the different types of ground-based passive DOAS measurements are further described here since only this type of measurements is exploited in the present thesis.
As stated above, ground-based passive DOAS systems use a natural source of light, with the two most important ones being the Sun and the moon.
Two different sub-categories can be distinguished: (1) the direct pointing at the light source, which is referred to as direct-light measurements, and (2) the measurement of the scattered sunlight by air molecules and particles in the atmosphere.
Ground-based passive DOAS measurements are further categorized depending on the location in the atmosphere of the measured trace gas.
For stratospheric absorbers, like O_3 and NO_2, the highest sensitivity is obtained during dawn and dusk in the zenith pointing direction. During twilight conditions, the Sun is very low, so the light path through the stratosphere is maximum and can reach several hundreds of kilometers at SZA larger than 90^o, while the light path through the troposphere is minimum and stays almost constant with increasing SZA. During this period of the day, the mean scattering height is also shifted towards higher altitudes in the stratosphere. The instruments performing these kind of measurements are called zenith-sky DOAS instruments.
The second type of ground-based DOAS measurements consists in pointing to the direct sunlight (direct-sun mode). With these measurements, the light path traverses both troposphere and stratosphere. The instruments performing these type of measurements are called direct-sun spectrometers and measure the trace gas' total vertical column.

A third type of viewing geometry is the off-axis mode where the scattered sunlight is collected at different elevation angles towards the horizon in addition to the zenith. During daytime, the light path through the troposphere becomes larger as the elevation angle becomes lower, resulting in higher sensitivity on trace gases located in the lower atmospheric layers close to the surface. In these high sun conditions, the light path in the stratosphere corresponding to the different elevation viewing angles is similar and the stratospheric content in the off-axis directions can be removed by taking the zenith spectrum of the elevation scan as reference for the estimation of the off-axis differential slant column densities. The latter are therefore only representative of the tropospheric content of the target trace gas. The instruments operating in the off-axis mode are called Multi-AXis DOAS (MAX-DOAS) spectrometers. They can provide information about the vertical profiles of tropospheric trace gases and consequently, also about the near-surface concentrations and vertical column densities. MAX-DOAS spectrometers offer the possibility of performing vertical scans or single elevation angle measurements in more than one azimuthal directions and therefore, provide information about the horizontal distribution of aerosol and trace gases. Only this third type of ground-based passive DOAS measurements are exploited in the present thesis (see Figure 4.4). Additionally, the satellite (chapter 8) and aircraft observations (chapter 9) used in this thesis also use the DOAS technique.

A sketch describing the three different types of ground-based MAX-DOAS spectrometers is shown in Figure 4.4.

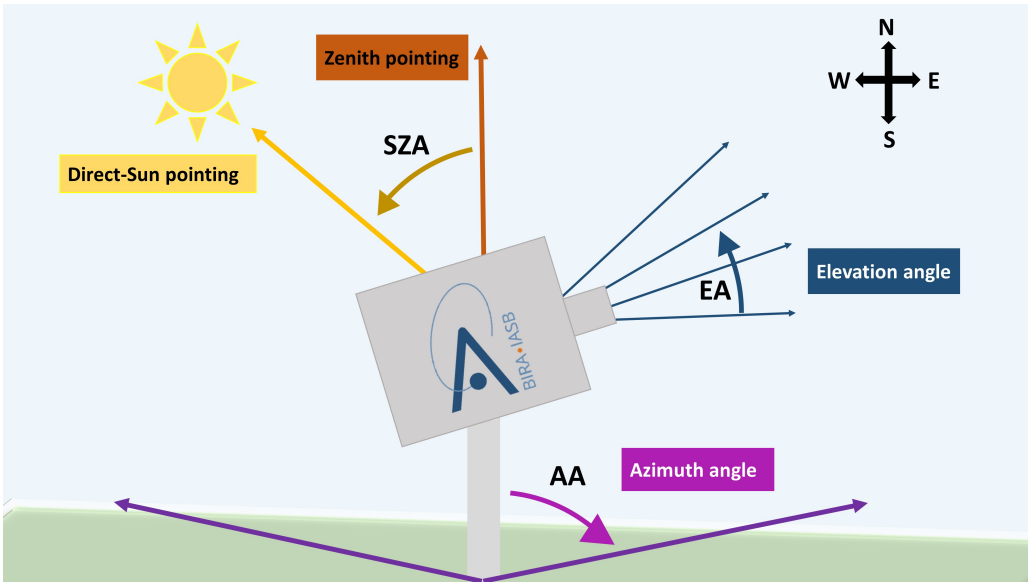

Figure 4.4: Sketch of typical dual-scan MAX-DOAS measurement geometries for a MAX-DOAS instrument.

4.5 Advantages/drawbacks of the ground-based passive DOAS technique

As described above, the passive DOAS technique is a powerful, simple and well-established method for measuring many important atmospheric trace gas species.

The main advantages of this technique are the following:

1. It is a self-calibrated method that by principle does not require constant calibration, in contrast to in-situ techniques.
2. The simultaneous measurements of various atmospheric species.

3. It is a relatively cheap technique which offers the possibility to operate simultaneously multiple instruments at a regional and/or global scale like in the NDACC network.
4. In addition to the vertical column content, information on the vertical distribution of trace gases can be retrieved by using appropriate inversion methods (see chapter 6.2).

Like every method, DOAS has some drawbacks:
1. Absorption cross-sections are considered independent of altitude. So, no information can be gained from spectral measurements on the vertical distribution of the trace gases.
2. Only trace gas species absorbing in the UV-Visible wavelength range can be measured.
3. Depending on the viewing geometry, clouds, rain, and fog can deteriorate the quality of the DOAS measurements.

Chapter 5

Atmospheric radiative transfer

Contents

In the present chapter, the radiative transfer, which is an essential aspect in atmospheric remote sensing applications, is presented. Contrary to direct-sun measurements, sky measurements require complex radiative transfer calculations. The interpretation and understanding of MAX-DOAS scattered-light observations is complicated by the fact that the photons that reach the instrument undergo scattering and absorption processes and therefore travel through various light paths before reaching the instrument. Atmospheric radiative models (RTM) are needed to take into account these aspects and to further interpret the slant column density provided by the DOAS analysis and which corresponds to the integrated concentration of a trace gas along the effective light path followed on average by the photons. This chapter presents the forward part and is divided into two sections: first, the radiative transfer equation is derived, and then, the main characteristics of the RTM used in the present thesis are described.

5.1 The radiative transfer equation

DOAS analysis provides the differential slant column density (dSCD), which is the integrated concentration of the absorber of interest along the light path of the measured spectrum relative to the same quantity in a reference spectrum (see previous chapter). The dSCDs cannot be easily exploited because they depend highly on the sun position, viewing geometry, and state of the atmosphere. Radiative transfer modeling is necessary to simulate the measurements (e.g. dSCDs) and after, with the aid of inversion, to translate these quantities to trace gas vertical profiles and vertical column densities (VCDs). The derivation of the radiative transfer equation (RTE) is described below (see also Friedeburg, 2003).

Assuming a homogeneous thin atmospheric layer with one absorber, the light intensity can be expressed as:

$$I = I_0 \exp(-b_a s) \tag{5.1}$$

where I_0 is the initial intensity, s is the distance traveled by the photon, and b_a the absorption coefficient.

Equation 5.1 is valid when light attenuation comes only from absorption. In reality, light extinction is because of both absorption and scattering. Consequently, the total extinction coefficient b_e is expressed as:

$$b_e(z,\lambda) = b_a(z,\lambda) + b_s(z,\lambda) \tag{5.2}$$

where b_s is the scattering coefficient, z is the vertical coordinate and λ is the wavelength.
Scattering is also characterized by the single scattering albedo (SSA), ω:

$$\omega = \frac{b_s}{b_a + b_s} \tag{5.3}$$

and the vertical optical depth τ:

$$\tau(z, \lambda) = \int_0^z b_e(z', \lambda) dz' \tag{5.4}$$

Let us consider the number of photons, f, as a function of wavelength, crossing an area dA of a solid angle $d\omega$ and which is titled by an angle ϑ against the surface normal n (see Figure 5.1).

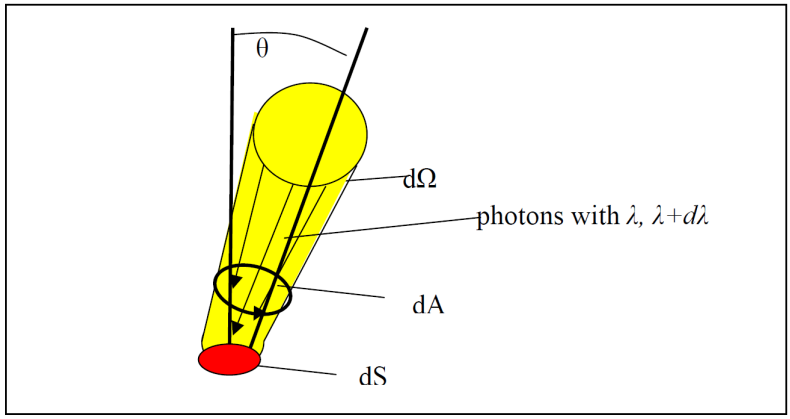

Figure 5.1: Schematic representation of the angles and areas which are used in the derivation of the radiative transfer equation (Friedeburg, 2003).

Boltzmann's equation gives the temporal and spatial evolution of f as follows:

$$\frac{df}{dt} + \frac{d}{d\vec{r}}(\vec{c}f) + \frac{d}{d\vec{c}}(\vec{a}f) = Q(\vec{r}, \vec{n}, \lambda, t) \tag{5.5}$$

where $\vec{c}$ is the light speed term which can be described with the radiation flux and is the net change of photons (i.e. energy) per unit time, f is the distribution function, t is the time, $\vec{a}$ is the azimuth angle, Q is the energy source term, r,$\vec{n}$ is the surface normal, λ is the wavelength.
Considering that $\vec{c}$ remains constant, Equation 5.5 becomes:

$$\frac{df}{dt} + c(\vec{n}\frac{d}{d\vec{r}})f = Q(\vec{r}, \vec{n}, \lambda, t) \tag{5.6}$$

The radiance I and the distribution function are related as:

$$I(\vec{r}, \vec{n}, \lambda, t) = c^2 h \lambda^{-1} f(\vec{r}, \vec{n}, \lambda, t) \tag{5.7}$$

Considering only the time interval dt, which is small compared to time scales of photon flux changes, Equation 5.6 is expressed as:

$$\left(\vec{n}\frac{d}{d\vec{r}}\right) I(\vec{r}, \vec{n}, \lambda, t) = hc\lambda^{-1} Q(\vec{r}, \vec{n}, \lambda, t) \tag{5.8}$$

To quantify the energy source term Q, we should consider a medium which scatters, absorbs and emits the radiation in plane-parallel geometry.

Then, the change in radiance can be expressed as:

$$\cos(\vartheta)\frac{\mathrm{dI}}{\mathrm{dz}} = -\mathrm{b_e(z,L)I} + \frac{\mathrm{b_s(z,L)}}{\mathrm{a}\pi}\int_0^{2\pi}\mathrm{d}\varphi'\int_0^{\pi}\varphi(\mathrm{z},\vartheta,\varphi,\vartheta',\varphi',\lambda)\mathrm{Isin}(\vartheta')\mathrm{d}\vartheta' + \mathrm{b_a(z,L)B(T(z),\lambda)} \tag{5.9}$$

where φ is the phase function for the scattering.

$\frac{\mathrm{dI}}{\mathrm{dz}}$ represents the change of the radiation after moving through a thin layer of thickness dz. The radiance changes via three main processes:

1) Extinction, which is proportional to the radiation available for extinction

2) Scattering coming from photons out of the domain 4π

3) Absorption, which is proportional to the emission

In the UV-Visible wavelength range, there is no emission because excited electronic states get de-excited by collisions and consequently, the last term can be neglected.

When inserting Equation 5.4 and 5.3, Equation 5.9 becomes:

$$\cos(\vartheta)\frac{\mathrm{dI}}{\mathrm{d}\tau} = -\mathrm{I} + \frac{\omega}{4\pi}\int_0^{2\pi}\mathrm{d}\varphi'\int_{-1}^{1}\varphi\mathrm{Id}\cos(\vartheta') \tag{5.10}$$

Equation 5.10 is the RTE for the UV-Visible wavelength range. By neglecting multiple scattering, the equation takes the following form, which is the Lambert-Beer's Law for an initial radiance $\mathrm{I_0}$:

$$\mathrm{I} = \mathrm{I_0}\exp(-\tau/\cos\vartheta) \tag{5.11}$$

The RTE is an integro-differential equation and thus, three main solution approaches exist: (1) analytical, (2) the Monte-Carlo approach. and (3) the doubling adding principle.

In the Radiative Transfer models, because of the complexity in solving Equation 5.10 analytically, a discrete ordinates method is generally applied. Sums replace the integrals in order to have a system of differential equations. We consider a single layer with homogeneous scattering and absorption properties. First, the scattering angle's phase function is expressed by its Legendre polynomials terms, while the intensity is expanded in its Fourier cosine series. Because of the Legendre and Fourier decomposition's orthogonality properties, a system of independent equations is obtained. The number of the equations is equal to the number of Fourier components. Therefore, we have a linear differential system of equations, which is solved for all the assumed atmospheric layers. As with every differential equation's system, boundary conditions are needed, which are the continuity of intensities at the layers' interfaces, the Sun's intensity at the top of the atmosphere, and the surface albedo at the bottom of the atmosphere.

5.2 VLIDORT

Radiative transfer models calculate the intensity of the electromagnetic radiation after traveling through the atmosphere until the instrument. The intensity depends on the wavelength, viewing direction, solar position, and instrument's altitude.

Various RTMs have been developed to be used as forward models for atmospheric trace gas retrievals, such as TRACY-2 and its successor McArtim (Wagner et al., 2007; Deutschmann et al., 2007,0), VLIDORT (Spurr, 2006), SCIATRAN (Rozanov et al., 2005), uvspec/disort (Mayer and Kylling, 2005), and MYSTIC/ALIS (Emde et al., 2011). For the radiative transfer simulations in this thesis, VLIDORT is used to simulate O_4, NO_2, and HCHO dSCDs at the wavelength of interest.

VLIDORT is a multi-scattering homogeneous multi-layer discrete ordinate RTM, which has a linearized pseudo-spherical capability to deal with curved atmosphere. It uses a Gaussian quadrature scheme for the differential

radiative transfer equation, expressed by Legendre expansion coefficients for the phase function and Fourier terms for the intensity. The main advantage of VLIDORT is its low computational time.

According to the investigated atmospheric scenario, the simulation grid and the a priori values of aerosols and trace gases (NO_2 or HCHO in the present work) concentration profiles are provided at the beginning of every simulation. The simulation grid extends from the instrument's altitude up to 60 km. The layer thickness is 100 m for the lower atmospheric layers (from the instrument's altitude to 4 km), 0.5 km between 4 to 8 km, 1 km between 8 and 12 km, 2 km from 12 to 30 km, and 5 km for the upper layers (30 - 60 km). The surface albedo is set according to the instrument's location (i.e. here it is set equal to 0.07, which is representative for urban sites). Concerning the aerosol properties, the main inputs are the total optical depth, single scattering albedo, and the phase function coefficients for every layer. Solar and viewing geometry, relative solar azimuth angle, and temperature and pressure atmospheric profiles should be provided as inputs. Last, the a priori aerosol extinction and NO_2 profile are defined before every simulation. The main output of VLIDORT are the intensities (Stokes vectors), weighting functions, simulated O_4 and NO_2 dSCDs, and consequently, O_4 and NO_2 differential air mass factor (dAMF) for the specific input parameters.

dAMF, which is used to convert the measured dSCDs into vertical column densities (VCDs), is the ratio of the simulated dSCD to the VCD calculated from the trace gas vertical profile provided as input to the RTM:

$$\mathrm{dAMF} = \frac{\mathrm{dSCD}}{\mathrm{VCD}} \tag{5.12}$$

The dAMF depends on the wavelength, geometry of the measurement, vertical distribution of the species, aerosol loading and surface albedo.

Chapter 6

Inversion theory

Contents

Atmospheric RTMs (See chapter 5) connect the state of the atmosphere (e.g. the NO_2 concentration vertical profile), to an atmospheric measurement (e.g. NO_2 dSCD). In remote sensing applications, the known variable is the measurement and what we want to retrieve is the state of the atmosphere. So, the inversion problem can be presented as follows: given a set of measured NO_2 dSCDs at multiple elevation angles, can we develop an inversion algorithm which can retrieve the vertical NO_2 profile from this set of dSCDs?

In this chapter, we present how both variables are connected to each other and the inversion theory for retrieving the atmospheric state from the MAX-DOAS observations.

6.1 The Inversion problem

MAX-DOAS instruments perform measurements in different elevation angles towards the horizon, and for each scan in elevation a set of NO_2 dSCDs is obtained. As shown in Figure 6.1, the light path through the upper atmosphere is independent on the viewing direction (i.e. the length of the blue line is the same for the different observations). On the contrary, the light path through the boundary layer increases as the viewing direction is pointing closer to the horizon.This dependence of the scattering point and consequently, the length of the light path in the boundary layer on the elevation angle of the observation can be used to derive information on the vertical distribution of NO_2 in this part of the atmosphere (Hönninger et al., 2004). Both variables (the set of NO_2 dSCDs at different elevation angles and the NO_2 vertical profile) are connected between them via a so-called forward model (Rodgers, 2000):

$$\mathrm{y} = \mathrm{F}(\mathrm{x}, \mathrm{b}) + \varepsilon_{\mathrm{y}} \tag{6.1}$$

where y is the measurement vector (i.e. set of NO_2 dSCDs), F is the forward model (in this case, RTM), x is the state vector (here, the NO_2 vertical profile), b are the forward model parameters (e.g. temperature and pressure profiles, aerosol extinction profile, surface albedo), and ε_{y} is the measurement error.

In the real atmosphere, the NO_2 vertical profile is continuous. However, to perform the inversion, this profile is sampled in a discrete altitude grid, and can be therefore represented by a vector.

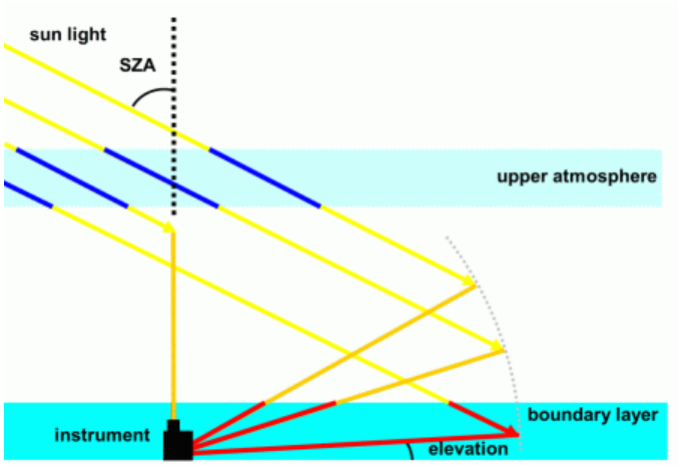

Figure 6.1: Schematic representation of tropospheric observations performed by a ground-based MAX-DOAS instrument in different elevation angles (Source: https://www.iup.uni-bremen.de/doas/)

Ideally, when the state vector is known, the related measurement vector can be directly calculated from it using a RTM. In the present case, the measurement vector is the known variable and the state vector is the unknown. The inverse inversion problem consists in retrieving the state vector from a known measurement vector, where real and simulated measurements are compared to find the state parameters which correspond the best to the measurements. A simplified representation of the retrieval problem with in particular the relation between the state and measurements spaces is shown in Figure 6.2.

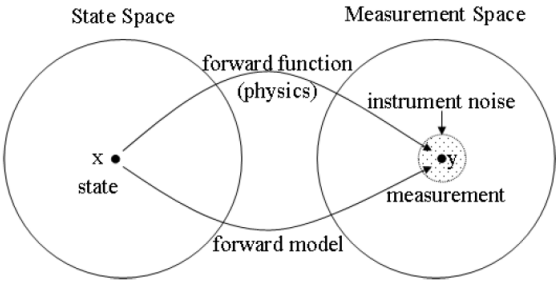

Figure 6.2: Schematic representation of the relationship between state and measurement space.

An important aspect about the inversion problem is that, based on a given measurement vector, more than one state vector can be retrieved from it. This is due to the fact that the true profile is a continuous function with height, while the number of measurements is finite, resulting in the lack of unique solution to Equation 6.1. Additionally, the error on some measurement components of the vector y can be large enough that these components become useless. Inversion techniques like the Optimal Estimation Method (OEM; Rodgers, 2000) proposes a way to solve this under-constrained problem by providing a priori information on the state vector in order to reject unrealistic solutions that could be consistent with the measurement vector. The OEM technique, which is used in the present work, is described in the section below.

6.2 Optimal estimation method

The optimal estimation method consists in finding the solution to the inversion problem by combining the a priori knowledge of the atmosphere and the information about the true profile contained in the measurements.

As mentioned above, the NO_2 profile retrieval is performed on a discrete altitude grid. Equation 6.1 can be reformulated as:

$$y = Kx \tag{6.2}$$

where

$$K = \frac{dy}{dx} \tag{6.3}$$

K is a matrix where each row corresponds to the so-called weighting function (WF). The WFs indicate the sensitivity of the measurements (here the NO_2 dSCDs) with respect to any change in the state vector (here the NO_2 vertical profile).

The OEM uses the Bayes theorem based on probabilities.

Here, the probability density function P(x) of a variable x, which is the probability that x lies in the space [x, x+dx], should be defined. Probabilities can be defined for state and measurement vectors because most of them can be represented by a Gaussian function.

According to Rodgers (2000):

$$P(x, y) = P(x|y)P(y) \tag{6.4}$$

where P(x, y) is the probability that x lies in [x, x+dx] and y lies in [y, y+dy], and P(x|y) is defined as the probability that x lies in [x, x+dx] when y has a given value.

Taking into account that P(x,y) = P(y, x):

$$P(x|y)P(y) = P(y|x)P(x) \tag{6.5}$$

By inserting Equation 6.5 to Equation 6.4, we have:

$$P(x|y) = \frac{P(y|x)P(x)}{P(y)} \tag{6.6}$$

which is the Bayes theorem.

For atmospheric retrievals, each term of Eq. 6.6 describe:

1) The probability of measuring the vector y when the state vector x is known (P(y|x))

2) The prior knowledge of the state vector before the measurement (P(x))

3) The probability of the measurement (P(y))

The unknown variable is P(x|y) which is the probability to obtain the state vector when the measurement is known.

The OEM aims to find the state vector for which the probability P(x|y) is maximum. This state x is called the maximum a posteriori (MAP) solution, which is estimated by using the Bayes theorem and the a priori information of the state vector.

For an inverse linear problem in which all the probability density functions are Gaussian distributions, P(x), P(y|x), and P(x) are:

$$P(x) = \frac{1}{(2\pi)^{n/2}|S_a|^{1/2}} \exp\left(\frac{-1}{2}(x - x_a)^T S_a^{-1}(x - x_a)\right) \tag{6.7}$$

$$P(y|x) = \frac{1}{(2\pi)^{m/2}|S_e|^{1/2}} \exp\left(\frac{-1}{2}(y - Kx)^T S_e^{-1}(y - Kx)\right) \tag{6.8}$$

$$P(y) = \frac{1}{(2\pi)^{m/2}|S_e|^{1/2}} \exp\left(\frac{-1}{2}(y-\overline{y})^T S_e^{-1}(y-\overline{y})\right) \tag{6.9}$$

Inserting Equations 6.7, 6.8, and 6.9 to 6.6, the MAP for linear problems can be derived as follows:

$$x = x_a + (K^T S_\varepsilon^{-1} K + S_a^{-1})^{-1} K^T S_\varepsilon^{-1}(y - Kx_a) \tag{6.10}$$

where x_a is the a priori NO_2 profile, S_a is the a priori covariance matrix and S_ε is the measurement error covariance matrix. This equation can be solved as a matrix equation.

In the present thesis, the elements of the S_a matrix are set equal to the square of a scaling factor times the NO_2 concentration a priori profile. The non-diagonal elements, which account for correlation between the different grid cells, are set as follows (Barret et al., 2002):

$$S_{a_{ij}} = \sqrt{S_{a_{ii}} S_{a_{jj}} \exp\left(-\ln(2)\left(\frac{z_i - z_j}{\gamma}\right)^2\right)} \tag{6.11}$$

where z_i and z_j are the distances at the i_{th}, and j_{th} vertical boxes and γ is the half of the correlation length.

S_e is often chosen to be diagonal, with elements corresponding to the square of the measurement errors.

6.3 Characterization of the retrieval

The solution x of the retrieval can be characterized by making use of the retrieval errors and the vertical sensitivity of the retrieval, i.e. the so-called averaging kernels.

6.3.1 Averaging kernels

The measure of the sensitivity of the state vector x to the true state x_t is quantified with the averaging kernels (AK) functions:

$$AK = \frac{dx}{dx_t} \tag{6.12}$$

Every change on the retrieved profile x can be expressed as a smoothing of the true atmospheric profile x_t times its kernel:

$$x - x_a = AK(x_{true} - x_a) + \varepsilon_x \tag{6.13}$$

where ε_x is the retrieval error.

Every row of the averaging kernel matrix corresponds to one altitude level of the retrieval. The width of the kernel is a measure of the retrieval resolution. Consequently, every row describes how each component of the retrieved profile is related to all other components of the real profile and also, how the retrieval smooths the true atmospheric profile.

AK can be expressed as:

$$AK = (K^T S_\varepsilon^{-1} K + S_a^{-1})^{-1} K^T S_\varepsilon^{-1} K \tag{6.14}$$

The AKs peak at the altitude of the maximum information found. Ideally, AKs would be an identity matrix. The magnitude of the peaks is proportional to the information content of the measurement at their nominal altitudes. If the AKs are broad and no peak is appearing at their altitude, the retrieved profile depends on the a priori profile and does not correspond to the true vertical profile, which means that the measurements are not sensitive to the measured trace gas at these altitudes.

The trace of the matrix AK is the number of independent pieces of information retrieved and is called degrees of freedom for signal (DOFS). Ideally, DOFS would be equal to the number of vertical altitude levels included in the retrieval.

6.3.2 Retrieval errors

The error covariance matrix S of the retrieval can be calculated as:

$$S = (K^T S_\varepsilon^{-1} K + S_a^{-1})^{-1} \tag{6.15}$$

S contains three different types of errors:

(1) The smoothing error

The retrieved profile is smoothed compared to the real atmospheric profile because the instrument can not detect fine vertical structures. It comes from the difference between the true atmospheric and the a priori profile. The retrieval error covariance due to smoothing error is calculated as follows:

$$S_{smooth} = (AK - I)S_x(AK - I)^T \tag{6.16}$$

where S_x is a realistic covariance matrix of a true trace gas profile.

(2) The noise/measurement error

This error source is related to the contribution of the uncertainty/noise of the measurement to the retrieval error. The measurement error is generated by the instrument, the spectral analysis, and the absorption cross-sections. The noise or measurement error is estimated as follows:

$$S_{meas} = GS_eG^T \tag{6.17}$$

where S_e is the measurement error covariance matrix and G is the contribution functions matrix and is calculated as follows:

$$G = (K^T S_e^{-1} K + S_a^{-1})^{-1} K^T S_e^{-1} \tag{6.18}$$

(3) The systematic errors in the forward model

This error describes the uncertainties in the parameters b in the forward model, which are the physics or chemistry of the retrieval. For instance, it can be related to the use of aerosol and temperature and pressure vertical profiles that are different from the true atmospheric profiles.

The retrieval error covariance due to errors coming from the forward model is calculated as follows;

$$S_f = GK_bS_bK_b^TG^T \tag{6.19}$$

where K_b is the sensitivity of the forward model to perturbations on the parameters b and S_b is the covariance matrix of b.

It should be noted that S_f can be sometimes difficult to estimate because of the large number of forward model parameters.

Part II

Measurement site and instrumentation

In this Part II, the MAX-DOAS measurement site and the remote sensing techniques (i.e. ground-based, airborne, and satellite measurements) used in this work to retrieve tropospheric NO_2 vertical profiles and columns are presented. All the above-cited measurement techniques measure UV-Visible light scattered by the Earth's atmosphere or reflected by the Earth's surface and use the DOAS method to analyze the measured radiance spectra.

At this point, it should be noted that remote sensing is not the only measurement technique for NO_2. In national-scale air quality monitoring, chemiluminescence NO_x techniques are widely used to monitor continuously NO and NO_2 levels. These measurements also provide a-priori information about the NO_2 horizontal concentration field, which is a very important a priori knowledge for exploiting remote sensing observations.

Chapter 7

Ground-based DOAS measurements

Contents

Ground-based MAX-DOAS instruments collect scattered sunlight through sequential observations at different elevation angles above the horizon in one or more azimuthal directions. For near-horizon pointing directions, the light path is the longest through the lower troposphere, increasing the sensitivity to traces gases located in the boundary layer and lower troposphere, such as NO_2. By using ad-hoc profile retrieval techniques, information about the vertical distribution of trace gases absorbing in the UV/Visible wavelength range but also aerosols can be derived from these sequential observations at different elevation angles. The relative low cost-of the MAX-DOAS instruments as well as their self-calibration-based operation mode give the possibility of installing multiple instruments around the world, which is essential for atmospheric composition satellite validation and continuous monitoring of trace gases at different locations and in various air quality regimes.

7.1 The measurement site of Uccle

The Space Pole in Uccle (50.8^o N, 4.34^o E; 125 m a.s.l.) is situated in the South of the Brussels-Capital Region, one of the most densely populated areas of Belgium. Frequently, the NO_2 concentration monitored by the network of telemetric air quality stations from Bruxelles Environment/Leefmilieu Brussel (https: //environnement.brussels/, last access: 15 February 2020) exceeds the European standard upper limit fixed to 40 and 200 μgm^{-3} for the NO_2 annual and hourly mean concentrations, respectively. For instance, in 2015, the NO_2 annual mean concentrations were found to exceed the European standards in narrow busy streets in Brussels, with an annual mean concentration between 42.5 and 52.5 μgm^{-3} (see https://environnement.brussels/, last access: last access: 15 February 2020). Additionally, as detected by satellite sensors like OMI (Huijnen et al., 2010), the NO_2 columns over Brussels are among the highest in Europe.

7.2 MAX-DOAS instrument

The MAX-DOAS instrument operated by BIRA-IASB (Koninklijk Belgisch Instituut voor Ruimte-Aeronomie - Institut royal d'Aeronomie Spatiale de Belgique) is an improved version of the system described in (Clémer et al.,

2010). Developed for contributing to the CINDI-2 intercomparison campaign held in Cabauw in September 2016 (Kreher et al., 2020), it was subsequently installed on the rooftop of the Royal Meteorological Institute (RMI) in Uccle and has been continuously operating at this location from January 2017 to February 2020.

The Uccle MAX-DOAS instrument (Figure 7.1) is composed of three main parts: (1) an optical head mounted on a sun tracker, (2) a thermoregulated box with two spectrometers (UV and visible) and (3) the acquisition unit. Optical fibers connect the optical head with the two spectrometers.

Figure 7.1: Picture of the MAX-DOAS instrument at Uccle, Belgium (Source: A. Merlaud).

The optical head is equipped with a filter wheel that allows switching between skylight and direct-sun measurements. The UV optical fiber consists of a 6 m x 1000 µm long monofiber attached to a 2 m bundle made of 51 fibers. Likewise, the visible fiber consists of a 6 m x 800 µm long monofiber attached to a 2 m bundle of 37 fibers. Both monofibers are placed at the focal point of a telescope lens having a 50 mm focal length, resulting in a field of view of 1^{o} and 0.5^{o} for the UV and visible channels, respectively. The optical head is also equipped with a digital inclinometer to correct for potential misalignment of the elevation scanner.

Installed indoor, the thermo-regulated box is equipped with visible and UV grating spectrometers covering the wavelength ranges of 405 to 540 nm and 300 to 390 nm, respectively. The UV spectrometer is from Newport (model 74086) with a spectral resolution of 0.4 nm. To block the visible light and to reduce the stray-light in the UV wavelength region, a band pass filter (U-340 Hoya) is used. The output of the UV spectrometer is connected to a back-illuminated UV-enhanced Charge Coupled Device (CCD) detector system (Princeton Instrument Pixis 2K). The visible spectrometer from Horiba (model Micro HR) has a spectral resolution of 0.7 nm and is also mounted on a back-illuminated CCD system (Princeton Instrument Pixis 100). Both CCD detectors are cooled at 223 K using multi-stage Peltier system. The overall spectrometric unit is thermally stabilized to better than 1^{o}C.

To control the data acquisition, two computers are used. The first one records spectra coming from the Vis spectrometer and controls the sun tracker while the second, synchronized with the first one, records the spectra from the UV spectrometer. A scheme of the MAX-DOAS instruments in Uccle is presented in Figure 7.2.

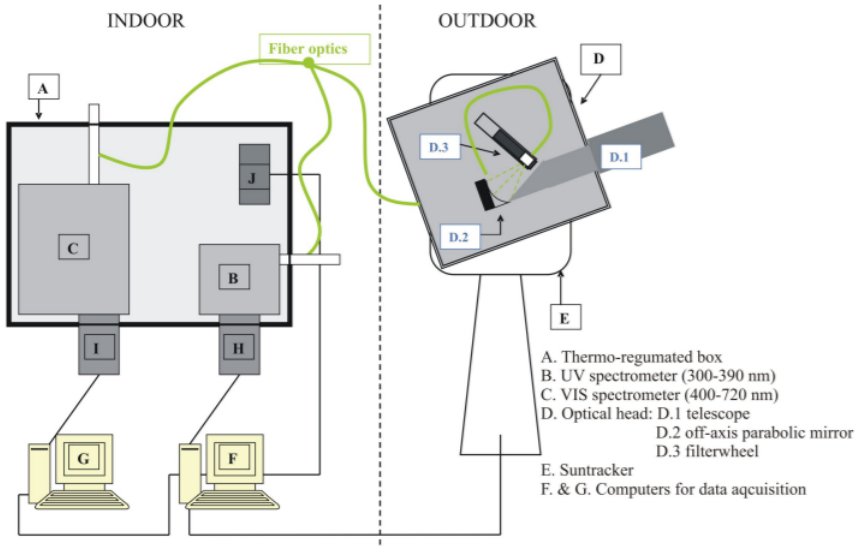

Figure 7.2: Schematic view of the MAX-DOAS instrument (Source: Clémer et al., 2010).

7.2.1 Experimental set-up

In order to measure in dual-scan (elevation + azimuthal scans) viewing mode (Figure 4.4), the initial operation mode (elevation scanning in one azimuthal direction) of the instrument was modified. From March 2018, the instrument was operated in two modes: (1) a vertical scan mode covering nine different elevation angles in one fixed (standard) azimuthal direction (35.5^{o} with respect to north in the eastward direction) and (2) a horizontal scan mode covering nine different azimuthal directions at a fixed elevation angle of 2^{o} above the horizon (see Figure 7.3). As can be seen in Table 7.1 and Figure 7.3, several configurations were tested in order to select the best combination of horizontal and vertical viewing directions, which is a trade-off between the acquisition time and the horizontal representativeness. Since the NO_2 emission sources are located towards the north, more azimuthal directions are selected in this direction. With an integration time of 60 s for each measured spectrum, the total scan duration (azimuthal + elevation viewing modes) ranges between 20 and 30 min, depending on the configuration. Each azimuthal direction was quality-checked by performing horizon scans as during the CINDI-2 campaign (Dönner et al., 2020) in order to ensure that obstacles, like trees and buildings, are not present in the different lines of sight.

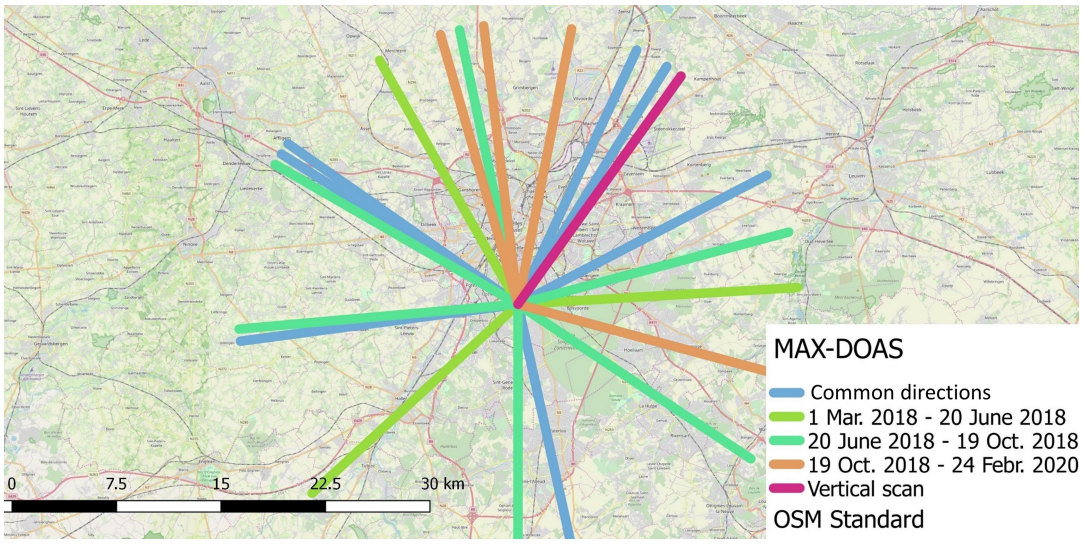

Figure 7.3: The experimental set-up of the BIRA-IASB dual-scan MAX-DOAS instrument. Each line is color-coded according to the different set-ups that were used from March 2018 to February 2020. The length of each line is equal to 20 km, which corresponds to the typical horizontal sensitivity for the MAX-DOAS measurements in the present study. OpenStreetMap contributors 2021. Distributed under a Creative Commons BY-SA License (OSM Humanitarian Data Model).

Table 7.1: MAX-DOAS experimental set-up.

Date	Scan-mode	Azimuth angle (° with respect to the North clockwise)	Elevation angle (°)	Scan duration
01/03/2018 - 20/06/2018	Vertical	35.5	0, 1, 2, 3, 4, 5, 6, 8, 12, 30, 90	11
	Horizontal	330.5, 302.5, 227.5, 167.5, 86.5	0, 1, 2	15
20/06/2018 - 19/10/2018	Vertical	35.5	0, 1, 2, 3, 4, 5, 6, 8, 12, 30, 90	11
	Horizontal	25, 32, 348, 305, 302.5, 300, 265, 262.5, 180, 167.5, 123.5, 105, 75, 62.5	2	14
19/10/2018 - 24/02/2020	Vertical	35.5	1, 2, 3, 4, 5, 6, 8, 12, 30, 90	10
	Horizontal	11, 25, 32, 62.5, 105, 262.5, 305, 353, 344	2	9

Chapter 8

Satellite measurements

Contents

Over more than two decades, satellite nadir measurements of atmospheric backscattered sunlight in the UV and visible spectral range have provided measurements of atmospheric trace gases, such as NO_2, on a daily global basis. Measuring NO_2 from space is crucial to monitor its abundances at different locations around the world. In operation from 1995 until 2011, ERS-2/GOME was the first satellite instrument to measure atmospheric NO_2 columns from space at a spatial resolution of 40x320 km^2 from 1995 to 2011. Many satellite missions have followed like ENVISAT-SCIAMACHY (30x60 km^2; Bovensmann et al., 1999), GOME-2 (80x40 km^2; Munro et al., 2016), and AURA/OMI (Levelt et al. (2006)) with all of them being in low-earth sun-sunchronous polar orbits. In October 2017, the TROPOspheric Monitoring Instrument (TROPOMI) sensor was launched onboard the Sentinel-5p (S5P) platform. Compared to its predecessors, this instrument has a significantly higher spatial resolution of 7x3.5 km^2, which was further improved to 3.5x5.5 km^2 in August 2019. In the following subsections, the main characteristics of the TROPOMI instrument and its tropospheric NO_2 product are presented. We also explain the importance of satellite measurements validation.

8.1 TROPOMI/S5P instrument

The TROPOMI instrument (see Figure 8.1) is flying onboard the S5p satellite platform at about 824 km height in a near-polar sun-sychronous orbit. S5p has been developed by a joint collaboration between the Netherlands Space Office (NSO), the Royal Netherlands Meteorological Institute (KNMI), the Netherlands Organization for Applied Scientific Research (TNO), the Netherlands Institute for Space Research (SRON), Airbus Defense and Space Netherlands, and the European Space Agency (ESA).

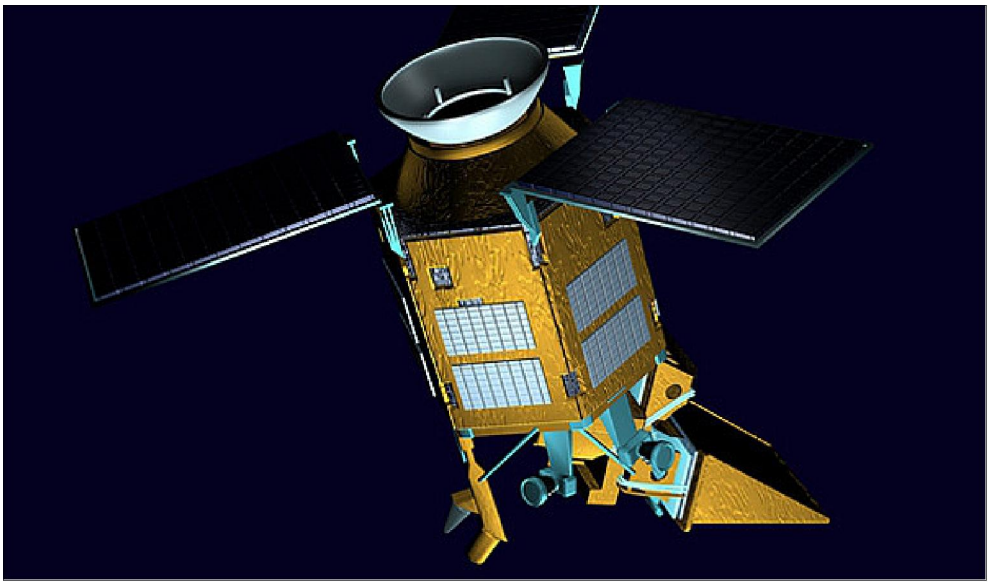

Figure 8.1: Artist's view of the S-5P spacecraft in orbit (Source: ESA, Airbus DS)

TROPOMI is a passive grating imaging spectrometer measuring in nadir viewing geometry. In nadir mode, the instrument observes the light reflected by the Earth's surface and scattered from the air masses beneath the satellite platform (see Figure 8.2). It covers the UV-visible (270-500 nm), near-infrared (710-770 nm) and shortwave infrared (2314-2382 nm) spectral ranges (Veefkind et al., 2011). It measures the solar backscattered earthshine radiance in a push-broom configuration. Compared to its predecessors, TROPOMI is a major improvement in terms of spatial resolution. With a full swath width as wide as 2600 km, TROPOMI provides daily global coverage with a true-nadir pixel size of 7x3.5 km^2 in the UV, visible and near-infrared bands. Since 6 August 2019, the TROPOMI spatial resolution is even higher, with a pixel size of 5.5x3.5 km^2.

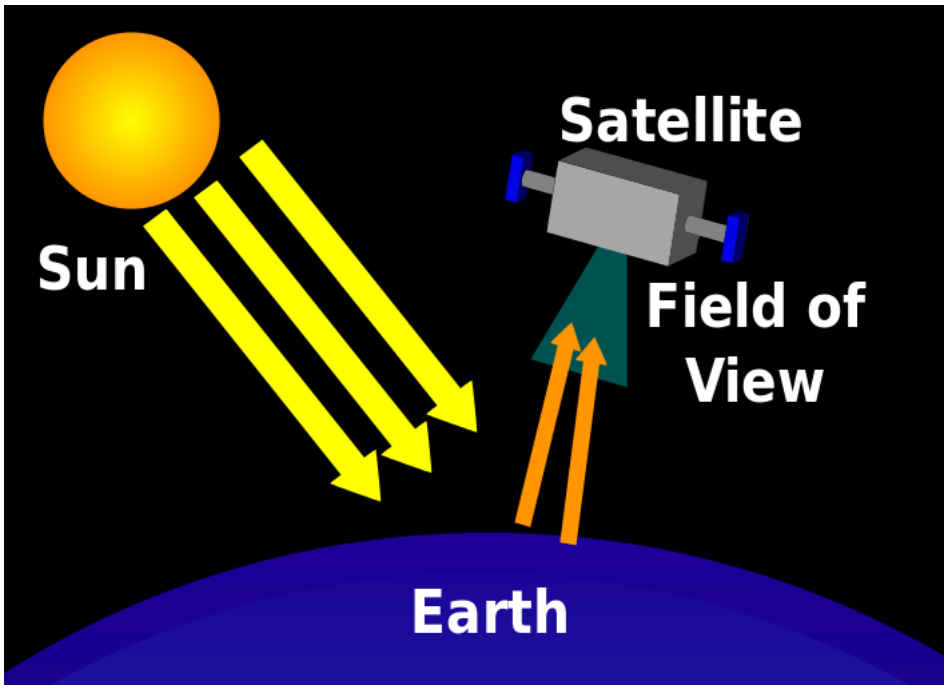

Figure 8.2: Sketch of a nadir-viewing satellite measurement (Source: Wikipedia, Author: PlanetUser)

8.1.1 Tropospheric NO_2 measurements from TROPOMI

Developed at KNMI (Veefkind et al., 2011), the TROPOMI tropospheric NO_2 algorithm uses a retrieval-assimilation-modeling system based on the 3-D global TM5 chemistry transport model. This retrieval scheme consists of three main steps. First, the total NO_2 slant column density is retrieved from Level-1b radiance and irradiance spectra by applying the DOAS method. In a second step, the total NO_2 slant column density is separated into its stratospheric and tropospheric components by using the TM5-based data assimilation system. Finally, the tropospheric and stratospheric NO_2 slant column densities are converted to vertical column densities by applying altitude-dependent AMFs. The AMFs are calculated for each individual field of view (FOV) or pixel by using the viewing and solar geometry, surface pressure and NO_2 profile shape a priori information from the 1^ox1^o TM5-MP model (Williams et al., 2017), a 0.5^o x 0.5^o surface albedo climatology built upon 5 years of OMI data, and the FRESCO-S cloud fraction and cloud height as retrieved from the Oxygen A-band by fitting the spectral reflectance inside and outside the O_2 A-band at 760 nm by a Lambertian cloud model.

8.2 Validation of satellite observations

Satellite observations are crucial for the regional and global long-term monitoring of the spatial and temporal distribution of the atmospheric composition as well as for the global transport and chemical cycles. However, the satellite retrievals are subject to several error sources, which can potentially lead to large uncertainties and on the retrieved quantities such as the NO_2 vertical column densities.

Validation exercises are very often performed in order to test the performance of satellite measurements under different geophysical conditions since it is known that the surface albedo, clouds, surface altitude, aerosols and other parameters play an important role on satellite-based retrievals. Ideally, the independent measurements used for

the validation should measure the same quantity as the satellite, integrate over the same volume (in the case of tropospheric columns), be coincident in time and space, and have higher accuracy and precision than the satellite measurements. Every measurement technique has its advantages and disadvantages and the most adequate ancillary observations should be used for satellite validation.

Ground-based MAX-DOAS instruments correspond to most of these criteria and have been widely used for satellite validation over the last decades. As seen in the previous chapter, they provide trace gases concentration profiles and VCDs of tropospheric trace gases like NO_2. The main advantage of these instruments is that they perform continuous measurements in various locations worldwide covering different geophysical conditions. Some of them are also part of networks, like the Network for the Detection of Atmospheric Composition Change (NDACC).

Chapter 9

Airborne measurements

Contents

Over the last years, measurements of reactive trace gases, such as NO_2, by airborne hyperspectral imaging systems have been carried out (Judd et al., 2020; Tack et al., 2021). Those instruments can map the horizontal distribution of tropospheric gases at a high spatial resolution (∼75 m x 120 m), which is highly valuable for the validation of satellite instruments like TROPOMI. An additional advantage of airborne measurements over urban cities, such as Brussels, is the detection of city-scale NO_2 variability and the identification of the main emissions sources. In the following subsection, the main characteristics of the Airborne Prism EXperiment (APEX) instrument, whose data are used in the present thesis, are presented.

9.1 APEX instrument

The APEX instrument (see Figure 9.1), designed and developed by a Swiss-Belgian consortium on behalf of ESA, measures the backscattered radiation by the Earth's surface or atmosphere.

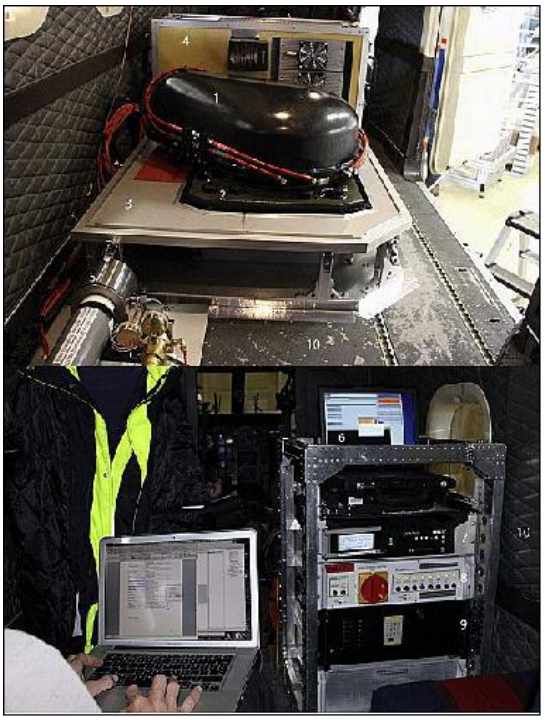

Figure 9.1: (Top picture) APEX instrument as mounted in Dornier DO-228 aircraft; (Bottom picture) operator rack (right) and upload of configuration and flight data (left). Credit: M. Jehle, Source: https://eoportal.org/web/eoportal/airborne-sensors/apex

When the radiation enters the optical unit of the instrument, a collimator groups and redirects the light towards a beam splitter. There, the visible-near infrared (370 - 970 nm) is separated from the shortwave infrared (950 - 2500 nm) wavelength range. At this point, the shortwave infrared radiation is not further exploited. A prism disperses spectrally the Visible-near infrared radiation and then, the dispersed radiation is projected on a 2-D charge-coupled device (CCD). The CCD records the intensity in a series of narrow spectral bands. To stabilize thermally the optical unit is kept enclosed to a thermo-regulated box. Additionally, the pressure in the spectrometer is kept stable at 200 hPa above ambient pressure. It is crucial that the aircraft's movement does not influence the performance of the APEX instrument. For this reason, the instrument is mounted on a Leica PAV-30 stabilized platform.

The pushbroom imaging spectrometer consists in a 1000 pixels across-track (spatial dimension), which are illuminated at the same time. The spectral dimension consists of 335 pixels. The two dimensions form a plane which is called frame.

By using the swath imaging of the pushbroom scanner and the forward motion of the airborne platform, APEX maps the NO_2 distribution below the aircraft, which flies in an altitude equal to 6.1 km above ground level (a.g.l). The flight altitude allows the detection of NO_2, given that the bulk of tropospheric NO_2 is located between the surface and this altitude.

In the framework of the S5P validation campaign over Belgium (S5PVAL-BE), APEX has been deployed during four flights (26 - 29 June 2019) above the two largest Belgian urban regions (i.e. Brussels and Antwerp). In Figure 9.2, tropospheric NO_2 columns as retrieved by APEX over Brussels on 28 June 2019 are presented. The high spatial resolution of APEX measurements and its ability to pinpoint NO_2 hotspots inside an urban region can be seen from this picture. A large city plume in the SW direction is observed, as well as some of the main hotspots (Brussels

city-center, the Brussels international airport, and the Brussels ring motorway.

A more detailed description of the APEX instrument and the performed DOAS analysis can be found in Tack et al. (2017,0).

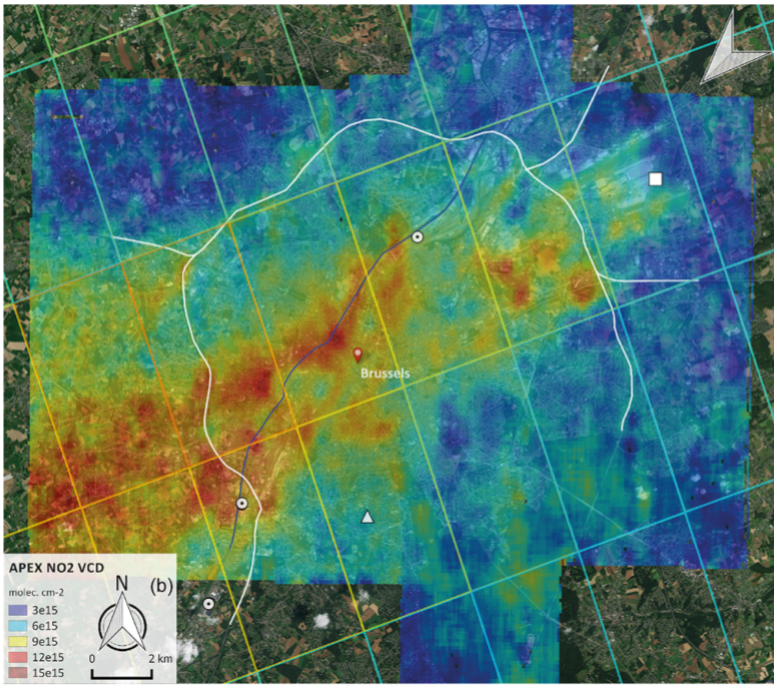

Figure 9.2: Tropospheric NO_2 column grids as retrieved over Brussels on 28 June 2019. White dots show the point sources, emitting more than 10 kg of NOx per hour (2017 emission inventory of the Belgian Interregional Environment Agency). The white triangle and white square demonstrate the location of the Uccle measurement site and the Brussels International airport, respectively. While lines show line sources (i.e. key highways and city ring road). White wind vector indicates the surface wind direction. The color-coded polygons are the coincident TROPOMI pixels (Source: Tack et al., 2021)

.

Part III

Validation of TROPOMI tropospheric NO_2 columns using dual-scan MAX-DOAS measurements in Uccle, Belgium

Ground-based multi-axis differential optical absorption spectroscopy (MAX-DOAS) measurements of aerosols and tropospheric nitrogen dioxide (NO_2) were carried out in Uccle (50.8^o N, 4.35^o E), Brussels, during 1 year from March 2018 until March 2019. The instrument was operated in both the UV and Visible wavelength ranges in a dual-scan configuration consisting of two sub-modes: (1) an elevation scan in a fixed viewing azimuthal direction (the so-called main azimuthal direction) pointing to the northeast and (2) an azimuthal scan in a fixed low elevation angle (2^o). By applying a vertical profile inversion algorithm in the main azimuthal direction and a parameterization technique in the other azimuthal directions, near-surface NO_2 volume mixing ratios (VMRs) and vertical column densities (VCDs) were retrieved in 10 different azimuthal directions. The dual-scan MAX-DOAS dataset allows for partly resolving the horizontal distribution of NO_2 around the measurement site and studying its seasonal variations. Furthermore, we show that measuring the tropospheric NO_2 VCDs in different azimuthal directions improves the spatial colocation with measurements from the Sentinel-5 precursor (S5P), leading to a reduction of the spread in validation results. By using NO_2 vertical profile information derived from the MAX-DOAS measurements, we also resolve a systematic underestimation in S5p NO_2 data due to the use of inadequate a priori NO_2 profile shape data in the satellite retrieval. [1]

[1]This chapter is based on: Dimitropoulou, E., Hendrick, F., Pinardi, G., Friedrich, M. M., Merlaud, A., Tack, F., De Longueville, H., Fayt, C., Hermans, C., Laffineur, Q., Fierens, F., and Van Roozendael, M.: Validation of TROPOMI tropospheric NO_2 columns using dual-scan multi-axis differential optical absorption spectroscopy (MAX-DOAS) measurements in Uccle, Brussels, Atmos. Meas. Tech., 13, 5165-5191, https://doi.org/10.5194/amt-13-5165-2020, 2020.

Chapter 10

Part III: Objectives

The Part III aims to investigate the use of multi-azimuthal MAX-DOAS measurements in Uccle (Belgium) to validate the TROPOMI tropospheric NO_2 column observations in urban conditions. The measurement site (see chapter 7.2.1) is located south of Brussels at a distance of around 6 km from the city center and is therefore representative of moderate to high pollution levels at which the NO_2 spatial distribution can be highly heterogeneous. One complete year (March 2018-March 2019) of MAX-DOAS measurements is used to quantify the agreement between the two datasets and its seasonal dependence, as well as to investigate to what extent the multi-azimuthal capability of the Uccle instrument can contribute to improve this agreement.

Part III is organized as follows: in chapter 11, the DOAS analysis and the retrieval methodologies applied to the MAX-DOAS observations and their validation are described. Chapter 12 focuses on the tropospheric NO_2 measurements performed by TROPOMI and used in Part III. Thereafter, in chapter 13, results are separated into two main parts: the demonstration of the dual-scan MAX-DOAS retrievals and afterwards their use for the TROPOMI/S5P validation. Finally, in chapter 14, a summary, concluding remarks and perspectives are given.

Chapter 11

Retrieval methods

Contents

11.1 DOAS analysis

The spectra measured in both sub-modes are analyzed using the QDOAS spectral fitting software developed at BIRA-IASB (Fayt et al., 2011) for the retrieval of atmospheric trace gas abundances in the UV, visible and near-infrared spectral ranges. The DOAS technique consists of a separation between narrow absorption features characteristic of molecular species and a spectral background resulting mainly from Mie and Rayleigh scattering as well as instrumental effects (Platt and Stutz, 2008). Its primary product is the differential slant column density (dSCD), which represents the light path-integrated trace gas concentration in a measured spectrum relative to the amount of the same absorber in a reference spectrum. In the present case, daily noon zenith spectra are used as a reference.

NO_2 dSCDs are retrieved in both the visible and UV ranges according to settings defined during the CINDI-2 campaign (see Tables 11.1 and 11.2; Kreher et al., 2020). For retrievals in the visible spectral range, we use the 425-490 nm fitting interval, while UV retrievals are performed in the 338-370 nm spectral range.

11.2 Aerosol and NO_2 OEM-based profile retrievals

The aerosol extinction coefficient and NO_2 vertical profiles are retrieved for each MAX-DOAS elevation scan in the main azimuthal direction by applying the Mexican MAX-DOAS fit (MMF; Friedrich et al., 2019) inversion algorithm to the corresponding measured O_4 and NO_2 dSCDs. The inversion is performed in two successive steps. First, an aerosol extinction profile is retrieved using O_4 measurements according to the principles described in Frieß et al. (2006). This aerosol profile is then used as an input for the radiative transfer calculations needed to invert the NO_2 vertical profile.

Table 11.1: DOAS settings for NO_2 and O_4 in the Vis spectral range.

Wavelength range	425-490 nm
Fraunhofer reference spectra	Noon zenith spectra
Cross-sections:	
NO_2 (294 K)	Vandaele et al. (1998) with I_0 correction (SCD of 10^{17} molecules/cm^2)
NO_2 (220 K)	Pre-orthogonalized Vandaele et al. (1998) with I_0 correction (SCD of 10^{17}molecules/cm^2)
O_3 (223 K)	Serdyuchenko et al. (2014) with I_0 correction (SCD of 10^{20}molecules/cm^2)
O_4 (293 K)	Thalman and Volkamer (2013)
H2O	HITEMP Rothman et al. (2009)
Ring	RING QDOAS SAO2010

Table 11.2: Same as Table 11.1 for the UV spectral range.

Wavelength range	338-370 nm
Fraunhofer reference spectra	Noon zenith spectra
Cross-sections:	
NO_2 (294 K)	Vandaele et al. (1998) with I_0 correction (SCD of 10^{17} molecules/cm^2)
NO_2 (220 K)	Pre-orthogonalized Vandaele et al. (1998) with I_0 correction (SCD of 10^{17} molecules/cm^2)
O_3 (223 K)	Serdyuchenko et al. (2014) with I_0 correction (SCD of 10^{20} molecules/cm^2)
O_3 (243 K)	Pre-orthogonalized Serdyuchenko et al. (2014) with I_0 correction (SCD of 10^{20} molecules/cm^2)
O_4 (293 K)	Thalman and Volkamer (2013)
HCHO (297 K)	Meller and Moortgat (2000)
BrO (223 K)	Fleischmann et al. (2004)
Ring	RING QDOAS SAO2010

The MMF algorithm uses the optimal estimation method (OEM; Rodgers, 2000) formalism, the VLIDORT (Spurr, 2006) version 2.7 radiative transfer model (RTM) as a forward model and a Levenberg-Marquardt (LM) iteration scheme.

MMF works in linear measurement space and logarithmic retrieval space. Further details about this algorithm can be found in Friedrich et al. (2019). MMF was one of the retrieval codes used during the CINDI-2 campaign (Tirpitz et al., 2021), and it also participated in the round-robin comparison of profiling algorithms as part of the fiducial reference measurements for the Ground-Based DOAS Air-Quality Observations (FRM4DOAS) project (Frieß et al., 2019). The main advantages of MMF are (1) the online calculation of Jacobians with operation in a logarithmic state vector space, which prevents unphysical negative partial columns from being retrieved, (2) the use of a stable Levenberg-Marquardt nonlinear iteration scheme (in replacement for a Gauss-Newton scheme) and (3) the fast computing time (5 s per scan for both aerosols and trace gases). A drawback of OEM-based profiling algorithms such as MMF is that a priori profiles should be carefully chosen in order to avoid biases in the retrieved profiles and columns at altitudes characterized by a low information content.

An important parameter in the OEM approach is the a priori profile. Here, exponentially decreasing a priori profiles are used for both aerosols and NO_2, with a scaling height of 1 km and aerosol optical depth (AOD) and NO_2 vertical columns fixed to 0.18 and 9.15×10^{15} molec.cm^{-2} , respectively. For the diagonal elements of the a priori covariance matrix, we use 50 % of the a priori profile, with a correlation length of 200 m for the nondiagonal elements Clémer et al. (2010).

The pressure and temperature profiles are prescribed using 20-year monthly averaged data extracted from the European Centre for Medium-Range Weather Forecasts (ECMWF) ERA-Interim reanalysis (see Beirle et al., 2019) for the location of Uccle. The retrieval altitude grid consists of 20 layers of 200 m thickness between the surface and 4 km of altitude. The surface albedo is set to 0.06 and the aerosol optical properties, such as the single-scattering albedo and the asymmetry parameter, are taken from colocated AERONET measurements. Regarding the retrieval wavelengths, aerosol extinction vertical profiles are retrieved at 360 and 477 nm and the NO_2 vertical profiles at 360 and 460 nm.

Each retrieval is quality-checked based on three different criteria. First, the degrees of freedom (DOFs) should be larger than 2. This ensures that the profile information comes mostly from the measurements and not from the a priori profile. Second, the relative root mean square error (RMSE) of the difference between measured and calculated differential slant column densities with respect to the zenith spectrum of each scan should be smaller than 15 %. This excludes local minima. Third, the AODs should be smaller than 5 because of the high profile uncertainties on the trace gas retrieval in such conditions (Hendrick et al., 2014). The above-mentioned criteria are applied to the NO_2 and aerosol profile retrievals in the visible and UV ranges.

The presence of aerosols and clouds in the atmosphere can strongly affect the MAX-DOAS trace gas retrieval (Frieß et al., 2006; Gielen et al., 2014; Wagner et al., 2014). In order to exclude MAX-DOAS measurements strongly influenced by the presence of clouds, a cloud-filtering approach is applied using a colocated thermal infrared pyrometer. The pyrometer determines the total cloud-cover fraction based on the temperature data over a field of view of 6^{o} (Gillotay et al., 2001). Generally, the method is able to determine most cloudy conditions, with the exception of cirrus clouds. The total cloud-cover fraction is defined as the ratio between the observed cloudy solid angle elements and clear-sky elements. In the present study, only MAX-DOAS scans with a total cloud-cover fraction less than 0.8 (80 %) are selected for further analysis. The application of the above-mentioned upper limit allows for the rejection of scans under fully cloudy conditions and does not significantly reduce the total number of accepted MAX-DOAS scans.

The uncertainties of the vertical profiles retrieved by MMF include three types of errors (Rodgers, 2000): (1) the smoothing error, which represents the difference between the retrieved and the true profile due to the vertical smoothing, (2) the noise error, which represents the uncertainty arising from the dSCD measurement, and (3) the error coming from the forward model. In Table 11.3, an overview of the main error sources for the NO_2 near-surface VMR and VCD retrievals is presented. For the visible range, the smoothing error amounts to around 3 % of the NO_2 near-surface VMR and 8 % of the VCD, and the noise error is about 2 % of the near-surface VMR and 2 % of

Table 11.3: Error budget overview of the MMF retrieved NO_2 VMR and VCD in the Vis and UV spectral ranges. The total uncertainty is calculated as the square root of the sum of the squares of the different error sources.

Error overview (%)	NO_2 VMR (VIS)	NO_2 VCD (VIS)	NO_2 VMR (UV)	NO_2 VCD (UV)
Noise error	2	2	2	3
Smoothing error	3	8	2	9
Forward model uncertainty	3	4	2	1
Uncertainty on NO_2 cross-sections	3	3	3	3
Uncertainty related to the temperature dependence of NO_2 cross-sections	9	9	9	9
Total uncertainty	11	13	10	13
Difference between retrievals in Vis and UV spectral ranges	16	15	16	15

the VCD. In the UV range, the smoothing error amounts to around 2 % of the NO_2 near-surface VMR and 9 % of the VCD, and the noise error is about 2 % of the near-surface VMR and 3 % of the VCD. Despite the fact that the smoothing error seems to be small, it is the main error source in the profile retrieval (Rodgers, 2000). The use of a constructed covariance matrix results in the underestimation of the smoothing error because daily variations of the a priori profile are not taken into account. The uncertainty associated with the forward model parameters has been estimated by modifying the input parameters, such as the single-scattering albedo and the asymmetry parameter, in the RTM calculations and quantifying the impact on the NO_2 near-surface VMR and VCD. For the visible range, it is up to 3 % of the near-surface VMR and 4 % of the VCD, and in the UV range, the corresponding values are 2 % and 1 %, respectively.

We also consider the systematic uncertainty on the NO_2 cross sections at the assumed fixed temperature of 294 K, which is about 3 % (Vandaele et al., 1998). Taking into account the temperature dependence (0.4 % K^{-1} for the visible fitting window; Takashima et al. (2012)) and assuming a mean temperature difference between winter and summer of 23 K, the total systematic error due to NO_2 cross sections reaches a maximum of 9 %. Combining all the above-mentioned sources of error, the following uncertainties for NO_2 retrievals are estimated: 11 % and 13 % on NO_2 VMR and VCD in the visible range, respectively, and 10 % and 13 % on NO_2 VMR and VCD in the UV, respectively. Another source of uncertainty is estimated by comparing the NO_2 near-surface VMR and VCD in the UV and visible wavelength ranges. The uncertainty is up to 15.5 % of the near-surface VMR and 15.4 % of the VCD. This percentage difference is slightly larger than the above-mentioned retrieval uncertainties. The main origin of this uncertainty is the different horizontal sensitivity in the UV and visible wavelength ranges and therefore a different air mass sampling.

11.3 Dual-scan MAX-DOAS retrieval strategy

The dual-scan MAX-DOAS retrieval strategy refers to the near-surface NO_2 box-averaged VMR in the lowest layer(s) of the mixing layer height (MLH) and VCD retrieval over one complete MAX-DOAS elevation and azimuthal scan by using (1) an OEM-based profile retrieval and (2) a parameterization approach. Both methods are described in section 11.3.1 and 11.3.2 below.

11.3.1 The parameterization method

The parameterization approach used in this study is an adaptation of the one introduced in Sinreich et al. (2013). It consists of a conversion of NO_2 dSCDs measured at one low elevation angle (2^o) to near-surface box-averaged mixing ratios. If sufficient aerosols are present in the lower troposphere (boundary layer), the measured dSCD at two low elevation angles (in the present study, 1 and 2^o) are equal. In this case, the concentration of an absorber close to the surface (e.g. NO_2) can be considered the box-averaged near-surface concentration c and is related to the dSCD as follows (Sinreich et al., 2013):

$$\mathrm{dSCD} = \bar{c}\mathrm{dL_{eff}} \tag{11.1}$$

where dSCD is the differential slant column density of the absorber (molec.cm^{-2}) and c its mean concentration (molec.cm^{-3}) along the differential effective path lengths ($\mathrm{dL_{eff}}$) in centimeters. The unknown variable in equation 11.1 is the differential effective path length of the measurement. The absorption of the oxygen collisional complex (O_4) can be used as a tracer for the light path distribution. The concentration of O_4 is proportional to the square of the concentration of molecular oxygen (O_2), which can be accurately determined. Variations in the O_4 dSCD are therefore directly related to changes in the state of the atmosphere and changes in the measurement geometry.

For each measurement, the differential effective path lengths can be calculated as a ratio of the measured O_4 dSCDs to the typical O_4 concentration at the altitude of the instrument $\mathrm{c_{O_4(instr)}}$:

$$\mathrm{dL_{eff}}(O_4) = \frac{\mathrm{dSCD_{O_4}}}{\mathrm{c_{O_4(instr)}}} \tag{11.2}$$

As mentioned above, the profile shape of O_4 is an exponentially decreasing profile with altitude. In contrast, the NO_2 profile has a different shape, as this trace gas is emitted close to the surface. Therefore, the $\mathrm{dL_{eff}}(O_4)$ cannot be used directly in equation 11.1 in order to estimate the near-surface NO_2 VMR. As indicated by Sinreich et al. (2013), Wang et al. (2014), and Ortega et al. (2015), the direct use of the $\mathrm{dL_{eff}}$ derived from O_4 measurements introduces systematic errors in the near-surface $\mathrm{VMR_{NO_2}}$. In general, if no correction factors are applied, $\mathrm{dL_{eff}}$ will be overestimated, leading to an underestimation of the $\mathrm{VMR_{NO_2}}$ by up to a factor of 3 (Sinreich et al., 2013). In the present study, in which off-axis measurements were performed at 2^o elevation in an urban polluted environment, the $\mathrm{dL_{eff}}$ of NO_2 was found to be smaller than the corresponding $\mathrm{dL_{eff_{O_4}}}$ by an average factor of 2 and 1.6 in the visible and UV wavelength ranges, respectively (Fig. 13.1).

The introduction of a unitless correction factor ($\mathrm{f_c}$) accounting for differences between the O_4 and NO_2 profile shapes is therefore necessary. $\mathrm{f_c}$ connects the two different $\mathrm{dL_{eff}}$ as follows:

$$\mathrm{dL_{eff}}(NO_2) = \mathrm{dL_{eff}}(O_4)\mathrm{f_c} \tag{11.3}$$

Taking this relation into account and combining with equations 11.1, 11.2 and 11.3, the near-surface concentration of NO_2 can be expressed as:

$$\mathrm{c_{NO_2}} = \mathrm{dSCD_{NO_2}} \frac{\mathrm{c_{O_4}(instr)}}{\mathrm{dSCD_{O_4}}} \frac{1}{\mathrm{f_c}} \tag{11.4}$$

Previous studies (Sinreich et al., 2013; Wang et al., 2014; Ortega et al., 2015; Seyler et al., 2019) have highlighted the importance of properly estimating the correction factors, especially in polluted conditions such as those observed in Brussels. The NO_2 concentration corresponds to the ratio of $\mathrm{dSCD_{NO_2}}$ to the light path length $\mathrm{dL_{eff}}(NO_2)$. Assuming that the NO_2 vertical distribution can be approximated by a box profile of height equal to MLH, one can also express it as the ratio between the $\mathrm{VCD_{NO_2}}$ and the MLH:

$$\frac{\mathrm{dSCD_{NO_2}}}{\mathrm{dL_{eff}}(NO_2)} = \frac{\mathrm{VCD_{NO_2}}}{\mathrm{MLH_{NO_2}}} \tag{11.5}$$

Combining equations 11.3 and 11.5 and expressing the dSCD as the product of the VCD and a differential air mass factor (dAMF), f_c becomes:

$$f_c = \frac{dAMF_{NO_2} MLH_{NO_2} c_{O_4(instr)}}{dAMF_{O_4} VCD_{O_4}} \tag{11.6}$$

where MLH_{NO_2} is the mixing layer height of NO_2, $dAMF_{NO_2}$ and $dAMF_{O_4}$ are the NO_2 and O_4 differential air mass factors, and VCD_{O_4} is the typical vertical column density of O_4 above the instrument. The dAMF of a trace gas expresses the light path enhancement with respect to the vertical path through the atmosphere. The correction factor depends on the aerosol load in the atmosphere, the solar zenith angle (SZA), the relative solar azimuth angle (RSAA), the MLH of the trace gas and the vertical distribution of the aerosols inside the MLH during the measurement.

11.3.2 Dual-scan MAX-DOAS retrieval in Uccle

In this section, the above-mentioned parameterization method is applied to our dual-scan MAX-DOAS measurements in Uccle.

To estimate MLH, we use the NO_2 vertical profile information derived in the main azimuthal direction. Assuming homogeneous mixing in the mixing layer, MLH is derived from the ratio of VCD_{NO_2} to the near-surface concentration of NO_2. Moreover, during one MAX-DOAS scan, the vertical extent of the trace gas profile is considered homogeneous around the measurement site, and the MLH values in the main azimuthal direction can also be applied to the other azimuthal directions. Despite its simplicity, this approach provides robust estimates of the MLH, consistent with local ceilometer observations (for more details, see section 11.3.4). As indicated by Sinreich et al. (2013) and Ortega et al. (2015), the use of realistic MLH daily variation is a crucial element in the parameterization method. Our approach represents an improvement over the more empirical approach used in previous studies. The dAMF depends on the geometry (SZA, RSAA and elevation angle) as well as the aerosol and trace gas concentration profiles. For its calculation, we used VLIDORT (Spurr, 2006) version 2.7. The dAMF of O_4 and NO_2 was estimated for eight different MLH scenarios (250-2000 m range) and for the visible and UV wavelengths, separately. In these scenarios, the aerosol and NO_2 a priori profiles are specified as box profiles with a constant concentration from the surface to the MLH. The AOD varies from 0.30 to 0.60, the asymmetry parameter is set to 0.68 and the SSA to 0.92. The resulting correction factors are represented in Fig. 11.1 as a function of RSAA and for different values of the SZA (for an AOD equal to 0.30). They strongly depend on the RSAA and the MLH. For a low RSAA and a thick MLH fc reaches a maximum, while a minimum is obtained at a high RSAA for a thin MLH. When investigating the dependency of fc on the SZA for different AOD and RSAA values (Figure 11.1), we observe that it becomes highly dependent on AOD for a low RSAA and SZA values close to $50-60^o$, indicating the limitations of the parameterization technique in those conditions.

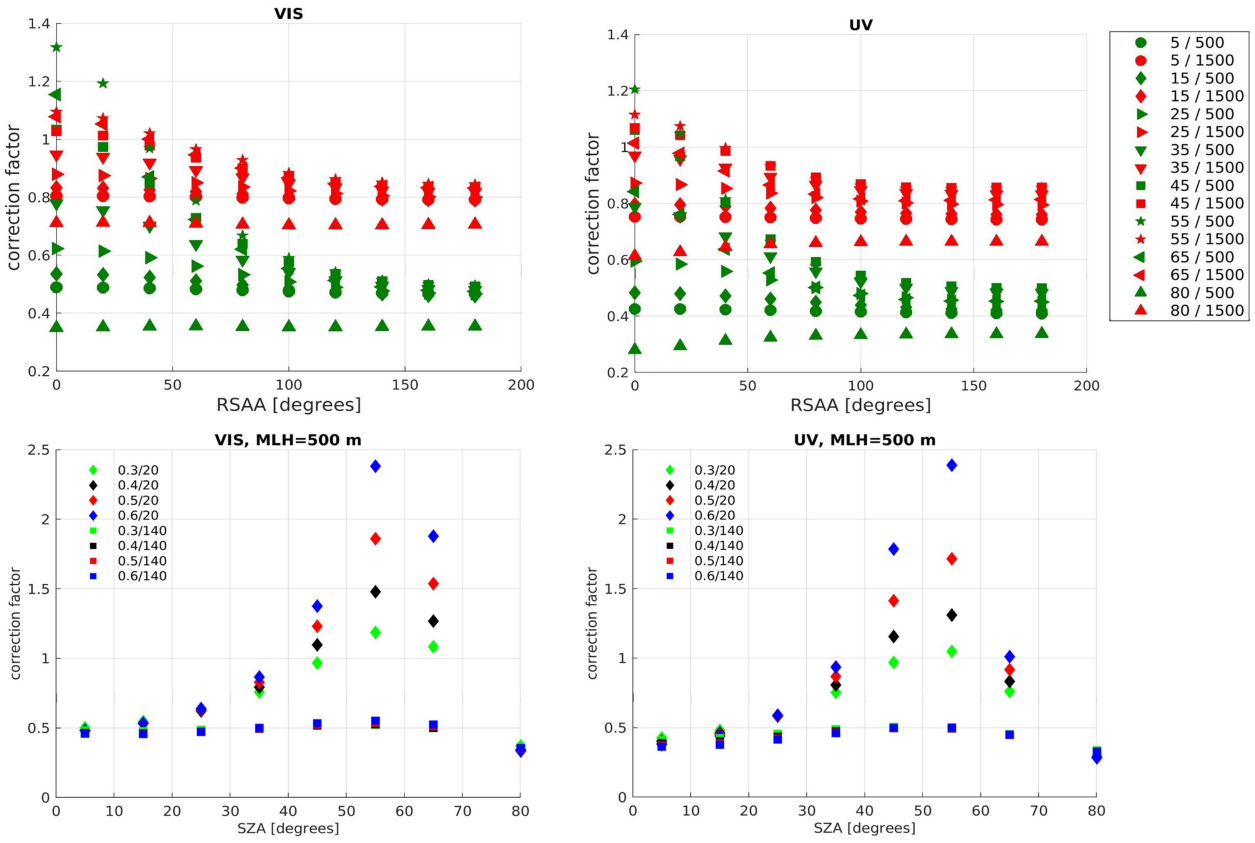

Figure 11.1: Upper panels correspond to the correction factors as a function of RSAA for two different MLH values (in every RSAA and MLH values, the different data points correspond to different SZA values) in the Vis and UV wavelength ranges. The first value in the symbols list corresponds to the SZA and the second to the MLH. Lower panels show the correction factors as a function of SZA for different AOD scenarios and RSAA values in the Vis and UV ranges for a MLH set to 500 m. The first value in the symbols list corresponds to the AOD and the second to the RSAA.

The correction factor fc provides information about the state of the atmosphere such that each measurement can be classified into one of the following three regimes. For fc equal or close to 1, the effective light paths of O_4 and NO_2 are similar (Equation 11.3), which means that there is a moderate to high aerosol load during the measurement. In contrast, when fc is significantly smaller than 1, the measurement is done under aerosol-free conditions or a thin MLH. Finally, fc can take values larger than 1 for cases of high SZA and low RSAA (Figure 11.1), which are special conditions in which the parameterization method becomes highly dependent on the AOD. Such cases are highly uncertain and we excluded them from further analysis.

To estimate fc (Equation 11.6) for every MAX-DOAS measurement in the visible and UV wavelengths, O_4 and NO_2 dAMFs were tabulated for eight different values of MLH (AOD set to 0.3) and for a suitable range of RSAA and SZA values. Using this lookup table, O_4 and NO_2 dAMFs are interpolated at the SZA, RSAA and MLH of each measurement. The near-surface VMR is then obtained by dividing the concentration of the trace gas (Equation 11.4) by the air number density (n_{air}) derived from monthly averaged temperature and pressure profiles extracted from the ERA-Interim reanalysis (see chapter 11.2). The VCD is then estimated from the product of the near-surface concentration with the MLH.

For the analysis, only measurements at SZA smaller than 80° were selected. As presented in (Sinreich et al., 2013), the method is independent of the actual aerosol load, as long as a sufficient amount of aerosol is present in the troposphere (AOD > 0.2). However, it slightly depends on the aerosol layer height. In order to select measurements wherein the near-surface layer can be parameterized as a box profile (i.e. with a homogeneous concentration inside the layer), two conditions should be satisfied. First, the scattering events corresponding to the lowest two elevation angles should occur in a comparable distance; secondly, those scattering events should happen inside the NO_2 layer, which can then be considered homogeneous and therefore parameterized as a box profile. In order to ensure that those conditions were satisfied, only scans for which the differences between O_4 and NO_2 dSCDs in the lowest two elevation angles were smaller than 10^{44} and 10^{16} molec.cm^{-2} , respectively, were selected. Furthermore, when the O_4 dSCD, and consequently the dLeff (O_4), is negative or too small because of bad weather conditions, the VMR can become close to zero or negative (unphysical). In consequence, measurements with a value of dLeff (NO_2) smaller than 5 km (for both visible and UV) are excluded from the study. An upper limit of 30 km is also adopted to exclude numerical outliers. To estimate uncertainties on the retrieved NO_2 VMR and VCD using the parameterization method, two main error sources are considered: (1) uncertainties on O_4 and NO_2 dSCDs and (2) uncertainties related to the estimation of the correction factors. Based on Equation 11.4 and using a standard error propagation method, the overall uncertainty on the near-surface VMR is given by:

$$\sigma^2_{\mathrm{VMR}} = \left(\sigma_{\mathrm{dSCD_{O_4}}} \frac{\mathrm{VMR}}{\mathrm{dSCD_{O_4}}}\right)^2 + \left(\sigma_{\mathrm{dSCD_{NO_2}}} \frac{\mathrm{VMR}}{\mathrm{dSCD_{NO_2}}}\right)^2 + \left(\sigma_{\mathrm{f_c}} \frac{\mathrm{VMR}}{\mathrm{f_c}}\right)^2 \tag{11.7}$$

where:

$$\sigma^2_{\mathrm{f_c}} = \left(\sigma_{\mathrm{dAMF_{NO_2}}} \frac{\mathrm{f_c}}{\mathrm{dAMF_{NO_2}}}\right)^2 + \left(\sigma_{\mathrm{dAMF_{O_4}}} \frac{\mathrm{f_c}}{\mathrm{dAMF_{O_4}}}\right)^2 + \left(\sigma_{\mathrm{MLH}} \frac{\mathrm{f_c}}{\mathrm{MLH}}\right)^2 \tag{11.8}$$

Regarding the σ_{dSCD}, Bösch et al. (2018) and Kreher et al. (2020) indicated that, in urban or suburban polluted conditions, the DOAS fit uncertainty of both O_4 and NO_2 significantly underestimates the actual dSCD uncertainty, which is mostly driven by atmospheric variability as well as spatial and temporal fluctuations in the O_4 and NO_2 fields. In the present study, based on values derived during the CINDI2 campaign, conservative values of 3.5x10^{15}molec.cm^{-2} (NO_2) and 1.5x10^{42}molec.cm^{-5} (O_4) were used for the dSCD uncertainties in the UV and visible ranges. This represents an error of up to 5 %-6 % in the O_4 dSCD and 4 %-5 % in the NO_2 dSCD in both the visible and UV ranges. The second important error source is related to the correction factors, which depend on the air mass factor and $\mathrm{MLH_{MAX-DOAS}}$ calculations (equation 11.7). The uncertainty related to $\mathrm{MLH_{MAX-DOAS}}$ can be estimated as a combination of two terms: the total uncertainty of the NO_2 near-surface VMR and the NO_2 VCD derived by the MMF inversion algorithm. In the visible range, the error related to $\mathrm{MLH_{MAX-DOAS}}$ is about 4 % and 5 %

Table 11.4: Error budget overview of the parameterized NO_2 VMR in the Vis and UV spectral ranges.

Error overview (%)	VIS	UV
NO_2 DOAS fit	4	5
O_4 DOAS fit	5	6
MLH	4	5
dAMF NO_2	2	6
dAMF O_4	18	13
Total uncertainty on the VMR	20	17
Total uncertainty on the VCD	19	16

in the UV range. In order to estimate the uncertainty related to the air mass factor calculation, sensitivity tests on the input parameters in the RTM simulation were performed. In these sensitivity tests, the main inputs in the RTM calculations, such as the height of the assumed trace gas profile and the aerosol properties, are modified. The corresponding dAMF variability is attributed to the uncertainty of the dAMF calculation. The error related to the $dAMF_{NO_2}$ estimation is about 2 % and 6 % in the UV and visible ranges, respectively. The error related to $dAMF_{O_4}$ is larger, reaching 18 % and 13 % in the visible and UV ranges, respectively. Combining all error sources, the total uncertainties on the parameterized NO_2 are about 20 % and 19 % for the near-surface VMR and VCD in the visible range, while the corresponding errors in the UV are 17 % and 16 %. A summary of the above-mentioned error sources in the parameterized NO_2 is presented in Table 11.4.

11.3.3 Horizontal distribution of NO_2

Qualitative information about the horizontal distribution of NO_2 along each azimuthal direction can be obtained by considering how the dSCDs derived in the visible and UV ranges depend on the retrieved horizontal light path lengths (dLeff (NO_2)) (Ortega et al., 2015; Seyler et al., 2019). Indeed, dLeff (NO_2) values depend strongly on scattering and atmospheric conditions, and, since scattering processes are more pronounced at shorter wavelengths, dLeff (NO_2) is shorter in the UV than in the visible (dLeff(NO_2Vis) > dLeff(NO_2UV)).

During one measurement, four useful pieces of information can be used in order to estimate the distance of the NO_2 concentration peak with respect to the instrument: the measured NO_2 near-surface VMR and the dLeff (NO_2) in the visible and UV ranges. Three different cases can be distinguished.

(1) VMR(NO_2Vis) > VMR(NO_2UV). In this case, the NO_2 peak (dVMR (NO_2) = (dSCD (Vis) - dSCD (UV))/dLeff(NO_2 UV) n_{air}) is located further away from the measurement site and approximately, at the distance dLeff(NO_2UV) < dL < dLeff(NO_2Vis).

(2) VMR(NO_2Vis) < VMR(NO_2UV). Here, the NO_2 peak (dVMR (NO_2) = VMR (NO_2 UV)) is located close to the MAX-DOAS instrument in a distance equal to dLeff (NO_2 UV).

(3) VMR (NO_2 Vis) = VMR (NO_2 UV). If both NO_2 VMR in the Vis and UV ranges are equal, it can be concluded that the NO_2 field (dVMR (NO_2) = VMR (NO_2 Vis) = VMR (NO_2 UV)) is homogenously distributed along the line-of-sight.

This information is further exploited in chapter 13.1, where the seasonal variation of the dual-scan MAX-DOAS measurements is presented.

11.3.4 Validation of the parameterization method

To validate the dual-scan parameterization method used in this study, two different approaches are adopted. First, the MLH, which is used in the calculation of the correction factors, is compared with MLH measurements using a colocated ceilometer. Second, the NO_2 near-surface VMRs and VCDs calculated by the parameterization technique in the main azimuthal angle (35.5^o with respect to north) are compared to corresponding results obtained with the MMF inversion algorithm.

To validate the MLH estimations, we use a colocated Vaisala CL51 ALC ceilometer operated by RMI. With this instrument, the MLH is retrieved according to an algorithm based on the direct analysis of the backscatter gradient and variance (De Haij et al., 2007; Haeffelin et al., 2016; Menut et al., 1999).

Figure 11.2 displays the diurnal variation of monthly averaged MLH values derived from the ceilometer and MAX-DOAS data during one full year, from March 2018 until March 2019. As can be seen, the MAX-DOAS data capture the diurnal variation of the MLH measured by the ceilometer well. The corresponding scatter plot is presented in Figure 11.3. Both datasets are highly correlated (R=0.84); however, the slope value (0.84) indicates that $MLH_{MAX-DOAS}$ tends to slightly overestimate MLH_{CEIL}, with the difference between the two MLH values generally being smaller than 500 m. We note that the offset is larger during spring and summer. Since the ceilometer relies on the aerosol vertical distribution to derive MLH and the MAX-DOAS uses the NO_2 vertical profile, differences in the absolute height values are expected. The NO_2 tropospheric columns, near-surface concentrations and atmospheric lifetime show a strong seasonality, with maximum values during cold months. During warm months, the solar heating causes warmer air to rise. The typical time for air to rise from the surface to the top of the MLH is about 1 h or less (Stull, 1988). During spring and summer, the differences between the ceilometer and MAX-DOAS MLH could be explained as follows: since the NO_2 lifetime is greater than 1 h (Ehhalt et al., 1992) and in combination with air uplifting activity (only present during warm seasons), NO_2 could be transported to higher heights than the ones estimated by the ceilometer.

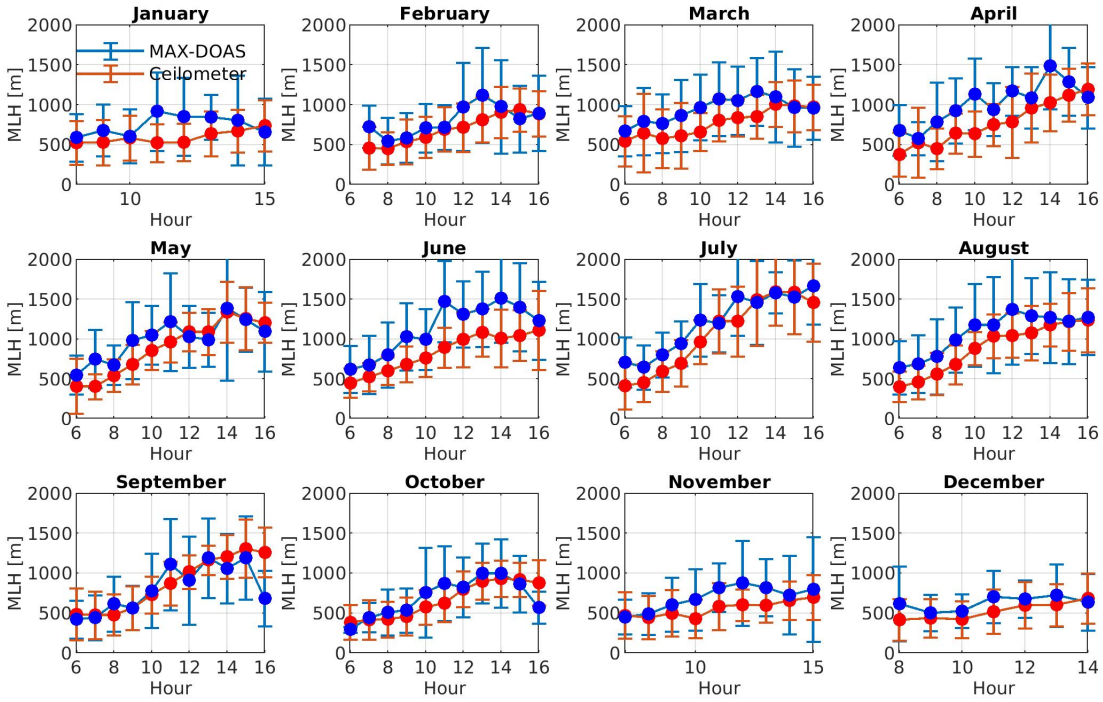

Figure 11.2: Comparison of monthly averaged MLH diurnal variations as estimated by the BIRA-IASB MAX-DOAS measurements and the co-located ceilometer. The error bars for both datasets represent the standard deviation ($\pm 1\sigma$) of the hourly mean over one month.

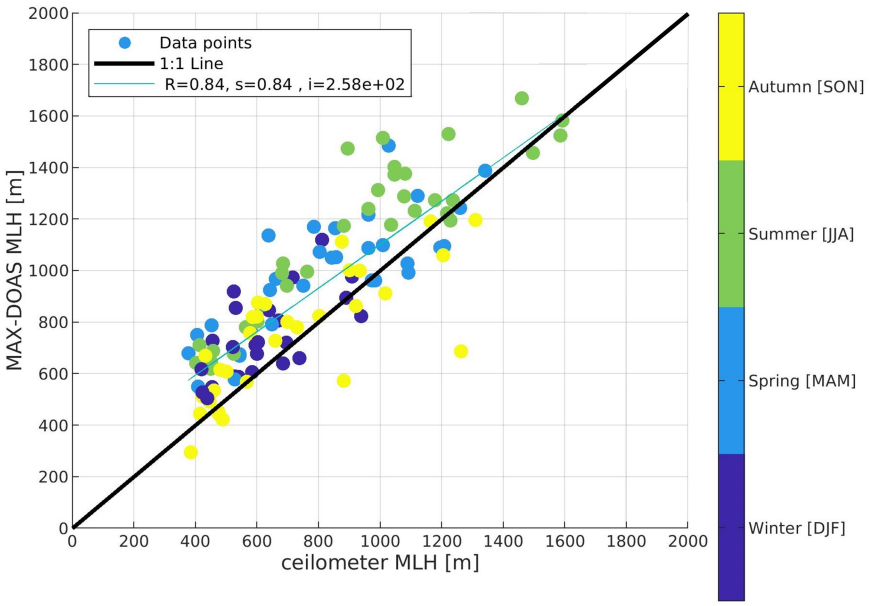

Figure 11.3: Scatter plot of the monthly average MLH diurnal variation values of the MAX-DOAS and the co-located ceilometer. The color bar separates the data by season.

The second approach to validate the parameterization technique consists of comparing the retrieved NO_2 near-surface VMR and VCD to the near-surface VMR (0-200 m) and VCD derived by using the MMF inversion algorithm. The only variable derived from MMF calculations and used in the parameterization technique is the MLH. As we can see in Figures 11.4 and 11.5, results from both methods are highly correlated. The few cases in which the two methods differ more substantially correspond to low $dAMF_{O_4}$ values, which are associated with larger uncertainties.

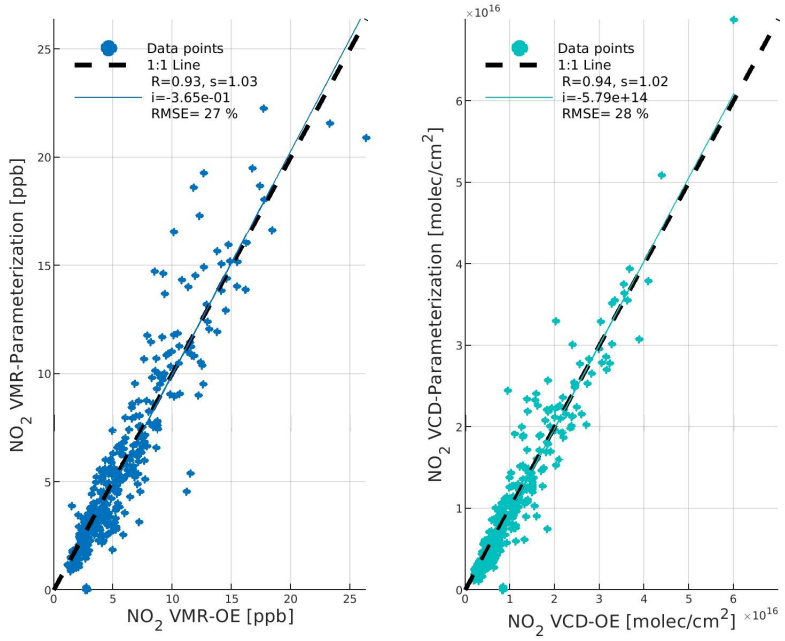

Figure 11.4: Vis Range: Comparison between (left panel) MMF and parameterized NO_2 near-surface VMR and (right panel) MMF and parameterized NO_2 VCD.

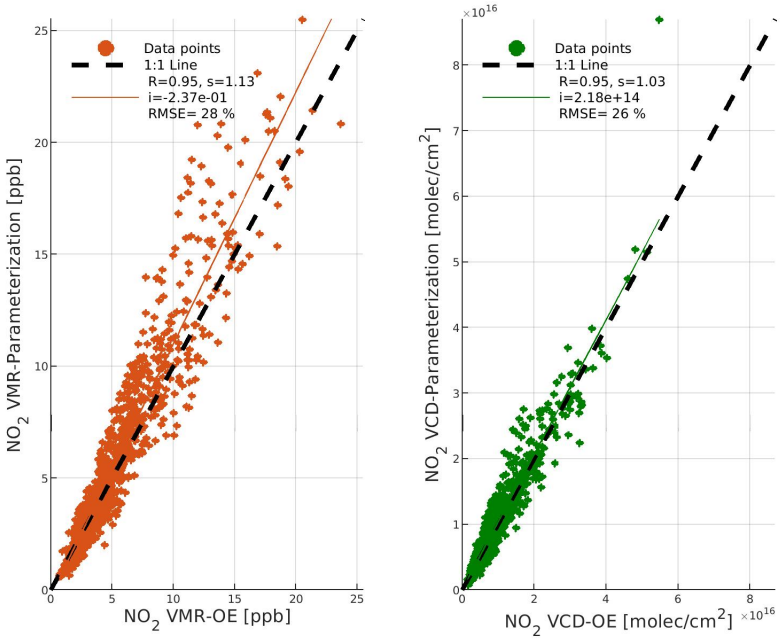

Figure 11.5: Same as Figure 11.4 for the UV channel.

Chapter 12

TROPOMI tropospheric NO_2 dataset

In Part III, reprocessed (RPRO) and offline (OFFL) datasets of the TROPOMI L2 tropospheric NO_2 column product (see Table 12.1 for the corresponding versions) are used. To focus on high-quality measurements, only pixels characterized by a quality assurance value larger than 0.75 are used so that pixels covered by clouds (pixels with a cloud radiance fraction larger than 0.5), snow or ice and erroneous retrievals are excluded from the analysis. The TROPOMI overpass over Brussels is around 13:30 LT. Figure 12.1 illustrates a typical comparison case. Superimposed on TROPOMI ground pixels as measured above Brussels on 6 June 2018, one can distinguish the different azimuthal viewing directions sampled by the Uccle dual-scan MAX-DOAS system. As can be seen, multiple pixels are coincident with one MAX-DOAS azimuthal direction, showing the high spatial resolution of TROPOMI and the challenges concerning its validation.

In chapter 8.1.1, the reader can find a detailed description of the TROPOMI characteristics and the tropospheric NO_2 algorithm.

Table 12.1: TROPOMI NO_2 processor versions used in Part III.

Dataset	Number of version	Starting date of operation	End date of operation
RPRO	010202	17/03/2018	17/10/2018
OFFL	010200	17/10/2018	27/11/2018
OFFL	010202	28/11/2018	20/03/2019

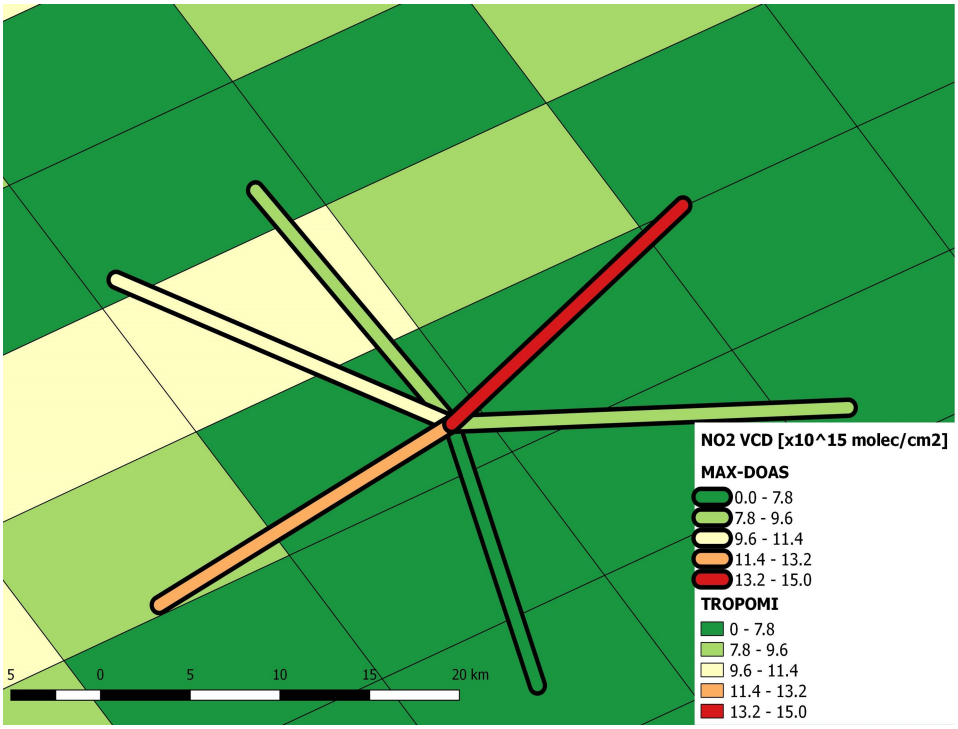

Figure 12.1: Tropospheric NO_2 columns derived from the TROPOMI (pixel size equal to 7x3.5 km^2) and the MAX-DOAS instrument on 06 June 2018 near the measurement site of Uccle.

Chapter 13

Results and discussion

Contents

13.1 Seasonal variation of dual-scan MAX-DOAS measurements

Box-and-whisker plots of MAX-DOAS horizontal effective light paths (dLeff (NO_2), see Equation 11.3) determined in each season for all the viewing azimuthal directions are presented in Figure 13.1 for the visible and UV wavelength ranges. As can be seen, the dLeff (NO_2) shows maximum median values during summer and a minimum during winter for both wavelength ranges. The seasonality of dLeff (NO_2) is related to the seasonal variation of the aerosol content in the troposphere. For high aerosol load conditions, the light path tends to become shorter due to increased scattering. In the visible range, dLeff (NO_2) can reach values of up to 19 km during winter with a mean value of 10 km, while in the UV, the maximum value is around 12 km with a mean value of 8 km. Similar horizontal distance values have been found by Schreier et al. (2020) using MAX-DOAS measurements in Vienna. Horizontal sensitivities (dLeff (NO_2) are generally larger in the visible than in the UV because of the more pronounced Rayleigh scattering at UV wavelengths. Similarly, dLeff (O_4), which is the horizontal sensitivity before applying the appropriate correction factors, is larger in the visible than in the UV range. The dLeff(O_4) visible can reach values of up to 28 km, while the maximum value for UV is around 18 km. The difference between dLeff (NO_2) and dLeff (O_4) can become quite large by approximately a mean factor of 2 and 1.6 for visible and UV, respectively. For extreme cases, this difference factor can be up to 5 and 4 for visible and UV, respectively.

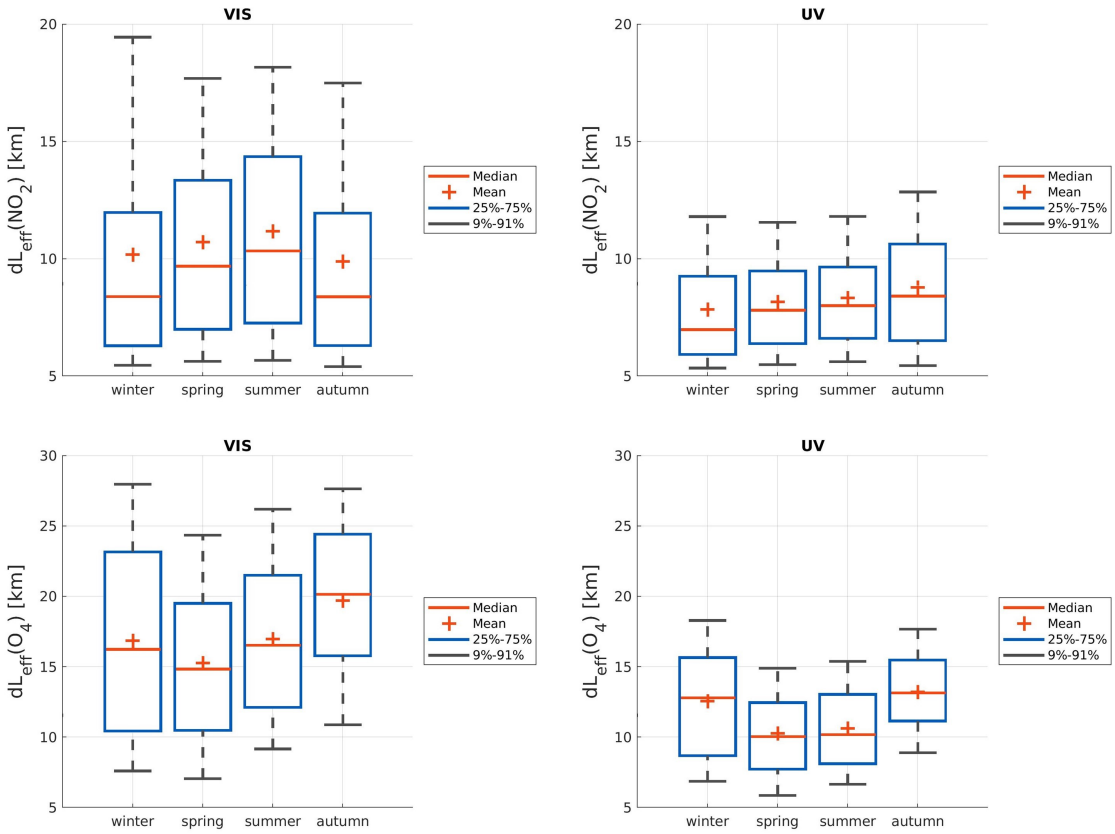

Figure 13.1: Upper panels show the box and whisker plots representing the seasonal horizontal sensitivity as derived from all the azimuthal viewing directions by applying the parameterization method for the Vis (left panel) and UV (right panel) spectral ranges. Every seasonal box contains the estimated dLeff (NO_2) of all the azimuthal viewing directions. Lower panels show the corresponding estimates of dLeff (O_4).

In Figure 13.2, the seasonal variation of the MAX-DOAS near-surface NO_2 VMR is presented for both visible and UV channels in each azimuthal direction at 11:00 UTC. The choice of presenting the MAX-DOAS measurements at 11:00 UTC is based on the TROPOMI overpass time, which varies between 10:00 and 12:00 UTC. The length of the lines corresponds to the seasonally averaged dLeff (NO_2). As mentioned above, dLeff (NO_2) is longer in the visible than in the UV range, which leads to a more extended spatial sensitivity in the visible than in the UV range. As explained in chapter 11.3.3, the relationship between NO_2 VMRs and dLeff (NO_2) values contains information about the horizontal distribution of NO_2 . This relationship and the wavelength dependence of the horizontal effective light path were also used by Seyler et al. (2019) to characterize the horizontal inhomogeneity of the NO_2 concentration above a shipping lane.

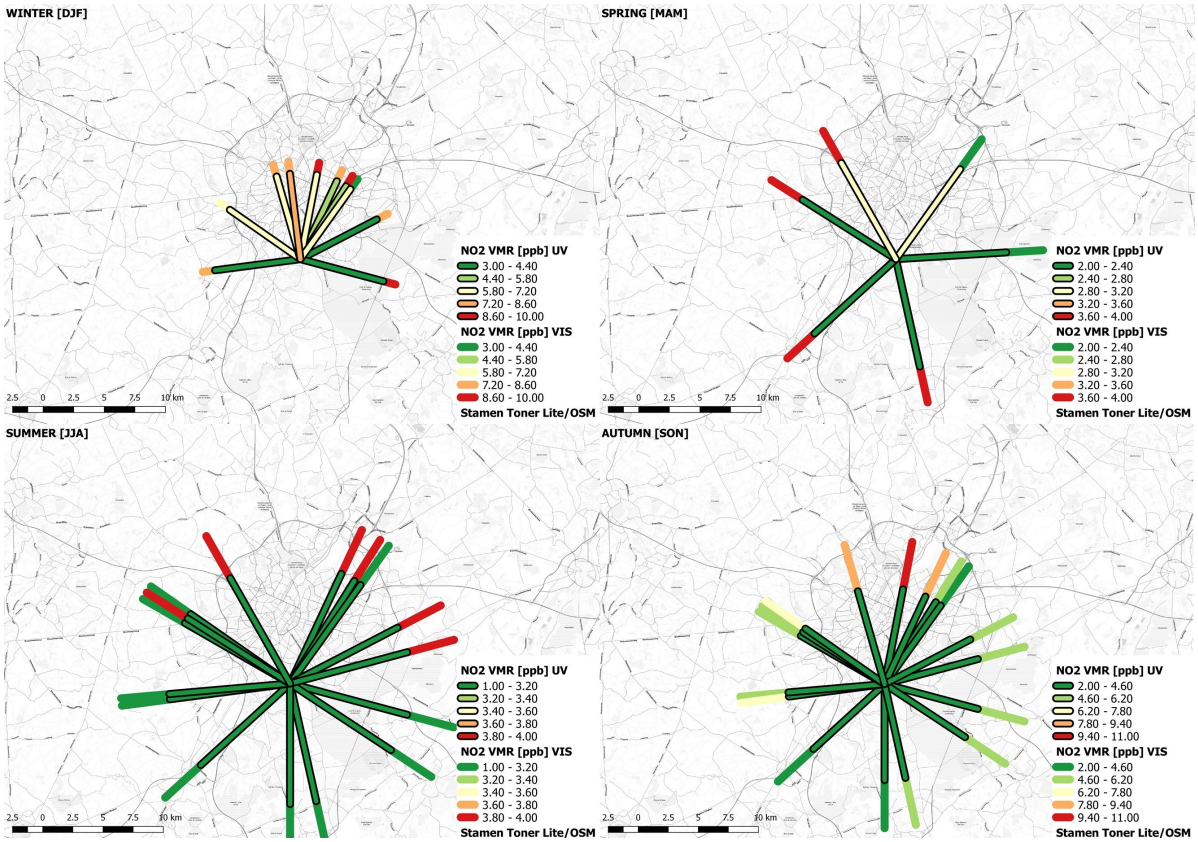

Figure 13.2: Seasonally-averaged near-surface NO_2 VMR around 11 UTC as a function of azimuthal viewing direction derived by the parameterization technique in the Vis and UV wavelength ranges. Lines with black borders represent the UV VMRs, and lines without black borders show the Vis VMRs. The length of each line represents the seasonally-averaged horizontal sensitivity. Different color scales are used per season. © OpenStreetMap contributors 2019. Distributed under a Creative Commons BY-SA License.

The near-surface NO_2 VMR has a clear seasonal cycle, with a maximum during winter and autumn due to higher emissions, lower temperature (and thus longer NO_2 lifetime) and shallower MLH and a minimum in spring and summer. Moreover, the spatial distribution of NO_2 concentrations around Uccle shows a seasonal dependence. It should be noted that the main emission sources are located in the north and west part of the city and are associated mainly with the motorway around Brussels (the so-called Ring), the national airport in Zaventem and the Drogenbos power plant, the latter being located to the west of Uccle (Tack et al., 2017). In the absence of transport by the wind and given the fact that NO_2 has a shorter lifetime in the MLH (Beirle et al., 2011), the higher NO_2 concentrations should appear at the location of main emission sources. As can be seen in Figure 13.2, this is not the case during all seasons due to the influence of seasonal wind patterns. During winter, higher NO_2 concentrations are retrieved mainly in the north (N) and northeast (NE) directions. The fact that the NO_2 concentration in the NE direction is higher in the visible than in the UV suggests that the NO_2 peak is located away from Uccle and closer to the Brussels national airport. On the other hand, in the northwest (NW) direction, the NO_2 concentrations are lower in the visible than in the UV. This can be associated with higher anthropogenic activity in the city center of Brussels. During spring and summer, the observed NO_2 VMRs are the lowest of the March 2018-March 2019 period. For

spring, the maximum concentrations are measured away from the measurement site (visible) in the south (S) and NW direction. It is worth mentioning that in the east (E) direction, the visible and UV measurements have almost the same concentrations, indicating that the NO_2 field is homogeneous in those areas. During summer, the maximum NO_2 VMRs are retrieved in the visible range and in the NE and NW directions, suggesting that the sources are mainly located away from the measurement site, possibly linked to the airport and city-center activity. One observes that in the south (in the direction of a large forested area), the retrieved concentrations are very low, while they are substantially higher in the NW and NE. Finally, during autumn, higher values are observed away from Uccle in the north direction, corresponding to sources located away from the measurement site and mostly traffic-related.

As already noted, the retrieved NO_2 VCDs can be influenced by the wind direction. In Figure 13.3, MAX-DOAS NO_2 VCDs are represented as a function of the wind direction during the MAX-DOAS observations. The wind direction is measured by the BIRA-IASB meteorological station in Uccle. Generally, when the wind is blowing from the NE and SE direction, higher NO_2 columns are retrieved. During winter and autumn, the NO_2 VCDs, which are retrieved under different wind directions, differ significantly compared to summer and spring. We conclude that emission sources located away from the measurement site influence the measured NO_2 concentration levels when the wind is blowing in the direction of the site.

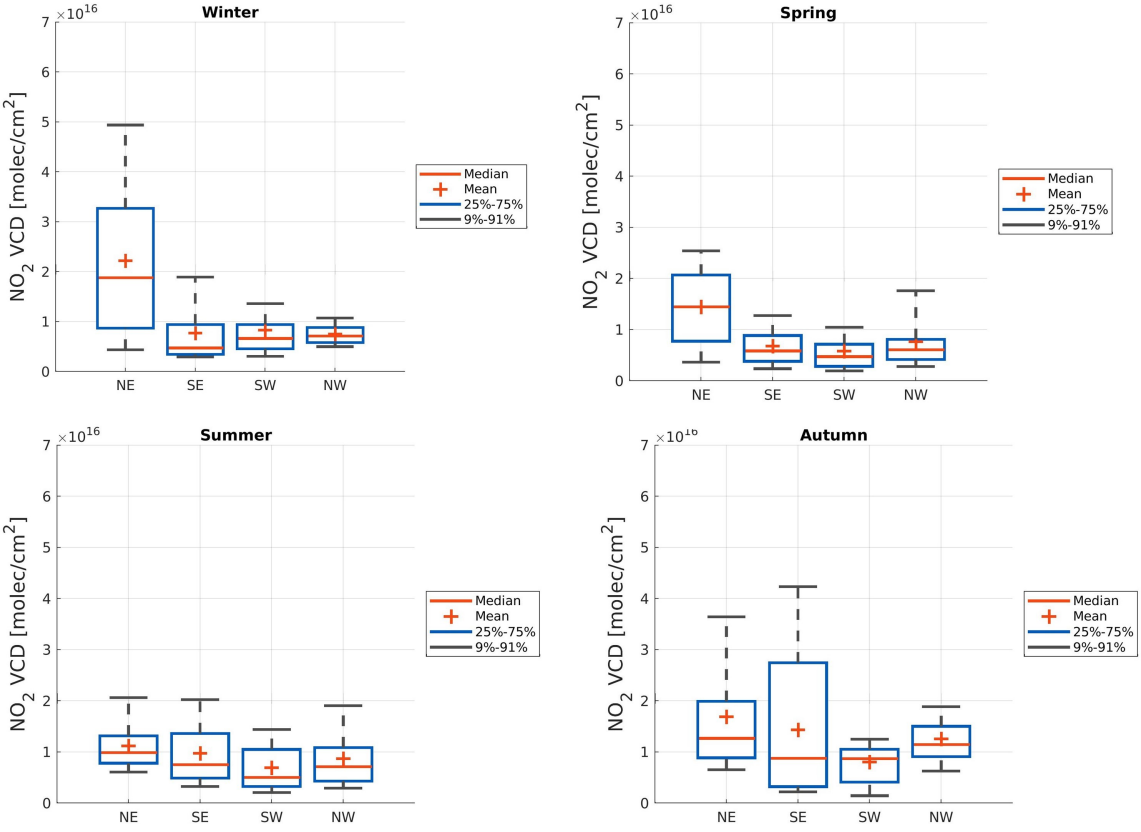

Figure 13.3: Box and whisker plots representing, for each season, the tropospheric NO_2 column as a function of the wind direction. The MAX-DOAS columns are derived by the parameterization technique in the Vis wavelength range (all the azimuthal directions are included) and the wind observations from the meteorological station on the BIRA-IASB rooftop.

13.2 Comparison of MAX-DOAS and in-situ measurements

The in situ telemetric air quality network (Bruxelles Environnement/Leefmilieu Brussel) of the Brussels region is used to verify the retrieved near-surface NO_2 VMR. Previous studies (e.g. Kramer et al., 2008; Schreier et al., 2019) have compared NO_2 MAX-DOAS measurements with in situ concentrations, concluding that there is a considerable underestimation of NO_2 near-surface VMR by the MAX-DOAS instrument. The present work uses hourly NO_2 near-surface concentrations from 10 monitoring stations distributed in the Brussels city area and provided by the Belgian Interregional Environment Agency (see http://www.irceline.be/en, last access: 11 September 2020). Each station is characterized according to its location: urban, urban background, traffic, rural or industrial.

In some directions, several in situ stations are located in proximity to the MAX-DOAS line of sight so that MAXDOAS NO_2 concentrations can be compared to an average of the in situ values reported at these stations. Because of the different spatial representativeness of the MAX-DOAS and in situ techniques, one expects differences in the observed surface concentrations (e.g. a VMR underestimation by the MAX-DOAS if the in situ station is located close to a strong local emission source). However, for days on which NO_2 is homogeneously distributed along the light path, both instruments should measure similar concentration levels. To restrict the comparison to conditions of good horizontal homogeneity, the hourly in situ NO_2 near-surface concentrations for each in situ station category were compared to each other, and only measurements wherein the concentrations of the in situ stations differed by less than 2 ppb within a time window of 1 h were selected. Additionally, we only considered MAX-DOAS measurements for which the horizontal sensitivity was less than 10 km. This distance is the maximum between the MAX-DOAS site and all the chosen in situ stations.

Based on the different categories of in situ stations, three groups were created, similarly to the study of Kramer et al. (2008): (1) urban background, (2) urban and (3) traffic. The in situ data were interpolated on the MAX-DOAS time grid and compared with the retrieved MAX-DOAS nearsurface VMR. For the comparison, the in situ dataset was averaged in bins of 2.5 ppb length each. In Figure 13.4, the results of this comparison show that the MAX-DOAS near-surface NO_2 VMRs have a systematic low bias when compared to in situ data. As expected, the best agreement is found at urban background stations. For these sites, correlation coefficients of 0.91 and 0.83 and slope values of 0.39 and 0.39 are obtained for visible and UV data, respectively. The majority of the comparison data points show that the MAX-DOAS NO_2 VMRs are lower than the in situ NO_2 observations by approximately a factor of 2. However, a more careful inspection of the results indicates that much better agreement is obtained when considering NO_2 VMR values smaller than 12 ppb at urban background stations (R close to unity and slope close to 0.69). Such moderately polluted conditions likely correspond to homogeneously distributed NO_2 fields similarly sampled by in situ and remote-sensing measurements.

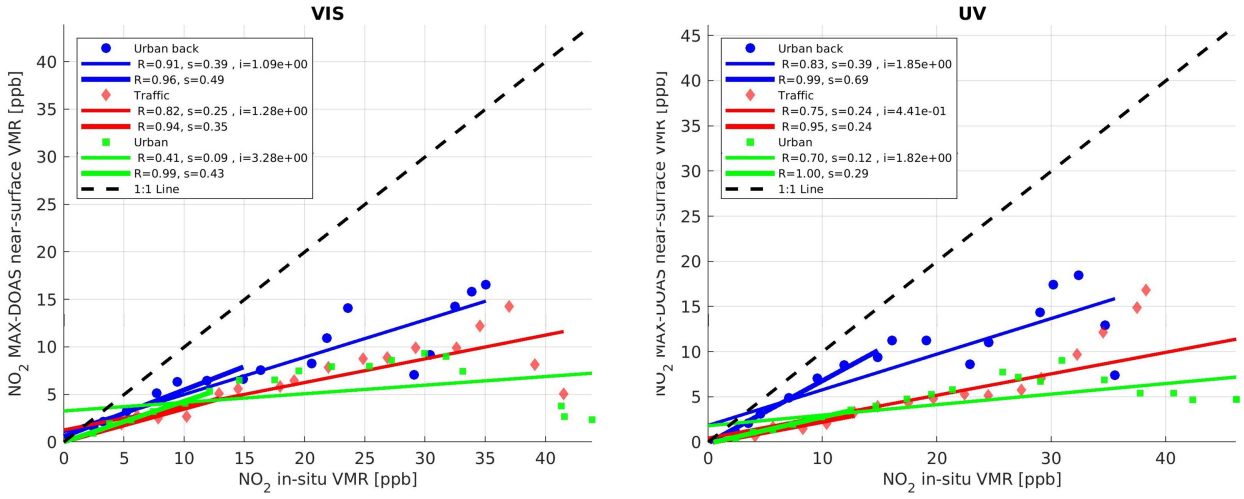

Figure 13.4: Scatter plots of binned MAX-DOAS and in-situ NO_2 near-surface VMR in the (left panel) VIS and (right panel) UV channels. The solid thick lines are the regression analysis results for the 0-12 ppb in-situ NO_2 concentration range.

The worst agreement is found at traffic and urban stations (R in the 0.41-82 range). At these stations, the MAX-DOAS NO_2 VMRs are lower than the in situ NO_2 observations by approximately a factor of 2 and 3, respectively. Three factors can explain these findings. First, MAX-DOAS concentrations are integrated along a long light path, which smooths out the variability of the NO_2 field along this path, while the in situ instruments perform measurements at a single location point. Secondly, the in situ stations are typically located at 3-10 m of altitude, while the MAX-DOAS near-surface measurements correspond to a layer extending from the surface to approximately 420 m of altitude for the visible range considering a horizontal distance of 12 km and from the surface to 280 m of altitude for UV based on a horizontal distance of 8 km (see corresponding dLeff (NO_2) in Fig. 13.1). Hence, the MAX-DOAS near-surface concentration is not fully representative of the in situ surface concentration, as reported in Kramer et al. (2008). Thirdly, the comparison discrepancies could also come from errors in either MAX-DOAS retrievals, as documented in Tables 11.3 and 11.4, or surface NO_2 measurements because of instrumental errors and biases.

13.3 Validation of TROPOMI tropospheric NO_2 columns

To validate the TROPOMI tropospheric NO_2 columns, we adopted three successive approaches.

A first comparison is performed by selecting only MAX-DOAS data in the main azimuthal direction (35.5° with respect to north) and the TROPOMI value from the closest pixel located in the same direction as the MAX-DOAS measurement.

To improve the spatial coincidence between MAX-DOAS and TROPOMI observations, a second comparison is performed by using the dual-scan MAX-DOAS observations: measurements in every MAX-DOAS azimuthal direction are compared with a weighted average of TROPOMI columns as measured in coincident pixels with the weighting being determined by the MAX-DOAS horizontal segment crossing every pixel.

The impact of possible systematic uncertainties on the satellite retrieval (in particular the a priori profile shape) is investigated. In order to increase the number of colocation pairs, we compare both UV and visible MAX-DOAS measurements with TROPOMI. It should be emphasized that UV and visible MAX-DOAS VCDs correspond to

different dLeff (NO_2) values (see Figure 13.1 and section 11.3.3) and consequently different sampling of TROPOMI pixels. In the following sections, the regression analysis parameters (correlation coefficient and slope value) refer to both UV and visible MAX-DOAS measurements together.

13.3.1 Validation based on one MAX-DOAS azimuthal direction measurements

In this first approach, the MAX-DOAS tropospheric NO_2 VCDs, derived in the main azimuthal direction by applying the MMF algorithm, are compared to TROPOMI observations in the same direction as the MAX-DOAS measurement. We select the closest TROPOMI pixel that intercepts the MAX-DOAS line of sight within a radius of 20 km around Uccle. This approach has generally been used in previous satellite validation studies based on MAX-DOAS observations (e.g., Irie et al., 2008; Chen et al., 2009; Ma et al., 2013). It is adopted for reference against other comparison strategies that make use of more than one azimuthal MAX-DOAS measurement (see section 13.3.2).

We compare TROPOMI daily measurements with MAX-DOAS NO_2 VCDs averaged around ($\pm$1 h) the TROPOMI overpass time. A first comparison plot is presented in Figure 13.5, where the time series of the TROPOMI tropospheric NO_2 VCD is displayed together with the visible MAX-DOAS measurements. All TROPOMI and MAX-DOAS data points presented in Figure 13.5 satisfy the quality check requirements for both datasets. The MAX-DOAS error bars represent the standard deviation of the mean values ($\pm$1 h) and the typical retrieval uncertainty, while the TROPOMI bars are equal to the tropospheric column error of the pixel. Results show that MAX-DOAS measurements have larger variability than corresponding TROPOMI observations. In addition, TROPOMI tropospheric NO_2 columns are systematically lower than colocated MAX-DOAS data. This finding is in agreement with the recent studies of Griffin et al. (2019), Zhao et al. (2020) and Ialongo et al. (2020).

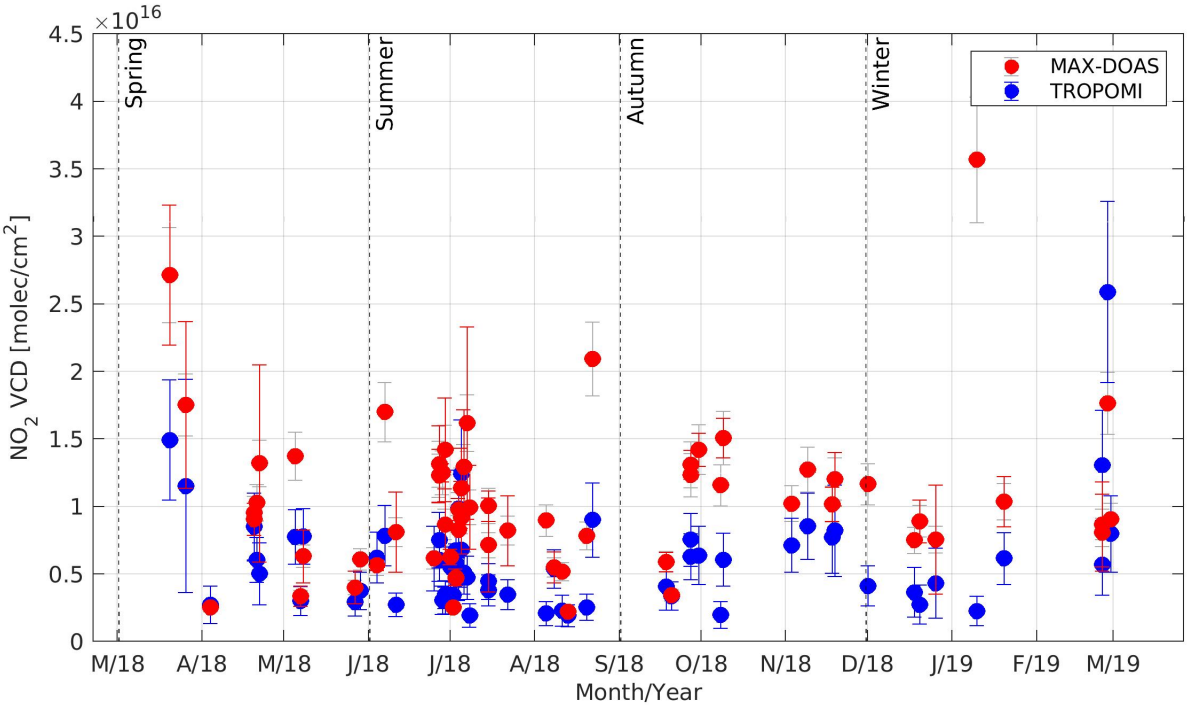

Figure 13.5: Time series of the tropospheric NO_2 columns derived from the main azimuthal MAX-DOAS direction observations in the Vis range and the closest TROPOMI pixel located along the MAX-DOAS azimuthal direction. The MAX-DOAS error bars (red lines) represent the standard deviation of the averaged values within one hour before and after TROPOMI's overpass time and the grey error bars correspond to typical MAX-DOAS inversion uncertainty. The TROPOMI error bars are equal to the TROPOMI VCD error as provided in the data files.

Figure 13.6 presents scatter plots of TROPOMI tropospheric NO_2 VCDs against MAX-DOAS data for the four seasons from March 2018 to March 2019. The highest correlation is found during spring (R = 0.71), while lower correlations are obtained in summer, winter and fall, with correlation coefficient values in the 0.25-0.63 range. During autumn 2018, the number of visible data points is significantly smaller than in the UV because of more frequent unrealistic retrieved profiles. On the other hand, during summer, the accepted scans are almost equal for the UV and visible ranges. The same ratio of accepted scans to the total number of scans is observed during autumn and summer 2019, indicating that the meteorological conditions (mostly cloud cover) during autumn strongly affect the visible retrieval. Regarding the slope values, they are all smaller than 0.5, except for spring, indicating that TROPOMI columns are about a factor of 2 lower than MAX-DOAS columns (in agreement with the S5P MPC VDAF validation web article, available at: http://mpc-vdaf.tropomi.eu/, last access: 16 January 2020).

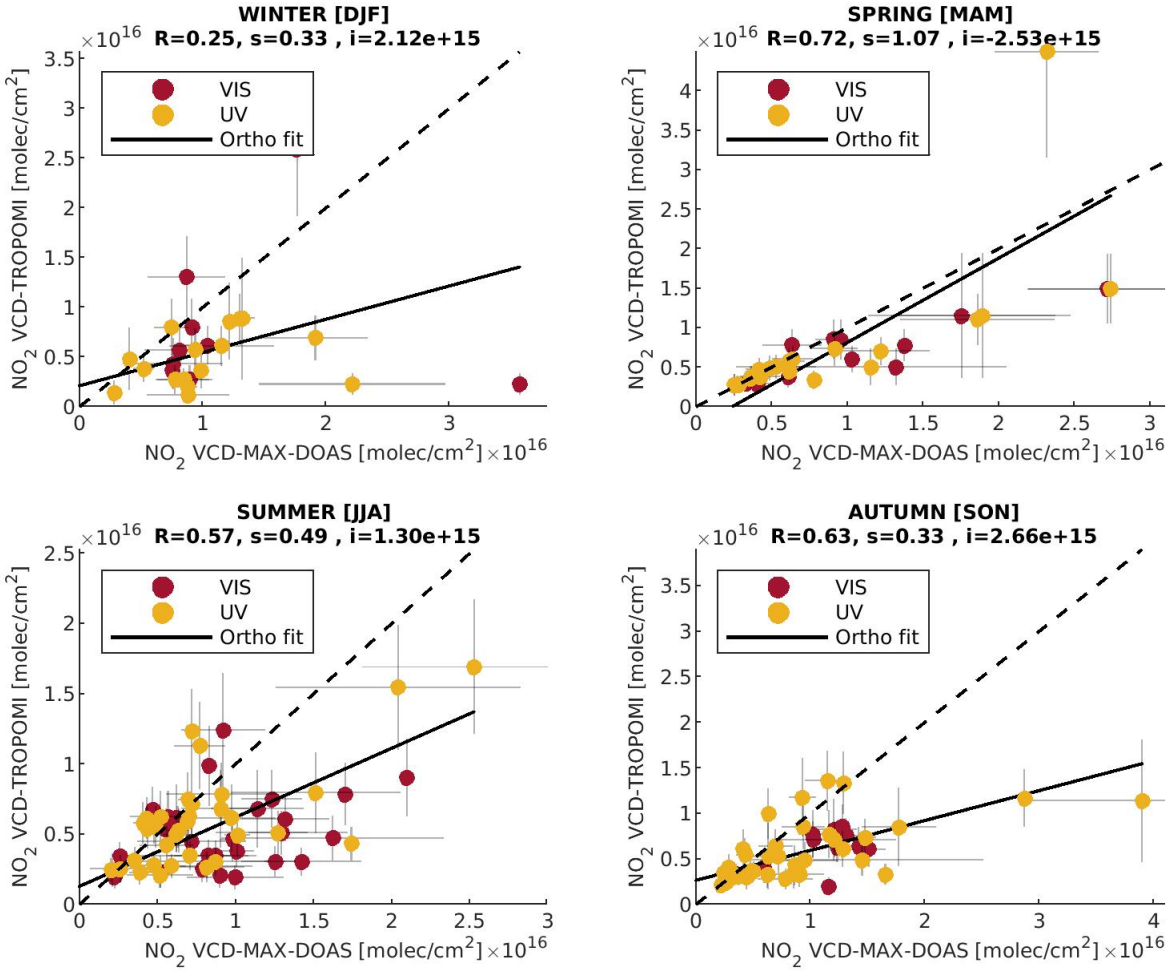

Figure 13.6: Seasonal scatter plots between the tropospheric NO_2 columns derived by UV and Vis MAX-DOAS observations (yellow and red circles, respectively) in the main azimuthal direction and the closest TROPOMI pixel with respect to the measurement site. The slope is estimated by using orthogonal regression analysis. The error bars are the same as in Figure 13.5.

These results indicate that the discrepancy between TROPOMI and MAX-DOAS measurements is significant during all seasons and particularly marked during winter and autumn. A possible explanation could be differences in the air masses probed by the two instruments. The use of only one satellite pixel, even if its direction with respect to the MAX-DOAS line of sight is taken into account, is not necessarily the most appropriate comparison method. One azimuthal MAX-DOAS measurement samples air masses along a light path of several kilometers in a fixed direction, which corresponds to more than one TROPOMI pixel, as outlined in Fig. 12.1. One expects this horizontal sampling effect to be more marked in winter and fall given the larger NO_2 concentration gradients observed during these seasons compared to the other ones (see Sect. 13.1 and Fig. 13.2).

13.3.2 Validation based on dual-scan MAX-DOAS azimuthal direction measurements

In a second step, we compare TROPOMI tropospheric NO_2 columns with the dual-scan parameterized MAX-DOAS NO_2 VCDs. Two modifications are introduced: (1) the use of more than one MAX-DOAS azimuthal direction and (2) a better spatial selection of the TROPOMI pixels accounting for the MAX-DOAS horizontal sensitivity (dLeff (NO_2)). Only satellite pixels located along the segments of length dLeff (NO_2) in the different MAX-DOAS azimuthal directions and timely coincident dual-scan MAX-DOAS observations (TROPOMI overpass time $\pm$ 1 h) are selected. MAXDOAS NO_2 VCDs in every MAX-DOAS azimuthal direction are compared to a weighted average of TROPOMI columns from the different pixels that are crossed by the corresponding MAX-DOAS horizontal line-of-sight segment. The weight of a given pixel is derived from the length of the segment portion that crosses the pixel. We can use Figure 12.1 as a simplified scheme to show two important aspects of this comparison: (1) every MAX-DOAS azimuthal line of sight is representative of a segment section that extends from the instrument to a distance equal to dLeff (NO_2), and (2) dLeff (NO_2) in one azimuthal direction can be separated into different portions that cross each of the selected satellite pixels.

Results displayed in Figure 13.7 show that the agreement between TROPOMI and MAX-DOAS datasets is significantly improved, especially in terms of correlation (R in the 0.60-0.85 range instead of 0.25-0.72). Owing to the improved spatial coincidence associated with the use of dual-scan MAXDOAS data and the better spatial coincident criterion between TROPOMI and MAX-DOAS data, the scatter in the data points is also substantially reduced during all seasons, especially in winter. Another interesting feature is the improvement of the slope values observed in winter and autumn (slopes of 0.81 and 0.61, respectively, instead of 0.33). During seasons (spring, summer) with a more homogeneous NO_2 field, the improvement of the slope values is less pronounced than during seasons when the NO_2 field can be highly inhomogeneous (i.e. winter and autumn). During spring, the slope value is reduced despite the better correlation. Overall, TROPOMI still underestimates MAX-DOAS measurements by about 40 %-50 %.

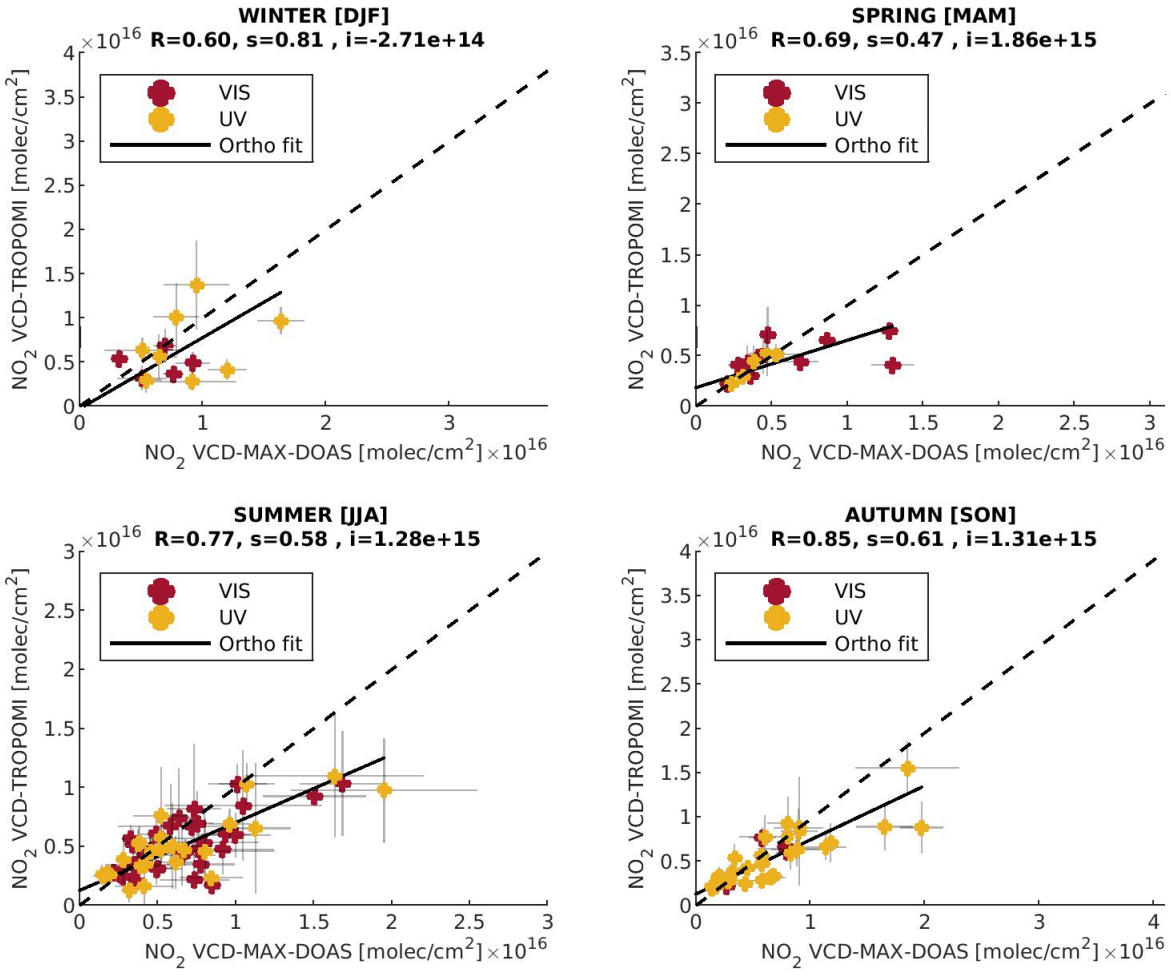

Figure 13.7: Seasonal scatter plots between the tropospheric NO_2 columns derived from the dual-scan MAX-DOAS observations (in the Vis and UV together) and the TROPOMI pixels by using information about the MAX-DOAS horizontal effective light path and the co-location between pixels and azimuthal directions. The MAX-DOAS error bars are the same as in Figure 13.5. The TROPOMI error bars represent the standard deviation of the averaged pixel values within a circle with radius equal to the MAX-DOAS horizontal effective light path.

13.4 Systematic uncertainties in TROPOMI NO_2 retrievals

To identify the origin of the persisting underestimation of TROPOMI NO_2 measurements, we investigated the most relevant sources of uncertainties in the satellite retrievals.

Boersma et al. (2004) presented a thorough analysis of satellite tropospheric NO_2 column retrieval uncertainties. Main error sources are related to the spectral fitting (dominated by measurement noise), the estimation of the stratospheric NO_2 column and knowledge of the main ancillary parameters used for the AMF calculation, i.e. surface albedo, cloud fraction, cloud-top height, aerosols and the a priori NO_2 profile shape. In the following subsections, we briefly discuss uncertainties related to cloud, aerosol and surface albedo, and afterwards we investigate in more detail the role of the a priori NO_2 profile.

13.4.1 Clouds and aerosols

Clouds can have a major impact on tropospheric NO_2 observations from space because of their strong influence on incoming solar radiation (Boersma et al., 2004; Koelemeijer et al., 2001). In the TROPOMI tropospheric NO_2 retrieval algorithm, only cloud-free and weakly cloudy scenes are considered valid measurements satisfying the recommended quality assurance value (QA $>= 0.75$) (see section 12). Although this quality flagging effectively minimizes uncertainties due to clouds on the NO_2 product, many selected scenes are still partially cloud-covered and affected by cloud-related errors. In the TROPOMI processor, clouds are characterized by using cloud fraction and cloud-top height parameters, which are both derived from radiance observations in the O_2 A band. This cloud information is used as an input in a cloud correction scheme applied to NO_2 retrieval (Geffen et al., 2020). Cloud-induced errors are complex and can lead to positive or negative biases in the tropospheric NO_2 column, resulting in considerable scatter in the retrieved columns, especially for small cloud fractions.

Like clouds, aerosols can affect the accuracy of tropospheric NO_2 retrieval from space (Leitão et al., 2010; Heckel et al., 2011; McLinden et al., 2014). In the TROPOMI NO_2 algorithm, aerosols are not explicitly treated, which means that all AMF calculations are performed for a Rayleigh atmosphere (clouds being treated as simple Lambertian reflectors). The impact of aerosols is, however, considered indirectly through the cloud correction algorithm under the assumption that scattering aerosols will tend to increase the cloud fraction. For non-absorbing aerosols of moderate optical thickness, like typically observed in Brussels, this simplified approach was shown to be effective in accounting for the impact of reflecting aerosols on tropospheric NO_2 AMFs (Boersma et al., 2004).

13.4.2 Surface albedo

Surface albedo is another parameter having a significant influence on satellite tropospheric NO_2 AMFs. In the study of Boersma et al. (2004), it was shown that the NO_2 AMF sensitivity to albedo is large, especially for albedos smaller than 0.2. For albedo values between 0.0 and 0.2, which are common in the blue spectral range over land, a difference of 0.015 in the surface albedo can lead to a 12 % change in the tropospheric NO_2 AMF. In order to estimate surface albedo uncertainties in the Uccle conditions, observations from the Airborne Prism Experiment (APEX) performed above Brussels during June 2015 (Tack et al., 2017) were compared with climatological values used in the TROPOMI operational algorithm. The difference between these two independent estimates of the albedo was found to be small on average (smaller than 0.01), suggesting that albedo data used in the TROPOMI algorithm are representative of the Brussels area in June.

However, we should keep in mind that the surface albedo values used in the TROPOMI NO_2 AMF calculations have a spatial resolution of 0.5^ox0.5^o and are monthly mean climatology values (Kleipool et al., 2008). In reality, inside an area 0.5^ox0.5^o of an urban environment, we expect to have considerable differences between the albedo values at the scale of TROPOMI pixels. So even if the difference between APEX and TROPOMI albedos was found to be small on average for the June 2015 flight, further investigation is needed to fully assess the impact of albedo uncertainties on the TROPOMI NO_2 product (F. Tack, personal communication, 2020). The impact of surface

albedo on the NO_2 retrievals from satellites, such as GOME-2 and OMI, has been investigated in the recent studies of Liu et al. (2020) and Lamsal et al. (2021), respectively.

13.4.3 A priori NO_2 profile shape

The TROPOMI NO_2 retrieval algorithm uses NO_2 vertical profiles specified by the TM5-MP model for 34 vertical layers at the horizontal resolution of 1^ox1^o in latitude-longitude (Williams et al., 2017). In comparison to the TROPOMI pixel size (3.5x7 km^2), the resolution of TM5-MP (approximately 100x100 km^2) is thus very coarse and cannot capture spatial gradients at the scale of a city like Brussels.

A way to test how uncertainties on the a priori profile influence the TROPOMI NO_2 VCDs in our observation conditions is to use vertical profiles derived from our MAX-DOAS measurements to recalculate the satellite NO_2 VCDs. In order to perform this transformation, we use the averaging kernel (AK) information provided in the TROPOMI NO_2 product. The AK describes how the sensitivity of the retrieval depends on altitude. For satellite measurements of tropospheric species in the UV-Visible range, the AK generally increases with altitude in the first kilometers above the surface (Figure 13.8). Since the NO_2 profile has its maximum close to the surface, accurate knowledge of the NO_2 vertical distribution in this altitude range is therefore critical for the calculation of the NO_2 AMFs.

We start from the general formula used to derive the NO_2 VCD from satellite measurements (e.g. Veefkind et al., 2011):

$$\mathrm{VCD_{SAT}} = \frac{\mathrm{SCD_{SAT}}}{\mathrm{AMF_{SAT}}} \tag{13.1}$$

where $\mathrm{SCD_{SAT}}$ stands for the NO_2 slant column density, and $\mathrm{AMF_{SAT}}$ for the NO_2 air mass factor as used in the operational algorithm, i.e. based on a-priori NO_2 vertical profiles specified by the TM5 chemistry-transport model.

For optically thin conditions valid in the blue spectral range where NO_2 is retrieved, the satellite AMF ($\mathrm{AMF_{SAT}}$) can be expressed as a linear sum of layer (or box) air mass factors ($\mathrm{AMF_i^{SAT}}$), weighted by the NO_2 VCD contribution in each atmospheric layer:

$$\mathrm{AMF_{SAT}} = \frac{1}{\mathrm{VCD_{apriori}}} \sum (\mathrm{AMF_i^{SAT}} \mathrm{c_i^{apriori}}) \tag{13.2}$$

where $\mathrm{c_i^{apriori}}$ represents the a-priori NO_2 partial column in atmospheric layer i. In addition, the vertical sensitivity of the NO_2 retrieval is given by the averaging kernel (AK) according to:

$$\mathrm{AK_i^{SAT}} = \frac{\mathrm{AMF_i^{SAT}}}{\mathrm{AMF_{SAT}}} \tag{13.3}$$

When comparing satellite and ground-based measurements (here from a MAX-DOAS instrument), it is a good practice to smooth the ground-based reference profile using the satellite AK (see e.g. Eskes and Boersma, 2003):

$$\mathrm{VCD_{MAX-DOAS}^{smoothed}} = \sum (\mathrm{AK_i^{SAT}} \mathrm{c_i^{MAXDOAS}}) \tag{13.4}$$

An alternative approach is to recalculate the satellite VCD using the MAX-DOAS profile as a-priori in the satellite retrieval. Only the AMF is concerned and, similarly to equation 13.2, we can write:

$$\mathrm{AMF_{SAT}^{MAX-DOASpro}} = \frac{1}{\mathrm{VCD_{MAXDOAS}}} \sum (\mathrm{AMF_i^{SAT}} \mathrm{c_i^{MAXDOAS}}) \tag{13.5}$$

or, using equations 13.3 and 13.4:

$$\mathrm{AMF}_{\mathrm{SAT}}^{\mathrm{MAXDOASpro}} = \frac{\mathrm{AMF}_{\mathrm{SAT}}}{\mathrm{VCD}_{\mathrm{MAXDOAS}}} \sum (\mathrm{AK}_{\mathrm{i}}^{\mathrm{SAT}} \mathrm{c}_{\mathrm{i}}^{\mathrm{MAXDOAS}}) = \mathrm{AMF}_{\mathrm{SAT}} \frac{\mathrm{VCD}_{\mathrm{MAXDOAS}}^{\mathrm{smoothed}}}{\mathrm{VCD}_{\mathrm{MAXDOAS}}} \tag{13.6}$$

which finally leads to:

$$\mathrm{VCD}_{\mathrm{SAT}}^{\mathrm{MAXDOASpro}} = \mathrm{VCD}_{\mathrm{SAT}} \frac{\mathrm{VCD}_{\mathrm{MAXDOAS}}}{\mathrm{VCD}_{\mathrm{MAXDOAS}}^{\mathrm{smoothed}}} \tag{13.7}$$

Using the Equation 13.7 and daily median MAX-DOAS concentration profiles derived in the main azimuthal direction using the MMF algorithm, a modified version of the TROPOMI tropospheric NO_2 column product was generated. Daily median MAX-DOAS profiles were used to minimize the impact of instabilities frequently observed in individual profile retrievals, as illustrated in Figure 13.9.

Figures 13.8 and 13.9 present a priori NO_2 profiles used in the TROPOMI retrieval. One can see that the a priori TROPOMI NO_2 profiles are lower than the median MAX-DOAS NO_2 profile (except for the example summer day in Figure 13.9). In the first kilometers above the surface, the difference between the two profiles is about 35 % in Figure 13.8 and can be up to 80 % for the example autumn day in Figure 13.9.

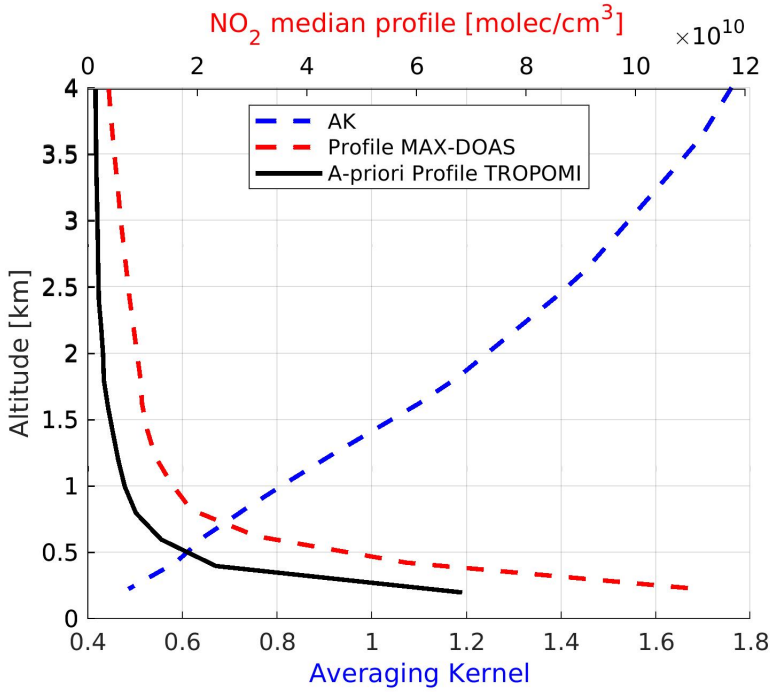

Figure 13.8: Mean TROPOMI averaging kernels (blue line), median MAX-DOAS NO_2 profile and median TROPOMI NO_2 a-priori profiles during summer as a function of altitude.

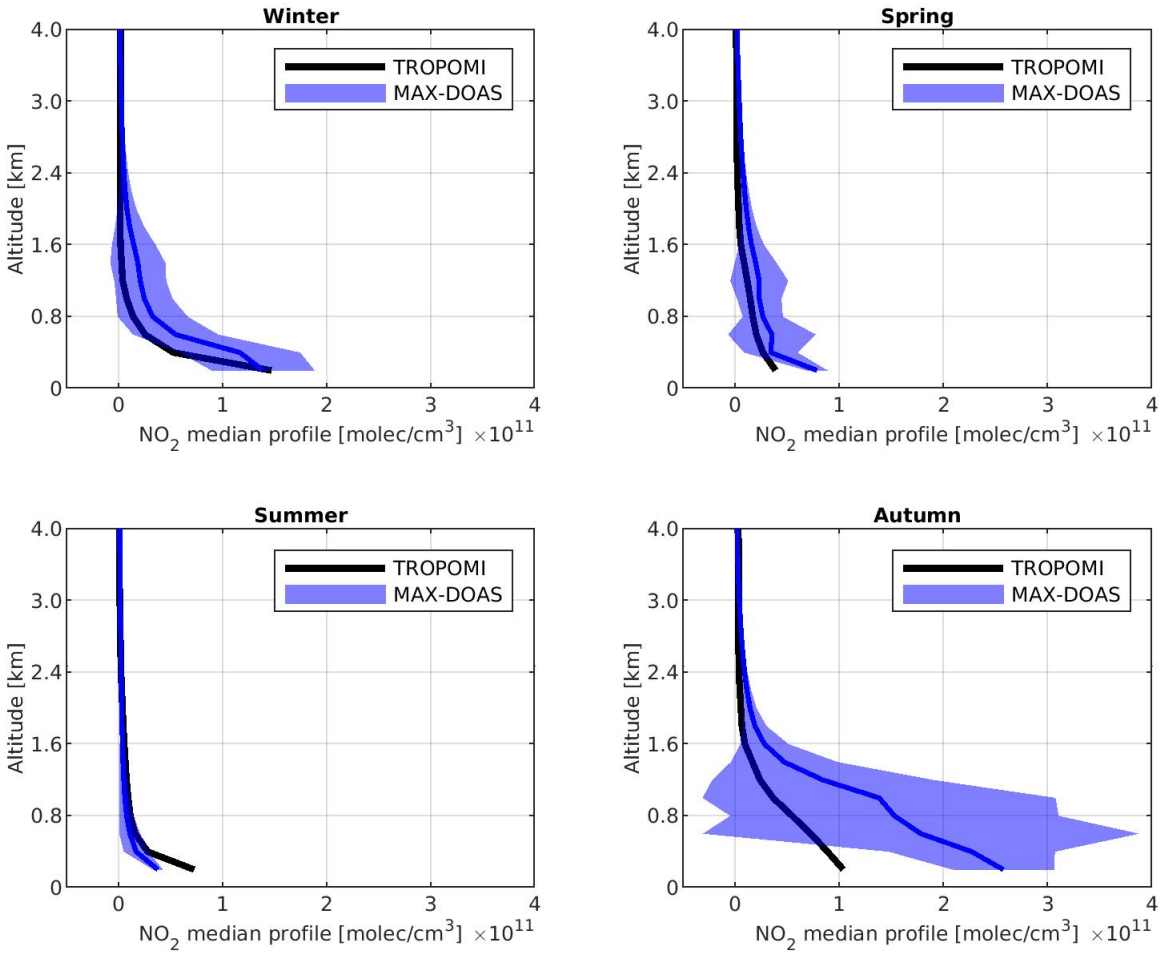

Figure 13.9: Example of median daily MAX-DOAS Vis NO_2 profiles, which are used for the recalculation of the TROPOMI NO_2 columns (one example day per season: 3 March 2019, 12 August 2018, 29 October 2018 and 19 January 2019) and the a-priori NO_2 profiles used in the TROPOMI retrieval in Uccle during the same example days. The shaded areas ($\pm 1\sigma$) represent the variability of the daily profiles.

Figure 13.10 presents validation results corresponding to the recalculated TROPOMI NO_2 columns. Comparing with results from Figure 13.7, one can see that the change in the NO_2 profile shape has a strong impact on validation results, leading to better agreement between satellite and ground-based datasets. During all seasons, the slopes of the linear regressions are largely improved (slopes in the 0.97-1.67 range), which essentially resolves the previously reported underestimation. On average, the recalculated TROPOMI columns increase by about 55 %. Looking more closely at Figures 13.7 and 13.10, one can see that the application of MAX-DOAS NO_2 vertical profiles mostly improves the agreement for tropospheric NO_2 columns larger than $1.0x10^{16}$ moleccm^{-2} (for the cases with NO_2 enhancement). One can also note that correlation coefficients are slightly degraded after application of the MAX-DOAS profiles, suggesting that the applied transformation introduces some more scatter in the comparison. Table 13.1 presents a detailed summary of all the regression analyses conducted.

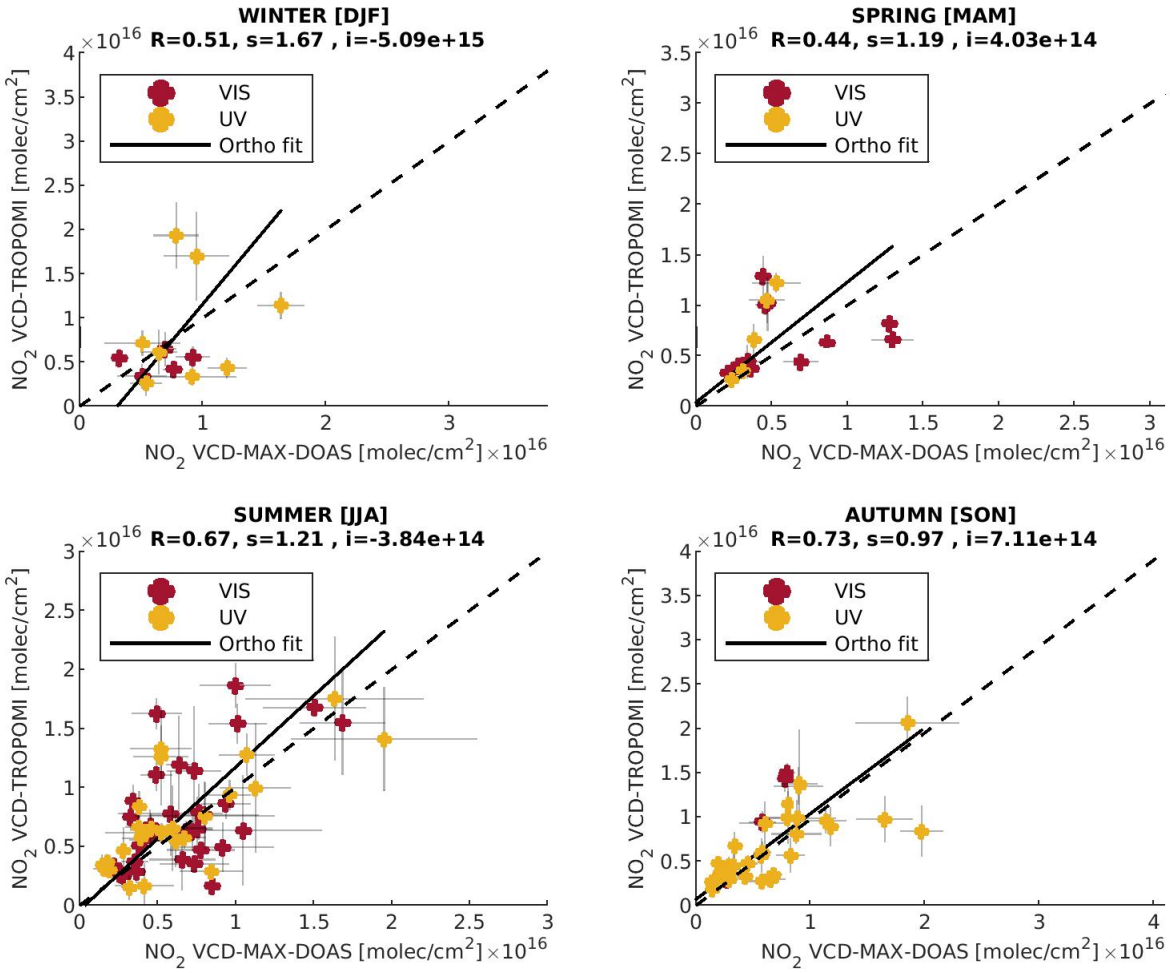

Figure 13.10: Seasonal scatter plots between the tropospheric NO_2 columns derived from the 2-D MAX-DOAS UV and VIS observations and TROPOMI NO_2 columns recalculated using the median daily MAX-DOAS vertical profiles as a-priori information.

Table 13.1: Summary table of the regression analysis parameters derived by the three validation exercises

TROPOMI dataset	MAX-DOAS dataset (Vis/UV together)	Season	Correlation coefficient (R)	Slope (s)
One pixel	One azimuthal direction	Winter	0.25	0.33
Closest pixel to the measurement site In the same direction as the MAX-DOAS line-of-sight		Spring Summer	0.72 0.57	1.07 0.49
		Autumn	0.63	0.33
More than one pixel	Multiple MAX-DOAS azimuthal directions	Winter	0.60	0.81
Weighted average of satellite columns In the same direction as the different MAX-DOAS line-of-sights		Spring Summer	0.69 0.77	0.47 0.58
		Autumn	0.85	0.61
More than one pixel	Multiple MAX-DOAS azimuthal directions	Winter	0.51	1.67
Use of MAX-DOAS a-priori profiles to recalculate the satellite columns		Spring	0.44	1.19
Weighted average of recalculated satellite columns		Summer	0.67	1.21
In the same direction as the different MAX-DOAS line-of-sights		Autumn	0.73	0.97

In conclusion, the change of the a priori profile in the TROPOMI retrieval has a significant impact on the agreement between the satellite and MAX-DOAS measurements, leading to a satisfying closure of the validation study. Although based on a different approach, these results are in agreement with the recent studies of Ialongo et al. (2020) and Judd et al. (2020).

Chapter 14

Conclusions

A total of 1 year of S5P/TROPOMI tropospheric NO_2 columns recorded above Brussels were validated using dualscan MAX-DOAS measurements. The MAX-DOAS instrument was installed in Uccle, a suburban site located in the south of the Brussels-Capital Region. A standard acquisition scheme was implemented by combining vertical scans in a fixed azimuthal direction (main azimuthal direction pointing to Brussels airport) and horizontal scans in 10 azimuth angles at a fixed elevation angle (2^o). OEM-based profile retrievals were performed in the main azimuthal direction, and a parameterization technique based on Sinreich et al. (2013) was applied in all the other azimuthal directions to retrieve dual-scan NO_2 near-surface VMRs and VCDs. An appropriate characterization of the MLH was obtained by using the vertical profile inversion results in the main azimuthal direction.

The dual-scan parameterized NO_2 VMRs and VCDs were validated using ancillary measurements. Three different comparisons were carried out: (1) the MAX-DOAS-based MLH values used in the parameterization were compared with measurements from a colocated ceilometer instrument; (2) the parameterized NO_2 near-surface VMRs and VCDs retrieved in the main azimuthal direction were compared with the same quantities derived from OEM-based profiles; and (3) the dual-scan NO_2 near-surface VMRs were compared with in situ NO_2 concentrations. Good overall agreement was found for both comparisons (UV and visible datasets) during the whole year of measurements.

The seasonal variability of the NO_2 near-surface VMR around the measurement site was investigated. As expected, higher NO_2 concentrations are observed during autumn and winter due to larger emissions, a shallower MLH and lower temperatures, resulting in longer lifetimes. Wind speed and direction are also found to play a significant role in the distribution of NO_2 around the site. As the main emission sources are located to the north of Uccle, concentration peaks are associated with wind blowing mainly from the NE direction. The dual-scan MAX-DOAS retrievals were also compared to NO_2 measurements from the in situ air quality telemetric network of the Brussels region. For this comparison, in situ stations were selected along the different MAX-DOAS azimuthal directions. Although the in situ measurements show systematically larger values than those derived from the MAX-DOAS instrument, a good correlation is found between the two datasets, especially for urban background sites under moderately polluted conditions.

In a second step, MAX-DOAS data were used to validate TROPOMI tropospheric NO_2 measurements. Two different approaches were used. First, the MAX-DOAS NO_2 VCDs, derived by applying an OEM-based inversion algorithm in the main azimuthal direction, were compared with the closest TROPOMI pixel located along the main MAX-DOAS pointing direction. Results show a clear seasonal behavior and a tendency for satellite data to underestimate the MAX-DOAS tropospheric NO_2 columns during all seasons. In the second approach, the dual-scan parameterized MAX-DOAS tropospheric NO_2 columns and corresponding effective horizontal distances were used to define a wider sampling area around the measurement site for the selection of the TROPOMI pixels. MAX-DOAS measurements in every azimuthal direction were compared to a weighted average of TROPOMI columns appropriately selected for optimal matching with MAX-DOAS observation directions and effective horizontal distances. Although

dual-scan MAX-DOAS measurements lead to improved agreement with satellite data, a systematic underestimation of the TROPOMI tropospheric columns is still observed.

Further, a detailed investigation of the main ancillary parameters used for the AMF calculation in the TROPOMI tropospheric NO_2 columns retrievals revealed that the a priori NO_2 profile shape uncertainty has a large impact on the satellite measurements. Recalculating the TROPOMI columns using daily median MAX-DOAS profiles as a priori results in much better agreement between satellite and MAX-DOAS data. This suggests that the use of more appropriate a priori profiles in the TROPOMI retrieval can substantially improve the accuracy of satellite tropospheric NO_2 data, especially in urban areas. The improvement is, however, less clear during seasons characterized by highly variable NO_2 fields and cloudy conditions.

The Part III shows that dual-scan MAXDOAS measurements conducted in an urban area offer the possibility (1) to better characterize the spatial variability of short-lived pollutants like NO_2 and (2) to improve the validation of satellite measurements in an urban environment. Moreover, the vertical profiling capability of MAX-DOAS measurements allows for testing the suitability of the a priori profile shape information used in satellite retrievals. Based on our results, additional work could be done to improve future TROPOMI validation exercises. For instance, the horizontal resolution of the satellite a priori profiles could be further improved by performing vertical MAX-DOAS scans during TROPOMI overpass in more than one azimuthal direction. Additionally, the satellite retrieval uncertainties related to clouds and aerosols could be investigated in more detail based on the azimuthal scan capability of MAX-DOAS instruments.

Part IV

Horizontal distribution of tropospheric NO_2 and aerosols derived by dual–scan multi–wavelength MAX–DOAS measurements in Uccle, Belgium

Dual-scan ground-based Multi-AXis Differential Optical Absorption Spectroscopy (MAX-DOAS) measurements of tropospheric nitrogen dioxide (NO_2) and aerosols have been carried out in Uccle (50.8°N, 4.35°E; Brussels region, Belgium) for two years, from March 2018 to February 2020. The MAX-DOAS instrument has been operating in both UV and Visible wavelength ranges in a dual-scan configuration consisting of two sub-modes: (1) an elevation scan in a fixed viewing azimuthal direction and (2) an azimuthal scan in a fixed low elevation angle (2°). By analyzing the O4 and NO2 dSCDs at six different wavelength intervals along every azimuthal direction and by applying a new Optimal-Estimation-based inversion approach, the horizontal distribution of the NO_2 near-surface concentrations and vertical column densities (VCDs) and the aerosols near-surface extinction coefficient are retrieved along ten azimuthal directions. The retrieved horizontal NO_2 concentration profiles allow the identification of the main NO_2 hotspots in the Brussels area. Correlative comparisons of the retrieved horizontal NO_2 distribution have been conducted with airborne, mobile, and satellite datasets, and overall a good agreement is found. The comparison with TROPOMI observations reveals that the characterization of the horizontal distribution of tropospheric NO_2 VCDs by ground-based measurements, the appropriate sampling of TROPOMI pixels, and an adequate a priori NO_2 profile shape in TROPOMI retrievals lead to a better consistency between satellite and ground-based datasets.[1]

[1]This chapter is based on: Dimitropoulou, E., Hendrick, F., Friedrich, M. M., Tack, F., Pinardi, G., Merlaud, A., Fayt, C., Hermans, C., Fierens, F., and Van Roozendael, M.: Horizontal distribution of tropospheric NO2 and aerosols derived by dual-scan multi-wavelength MAX-DOAS measurements in Uccle, Belgium, Atmos. Meas. Tech. Discuss. [preprint], https://doi.org/10.5194/amt-2021-308, in review, 2021.

Chapter 15

Part IV: Objectives

In this Part of this thesis, a new aerosol and NO_2 horizontal distribution inversion approach based on two years (March 2018-February 2020) of dual-scan multi-wavelength MAX-DOAS measurements in Uccle (Brussels-Capital region, Belgium) is presented. In every azimuthal viewing direction, parameterized NO_2 near-surface concentrations, NO_2 tropospheric columns and aerosol extinctions measured at six different wavelengths are used as input in a new horizontal distribution inversion approach. On this basis, the near-surface aerosol extinction and NO_2 horizontal distributions are retrieved at a spatial resolution of about 3km in a range of about 20 km around the measurement site. These horizontal profiles are used to validate collocated TROPOMI tropospheric NO_2 columns. One complete year of data (March 2018-March 2019) and two wavelength intervals (one in the UV and one in the Visible) have already been used in Part IV. It is proven that multi-azimuthal (the so-called dual-scan) MAX-DOAS measurements significantly improve the agreement between ground-based and TROPOMI tropospheric NO_2 column observations over the Brussels' area. By adding the multi-wavelength aspect, the present Part IV should be seen as an extension of the approach described in Part III.

Part IV is organized into six chapters: in section 16, the multi-wavelength DOAS analysis are presented. In chapter 17, the TROPOMI tropospheric NO_2 measurements are described. Chapter 18 is composed of two main parts: (a) a detailed description of the dual-scan multi-wavelength MAX-DOAS retrieval method and (b) the horizontal aerosol and NO_2 distribution inversion approach. In chapter 19, main results followed by correlative comparisons of the retrieved ground-based and satellite horizontal NO_2 distribution are presented. Finally, in chapter 20, conclusions and future perspectives are given.

Chapter 16

Dual-scan multi-wavelength MAX-DOAS measurements

Contents

16.1 Multi-wavelength DOAS analysis

The measured radiance spectra of a full measurement scan are analyzed using the QDOAS spectral fitting software developed by BIRA-IASB (Fayt et al., 2011). The DOAS technique separates the narrow absorption features of trace gases in the UV-Visible spectral range from a spectral background caused mainly by Mie and Rayleigh scattering and instrumental effects. The trace gas concentration integrated along the light-path in a measured spectrum relative to the amount of the same absorber in a reference spectrum is the primary product of the DOAS analysis and is called differential slant column density (dSCD). Here, average zenith spectra before and after each measurement scan are used as a reference.

The O_4 and NO_2 dSCDs are retrieved in six different wavelength intervals: Three intervals in the UV spectral range (330-361 nm, 350-370 nm, and 360-383.5 nm) and three in the Visible range (420-460 nm, 450-490 nm, and 510-540.1 nm). These fitting windows were selected to optimize the determination of the O_4 and NO_2 dSCDs at the maximum number of different O_4 absorption bands available in the wavelength domain of the instrument. Figure 16.1 shows an example of the O_4 and NO_2 fits in all the intervals used in the present work. In each chosen fitting window, we select a reference wavelength, which corresponds to the maximum of an O_4 absorption peak (or close to it) in the respective wavelength intervals (see Figure 16.1), and it is subsequently used for radiative transport calculations and further analysis. The different reference wavelengths are 343 nm, 360 nm, 380 nm, 447 nm, 477 nm and 530 nm (see Figure 16.1). To optimize the derivation of the dSCDs at the six selected wavelengths, the fit of a slope parameter, which accounts for the variation of the dSCD within the fitting interval (Puķīte et al., 2010) is necessary. This is especially important when the reference wavelength is not located in the center of the fitting window (i.e. 330-361 nm, 350-370 nm, 420-460 nm, and 450-490 nm). The DOAS settings used for each fitting interval are presented in Table 16.1. As shown in this table, two different O_4 cross-sections are used in this study: (1) Finkenzeller (private communication) in the UV fitting intervals and (2) Thalman and Volkamer (2013) in the Vis fitting intervals. The main motivation for using the O_4 cross-section from Finkenzeller (measured at 25^{o}C) in the UV fitting intervals is the significant improvement of the fit quality and the reduction of the uncertainties for the UV retrievals. Sensitivity tests and comparisons with radiative transport simulations also show that the resulting O_4

and NO_2 dSCDs are consistent throughout the whole wavelength range covered by the six intervals. For NO_2 and O_3, which are the strongest absorbers in all the fitting windows, a correction for the solar I_0 effect (Aliwell et al., 2002) is applied. A high-resolution solar atlas (Kurucz, 1984) is used for the wavelength calibration of the measured spectra.

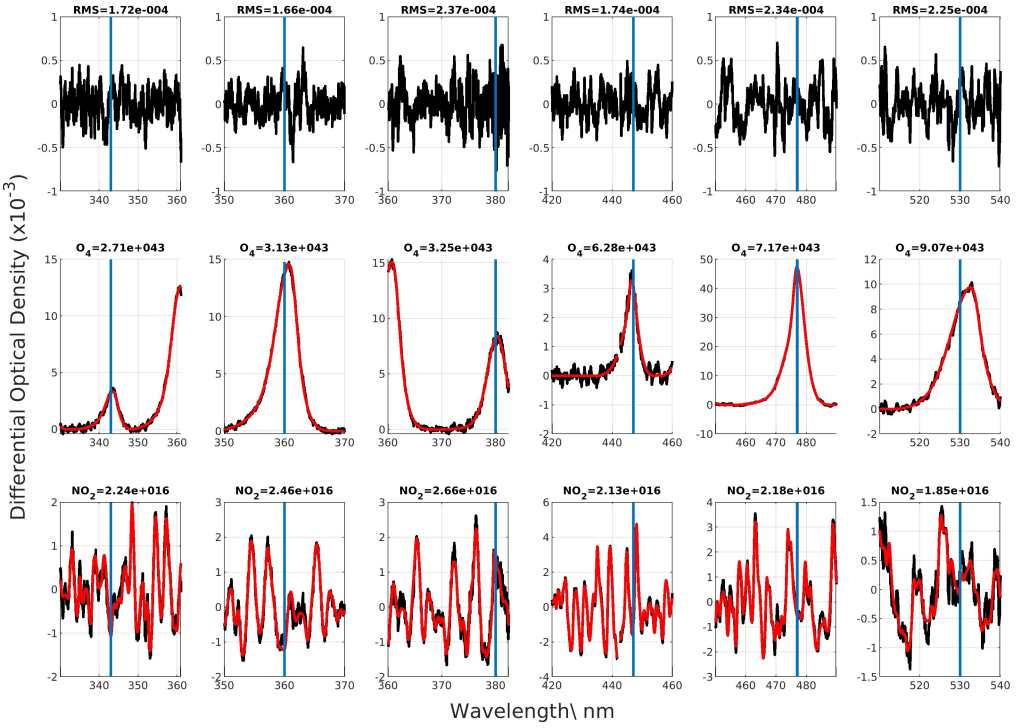

Figure 16.1: Fit results of the O_4 and NO_2 fit at the six selected fitting windows from the dual-scan MAX-DOAS measurements in Uccle (2 June 2019 at 07:05 UTC). The measured spectra are represented with black lines, while the fit results are shown with red lines. The blue lines represent the six reference wavelengths.

Table 16.1: DOAS settings for O_4 and NO_2 in the six different fitting intervals.

Fitting window (nm)	Reference wavelength (nm)	Molecule	Reference
330 - 361	343	BrO (223 K)	Fleischmann et al. (2004)
350 - 370	360	O_4	Finkenzeller, H. (private communication)
		NO_2 (298 K)	Vandaele et al. (1998) with I_0 correction (SCD of 10^{17} molec.cm^{-2})
		O_3 (223 K)	Serdyuchenko et al. (2014) with I_0 correction (SCD of 10^{20} molecule.cm$^-$2)
		HCHO (297 K)	Meller and Moortgat (2000)
		O_3 (243 K)	Pre-orthogonalized Serdyuchenko et al. (2014) with I_0 correction (SCD of 10^{20} molecules.cm$^-$2)

		Ring	Pseudo cross-section according to Chance and Spurr (1997) and normalized as in Wagner et al. (2009)
		Polynomial	Order 3 (4 coefficients)
360 - 383.5	380	BrO (223 K)	Fleischmann et al. (2004)
		O_4	Finkenzeller, H. (private communication)
		NO_2 (298 K)	Vandaele et al. (1998) with I^0 correction (SCD of 10^{17} molec.cm$^-$2)
		NO_2 (220 K)	Pre-orthogonalized Vandaele et al. (1998) with I_0 correction
		Ring	Pseudo cross-section according to Chance and Spurr (1997) and normalized as inWagner et al. (2009)
		Polynomial	Order 5 (6 coefficients)
420 - 460	447	NO_2 (298 K)	Vandaele et al. (1998) with I_0 correction (SCD of 10^{17} molec..cm$^-$2)
450 - 490	477	O_4 (293 K)	Thalman and Volkamer (2013)
		O_3 (223 K)	Serdyuchenko et al. (2014) with I_0 correction (SCD of 10^{20} molecules.cm$^-$2)
		H_2O	HITRAN Rothman et al. (2009)
		NO_2 (220 K)	Pre-orthogonalized Vandaele et al. (1998) with I_0 correction
		Ring	Pseudo cross-section according to Chance and Spurr (1997) and normalized as in Wagner et al. (2009)
		Polynomial	Order 3 (4 coefficients)
510 - 540.1	530	NO_2 (298 K)	Vandaele et al. (1998) with I_0 correction (SCD of 10^{17} molec.cm$^-$2)
		O_4 (293 K)	Thalman and Volkamer (2013)
		O_3 (223 K)	Serdyuchenko et al. (2014) with I_0 correction (SCD of 10^{20} molecules.cm$^-$2)
		H_2O	HITRAN Rothman et al. (2009)
		NO_2 (220 K)	Pre-orthogonalized Vandaele et al. (1998) with I_0 correction
		Ring	Pseudo cross-section according to Chance and Spurr (1997) and normalized as in Wagner et al. (2009)
		Polynomial	Order 3 (4 coefficients)

Chapter 17

TROPOMI tropospheric NO_2 dataset

In the present Part, MAX-DOAS tropospheric NO_2 VCDs are used to validate collocated TROPOMI satellite observations. TROPOMI is a passive grating imaging spectrometer flying onboard the S5P satellite platform. It covers the UV-Visible (250-500 nm), near-infrared (710-770 nm), and short-wave infrared (2314-2382 nm) spectral ranges (Veefkind et al., 2011). TROPOMI measures in a push-broom configuration with a full swath width as wide as 2600 km, and it provides daily global coverage at a spatial resolution (true-nadir pixel size) of 7x3.5 km^2, further improved to 5.5x3.5 km^2 on 6 August 2019. The TROPOMI tropospheric NO_2 algorithm has been developed at KNMI and uses a retrieval-assimilation-modeling system that is based on the 3-D global TM5 chemistry transport model (Williams et al., 2017; van Geffen et al., 2019).

We use the reprocessed (RPRO) and offline (OFFL) datasets of the TROPOMI L2 tropospheric NO_2 column product (see Table 17.1 for the corresponding versions). According to the guidelines provided by van Geffen et al. (2019), RPRO dataset are available only for the first period of the present study (see Table 17.1). For the remaining periods, OFFL datasets are used, which are the main data products being available within two weeks from the TROPOMI measurement. To ensure best measurements' quality, only pixels with a quality assurance value larger than 0.75 are used. This quality flagging eliminates pixels with a cloud radiance fraction larger than 0.5, snow or ice, and erroneous retrievals.

Next to operational products, two additional TROPOMI data sets are also used (see chapter 19). In the first one, the TROPOMI retrieval is performed with different a priori profiles (Douros et al., in preparation). The coarse TM5-MP a priori NO_2 profiles, using a spatial resolution of 1^o x 1^o, is replaced by NO_2 profile shapes from the CAMS (Copernicus Atmospheric Monitoring Service) regional Chemistry Transport Model (CTM) ensemble at a spatial resolution of 0.1^o x 0.1^o. The replacement of a coarse a priori information by a finer one can lead to significant changes in the TROPOMI retrieved NO_2 tropospheric columns. The available dataset covers October 2018 to March 2020 (OFFL dataset, L2, and version 01.03.01, 01.03.02, and 02.00.00).

In the second additional product, the TROPOMI retrieval is performed with an improved cloud product (Eskes et al., 2021; van Geffen et al., 2021). According to van Geffen et al. (2021), the improvement in the FRESCO-S cloud pressure retrieval scheme to the FRESCO-wide product, has an impact on the NO_2 AMFs and consequently, on the NO_2 tropospheric columns over polluted areas. More precisely, the existing FRESCO-S product had a negative bias in the cloud top pressure values, which resulted in a low NO_2 tropospheric column (Compernolle et al., 2021). The TROPOMI tropospheric NO_2 columns are retrieved using an improved FRESCO-S cloud retrieval scheme, called FRESCO-wide, in v1.4 since 29 November 2020. In the present study, the diagnostic data sets (DDS) are used, which are an ensemble of reprocessed data for past periods analyzed with new versions (van Geffen et al., in preparation). Over the MAX-DOAS measurement time-period, only DDS2 data corresponding to OFFL datasets (v1.2 and v1.3) are available. Excluding the spin-up period needed by TM5-MP, only four data periods are available for our comparisons (i.e. 30/06/2018 - 06/07/2018, 30/12/2018 - 5/01/2019, 30/03/2019-05/04/2019, and 17/09/2019-23/09/2019).

Table 17.1: TROPOMI NO_2 processor versions used in the present Part.

Dataset	Number of version	Starting date of operation	End date of operation
RPRO	01.02.02	30/04/2018	17/10/2018
OFFL	01.02.00	17/10/2018	28/11/2018
OFFL	01.02.02	28/11/2018	20/03/2019
OFFL	01.03.00	20/03/2019	30/04/2019
OFFL	01.03.01	23/04/2019	26/06/2019
OFFL	01.03.02	26/06/2019	24/02/2020

Chapter 18

Description of the dual-scan multi-wavelength inversion approach

Contents

First, the measured radiance spectra in the UV and Visible wavelength ranges is analyzed in six different fitting windows with the main output being the O_4 and NO_2 dSCDs at six wavelengths, which are 343 nm, 360 nm, 380 nm, 447 nm, 477 nm and 530 nm (see chapter 16). Then, the OEM-based MMF algorithm is applied to the O_4 and NO2 dSCDs in the main azimuthal direction (and at 477 nm) to retrieve vertical NO_2 profiles and obtain information about the vertical extent of NO_2 in the troposphere (MLH_{NO2}; see section 18.1).

As an intermediate step, radiative transfer model (RTM) simulations are performed (see Table 18.1) to obtain information about the horizontal sensitivity (L_{NO2}) and AOD as a function of O_4 dSCDs, wavelength, and MLH_{NO2}.

Then, in the next step, a new dual-scan parameterization technique is applied to the O_4 and NO_2 dSCDs at the six different wavelengths and in all the azimuthal directions with MLH_{NO2}, measured O_4 dSCDs, and measurement geometry being the main input parameters to retrieve the horizontal sensitivity of NO_2 and, consequently, the NO_2 near-surface concentrations and VCDs, and near-surface aerosol extinction (see section 18.2).

In the final step, a new OEM-based horizontal distribution inversion approach is developed using the six near-surface NO_2 concentrations and aerosol extinction values per azimuthal direction to retrieve horizontal NO_2 and aerosol extinction horizontal profiles in an output horizontal grid of 500m thickness (see section 18.3).

A flow chart describing the dual-scan multi-wavelength MAX-DOAS inversion approach is shown in Figure 18.1.

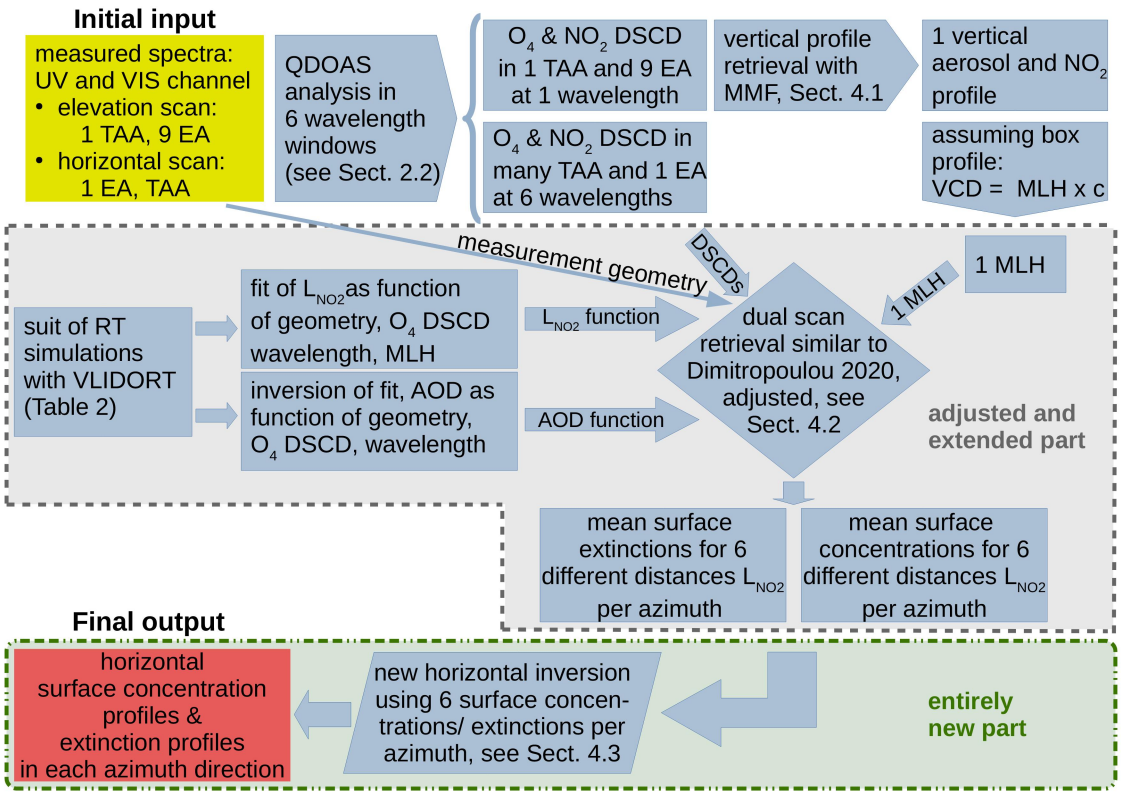

Figure 18.1: Dual-scan multi-wavelength MAX-DOAS inversion approach flow chart.

18.1 Aerosol and NO_2 OEM-based profile retrievals

The Optimal-estimation-based Mexican MAX-DOAS Fit (MMF) inversion algorithm (Friedrich et al., 2019) is applied to retrieve the aerosol extinction coefficient and NO_2 vertical profiles for each MAX-DOAS elevation scan in the main azimuthal direction at 360 nm and 477 nm. First, the O_4 measurements are used to retrieve the aerosol extinction profile. Several studies indicated the importance of applying a scaling factor (<1) to the observed O_4 dSCDs to bring them in agreement with simulated O_4 dSCDs by radiative transfer modeling (see Table 1/ Wagner et al., 2019) for a comprehensive list of all those studies). However, there is no consensus on the fundamental reason for applying this scaling (see e.g. Ortega et al., 2015). As found by Tirpitz et al. (2021), the choice of the scaling factor has only a small effect on the performance of the trace gas retrieval, so we decided not to apply it in the present study. The aerosol extinction profile retrieved from each scan is used as an input to the radiative transfer calculations used to retrieve the NO_2 retrieval profile. Further details about the MMF inversion algorithm, the input a priori parameters, the quality check of each scan, and the estimated uncertainties of the aerosol and NO_2 vertical profile can be found in Dimitropoulou et al. (2020).

A broken cloud-filtering approach based on Gielen et al. (2014) is applied to the MAX-DOAS measurements to exclude MAX-DOAS aerosol and NO_2 scans influenced by the presence of clouds, which are known to potentially degrade the quality of the retrievals (Gielen et al., 2014; Wagner et al., 2014). Three sky conditions can be distinguished with this flagging approach: (1) clear sky, (2) homogeneous cloud coverage and (3) broken clouds conditions. Retrievals under broken cloud conditions are rejected from the present study.

The profile retrieval has been performed to estimate the Mixing Layer Height of NO_2 (MLH_{NO2}). The MLH_{NO2}

is estimated per measurement scan, and it is the ratio of VCD_{NO2} to the NO_2 near-surface concentration as retrieved in the main azimuthal direction by the MMF inversion algorithm. Therefore, during one measurement scan, two assumptions are made: (1) the homogeneous distribution of NO_2 inside the MLH_{NO2} and (2) the homogeneous MLH_{NO2} around the measurement site and its use in all the azimuthal directions. The validity of the second assumption is tested in subsection 18.2.3.

18.2 Dual-scan MAX-DOAS retrieval method

A complete MAX-DOAS measurement scan is composed of two different sub-scans, as described in chapter 16. The aerosol and NO_2 vertical profiles are retrieved from the elevation scan in the main azimuthal direction. In the other azimuthal directions, measurements are performed only in a single low elevation angle (2^o), and therefore, the retrieval of aerosol and NO_2 vertical profiles is not possible. Using the fact that the lowest elevation angles have the highest sensitivity to trace gases located nearby the surface due to the long light path in this layer, a new dual-scan MAX-DOAS retrieval strategy was developed here. This new retrieval strategy is an extension of the work presented in Dimitropoulou et al. (2020) and aims to retrieve the near-surface NO_2 box-averaged volume mixing ratios (VMRs) and the NO_2 VCDs at six different wavelengths. In Dimitropoulou et al. (2020), the applied dual-scan NO_2 MAX-DOAS retrieval was itself an adaptation of the parameterization technique proposed by Sinreich et al. (2013). More precisely, in the presence of sufficient aerosols in the atmosphere (i.e. sufficient aerosols to constrain the light path in a near-surface layer and ensure that the near-surface NO_2 concentration can be approximated by a near-surface box profile), the measured NO_2 dSCDs at one low elevation angle (2^o) can be related to the near-surface NO_2 box-averaged concentration as follows:

$$dSCD_{NO_2} = c_{NO_2} L_{NO_2} \tag{18.1}$$

where $dSCD_{NO_2}$ is the differential slant column density of NO_2 and c_{NO_2} its mean concentration along the differential effective light path, L_{NO_2}.

Consequently, the knowledge of the differential effective light-path's length (i.e. L_{NO_2}) is crucial to derive the near-surface NO_2 concentrations. The oxygen collisional complex (O_4) can be used as a tracer for the effective light-path in the atmosphere: as its concentration is well-known (it is the square of O_2 concentration). As a result, observed changes of the O_4 dSCDs can be directly attributed to changes in the light-path due to the presence of particles like aerosols and clouds. L_{O_4} is calculated as follows:

$$L_{O_4} = \frac{dSCD_{O_4}}{c_{O_4}} \tag{18.2}$$

where c_{O_4} is the typical O_4 concentration at the altitude of the instrument.

However, the direct use of the O_4 light-path length in the NO_2 retrieval is not possible under moderate to high pollution conditions, such as those in Brussels, because the profile shapes of O_4 and NO_2 are not the same. In Dimitropoulou et al. (2020), we used radiative transfer model (RTM) simulations to estimate a unitless correction factor, which accounts for these profile shape differences. This unitless correction factor indicates that under moderate to high pollution conditions, L_{NO_2} is equal to or smaller than L_{O_4}. For a correction factor equal or close to one, L_{O_4} is equal to L_{NO_2}, which means that there is a moderate to high aerosol load in the atmosphere during the measurement. On the other hand, correction factors smaller than unity are obtained for measurements performed under aerosol-free conditions or a thin MLH. Assuming a homogeneous NO_2 distribution inside the MLH, the MLH is derived from the NO_2 vertical profiles in the main azimuthal direction and is defined as the ratio of the NO_2 VCD to the near-surface concentration of NO_2. For more information, we refer the reader to Dimitropoulou et al. (2020). The RTM simulations are performed for eight different MLH values of aerosols and NO2 in the range of 500-2000 m (i.e. eight different combinations) and for different measurement viewing geometries (Solar Zenith Angle (SZA),

Relative Azimuth Angle (RAA) and the corresponding elevation angle of 2°). For every MAX-DOAS measurement, one value of the correction factor is given according to its viewing geometry and MLH value during the measurement.

In the present study, a new dual-scan NO_2 MAX-DOAS retrieval method, which is more suitable for interpreting multi-wavelength measurements than the previous approach (Dimitropoulou et al., 2020), is developed. It is presented in detail in the following subsection.

18.2.1 Developed dual-scan MAX-DOAS retrieval method

The main advantages of the new dual-scan NO_2 MAX-DOAS retrieval method (which are also the main differences with respect to Dimitropoulou et al., 2020) are the following: (1) the direct use of the measured O_4 dSCDs to estimate L_{NO_2} for every measurement, (2) retrieval of near-surface aerosol extinction close to the ground, and (3) the exploitation of the wavelength dependency of the horizontal path representative of MAX-DOAS measurements for the retrieval of the horizontal distribution of aerosols (and therefore NO_2) around the measurement site. The latter is done using O_4 and NO_2 dSCDs measured at six different wavelengths. This new method is described below.

Assuming that the NO_2 vertical distribution can be approximated by a box profile of height equal to mixing layer height (MLH_{NO_2}), the following equation can be used:

$$c_{NO_2} = \frac{VCD_{NO_2}}{MLH_{NO_2}} = \frac{dSCD_{NO_2}}{L_{NO_2}} \tag{18.3}$$

This means that the NO_2 near-surface concentration can be expressed as a ratio of the $dSCD_{NO_2}$ to the L_{NO_2} (see Equation 18.2) or as a ratio of the VCD_{NO_2} to the MLH_{NO_2}. Using this equation, L_{NO_2} can be estimated as follows:

$$L_{NO_2} = dSCD_{NO_2(\text{simulated})} \frac{MLH_{NO_2}}{VCD_{NO_2}} \tag{18.4}$$

Here, O_4 dSCDs and L_{NO_2} are simulated using the radiative transfer model VLIDORT version 2.7 (Spurr, 2006). Seasonal median MAX-DOAS NO_2 vertical profiles, as retrieved by applying the MMF inversion algorithm in the main azimuthal direction (see section 18.1), show that the bulk (70 %) of the NO_2 concentration is located inside the MLH_{NO_2}, which is expected since MLH_{NO_2} is estimated as the ratio of VCD_{NO_2} to the near-surface NO_2 concentration. On the other hand, this is not the case for aerosols (only 30 % of the aerosol content is seen to be located inside the MLH_{NO_2}). Considering this feature, for the VLIDORT simulations, the NO_2 a priori profiles are modeled as box profiles with a constant concentration equal to $1.5\text{x}10^{11}$ molec/cm^3 from the surface to the MLH_{NO_2}. Two layers compose the aerosol a priori profiles: (1) the MLH_{NO_2} and (2) the free troposphere. The equation, which is applied to estimate the aerosol extinction profile a(z), is the following (see Wang et al., 2014):

$$a(z) = AOD \frac{p}{MLH_{NO_2}}, \text{for } z \leq MLH_{NO_2} \tag{18.5}$$

and,

$$a(z) = b(j, MLH_{NO_2}, p) \exp\left(\frac{-z}{j}\right), \text{for } z \geq MLH_{NO_2} \tag{18.6}$$

where AOD is the aerosol optical depth, p is the fraction of AOD inside the MLH_{NO_2}, b is a normalizing constant for the exponential component (see Equation 5 from Wang et al., 2014), z is the simulation altitude grid, and j is the scaling height for the aerosols located outside the MLH_{NO_2}, which is set to 5 km (Wang et al., 2014). In the present study, the fraction of AOD located within the MLH_{NO_2} is set to p=0.3 (see above). The effect of the p value and

Table 18.1: RTM inputs for the simulations of L_{NO_2} at the six selected wavelengths (343 nm, 360 nm, 380 nm, 447 nm, 477 nm, and 530 nm).

Parameter	Values
Wavelength (nm)	343, 360, 380, 447, 477, 530
SZA (°)	20, 30, 40, 50, 60, 70, 80
RSAA (°)	0, 10, 20, 30, 40, 50, 60, 90, 120, 150, 180
AOD	0, 0.1, 0.3, 0.4, 0.6, 0.8, 1
p of AOD	0.30
j of AOD (km)	5
asymmetry parameter	0.68
Single Scattering Albedo (SSA)	0.92
MLH (m)	500, 1000, 1500
Elevation angle (°)	2
c_{NO_2} (molec/cm^3)	1.5 x 10^{11}

the NO_2 profile shape on the retrieved NO_2 near-surface VMRs and VCDs have been investigated and have been taken into account in the error budget (see subsection 18.2.2).

The MLH_{NO_2} is estimated per measurement scan, as the ratio of VCD_{NO_2} to the NO_2 near-surface concentration as retrieved in the main azimuthal direction by the MMF inversion algorithm.

The RTM simulations have in total nine input parameters, which are the elevation angle, SZA, RAA, AOD, MLH_{NO_2}, c_{NO_2}, AOD (p and j), and wavelength. It should be noted that the elevation angle is kept constant (i.e. 2°). For the six different wavelengths (343 nm, 360 nm, 380 nm, 447 nm, 477 nm, and 530 nm), we separately perform RTM simulations and L_{NO_2} (see Equation 18.2.1) are calculated for the assumed SZA, RAA, MLH_{NO_2}, c_{NO_2}, and AOD input scenarios presented in Table 18.1.

The O_4 dSCDs are a function of the input parameter AOD. The relation between the simulated O_4 dSCDs and the input AOD values is shown in Figure 18.2. A Piecewise cubic hermite interpolating polynomial fitting through the AOD as a function of the simulated O_4 dSCDs for each SZA, RAA, and MLH_{NO_2} combination can be used in order to perform an inverse method (i.e. to estimate the near-surface aerosol extinction from the measured O_4 dSCDs).

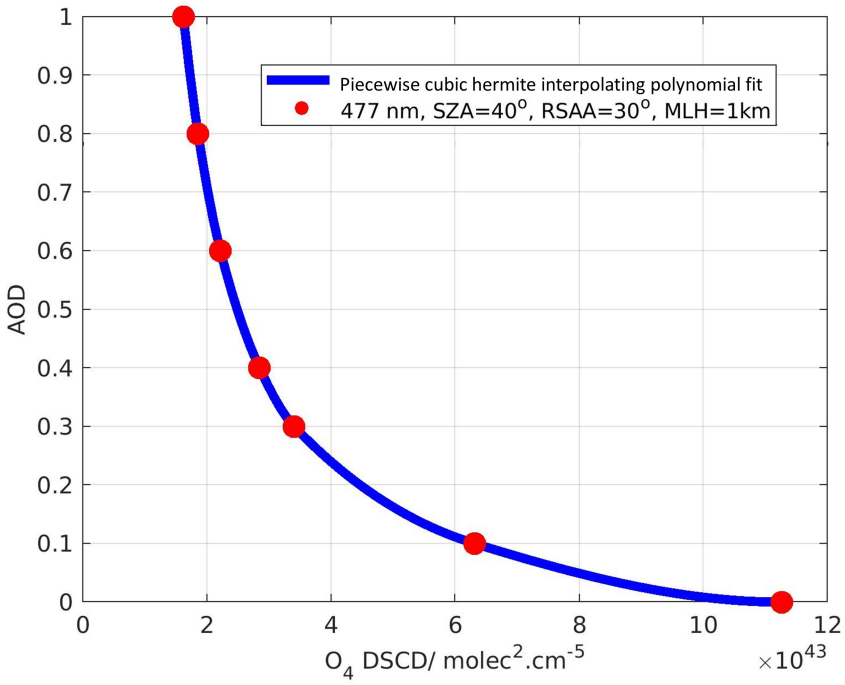

Figure 18.2: Dots: Simulated AOD for NO_2 box profile of 1 km at 477nm for a SZA of 40° and RAA of 30° as a function of the simulated O_4 DSCDs for the different AOD values (1, 0.8, 0.6, 0.4, 0.3, 0.1 and 0; see Table 18.1). Blue line: simulated AOD by applying a Piecewise cubic hermite interpolating polynomial fit through the data points.

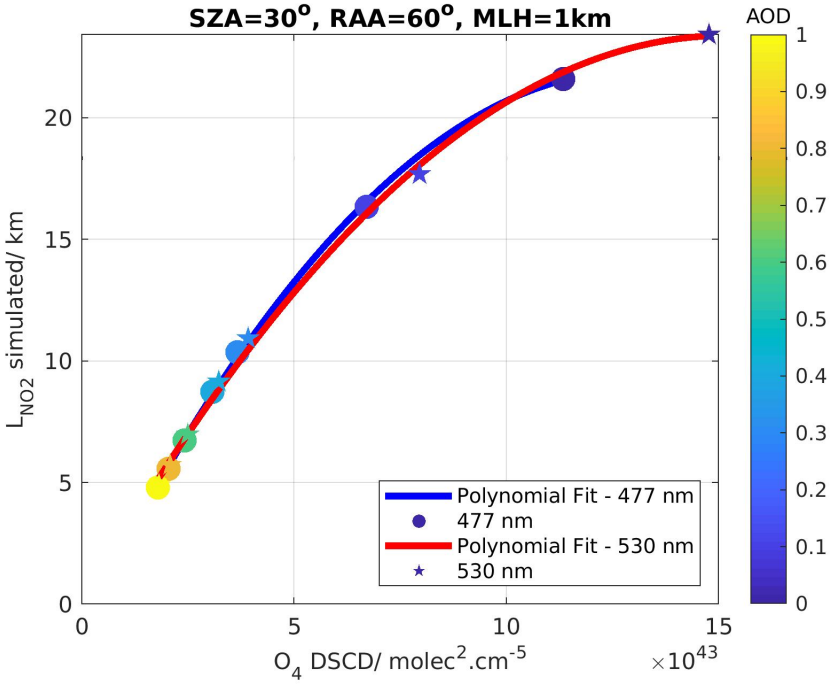

Figure 18.3: Dots (stars): Simulated L_{NO_2} for NO_2 box profile of 1 km at 477nm (530 nm) for a SZA of 30° and RAA of 60° as a function of the simulated O_4 DSCDs for the different AOD values (1, 0.8, 0.6, 0.4, 0.3, 0.1 and 0; see Table 18.1). Blue (red) line: 2nd-order polynomial fit through the data points.

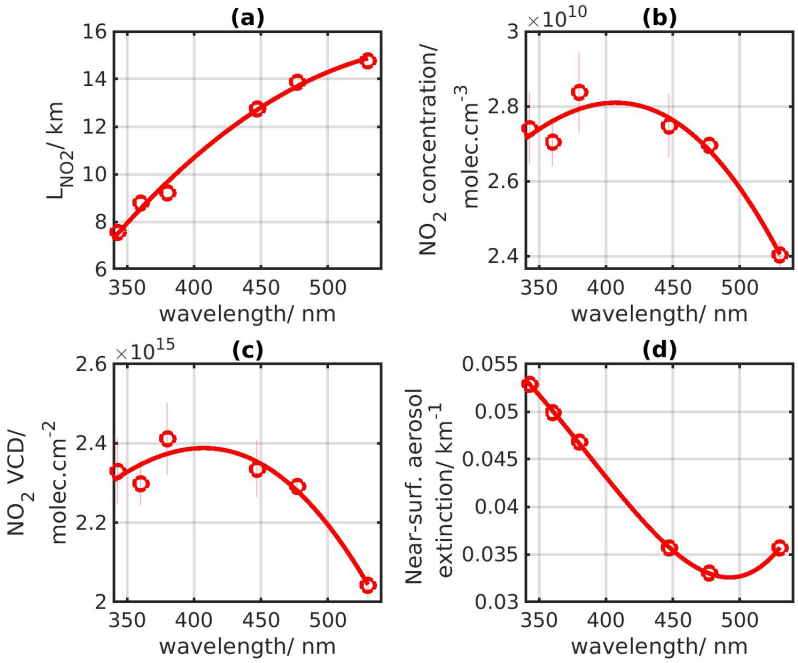

Figure 18.4: (a) Corresponding L_{NO_2}, (b) near-surface NO_2 concentrations, (c) NO_2 VCDs, and (d) aerosol optical densities as a function of the six wavelengths used in the retrieval (11 September 2018, 11:51 UTC, 123.5° azimuthal direction).

For every combination of all eight parameters (i.e. all the parameters of Table 18.1, except the AOD values), a polynomial fit of L_{NO_2} as a function of simulated O_4 dSCDs is applied Figure 18.3 shows simulated L_{NO_2} as a function of simulated O_4 dSCDs, and a second-order polynomial is fitted through the data points. Since NO_2 is an optically thin absorber, L_{NO_2} is not a function of c_{NO_2} and consequently, a L_{NO_2} value can be estimated for each measurement. Based on the corresponding SZA, RAA, measured O_4 dSCD, and MLH_{NO_2}, a L_{NO_2} is attributed to each low elevation MAX-DOAS measurement through this polynomial fit. To express L_{NO_2} as a function of four different parameters (i.e. O_4 dSCD, SZA, RAA, and MLH_{NO_2}), L_{NO_2} is interpolated linearly at the O_4 dSCD, SZA, RAA, and MLH_{NO_2} of each measurement. For example, a MAX-DOAS measurement with SZA=30°, RAA=60°, MLH_{NO_2}=1km, and measured O_4 dSCD=6.10^{43} molec^2.cm^{-5} will have a L_{NO_2} equal to 15 km at 477 nm (see Figure 18.4).

Based on this approach, the near-surface NO_2 concentration can be calculated at the six different wavelengths by using Equation 18.3 and the derived L_{NO_2} values. The corresponding near-surface NO_2 VMR are obtained by dividing the NO_2 concentrations by the air number density. To derive the air number density, we use monthly averaged pressure and temperature profiles over a 20-year period. These profiles are extracted from the European Centre for Medium-Range Weather Forecasts (ECMWF) ERA-Interim reanalysis. In the last step, the tropospheric NO_2 VCD is calculated from the product of the near-surface NO_2 concentration with the MLH_{NO_2}.

Regarding the aerosols, the AOD is estimated for every off-axis measurement (see Fig. 18.2). The near-surface aerosol extinction is then calculated as the ratio between the aerosols inside the MLH_{NO_2} (i.e. AOD times p) and MLH_{NO_2}. The near-surface aerosol extinction refers to the layer that extends from the surface to the MLH_{NO_2}. As discussed above, around 30% of the total aerosols is expected to be found inside this layer.

The effect of SZA, RAA, and MLH_{NO_2} on the simulated L_{NO_2} is investigated in the supplement. First, the

simulated L_{NO_2} are presented in Figure 18.5 as a function of RAA for different MLH_{NO_2} and wavelengths and a single AOD and SZA value. L_{NO_2} strongly depends on MLH_{NO_2}. The lower the MLH_{NO_2}, the shorter the L_{NO_2} is. The same NO_2 concentration and aerosol load are used for the three different MLH_{NO_2} scenarios. So, when aerosols are concentrated in a thin layer (i.e. MLH_{NO_2}=0.5 km), L_{NO_2} becomes shorter. Secondly, we observe that L_{NO_2} depends on RAA. The larger the RAA, the longer the L_{NO_2}. In Figure 18.6, simulated L_{NO_2} are plotted for each wavelength and each considered MLH_{NO_2} as a function of SZA (at a constant AOD and RAA). L_{NO_2} depends strongly on SZA. The highest dependency is observed for large SZA values, where L_{NO_2} becomes maximum. Finally, in both Figure 18.5 and 18.6, we observe that L_{NO_2} becomes longer with wavelength, which is expected because of the less pronounced Rayleigh scattering at longer wavelengths.

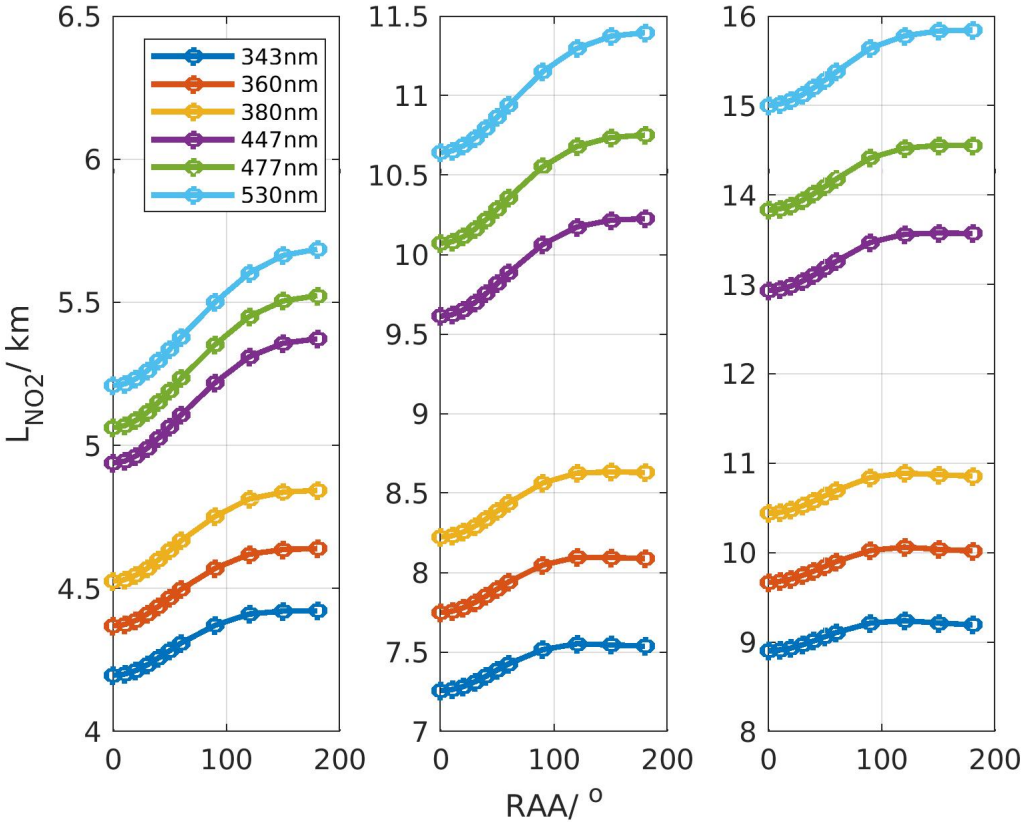

Figure 18.5: Simulated L_{NO_2} as a function of the RAA for different MLH_{NO_2} values (from left to right panel: MLH_{NO_2} equal to 500 m, 1000 m, and 1500 m), wavelengths, one SZA value (30^o), and one AOD value (0.3).

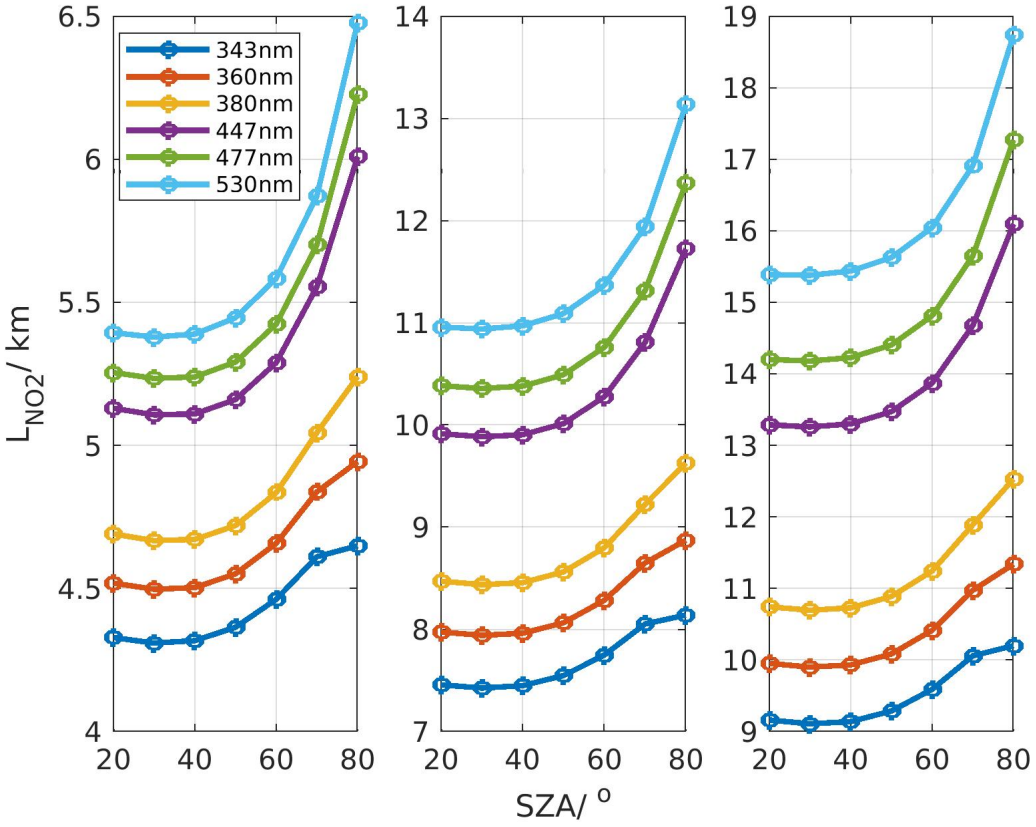

Figure 18.6: Simulated L_{NO_2} as a function of the SZA for different MLH_{NO_2} values (from left to right panel: MLH_{NO_2} equal to 500 m, 1000 m, and 1500 m), wavelengths, one RAA value (60°), and one AOD value (0.3).

An example of dual-scan MAX-DOAS retrieval is shown in Figure 18.4. Based on the RTM simulations described above, L_{NO_2} is derived for the wavelengths of interest, and ultimately, near-surface NO_2 concentrations and tropospheric NO_2 VCDs are estimated. In the last step, the near-surface aerosol extinction values are assigned to the six different wavelengths.

18.2.2 Uncertainty budget

To estimate uncertainties on the dual-scan parameterized NO_2 near-surface concentration and VCD, the standard error propagation method is used as:

$$\sigma^2_{c_{NO_2}} = \left(\sigma_{dSCD_{NO_2}} \frac{\delta c_{NO_2}}{\delta dSCD_{NO_2}}\right)^2 + \left(\sigma_{L_{NO_2}} \frac{\delta c_{NO_2}}{\delta L_{NO_2}}\right)^2 \tag{18.7}$$

which is solved as:

$$\sigma^2_{c_{NO_2}} = \left(\sigma_{dSCD_{NO_2}} \frac{c_{NO_2}}{dSCD_{NO_2}}\right)^2 + \left(\sigma_{L_{NO_2}} \frac{c_{NO_2}}{L_{NO_2}}\right)^2 \tag{18.8}$$

According to Kreher et al. (2020) and Bösch et al. (2018), in urban or suburban polluted conditions, the use of the DOAS fit uncertainty of NO_2 for the $dSCD_{NO_2}$ uncertainty is not appropriate, because the $dSCD_{NO_2}$ uncertainty is mostly driven by atmospheric variability as well as spatial and temporal fluctuations in the O_4 and NO_2 fields. In this study, a conservative value of $3.5x10^{15}$ molec.cm^{-2} is attributed to $\sigma_{dSCD_{NO_2}}$ (Kreher et al., 2020). This represents an error of up to 6.0% on the NO_2 dSCDs in the visible range (477 nm).

The second error source is related to the estimation of L_{NO_2} from the RTM simulations. To estimate this error, sensitivity tests on the input aerosol and NO_2 vertical profiles were performed. The fraction of aerosols located inside the MLH_{NO_2} (40% and 60% instead of 30%) and the NO_2 profile shape (linearly decreasing instead of box) were modified. The error related to the RTM simulations is about 9.6% in the Visible range (477 nm).

Combining all the error sources, the total uncertainties on the NO_2 near-surface concentration are about 12.7%, 12.4%,11.4%, 11.1%, 11.3%, and 12.6% in 343 nm, 360 nm, 380 nm, 447 nm, 477 nm, and 530 nm, respectively.

Finally, the total uncertainties on the NO_2 VCD are about 12.0%, 11.7%, 10.7%, 10.3%, 10.6%, and 11.9% in 343 nm, 360 nm, 380 nm, 447 nm, 477 nm, and 530 nm, respectively.

18.2.3 Validation of the dual-scan MAX-DOAS retrieval method

The sanity check and validation of the dual-scan MAX-DOAS retrieval method in Uccle is based on two different correlative comparisons.

The sanity check compares the NO_2 near-surface VMRs and tropospheric VCDs retrieved by the dual-scan parameterization in the main azimuthal direction to the same quantities retrieved with the MMF inversion algorithm at the two main wavelengths (360 nm and 477 nm). As can be seen in Figures 18.7 and 18.8, both data sets are in good agreement, with correlation coefficient values in the range of 0.86 to 0.95 and slope values close to unity for all the four comparisons.

The validation step is based on the same type of comparison as the first one but for three additional azimuthal directions, where elevation scans, and hence profile retrievals, are available for some periods. Onward July 3, 2019, elevation scans have been performed in these three additional azimuthal directions to complement the already existing measurement set-up. These elevation scans have been performed once per day, around noon, in the 11°, 105°, and 262.5° azimuthal directions. Figure 18.9 shows the comparison between near-surface NO_2 VMRs and tropospheric VCDs retrieved by the dual-scan parameterization method and the corresponding results obtained with the MMF inversion algorithm. Overall good agreement is obtained (R=0.79 and 0.84 for near-surface VMR and VCD, respectively). We observe that the comparison concerning the near-surface NO_2 VMR seems to be noisier than in the main azimuth direction. This is mainly due to the use of the MLH_{NO_2} calculated in the main azimuthal direction for all the different azimuth angles in the dual-scan method. Additionally, the parameterization technique slightly underestimated the near-surface NO_2 VMR (s=0.84) while a slope value of 1.00 is obtained for tropospheric VCDs.

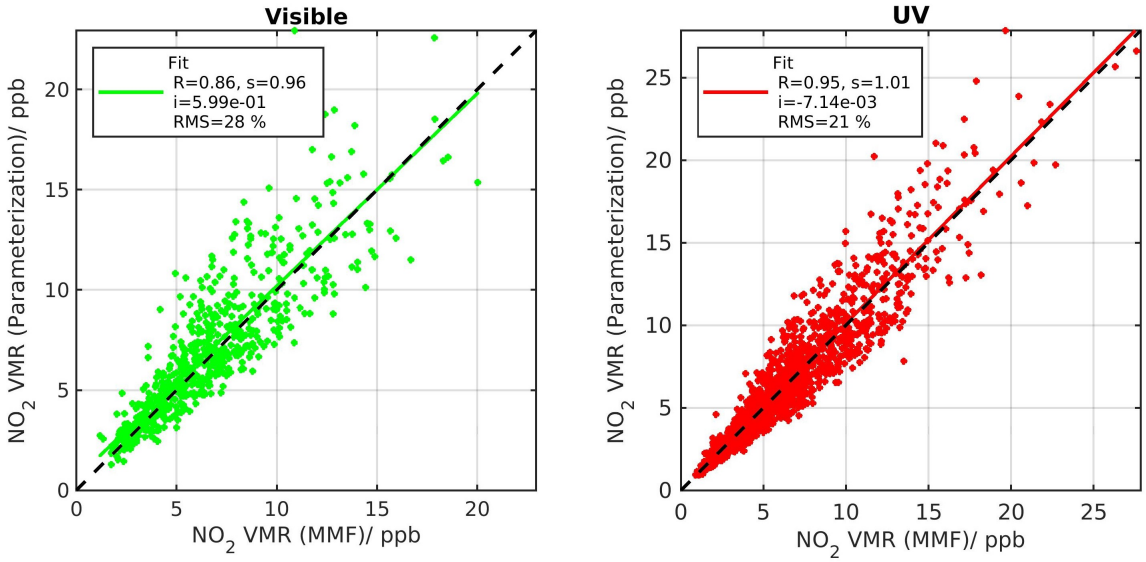

Figure 18.7: Comparison between MMF and parameterized NO_2 near-surface VMR at 477 nm (Visible, left panel), and 360 nm (UV, right panel), as derived from the main azimuthal direction (i.e. 35.5° azimuthal direction).

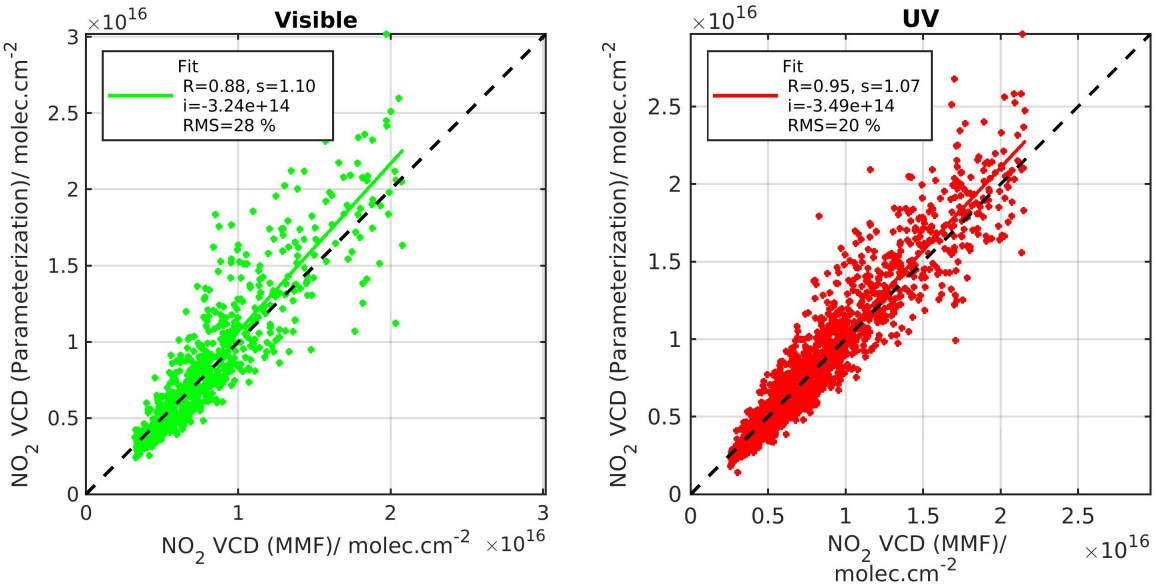

Figure 18.8: Comparison between MMF and parameterized NO_2 VCD at 477 nm (Visible, left panel), and 360 nm (UV, right panel), as derived from the main azimuthal direction (i.e. 35.5° azimuthal direction).

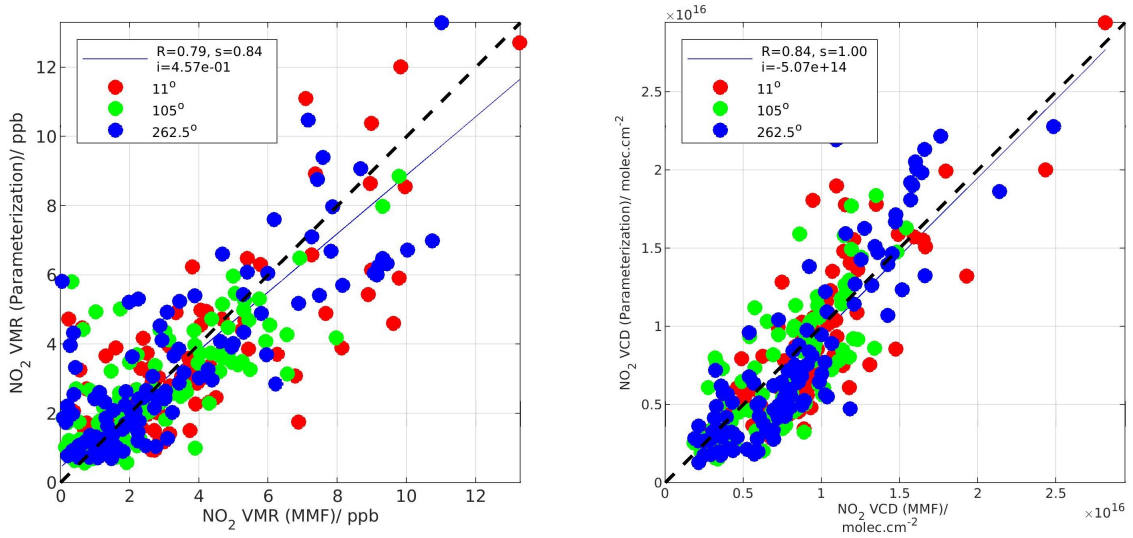

Figure 18.9: Visible range: comparison between MMF and (left panel) parameterized NO_2 near-surface VMR and (right panel) parameterized NO_2 VCD at three different azimuthal directions, as indicated in the color bar (11°, 105°, and 262.5° azimuthal directions). The elevation scans in these azimuthal directions have been performed once per day from 3 July 2019.

18.3 Horizontal distribution inversion approach

The parameterized NO_2 near-surface concentrations at the six different wavelengths are used as input in a new horizontal distribution inversion approach. As parameterized NO_2 near-surface concentrations, we refer to the conversion of the measured NO_2 dSCDs (i.e. at the elevation angle of 2°) to near-surface NO_2 concentrations by applying the dual-scan MAX-DOAS retrieval method as described in section 18.2. Figure 18.10 shows a sketch of the assumed horizontal box model configuration, in which successive boxes of concentration c_N between the horizontal distances x_{N-1} and x_N from the MAX-DOAS instrument are considered along the light path. The index N is equal to the total number of successive boxes.

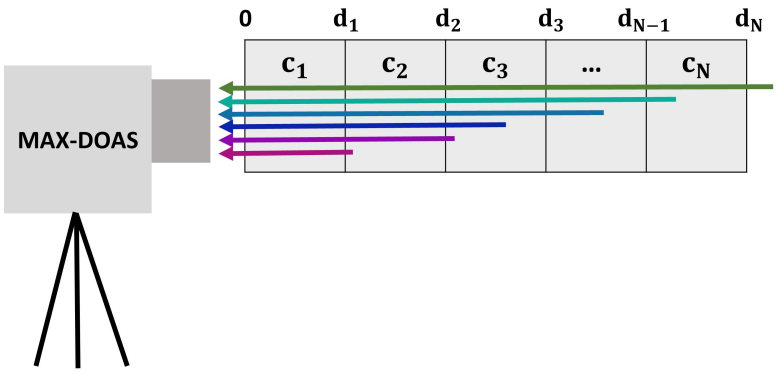

Figure 18.10: Schematic representation of the six different L_{NO_2} (i.e. one horizontal line for each wavelength) used in the new horizontal distribution inversion approach. The length of each line shows the sensitivity of each wavelength as a function of the horizontal distance. The shortest line represents the smallest wavelength.

The different horizontal lines illustrate the horizontal extent (or differential effective light path as described in subsection 18.2.1) in which the NO_2 near-surface concentrations are extended for the six different wavelengths. Generally, the MAX-DOAS horizontal sensitivities are longer for larger wavelengths because of the less pronounced Rayleigh scattering (see also Figure 18.4; Ortega et al., 2015; Dimitropoulou et al., 2020). In Figure 18.10, the shortest line represents the smallest wavelength's horizontal sensitivity (343 nm), and the longest line the largest wavelength's horizontal sensitivity (530 nm). As can be seen in the sketch, the effective horizontal light path at the six different wavelengths passes through different number of horizontal bins.

The parameterized NO_2 near-surface concentrations at the different wavelengths are the mean concentrations along the horizontal effective light paths, which are also called differential effective light paths because they are linked to the $dSCD_{NO_2}$. When having information coming from one wavelength only, it is not possible to know how the NO_2 is distributed along this light path. In the present work, the knowledge of mean NO_2 concentrations at six different wavelengths is used to retrieve a horizontal NO_2 profile, assuming the horizontal box model described in Figure 18.10. This new retrieval method is described below.

The measurement vector y consists of the six retrieved surface concentrations (called as $\bar{c}_{NO_2}$) at the six different wavelengths. These near-surface concentrations can be expressed as functions of the different effective light paths (L_{NO_2}) and correspond to the average surface concentrations along those L_{NO_2}:

$$y = F_{meas}(c_{NO_2 true}) = \bar{c}_{NO_2} = \frac{dSCD_{NO_2}}{L_{NO_2}} \tag{18.9}$$

F_{calc}, which represents the forward model, can be expressed as follows:

$$F_{calc}(c_{NO_2 true}) = \frac{1}{L_{NO_2}} \int_0^{L_{NO_2}} c_{NO_2}(x)dx \tag{18.10}$$

where x is the horizontal distance and c_{NO_2} the NO_2 near-surface concentration as a function of x, the distance from the MAX-DOAS instrument.

Our retrieval of the horizontal distribution of c_{NO_2} is based on the inversion theory (Rodgers, 2000), in which a horizontal profile c_{NO_2} (state vector) is retrieved given an a-priori horizontal profile x_a, the measurement vector y, the matrix of the weighting function K, the uncertainty covariance matrix of the a priori S_a and the uncertainty covariance matrix of the measurement S_e:

$$c_{NO_2} = x_a + (K^T S_e^{-1} K + S_a^{-1})^{-1} K^T S_e^{-1} (y - K x_a) \tag{18.11}$$

The weighting function indicates the sensitivity of the measurement vector to a change in the horizontal profile. It is given in the present case by the following analytical functions:

$$K(x, L_{NO_2}) = \frac{dF_{calc}}{d_{c_{NO_2}}} = \begin{cases} \frac{dx}{L_{NO_2}} & \text{for } 0 \leq z \leq L_{NO_2} \\ \frac{Adx}{L_{NO_2}} & \text{for } x(\text{last}) > L_{NO_2} \\ 0 & \text{for } x \geq LNO_2 \end{cases} \tag{18.12}$$

where A is the coverage percentage of the differential effective light path length at the last horizontal grid.

An example of weighting functions is presented in Figure 18.11. As can be seen, each measurement is sensitive from the MAX-DOAS instrument location to the horizontal distance equal to the differential effective light path length of each measurement. As each last horizontal grid is not fully covered by each measurement, the coverage percentage is considered for these grid cells. It should be noted that since NO_2 is an optically thin absorber, the measurements depend linearly on each horizontal box's concentration. For this reason, OEM for the linear case is considered here, and only one inversion step is needed (see Equation 18.3).

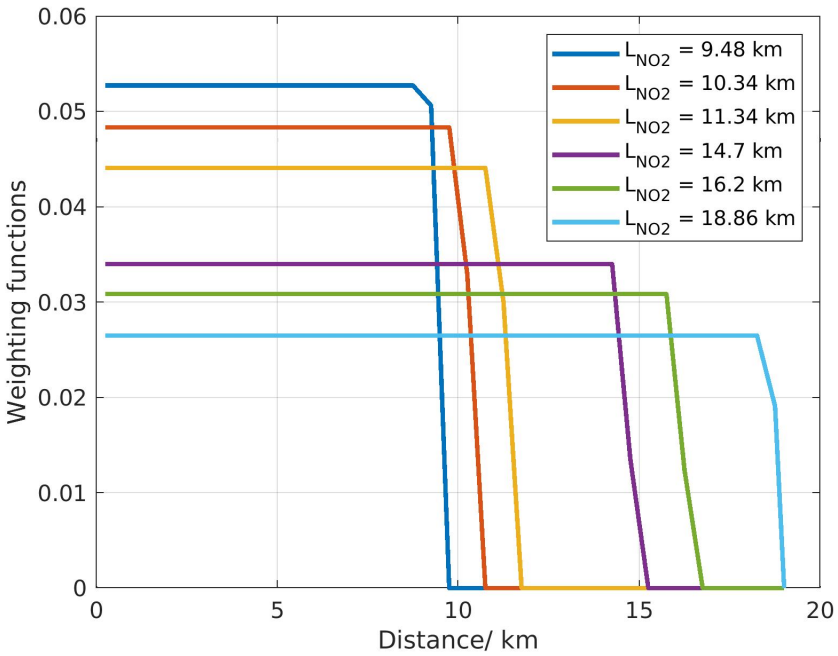

Figure 18.11: Examples of weighting functions used in the new horizontal distribution inversion approach (11 September 2018).

The selected output horizontal grid for the retrieval extends from the MAX-DOAS instrument to the maximum differential effective light path (L_{NO_2} at 530 nm) per azimuthal direction and consists of successive boxes of 0.5 km thickness on the horizontal axis.

Since this inversion problem is ill-conditioned, more than one horizontal NO_2 profile can be consistent with the measurement vector. To reject unrealistic solutions, the a priori profile x_a and its uncertainty covariance matrix must be included in the retrieval. In the OEM, the a priori information usually comes from an independent source, like a model or other correlative measurements. In the present study, RIO model data were chosen as a priori. RIO is a land-use regression model based on the interpolation of the hourly NO_2 near-surface concentrations measured by the in-situ telemetric air quality network in Belgium (Hooyberghs et al., 2005; Janssen et al., 2008). RIO provides hourly NO_2 concentration maps on a 4x4km^2 spatial resolution. Seasonal average maps of RIO NO_2 near-surface concentration are constructed (see Figure 18.12) and after, seasonal averages of RIO NO_2 near-surface concentration horizontal profiles were calculated in each azimuthal direction and interpolated on the retrieval's horizontal grid by regridding the initial 4x4 km^2 spatial resolution to a finer one (see Figure 18.13). The shape of the RIO a priori NO_2 profiles per azimuthal direction stays the same during different seasons of the year, indicating that the wind effect on NO_2 transportation disappears by the seasonal averaging and that the same sources contribute to the NO_2 horizontal field. A mean scaling factor equal to the mean ratio between the measured and RIO NO_2 near-surface concentrations is applied because of the systematic underestimation of NO_2 near-surface concentrations by MAX-DOAS when compared to in-situ measurements (Dimitropoulou et al., 2020).

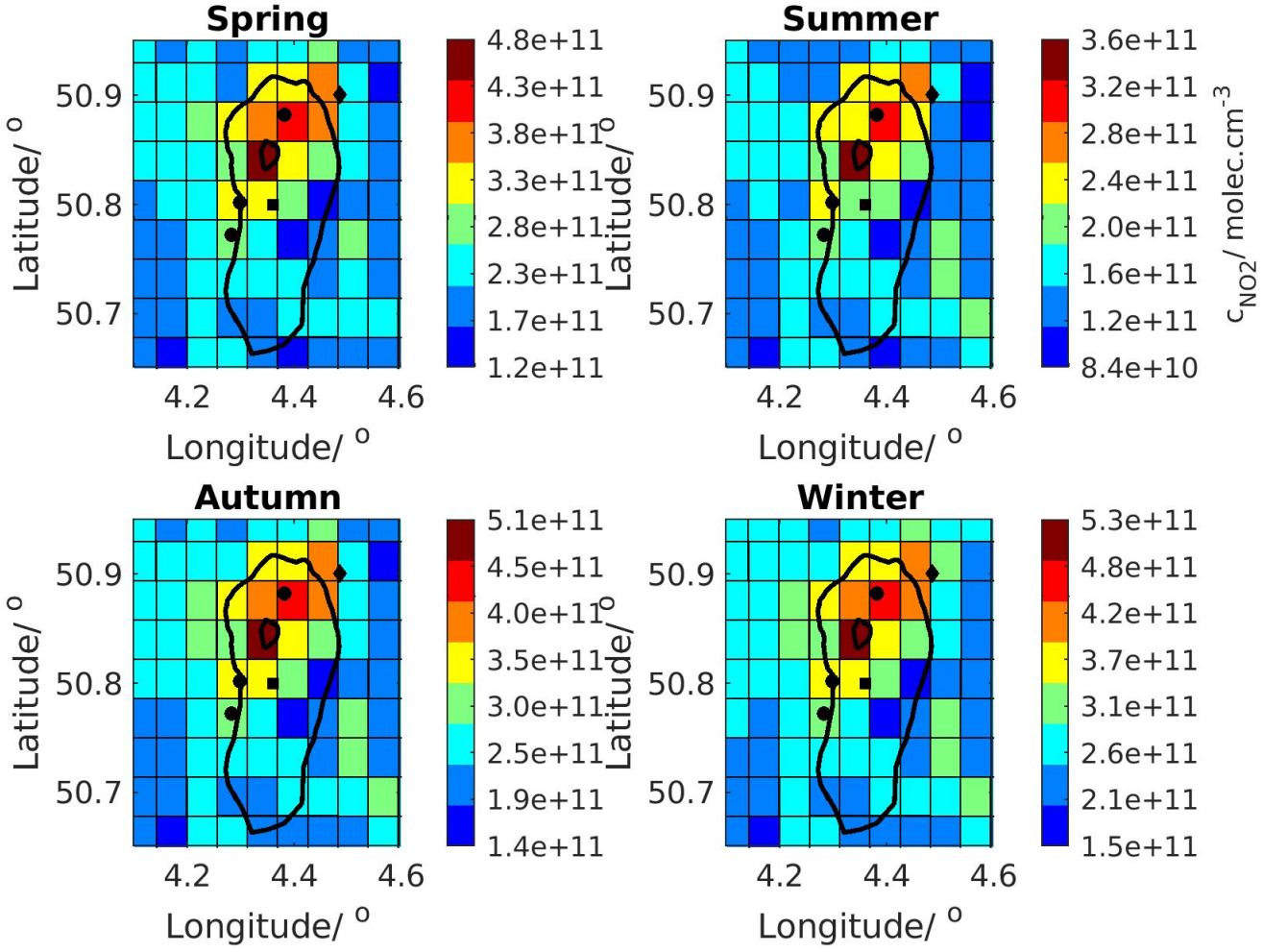

Figure 18.12: Seasonal near-surface NO_2 concentration grids as estimated over Brussels by the RIO air-quality model. The black square shows the MAX-DOAS position, the black polygon the National Airport, the black dots the NO_2 hotspots, and the black line represents the Brussels Ring motorway.

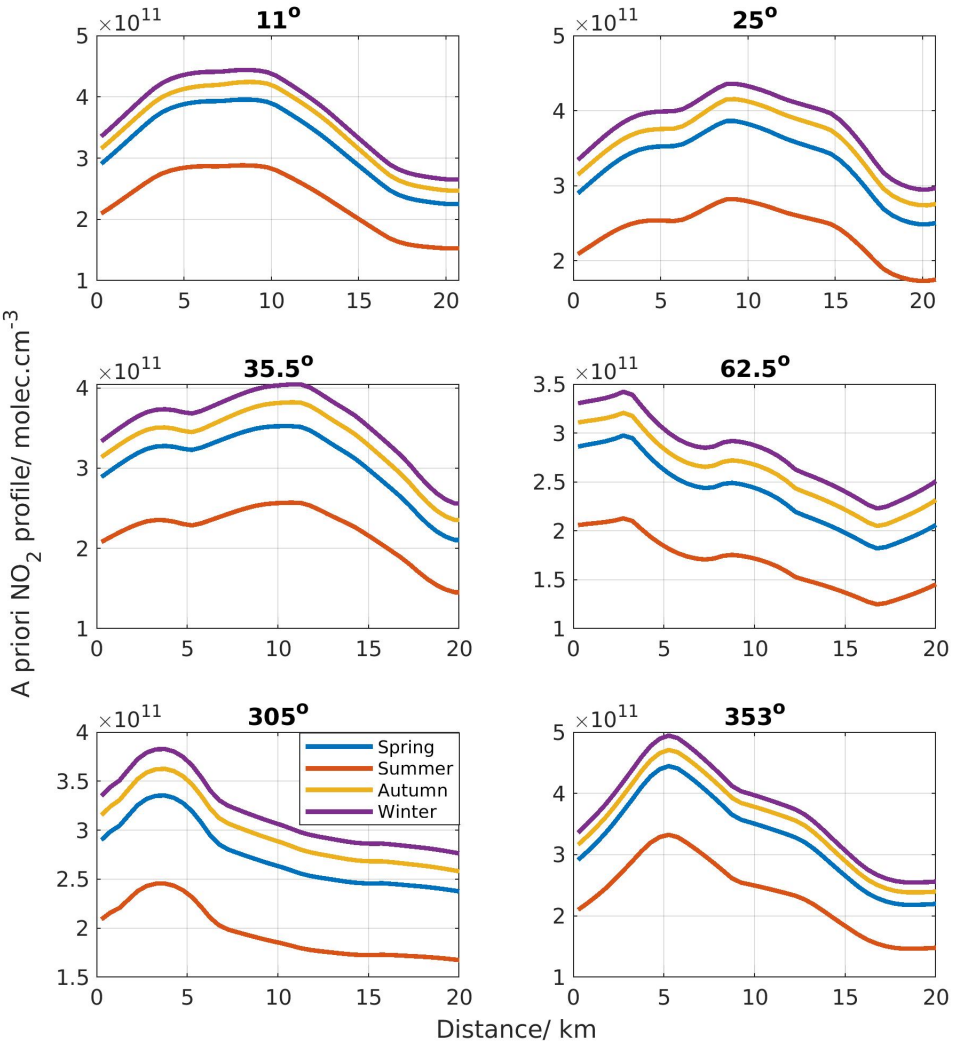

Figure 18.13: Example of seasonal a priori NO_2 horizontal profiles for the new horizontal distribution inversion approach as a function of the horizontal distance from the MAX-DOAS instrument in six different azimuthal viewing directions, before the application of the scaling factor.

For the aerosols horizontal distribution retrieval, there are not sufficient independent measurements that provide information about the horizontal distribution of AOD and can serve as an a priori AOD profile. Therefore, a horizontally constant a priori AOD profile is used in the AOD retrieval based on CIMEL observations. An AOD equal to 0.18, which is the yearly-averaged AOD value from CIMEL at 477 nm, is used. To construct the near-surface aerosol extinction a priori profiles, it is considered that 30% of the total amount of AOD is located inside the MLH (i.e. known for each MAX-DOAS vertical scan from the MMF inversion algorithm; see section 18.1).

The diagonal elements of the S_a matrix are set equal to the square of a scaling factor times the NO_2 concentration a priori profile. The non-diagonal elements, which account for correlation between the different horizontal grid cells, are set as follows (Barret et al., 2002):

$$S_{a_{ij}} = \sqrt{S_{a_{ii}} S_{a_{jj}} \exp\left(-\ln(2)\left(\frac{x_i - x_j}{\gamma}\right)^2\right)} \tag{18.13}$$

where xi and xj are the horizontal distances at the ith, and jth horizontal boxes and γ is half of the correlation length. γ is set equal to 3.5 km. To eliminate inversion instabilities, S_a elements which are smaller than 0.1% of the maximum Sa element are set equal to zero.

To estimate the correlation length, a covariance matrix has been constructed by exploiting the airborne observations above Brussels (28 June 2019). The airborne observations have a spatial resolution of approximately 100x100m^2. NO_2 horizontal profiles have been constructed in different azimuthal directions in a spatial resolution of 500x500m^2, expanding from the MAX-DOAS's position to a maximum distance of 20 km, and have been used to calculate a covariance matrix. A correlation length equal to 7 km, and consequently, a gamma value equal to 3.5 km, is found to be representative for the NO_2 horizontal profiles in Brussels.

Using this correlation length, a variance of 45% is used. This choice has been conducted based on the seasonal variance of the RIO a priori profiles compared to their seasonal mean value. It is found that the seasonal variance of RIO observations has a mean value of 45%. Additionally, it is found to be a good compromise for obtaining reasonable retrieval results e.g. in terms of information content, and while avoiding unrealistic oscillations in the retrieved aerosol and NO_2 profiles. The measurement covariance matrix S_e is chosen to be diagonal, with elements corresponding to the uncertainties of the dual-scan parameterized NO_2 near-surface concentration.

An example of the retrieved NO_2 horizontal profile is presented in Figure 18.14, together with corresponding measured and simulated $\bar{c}_{NO_2}$ at the six different wavelengths for July 2, 2018 (25^o azimuthal direction). RMS is calculated between measured and simulated NO_2 near-surface concentrations of the horizontal retrieval normalized by the mean of the measured NO_2 near-surface concentrations (upper panel in Figure 18.14). For distances smaller than the minimum L_{NO_2} (around 8 km), the measurements do not give information about the horizontal distribution of NO_2. Consequently, the retrieved NO_2 horizontal profile at these ranges is coming from the a priori profile. Similarly, the measured and retrieved near-surface aerosol extinction coefficient and the retrieved aerosol horizontal profile are shown in Figure 18.15, for one sample case on 11 September 2018 (167.5^o azimuthal direction).

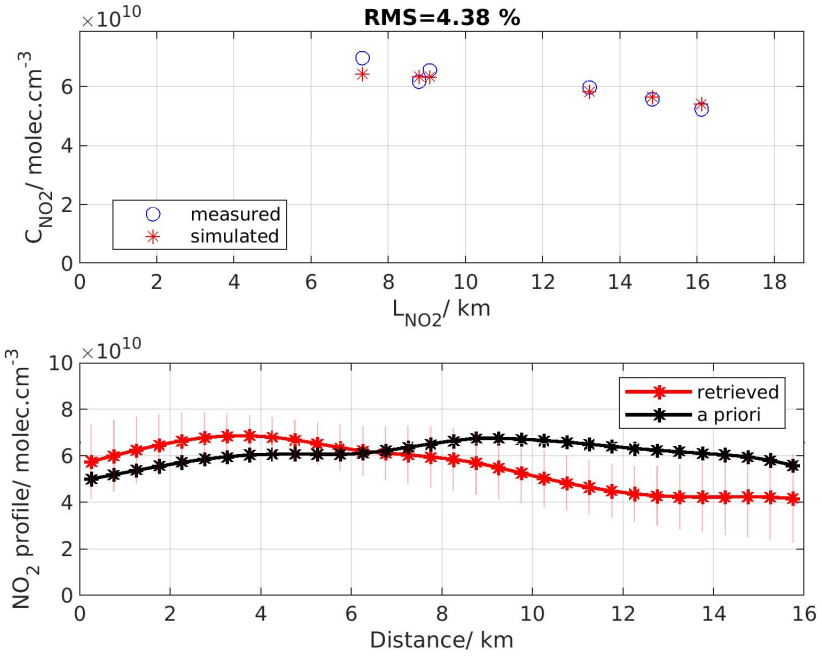

Figure 18.14: (Upper panel) Measured and retrieved NO_2 near-surface concentrations at the six different wavelengths (i.e. horizontal distances) as a function of the estimated horizontal distances and (lower panel) the retrieved NO_2 near-surface horizontal profile and a priori profile (02 July 2018, 10.42 UTC, 25^o azimuthal direction).

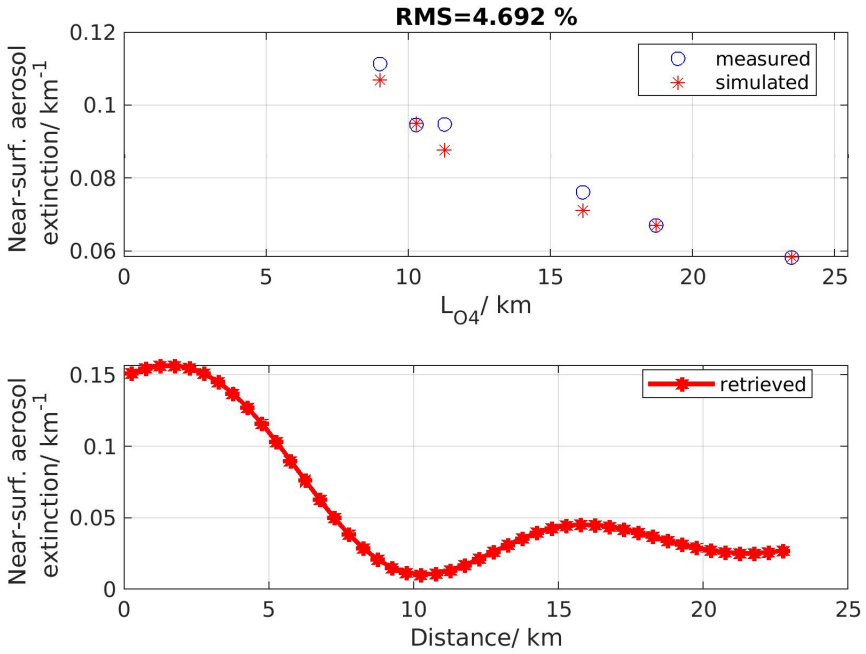

Figure 18.15: (Upper panel) Measured and retrieved near-surface aerosol extinction at the six different wavelengths (i.e. horizontal distances) as a function of the estimated horizontal distances and (lower panel) the retrieved near-surface aerosol extinction horizontal profile (11 September 2018, 11.48 UTC, 167.5^{o} azimuthal direction).

An essential condition of the dual-scan MAX-DOAS retrieval and the new horizontal inversion approach at six different wavelengths is the increasing trend of the horizontal sensitivity as a function of wavelength. Consequently, every wavelength is sensitive to a different horizontal region and the six different wavelengths can be used to retrieve the horizontal distribution of aerosols and trace gases. Sensitivity tests have been conducted in which simulated L_{O_4} are expressed as a function of the six different wavelengths for different aerosol conditions. As can be seen in Figure 18.16, the linear relationship between L_{O_4} (and L_{NO_2}) and wavelength exists for AOD values ranging from 0 to 1. An AOD equal to unity is chosen as the maximum AOD of the simulations because in Uccle, AOD values rarely exceed one (see in https://aeronet.gsfc.nasa.gov/ for the Brussels measurement site). Therefore, the relation stays linear as the aerosol load changes for the conditions observed in Uccle. The only condition leading to non-linearity is when clouds are present. However, a cloud filtering approach is applied, rejecting the broken cloud scenes, which are the more problematic ones.

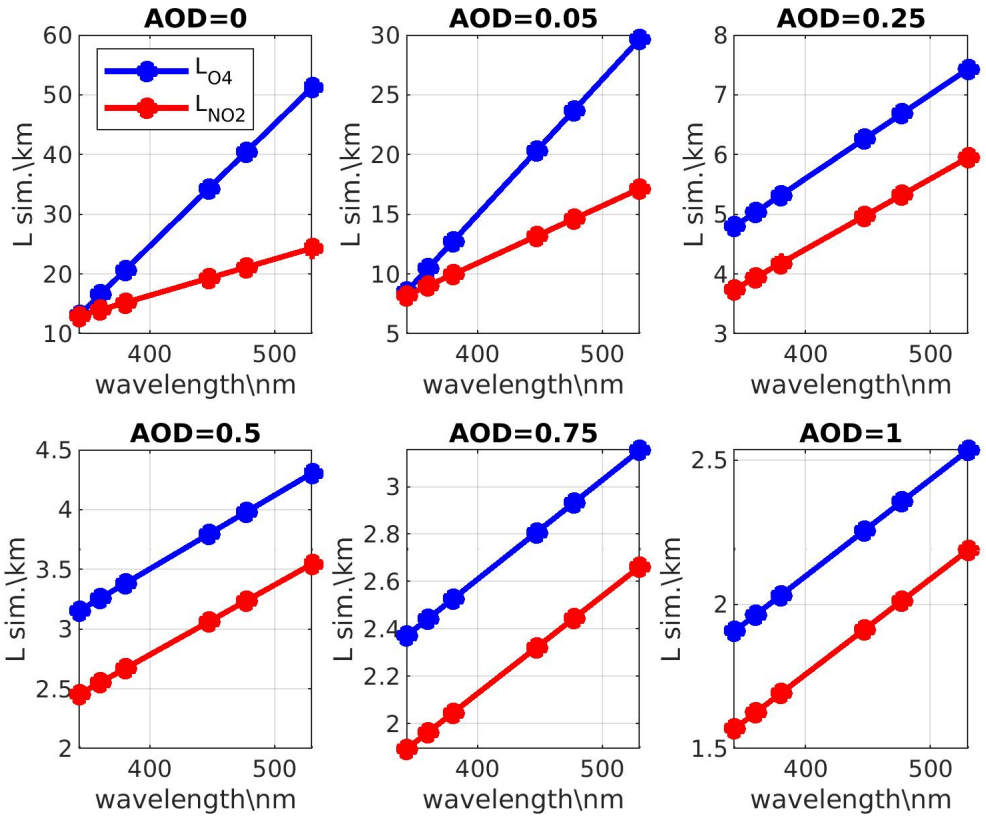

Figure 18.16: Simulated differential effective light path of O_4 dSCDs (L_{O_4} sim.) and NO_2 dSCDs (L_{NO_2} sim.) as a function of wavelength for different AOD scenarios.

18.4 Characterization of the retrieval

To characterize the retrieval, the averaging kernels, AK, play a crucial role. The AK matrix is calculated as follows Rodgers (2000):

$$A = \frac{dc_{NO_2}}{dc_{NO_2 true}} = (K^T S_e^{-1} K + S_a^{-1})^{-1} K^T S_e^{-1} K \tag{18.14}$$

The AKs are the rows of the AK matrix. They present the sensitivity of the retrieved (c_{NO_2}) on the true ($c_{NO_2 true}$) atmospheric profile. Ideally, the AK matrix should be an identity matrix. In Figure 18.17, an example of selected AKs is shown. As can be seen, for distances smaller than the first measurement (e.g. near-surface NO_2 concentration retrieved at 343 nm), the AKs are constantly zero (or have small values) from the MAX-DOAS instrument until these distances. This indicates a low sensitivity on these short distances, and therefore information about the horizontal distribution of NO_2 is coming essentially from the a priori profile. The AKs create a maximum flat plateau close their nominal horizontal distance for larger distances (d=7.25 km, d=8.75 km, and d=15.75 km). For this particular example, the AKs do not exceed the values of 0.25.

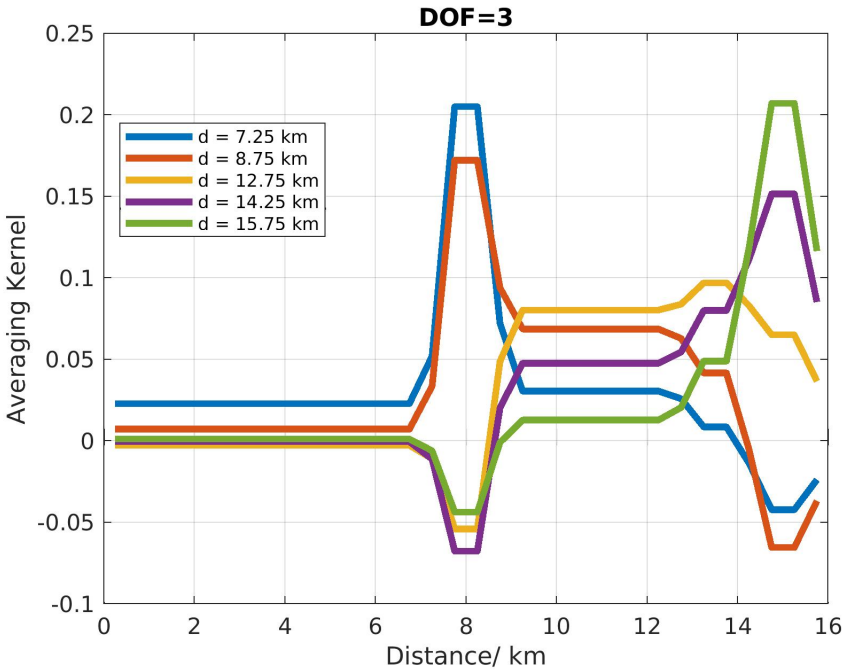

Figure 18.17: Example of NO_2 averaging kernels. They are calculated for observations on 11 September 2018 at 11:51 UTC and 300° azimuthal direction.

Another important information about the retrieval is the trace of the AK matrix, which refers to the number of degrees of freedom for signal (DOFS). The DOFS are an indication of the number of independent pieces of information that one can retrieve from the measurements. Ideally, the DOFS would be equal to the number of horizontal boxes for the horizontal distribution. In reality, the DOFS are lower, because of the limited horizontal resolution of the measurements. In Figure 18.17, the DOFS are close to three, which means that three independent pieces of information are contained in the measurements for this particular example.

In the present work, the total retrieval error is equal to the error related to the measurement noise. According to Rodgers (2000), the retrieval noise error is estimated as:

$$S_{meas} = GS_eG^T \tag{18.15}$$

with, G being the gain matrix:

$$G = (K^T S_e^{-1} K + S_a^{-1})^{-1} K^T S_e^{-1} \tag{18.16}$$

The horizontal profiles of the retrieval noise error in percentage are shown in Figure 18.18. As can be seen, the retrieval noise error becomes maximum for the longest distance.

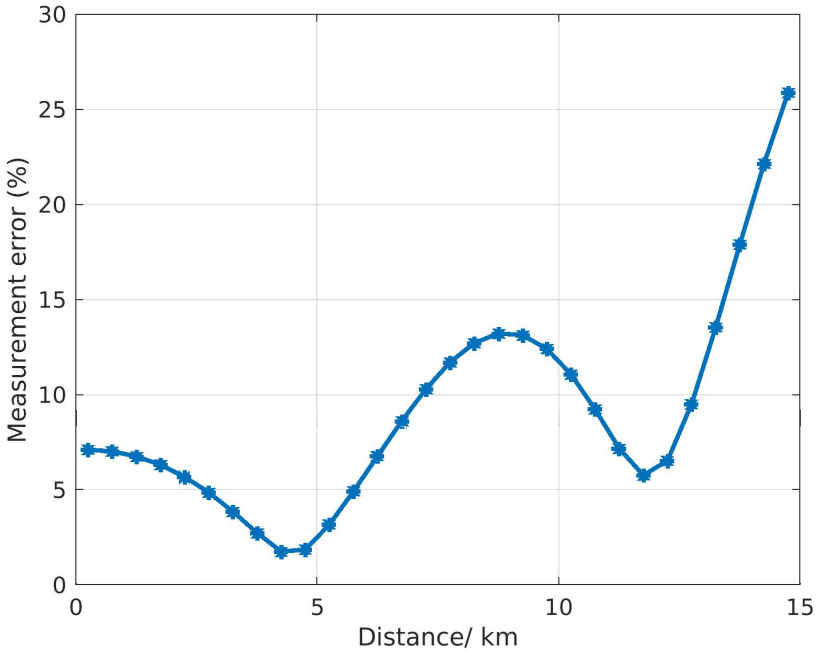

Figure 18.18: Example of the NO_2 retrieval noise error in percentage for the 2 July 2018 at 05:59 UTC and 300° azimuthal direction.

To eliminate the unsuccessful retrievals, the percentage of accepted retrievals with respect to the total number of retrievals during the four seasons is investigated when a specific filtering on RMS and DOFS is applied (see Table 18.2). From these tests, it is found that most of the retrievals have DOFS larger than 1.5. RMS is defined as the root-mean-square deviation between measured and simulated c_{NO_2} normalized by the mean of the measured c_{NO_2} (e.g. same RMS as in Figure 18.14). Table 18.2 indicates that most of the retrievals have an RMS smaller than 6% with a median RMS value of around 4.5% during all seasons. Based on these investigations, DOFS>1.5 and RMS<6% are used as retrieval quality control criteria.

Table 18.2: Seasonally averaged root-mean-square (RMS) and DOFS values. RMS is calculated between measured and retrieved NO_2 near-surface concentrations of the horizontal retrieval (Figure 18.14). DOFS represent the degrees of freedom of the horizontal retrieval (Figure 18.17). The percentage of the accepted retrievals is presented for the different selection criteria.

Season	Spring	Summer	Autumn	Winter
Median RMS (%)	3.8	4.7	4.7	4.8
Median DOFs	1.7	1.7	1.6	1.6
Accepted retrievals (%) (DOFs>1.5)	90	91	81	78
Accepted retrievals (%) (RMS < 6%)	87	72	70	73
Accepted retrievals (%) (RMS < 5%)	75	57	55	55
Accepted retrievals (%) (RMS < 4%)	56	33	36	32
Accepted retrievals (%) (RMS < 3%)	27	11	15	11
Total accepted retrievals (%) (DOFs>1.5 and RMS < 6%)	80	67	57	57

Chapter 19

Retrieval results and discussion

Contents

19.1 Example of daily horizontal NO_2 distribution

The variation of the MAX-DOAS horizontal distribution of tropospheric NO_2 VCDs as a function of time over the course of June 28 2019, is presented in Figure 19.1. This particular day is chosen because airborne measurements took place above the Brussels region (see chapter 19). The horizontal NO_2 profiles are plotted per azimuthal direction with the horizontal axis showing the time in UTC and the vertical axis the horizontal distance in km. Because of the quality check on the retrieved NO_2 horizontal profiles (see chapter 18), some profiles have been rejected (e.g. azimuthal direction equal to 262.5° and 265°).

During this day, maximum NO_2 columns are mainly observed around 05:00 UTC and 10:00 UTC, which correspond to 7am and noon local time. Early in the morning (05:00 UTC), high NO_2 columns are expected to be observed because of the low MLH (MLH_{NO_2} in the range of 300 - 600 m height) in combination with the morning rush hour NO_2 emissions. Around 10:00 UTC, the maximum NO_2 columns are detected in the north (N), northeast (NE), and northwest (NW) direction (see Figure 19.2). In the Brussels region, the main emission sources are located in the N and west (W) parts of the city and are linked to the motorway around Brussels (the so-called Ring), the Brussels city center, and the Drogenbos power plant (NW direction). Concerning the NO_2 peaks, they are located at a distance around 0 to 8 km from the measurement site. It can be seen from Figure 19.2 that the Ring, the Brussels city center, and the Drogenbos power plant are located within these distances. As measured by the meteorological station on the BIRA-IASB rooftop, the wind was coming from the NE direction during that day, resulting in the progressive displacement of the NO_2 peak from the NNE to the W direction. On the contrary, the azimuthal directions pointing towards a large forested area (i.e. 62.5°, 75°, and 105°), the Bois de la Cambre, detect considerably lower NO_2 columns than the other directions.

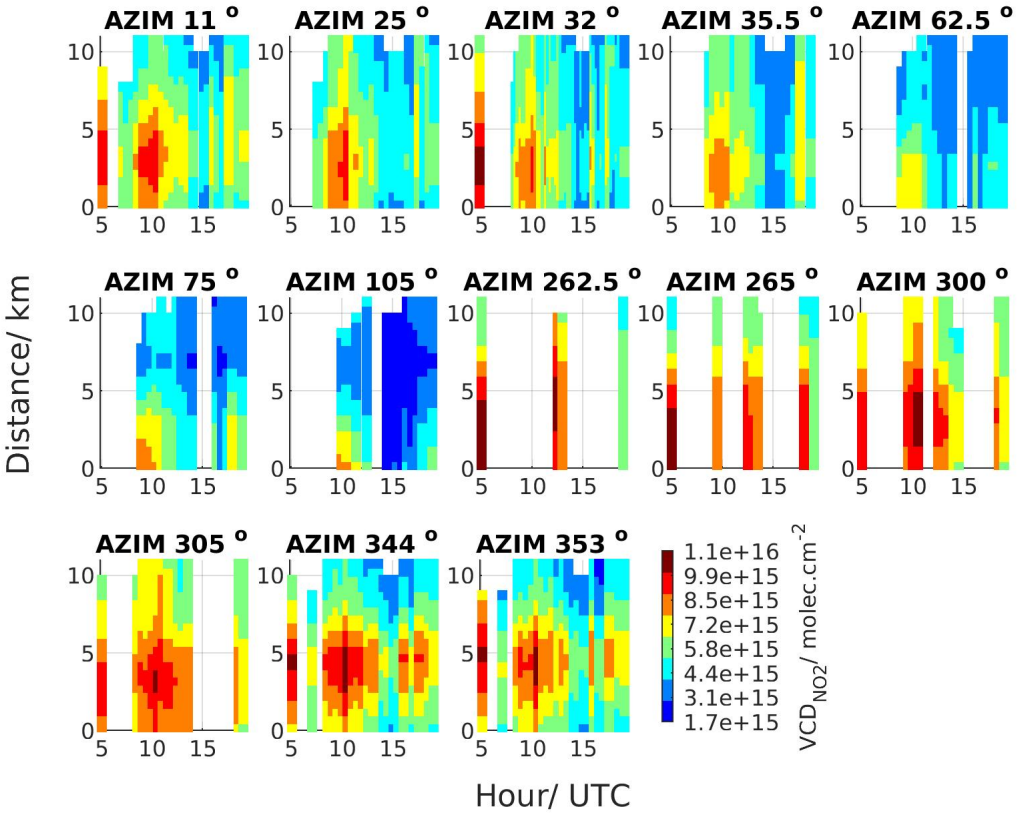

Figure 19.1: Diurnal variation of the retrieved NO_2 horizontal profiles per azimuthal direction as a function of time (UTC) for June 28, 2019.

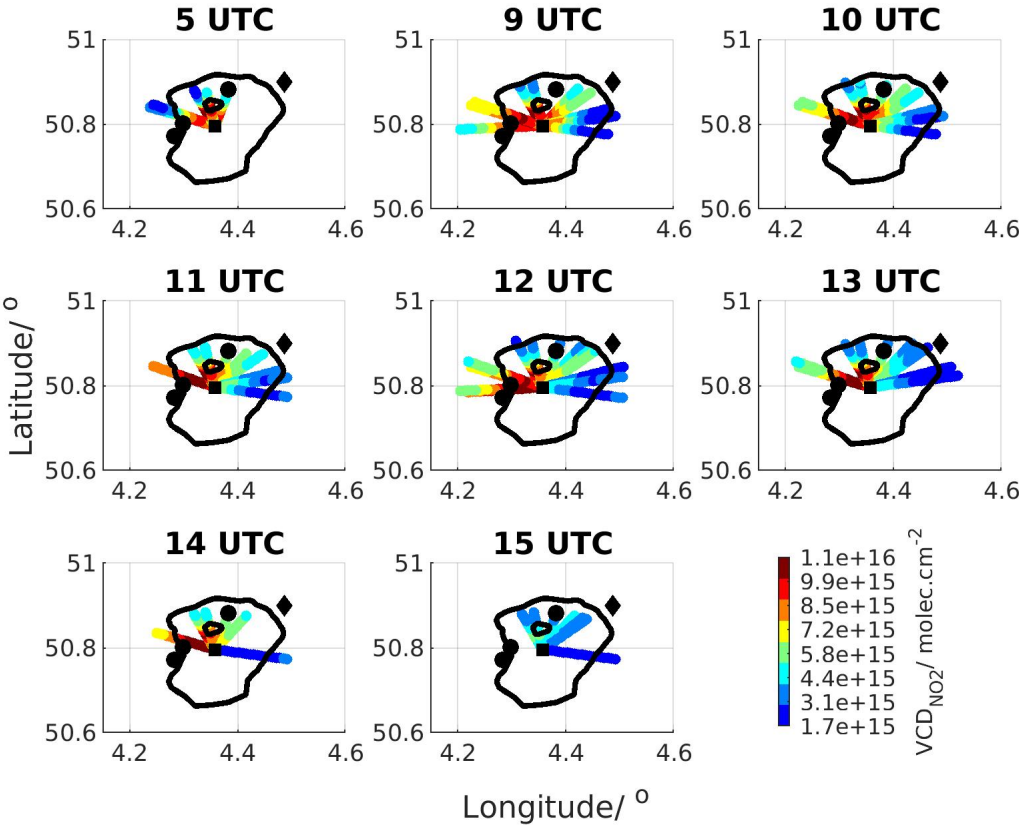

Figure 19.2: Maps of hourly averaged NO_2 horizontal profiles per azimuthal direction for June 28, 2019. The black square shows the MAX-DOAS instrument location, the black polygon the National Airport, the black dots the NO_2 hotspots emitting more than 10 kg of NO_x per hour (Emission Inventory of the Belgian Interregional Environment Agency, 2017) , and the black line represents the Brussels Ring road.

19.2 MAX-DOAS horizontal NO_2 distribution versus airborne, car mobile-DOAS, and TROPOMI: 28 June 2019 study case

For the S5P validation campaign over Belgium (S5PVAL-BE, https://s5pcampaigns.aeronomie.be/), airborne measurements of the two largest urban regions over Belgium, i.e. Antwerp and Brussels, took place from 26 to 29 June 2019 (Tack et al., 2021). The Airborne Prism EXperiment (APEX) imaging spectrometer has been used to measure the horizontal distribution of tropospheric NO_2 columns with a spatial resolution of approximately 75 m x 120 m (Tack et al., 2017,0)

The APEX tropospheric NO_2 columns are compared to the tropospheric NO_2 horizontal distribution as retrieved by applying our new MAX-DOAS inversion approach to the 28 June 2019 measurements. During the same day, TROPOMI pixels (OFFL 010302 product; see Table 1) selected over the Brussels region are compared to MAX-DOAS observations. MAX-DOAS horizontal profiles of tropospheric NO_2 VCDs are selected around TROPOMI overpass time ($\pm$ 1 hour). The horizontal profile of MAX-DOAS NO_2 VCDs on each horizontal line-of-sight has a horizontal sampling of 0.5 km (see Figure 18.14). The MAX-DOAS NO_2 VCDs on the horizontal segment crossing a TROPOMI pixel and located inside the pixel are averaged and compared to the corresponding TROPOMI NO_2 VCD. It should be noted that the MAX-DOAS segments are not weighted by their relative length inside each pixel. APEX observations located inside each TROPOMI pixel have been used to assign one APEX NO_2 VCD value per pixel. Maps of co-located TROPOMI, averaged MAX-DOAS, and averaged APEX NO_2 VCDs for the 28 June 2019 are shown in Figure 19.3. Two maps of APEX observations are presented: one with APEX in its initial resolution and one with spatially averaged APEX observations in the area covered by a TROPOMI pixel. The NO_2 plume as detected by APEX is covering the NW, N, and NE parts of the Brussels region. MAX-DOAS successfully detected the same NO_2 plume in the NW and N but not in the NE direction. The correlation and agreement between APEX and MAX-DOAS observations is very good (R=0.83 and s=1.10). As we can observe in Figure 19.4, the APEX tropospheric NO_2 VCDs tend to be larger than the MAX-DOAS ones, with an intercept equal to -2.10×10^{15} molec.cm^{-2}.

During the S5PVAL-BE flight over Brussels, car mobile-DOAS observations were performed by the BIRA-IASB mobile-DOAS, the so-called AEROMOBIL (Merlaud, 2013). The AEROMOBIL consists of a compact double Avantes spectrometer recording simultaneously scattered light in two channels (i.e. one at 30^o elevation angle and one at zenith). The AEROMOBIL has been used to measure the spatial distribution of tropospheric NO_2 columns mainly over the Ring road of Brussels. Similarly as with APEX, the AEROMOBIL NO_2 VCDs, which are located inside a TROPOMI pixel are averaged and compared to the corresponding MAX-DOAS VCDs (see Figure 19.3). AEROMOBIL and MAX-DOAS agree perfectly on the location of maximum (i.e. NW direction) and minimum (i.e. SE direction) NO_2 tropospheric VCDs (Figure 19.3). We can observe in Figure 19.4, that the correlation coefficient is moderate (R equal to 0.61) and the slope value is equal to 2.62. The correlation plot between both datasets reveals that AEROMOBIL gives higher NO_2 tropospheric VCDs compared to MAX-DOAS ones. This finding could be partly explained by the fact that AEROMOBIL follows busy routes, where the NO_2 tropospheric VCDs reach maximum values because of the contribution of NO_2 production resulted by vehicles' engines via fossil fuel combustion.

The correlation between TROPOMI and MAX-DOAS tropospheric NO_2 columns during the day of the airborne measurements above Brussels is presented in Figure 19.4. Excellent agreement is obtained, with a correlation coefficient value equal to 0.81. The slope value is equal to 0.72. During that day, MAX-DOAS and TROPOMI are in good agreement but TROPOMI tends to underestimate the tropospheric NO_2 columns. It should be noted that during that day, the range of observed NO_2 VCDs is from 3.4×10^{15} to 8.7×10^{15} molec.cm^{-2}, as retrieved by the MAX-DOAS observations.

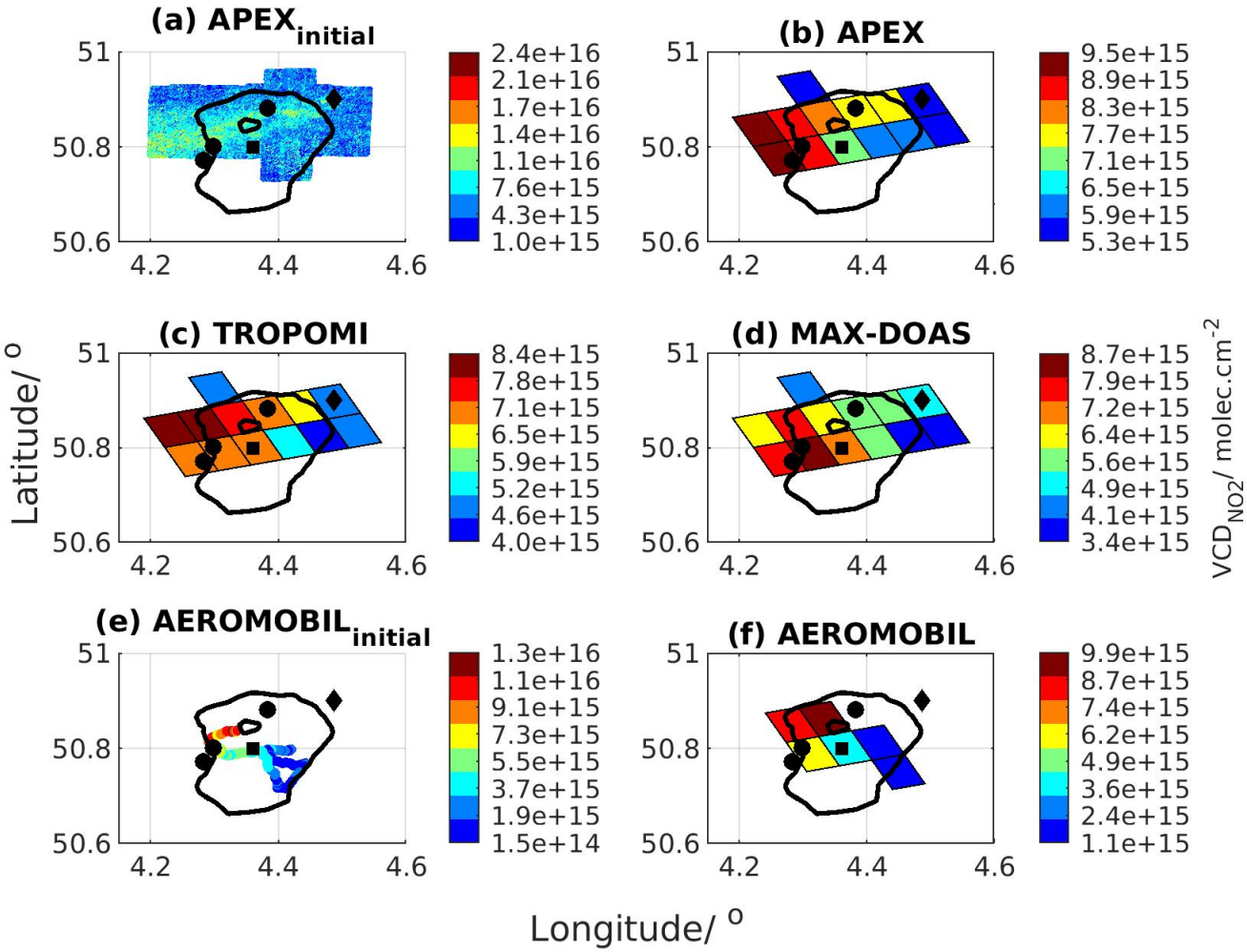

Figure 19.3: (a) Tropospheric NO_2 VCD as detected by the APEX instrument in its initial spatial resolution. Tropospheric NO_2 VCD maps (TROPOMI pixels) as retrieved over Brussels on 28th of June 2019 by the (b) APEX, (c) TROPOMI, (d) MAX-DOAS instruments. (e) Tropospheric NO_2 VCD as retrieved by the AEROMOBIL in its initial spatial resolution and (f) AEROMOBIL tropospheric NO_2 VCD in the TROPOMI pixels. The black square shows the MAX-DOAS instrument location, the black polygon the National Airport, the black dots the NO_2 hotspots emitting more than 10 kg of NO_x per hour (Emission Inventory of the Belgian Interregional Environment Agency, 2017) , and the black line represents the Brussels Ring road.

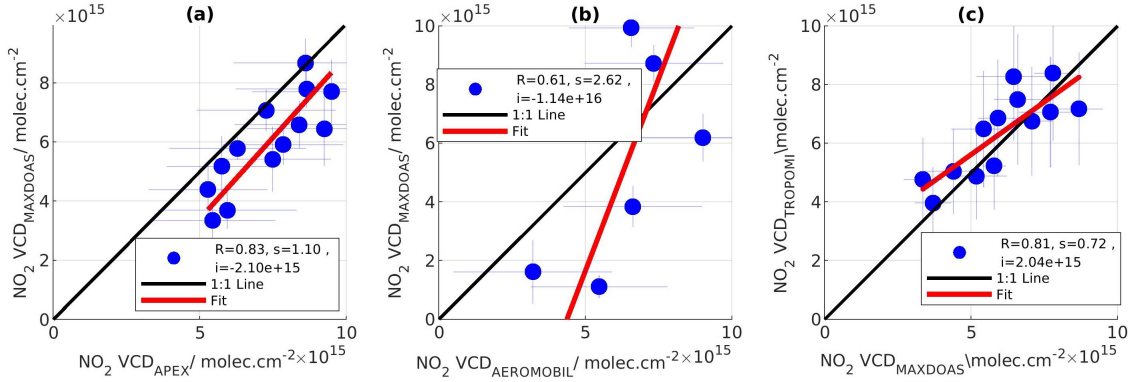

Figure 19.4: Scatter plot between (a) the tropospheric NO_2 columns derived by airborne measurements (APEX) and the MAX-DOAS observations, (b) the tropospheric NO_2 columns derived by car mobile-DOAS measurements (AEROMOBIL), and the MAX-DOAS observations and (c) the tropospheric NO_2 columns derived by MAX-DOAS observations and the TROPOMI tropospheric NO_2 columns over Brussels on 28th of June 2019.

19.3 MAX-DOAS horizontal NO_2 distribution versus TROPOMI observations

19.3.1 Comparison results over the March 2018-February 2020 period

To compare the TROPOMI and MAX-DOAS tropospheric NO_2 columns, the following 5-step approach is used, similarly as in previous chapter:

1. Only MAX-DOAS horizontal profiles of tropospheric NO_2 VCDs retrieved around ($\pm$1 hour) TROPOMI overpass time are selected.

2. The time-coincident MAX-DOAS tropospheric NO_2 VCD horizontal grids from all the azimuthal directions are spatially averaged (i.e. one MAX-DOAS mean NO_2 VCD value per pixel) within the overlapping TROPOMI pixels.

3. To take into account the distance between each azimuthal direction crossing a TROPOMI pixel and the TROPOMI pixel center, the MAX-DOAS average is a weighted mean with the weighting depending on their relative direction with respect to the direction of the TROPOMI pixel center. Consequently, the weights are equal to the difference between 360^o and the azimuthal difference between MAX-DOAS grid and TROPOMI pixel central coordinates.

4. The horizontal profiles of MAX-DOAS NO_2 columns have a horizontal sampling of 0.5 km in every azimuthal direction. The coverage percentage is estimated as the ratio of the area covered by MAX-DOAS (i.e. number of coincident MAX-DOAS NO_2 VCDs considering that every MAX-DOAS horizontal grid has a spatial resolution of 0.5 x 0.5 km^2) inside each TROPOMI pixel to the total number of MAX-DOAS NO_2 VCDs that could fill-in the TROPOMI pixel.

5. TROPOMI and MAX-DOAS tropospheric NO_2 columns are compared, and the seasonally-averaged maps of those VCDs on the area covered by the TROPOMI pixels are created. To generate these maps, the ensemble of TROPOMI pixels recorded on 28 June 2019 is chosen as reference and TROPOMI pixels that coincide with this reference grid are averaged. The daily horizontal profiles of MAX-DOAS NO_2 columns are averaged on the daily TROPOMI grids and then, the reference grid is used to create the seasonally-averaged MAX-DOAS maps.

The seasonally and annually-averaged maps of TROPOMI and MAX-DOAS NO_2 VCDs are presented in Figure 19.5 and Figure 19.6. Only pixels including at least 20 comparison days are taken into account in the analysis. It is found that the locations of the NO_2 peaks and dips show a reasonably high degree of similarity between TROPOMI and MAX-DOAS during all seasons. The NO_2 peaks appear mainly above Brussels city center, the Drogenbos power plant (W direction) and the NW part of the Ring road, which are the main known emission sources, as mentioned earlier. These maps also indicate that the tropospheric NO_2 column over the Brussels area has a clear seasonal cycle, with a maximum during winter.

Figure 19.6 shows the annual relative biases (e.g. 100 x (TROPOMI - MAX-DOAS)/MAX-DOAS) per pixel. It is found that positive biases (i.e. TROPOMI larger than MAX-DOAS) are observed mainly in the pixels located away from the measurement site during all seasons, while negative biases are found close to the measurement site and in the Brussels city center.

The seasonal correlation plots for April 2018-February 2020 are displayed in Figure 19.7. When all pixels are included, without any TROPOMI pixels coverage percentage filtering on MAX-DOAS data, the highest correlation is found during spring (R=0.66), while lower correlations are reported in autumn, summer, and winter, with correlation coefficient values of 0.65, 0.65, and 0.58, respectively. It should be noted that during spring (2018 and 2019), the number of comparison points is smaller than for the other seasons, because TROPOMI data start from end of April 2018. During spring, the slope value is equal to 0.90, while during winter, summer, and autumn, the slope values are smaller (0.64 0.56, and 0.64, respectively), which means that TROPOMI underestimates MAX-DOAS measurements up to 50 %. A similar underestimation has been reported in several studies (Judd et al., 2020; Dimitropoulou et al., 2020; Ialongo et al., 2020; Verhoelst et al., 2021; Tack et al., 2021). When seasonally-averaged TROPOMI and MAX-DOAS pixels (the pixels shown in Figure 19.5) are compared one-by-one (see SEAS in Figure 19.7), both correlation coefficient (R in the range of 0.57-0.93) and slope values (s in the range of 0.65-0.94) improve considerably.

In a second step, the impact of the spatial sampling is investigated. Generally, a varying number of MAX-DOAS NO_2 columns cover each TROPOMI pixel. The coverage percentage is estimated as the ratio of the covered area by MAX-DOAS (i.e. number of coincident MAX-DOAS NO_2 VCDs) inside each TROPOMI pixel to the total number of MAX-DOAS NO_2 VCDs that could fill-in the TROPOMI pixel. When selecting only TROPOMI pixels covered by at least a given percentage of MAX-DOAS grids (10% and 20%), it is found that the correlation between both datasets improves for all seasons, except summer for a coverage equal and greater than 20%. The most significant improvement is observed during spring. The correlation coefficient value is equal to 0.83 (instead of 0.66) when taking into account TROPOMI pixels covered more than 20% by MAX-DOAS retrievals. Despite the better agreement in terms of correlation coefficient, TROPOMI columns are still 30 % lower than MAX-DOAS measurements, in line with previously published studies.

The seasonal regression analysis parameters between TROPOMI and dual-scan MAX-DOAS measurements derived in the present study are compared to the same parameters presented in Dimitropoulou et al. (2020). Both studies make use of the dual-scan MAX-DOAS instrument in Uccle. In addition to the different approach (i.e. the retrieval of NO_2 horizontal profiles), in the present study, almost two years of measurements are used, while in Dimitropoulou et al. (2020), only one year is exploited for the TROPOMI validation. In Table 19.1, for the present study, only one year of measurements are used to have a comparable time coverage for both studies. As presented in Table 19.1, here, the largest slope value is found in spring, while in Dimitropoulou et al. (2020), in winter. The season in which the highest correlation coefficient is obtained differs between both studies (here, in spring, in autumn in Dimitropoulou et al., 2020). The main advantage of the new approach is the larger number of comparison points between TROPOMI and MAX-DOAS leading to significantly more reliable statistics. In the present study, the deviation of the comparison points from the fitted regression line is increased mainly because of the uncertainties in the horizontal inversion approach. The scatter increase is reflected in the correlation coefficient values, which are smaller for all seasons, except winter. Regarding the slope value, it is larger in spring and summer, and is smaller in autumn and winter. Overall, our investigation about the spatial sampling lead to the following three important findings:

1. The dual-scan multi-wavelength approach allows a better identification of the main emissions sources in urban

regions, in agreement with the spatial allocation of the main emission sources observed by APEX and TROPOMI.

2. The characterization of the NO_2 concentration horizontal field using the dual scan multi-wavelength approach results in obtaining larger slope values between TROPOMI and MAX-DOAS observations. The high spatial resolution of TROPOMI requires ground-based measurement that can provide information about the horizontal distribution of tropospheric NO_2 columns in urban regions.

3. Even for a better spatial sampling between TROPOMI and ground-based observations, TROPOMI still underestimates the ground-based measurements (see Figure 19.6). Therefore, this is an additional indication that this underestimation is caused by other factors.

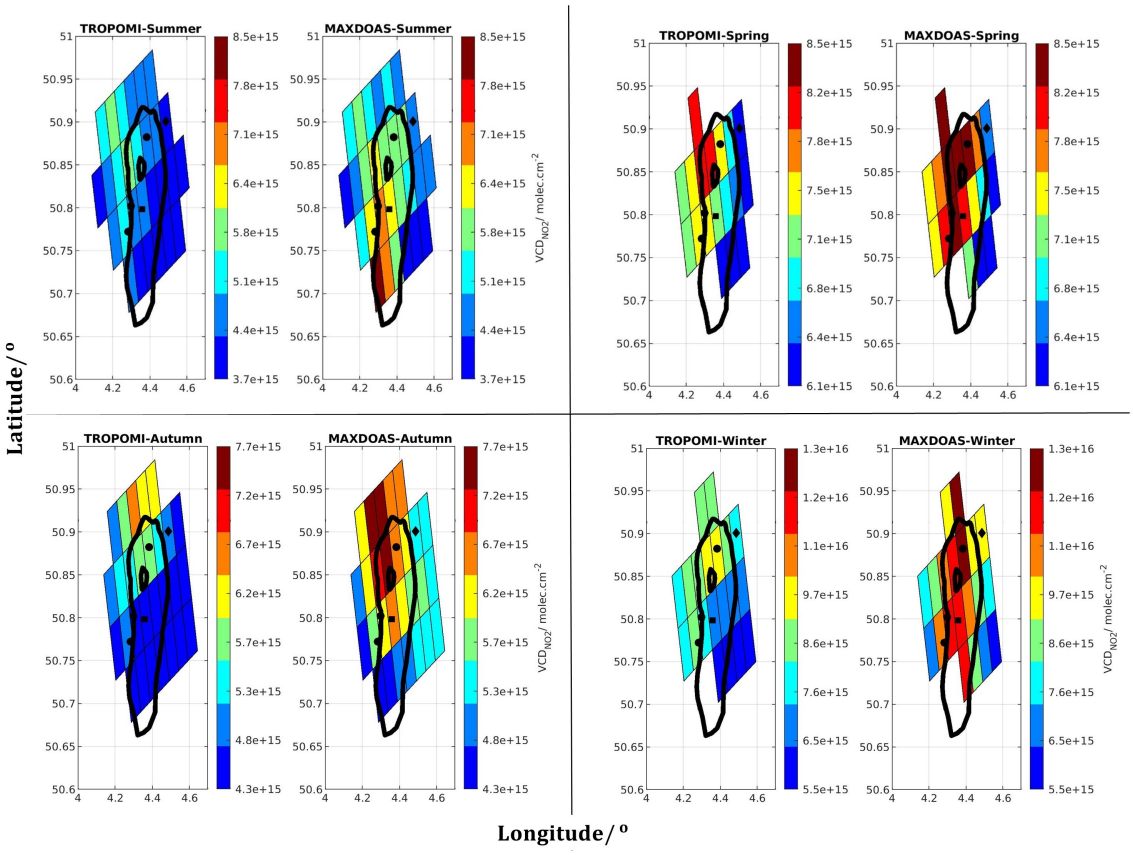

Figure 19.5: Seasonal tropospheric NO_2 VCD grids (TROPOMI grids) as retrieved over Brussels by the TROPOMI and MAX-DOAS instruments. The black square shows the MAX-DOAS position, the black polygon the National Airport, the black dots the NO_2 hotspots, and the black line represents the Brussels Ring motorway.

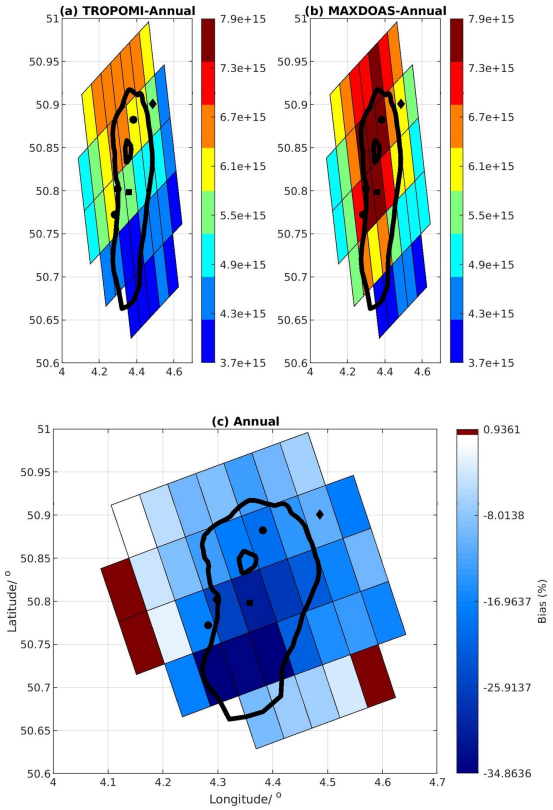

Figure 19.6: Annual (e.g. based over the two years of observations) tropospheric NO_2 VCD grids (TROPOMI grids) as retrieved over Brussels by the (a) TROPOMI and (b) MAX-DOAS instruments. (c) Annual bias between tropospheric NO_2 VCD as observed by TROPOMI and MAX-DOAS instruments (the negative values are shown with blue color, zero with white, and positive values with red). The black square shows the MAX-DOAS instrument location, the black polygon the National Airport, the black dots the NO_2 hotspots, and the black line represents the Brussels Ring road.

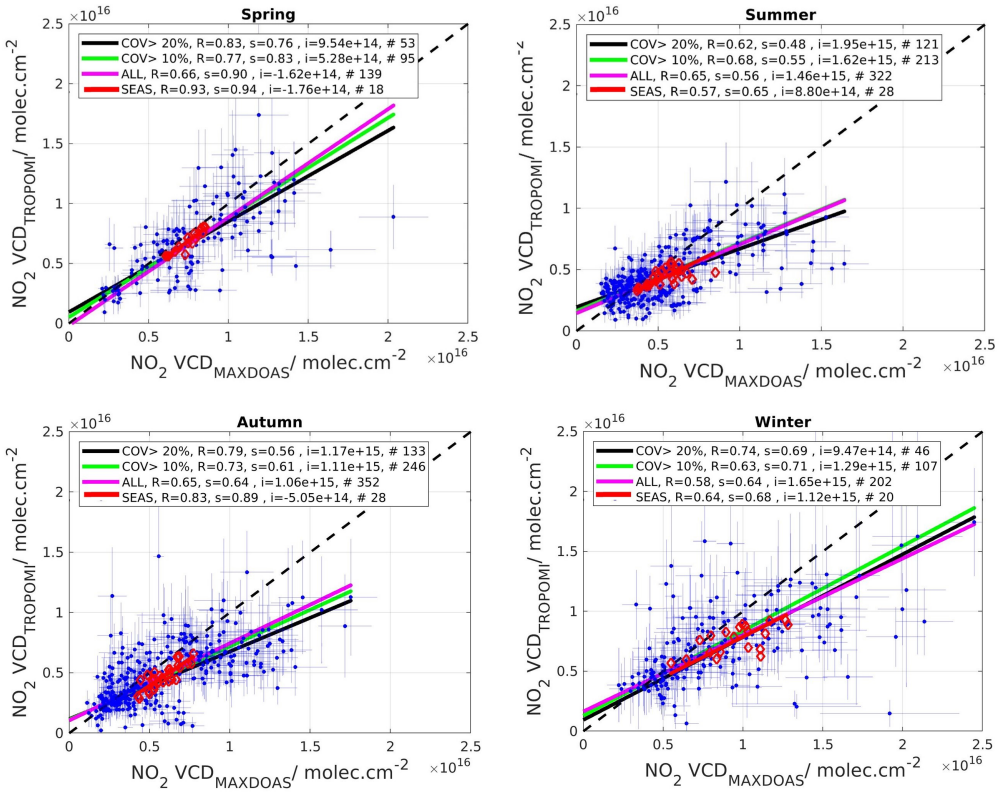

Figure 19.7: Seasonal scatter plots of tropospheric NO_2 columns derived from the dual-scan MAX-DOAS and TROPOMI measurements over Brussels. Magenta line: Regression analysis results when all the MAX-DOAS and TROPOMI pixels are included in the comparison. Green and black lines: Regression analysis results when TROPOMI pixels covered (i.e. COV) by more than 10 and 20 % of the horizontal profiles of MAX-DOAS NO_2 columns are included in the comparison. Red circles: Seasonal average analysis generated by the pixels in Figure 19.5.

19.3.2 Investigation of the a priori NO_2 profile shape and clouds in TROPOMI NO_2 retrievals

Three additional comparisons have been conducted in this study. First, a TROPOMI tropospheric NO_2 column product with an improved FRESCO-S cloud retrieval has been tested. As discussed in Dimitropoulou et al. (2020), clouds can significantly affect tropospheric NO_2 VCD retrievals from satellite observations. The dataset is available for four different periods in 2018 - 2019. Figure 19.8 shows that the slope value increases by about 56% (equal to 0.53 instead of 0.34 for the baseline product), as well as the correlation coefficient between both datasets (R equal to 0.68 instead of 0.45). This is in agreement with the TROPOMI Routine Operations Consolidated Validation Report (ROCVR; https://mpc-vdaf.tropomi.eu/), where the use of the improved FRESCO-wide resulted in a bias reduction with respect to ground-based NO_2 data.

Secondly, a new TROPOMI data product covering the November 2018 to February 2020 period is used. In this product, the coarse TM5-MP a priori NO_2 profiles are replaced by NO_2 profile shapes from the CAMS regional CTM ensemble at a spatial resolution of 0.1^ox0.1^o (Douros et al., in preparation; Ialongo et al., 2019; Tack et al., 2021). As can be seen in Figure 19.8, using a spatially finer a priori NO_2 vertical profile improves slightly the slope value, which is equal to 0.77 (instead of 0.75 for the baseline TROPOMI product). This represents an increase of the slope by about 3%. This finding indicates that part of the TROPOMI underestimation of tropospheric NO_2 columns is caused by inadequate a priori profiles in the TROPOMI retrievals for urban conditions. On the other hand, the fact that the slope value is still lower than unity, even when CAMS regional a priori profiles are used, indicate that other factors contribute to the TROPOMI underestimation or that CAMS profiles are still sub-optimal, as suggested by results obtained when applying MAX-DOAS profiles to TROPOMI (see below).

Finally, the impact of the a priori profile in the TROPOMI NO_2 retrieval is investigated using MAX-DOAS profile data. For this test, TROPOMI NO_2 columns are recalculated, similarly as in Dimitropoulou et al. (2020), using daily median MAX-DOAS vertical profiles derived in the main azimuthal direction by applying the MMF inversion algorithm. Those TROPOMI NO_2 columns are then compared to the horizontally-resolved MAX-DOAS data, as in section 19. Figure 19.9 presents the comparison results per season. When comparing it with Figure 19.7, we find that the change in the NO_2 vertical profile shape improves the slope value in the comparison with ground-based observations. Except for winter, the slopes are largely improved (slopes in the 0.56 - 1.11 range) due to an increase of the recalculated TROPOMI columns. This result confirms once again that the a priori profile in the TROPOMI retrieval is a key player in the TROPOMI underestimation of tropospheric NO_2 columns in urban conditions, as already stated in previous studies (see e.g. Dimitropoulou et al., 2020; Ialongo et al., 2019; Tack et al., 2021). The present study suggests that in urban conditions, daily median MAX-DOAS vertical profiles are more suitable than NO_2 profile shapes from the CAMS regional CTM ensemble in order to be applied as a priori information in the TROPOMI retrieval.

Table 19.1: Summary of the regression analysis parameters (e.g. correlation coefficient (R) and slope (s)) and the number of data points (N) derived in the present study during only one year of observations and in Dimitropoulou et al. (2020).

Season	Spring	Summer	Autumn	Winter
R	0.66	0.60	0.57	0.62
R (seasonal)	0.93	0.88	0.46	0.75
R (Dimitropoulou et al., 2020)	0.69	0.77	0.85	0.60
s	0.90	0.76	0.56	0.60
s (seasonal)	0.94	0.87	0.74	0.70
s (Dimitropoulou et al., 2020)	0.47	0.58	0.61	0.81
N	139	247	106	92
N (Dimitropoulou et al., 2020)	16	58	36	13

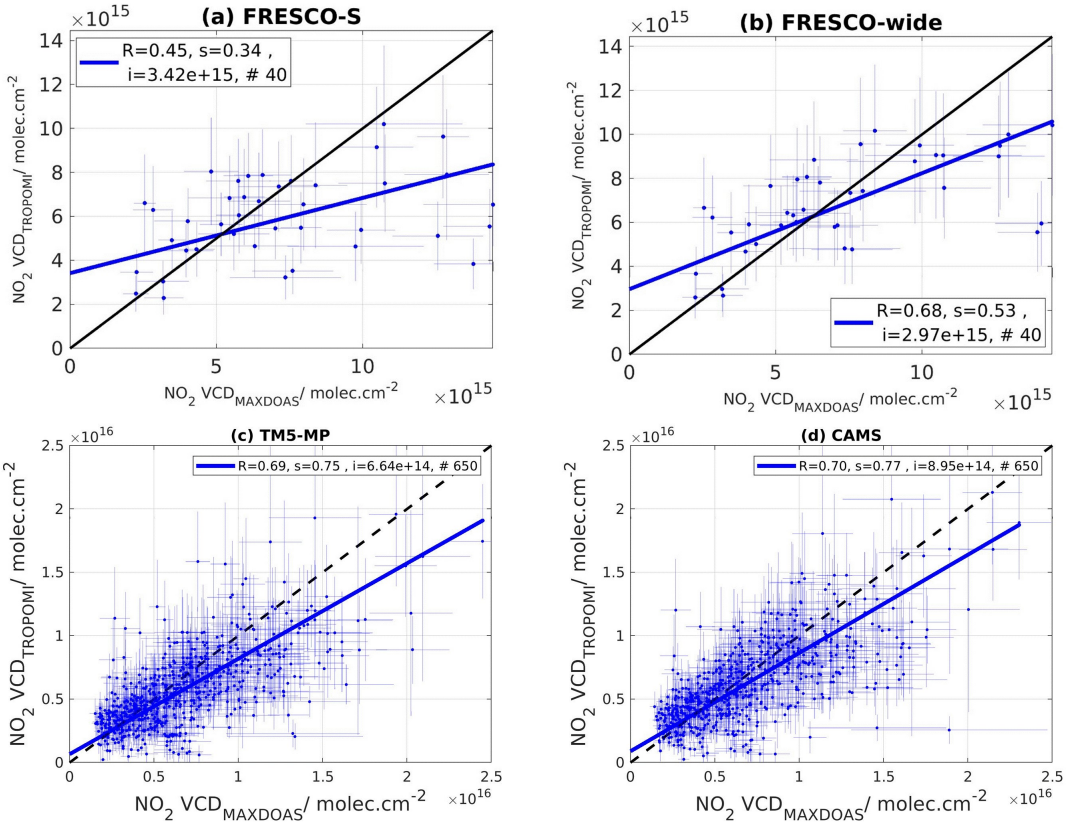

Figure 19.8: Scatter plots between the tropospheric NO_2 columns derived from the dual-scan MAX-DOAS instrument and the TROPOMI pixels over Brussels. The left plots are for the baseline TROPOMI dataset ((a) and (c) panels), while the right plots correspond to two new versions of TROPOMI datasets ((b): improved FRESCO-S cloud product; (d) NO_2 a priori profiles from the CAMS regional CTM ensemble).

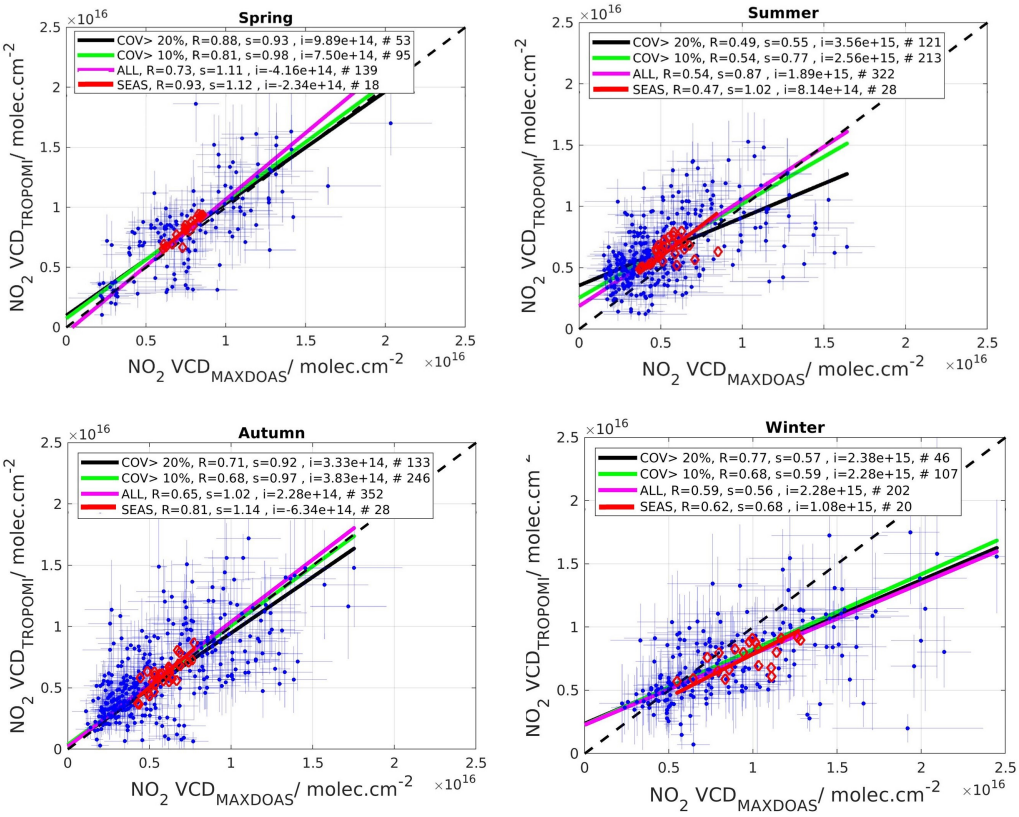

Figure 19.9: Seasonal scatter plots between the horizontally-averaged MAX-DOAS NO_2 VCDs and TROPOMI NO_2 columns recalculated using median daily MAX-DOAS vertical profiles as a priori information.

Chapter 20

Conclusions

Two years (March 2018 to February 2020) of dual-scan MAX-DOAS measurements in Uccle (urban background site located in the south of the Brussels-Capital Region) were used to develop a new strategy for the retrieval of near-surface NO_2 concentrations and aerosol extinction horizontal profiles. A full dual-scan measurement is composed of one vertical scan at a fixed azimuthal direction pointing towards the city center and horizontal scans in ten azimuthal directions at a fixed low elevation angle (2^o).

The first step of this new retrieval strategy is to analyze measured radiance spectra in six different fitting windows. This provides O_4 and NO_2 dSCDs at the following six wavelengths: 343 nm, 360 nm, 380 nm, 447 nm, 477 nm and 530 nm. Then, information about the vertical extent of NO_2 in the troposphere (MLH_{NO_2}) is derived from profile retrievals in the main azimuthal direction performed using the OEM-based MMF algorithm. In the third step, a new parameterization technique is applied, with MLH_{NO_2}, measured O_4 dSCDs, and measurement geometry being used as input parameters to retrieve the horizontal sensitivity of NO_2 and, consequently, the NO_2 near-surface concentrations and VCDs, and near-surface aerosol extinction in all the azimuthal directions for the six different wavelengths. Compared to the method presented in Dimitropoulou et al., (2020), the new retrieval method offers the possibility of the direct determination of L_{NO_2}, and near-surface aerosol extinction based on the measured O_4 dSCDs.

The retrieved dual-scan NO_2 near-surface concentrations and VCDs are verified via comparisons to the MMF NO_2 vertical profiles in the main azimuthal directions and in three additional azimuthal directions. A good overall agreement is found for the two comparisons during the two years of measurements. The dependence of the horizontal sensitivity on the wavelength is then used to develop a new OEM-based horizontal distribution inversion approach. Considering a horizontal box model, horizontal NO_2 and aerosol extinction profiles are retrieved in an output horizontal grid of 500m thickness starting from the instrument to each of the measurement maximum horizontal representative distance.

The daily variability of NO_2 horizontal profiles in all the azimuthal directions provides information about the location of the NO_2 hotspots in the Brussels-Capital Region and how the plumes are transported. Similarly, the NO_2 horizontal profiles' seasonal variability over March 2018-February 2020 reveals that the NO_2 hotspots are mainly found above the Brussels city-center, the Drogenbos power plant and the NW part of the Ring road during all seasons.

On 28 June 2019, airborne measurements (APEX) of NO_2 were performed over Brussels. The MAX-DOAS NO_2 VCD horizontal profiles are compared to APEX, mobile car-DOAS (i.e. AEROMOBIL), and TROPOMI measurements, and a good overall agreement is found between the different data sets for this day.

In the second part of the study, MAX-DOAS retrievals are compared to TROPOMI tropospheric NO_2 observations over the March 2018- February 2020 period. The comparison of seasonal maps shows a good overall agreement between both datasets as to the NO_2 horizontal distribution over the Brussels area. This agreement improves systematically when only TROPOMI pixels covered by a minimum of 20% of MAX-DOAS grid cells are compared,

showing the benefit of ground-based measurements at high horizontal resolution for the validation of high-resolution space-borne air-quality measurements. Results also show that during all seasons, TROPOMI underestimates the MAX-DOAS tropospheric NO_2 columns. The role of the a priori NO_2 profile shape in the TROPOMI retrievals has been investigated and TROPOMI tropospheric NO_2 columns are recalculated with the MAX-DOAS vertical profiles. We show that the knowledge of the NO_2 horizontal distribution derived by the MAX-DOAS measurements combined with a more adequate a priori profile in TROPOMI retrievals leads to a much better agreement between satellite and ground-based data.

To conclude, our study presents a new horizontal distribution inversion approach for NO_2 and aerosols developed by using dual-scan multi-wavelength MAX-DOAS measurements over an urban area. This approach provides a better characterization of the horizontal distribution of an important urban pollutant, NO_2, which leads to an improved agreement between satellite and MAX-DOAS measurements in moderate to highly polluted conditions. Based on our study, further modifications of the measurement mode aiming at a better sampling of the vertical and horizontal NO_2 distribution could be implemented and investigated. For instance, performing vertical scans in several azimuthal directions throughout the day and/or horizontal scans in more than ten azimuthal directions could further improve our knowledge about the tropospheric NO_2 spatial variability in urban regions, and therefore the satellite validation results in those conditions.

Part V

Improved TROPOMI HCHO column validation using dual-scan MAX-DOAS retrievals

Formaldehyde (HCHO) is the most abundant aldehyde in the atmosphere. HCHO ground-based Multi-Axis Differential Optical Absorption Spectroscopy (MAX-DOAS) measurements have been performed in Uccle, Belgium during one year and a half from May 2018 to December 2019. The MAX-DOAS instrument was measuring in a dual-scan viewing mode consisting of one scan in elevation in a main azimuthal direction followed by an azimuth scan at a fixed low elevation angle. Aerosols and HCHO vertical profiles are retrieved in the main azimuthal direction by applying a profile inversion algorithm based on the Optimal Estimation Method. With the aid of these vertical profiles and the dual-scan MAX-DOAS retrieval strategy presented in Part III, near-surface HCHO concentrations and columns are retrieved in all directions of the azimuth scan. This ground-based dataset is then used for two main purposes: (1) the characterization of the HCHO horizontal distribution around the station and (2) the validation of HCHO columns measured by the TROPOMI satellite instrument over the Brussels area. This study reveals that (1) the HCHO horizontal distribution differs per season as expected and (2) the use of dual-scan MAX-DOAS measurements improves the TROPOMI HCHO column validation results. [1]

[1]This chapter is based on: Dimitropoulou, E., Hendrick, F., Friedrich, M. M., Tack, F., Pinardi, G., Merlaud, A., Fayt, C., Hermans, C., and Van Roozendael, M. (2021, July). Improved TROPOMI HCHO Column Validation Using Dual-Scan MAX-DOAS Retrievals. In 2021 IEEE International Geoscience and Remote Sensing Symposium IGARSS (pp. 8026-8029). IEEE.

Chapter 21

Part V: Objectives

The main motivation of Part V is to investigate whether MAX-DOAS HCHO measurements performed in several azimuthal directions can improve the validation of the TROPOMI HCHO product (De Smedt et al., 2018,0) in urban conditions. To this aim, we use MAX-DOAS and TROPOMI observations over Uccle (Brussels-Capital Region, Belgium) as a case study.

Chapter 22

Retrieval methodologies of HCHO

22.1 DOAS analysis

The radiance spectra measured in the complete dual-scan are analyzed with the QDOAS spectral fitting software Fayt et al. (2011). The primary product of this analysis is the HCHO differential slant column density (dSCD), which is the difference between the effective light-path integrated HCHO concentration and the amount of the absorber (HCHO) in a measured reference spectrum. For tropospheric studies, a zenith spectrum (different for each scan) is chosen as a reference in order to remove the contribution of the stratosphere in the so-called off-axis dSCDs, i.e. the dSCDs corresponding to the different elevation angles above the horizon. In the present study, the zenith spectrum of each scan is used as reference.

HCHO dSCDs are retrieved in the 336-359 nm spectral range using the Meller and Moortgat (2000) HCHO cross section Meller and Moortgat (2000). This wavelength region is chosen because it contains three strong HCHO absorption bands.

22.2 Aerosol and HCHO vertical profile retrievals

For each MAX-DOAS elevation scan in the main azimuthal direction, the aerosol extinction coefficient and HCHO vertical profiles are retrieved by applying the Mexican MAX-DOAS Fit (MMF) inversion algorithm to the measured oxygen complex (O_4) and HCHO dSCDs (Friedrich et al., 2019). The aerosol extinction profile of each vertical scan derived from the O_4 dSCDs is used as input to derive the HCHO vertical profile, as the aerosol content and vertical distribution provide information about the effective light-path in the probed atmosphere. Each aerosol and HCHO retrieval is quality checked based on the degrees of freedom (DOFs), the difference between the measured and simulated O_4 and HCHO dSCDs and the aerosol optical density (AOD) value (Dimitropoulou et al., 2018).

As it will be presented in the next sections, the HCHO vertical profiles are also used to estimate the Mixing Layer Height (MLH) of HCHO, which is an effective height defining the atmospheric layer in which HCHO is expected to be uniformly distributed.

22.3 Dual-scan HCHO MAX-DOAS retrieval in Uccle

The dual-scan HCHO MAX-DOAS retrieval is an adaptation of the dual-scan MAX-DOAS retrieval, which was successfully applied to NO_2 retrieval in Uccle, Belgium (Dimitropoulou et al., 2020). It consists in the conversion of the measured trace gas dSCDs at 2^o elevation into (1) near-surface trace gas box-averaged Volume Mixing Ratios (VMRs) from the surface to the MLH and (2) trace gas vertical column densities (VCDs) (Sinreich et al., 2013).

The measured HCHO dSCDs in one low elevation angle provides information on the near-surface concentration. As mentioned before, the measured dSCDs is the light-path integrated concentration of HCHO. Consequently, the knowledge of the light-path's length is crucial to derive the near-surface HCHO VMRs. O_4 can be used as a tracer for the effective light-path in the atmosphere: as its concentration is well-known (it varies with the square of O_2 concentration), its variation can be attributed to changes in the light-path due to the presence of particles like aerosols and clouds.

However, the direct use of the O_4 light-path's in the HCHO retrieval is not possible under moderate to high pollution conditions, such as those in Brussels, because the profile shapes of O_4 and HCHO are not the same. For this reason, radiative transfer model (RTM) simulations are necessary in order to estimate a unitless correction factor, which will account for these profile shape differences (see Dimitropoulou et al., 2020). Those simulations are performed for eight different MLH values of aerosols and HCHO in the range of 500-2000 m and different measurement viewing geometries (Solar Zenith Angle (SZA), Relative Azimuth Angle (RAA) and the corresponding elevation angle of 2^o). For every MAX-DOAS measurement, one value of the correction factor is given according to its viewing geometry and MLH value during the measurement. The MLH is derived from the HCHO vertical profiles in the main azimuthal direction and is defined as the ratio of the HCHO VCD to the near-surface concentration of HCHO (Dimitropoulou et al., 2020).

The verification of the dual-scan HCHO MAX-DOAS retrieval is conducted by comparing the retrieved dual-scan HCHO VMR and VCD to the same quantities as retrieved by the MMF inversion algorithm in the main azimuthal direction. Both methods are highly correlated with a correlation coefficient equal to 0.98 for both HCHO VMRs and VCDs.

Chapter 23

Results

23.1 Dual-scan HCHO seasonal variation

The seasonal variation of the MAX-DOAS HCHO VCDs for the period May 2018-December 2019 is presented in Figure 23.1. Those VCDs correspond to seasonal mean HCHO values in every azimuth direction. It should be noted that only HCHO VCDs measured around TROPOMI overpass time (±1hour) have been considered. The length of each line corresponds to the seasonally mean HCHO representative horizontal distance, as estimated by the dual-scan HCHO MAX-DOAS retrieval (see Dimitropoulou et al., 2020). Note that the range of the color-coding differs per season for better visualization purpose.

The HCHO VCDs have a clear seasonal cycle, with maximum values during summer and a minimum during winter. To investigate the temperature dependence of HCHO VCDs, HCHO VCDs are plotted against surface temperature data, as measured by the BIRA-IASB meteorological station in Uccle (Figure 23.2). The increase of temperature during summer causes HCHO formation from isoprene, which is mostly emitted at forested areas under high temperature and radiation conditions (Dimitropoulou et al., 2018). As presented in Figure 23.2, higher temperature values are associated with higher HCHO VCDs. The maximum HCHO VCDs during summer is attributed to the temperature-dependent production of HCHO from biogenic sources, which is consistent with the location of the VCD peak towards the Soignes forest, a large forested area in the East/South-East of Brussels (Figure 23.1).

In order to investigate the role of the different wind regimes in the observed HCHO VCDs per season, the retrieved HCHO VCDs in the main azimuthal direction are classified in different groups according to the wind direction. During summer, the maximum HCHO VCDs are retrieved when the wind is blowing from the Southeast direction (only forested area; free from important anthropogenic sources), which indicates that biogenic sources dominate the HCHO production. During winter, the wind direction related to the maximum HCHO VCDs is N/NE, which suggests that anthropogenic sources provide a significant contribution to the HCHO production given the location of anthropogenic sources (city center, industrial area, and airport) in this direction.

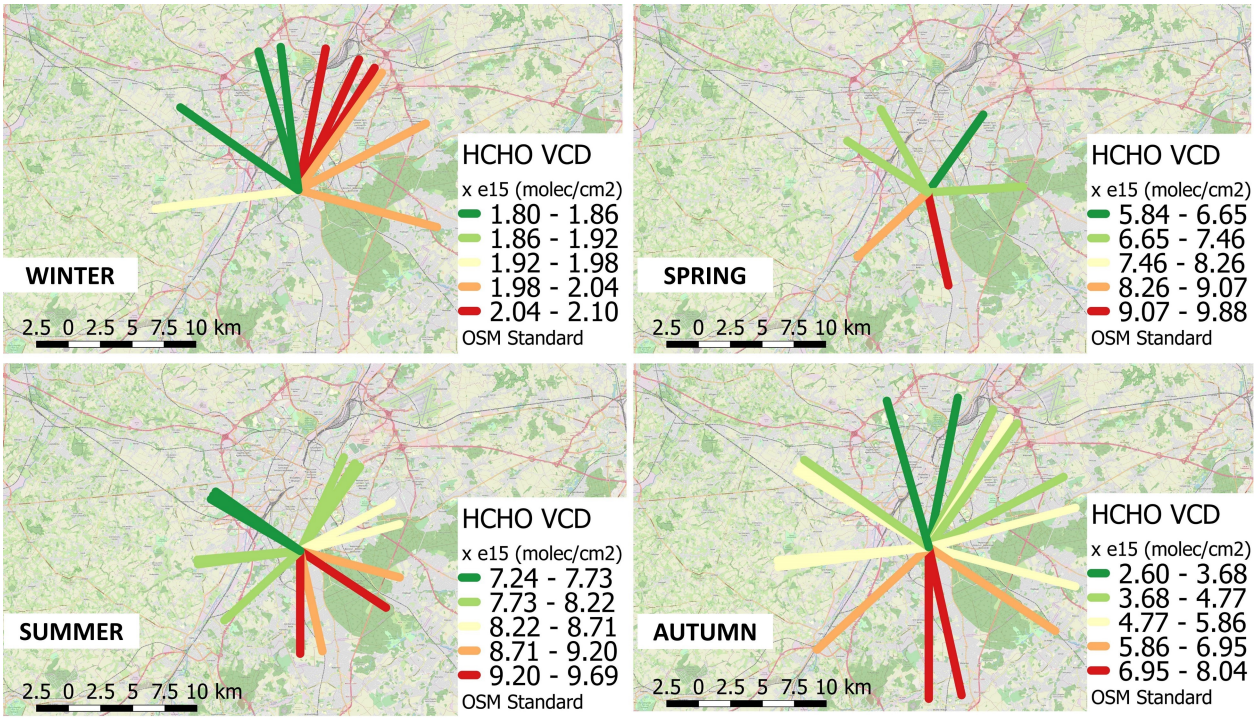

Figure 23.1: Seasonally mean HCHO VCDs in each azimuthal viewing direction. © OpenStreetMap contributors 2021. Distributed under a Creative Commons BY-SA License.

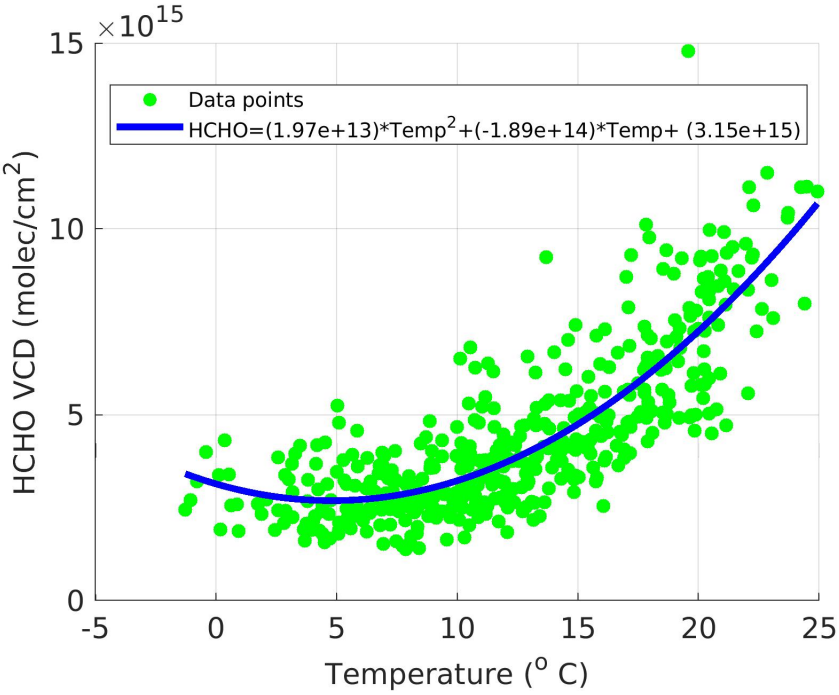

Figure 23.2: Scatter plot of surface temperature data and MAX-DOAS HCHO VCDs.

23.2 Validation of TROPOMI HCHO columns

23.2.1 Use of one MAX-DOAS azimuthal direction measurements

To investigate if the dual-scan MAX-DOAS HCHO measurements improve the TROPOMI HCHO column validation results in urban conditions, a first comparison between the MAX-DOAS HCHO VCDs derived in the main azimuthal direction by applying the MMF inversion algorithm, and daily-mean TROPOMI HCHO columns is done. Pixels in a radius of 20km around the measurement site are averaged and compared to mean MAX-DOAS HCHO VCDs extracted within ± 1 hour of the TROPOMI overpass time (around 13h30).

Figure 23.3 presents the comparison results between satellite and 1-D ground-based data during one year and a half. The dataset is highly correlated (R ± probable error = 0.72 ± 0.02) and the slope value (± its uncertainty) is equal to 0.76 (± 0.05). The median relative bias between satellite and 1-D ground-based data is - 6 %.

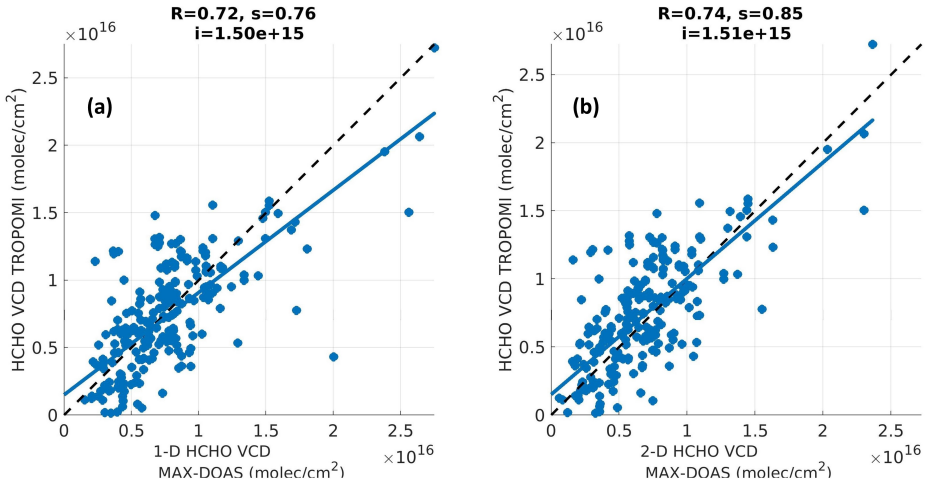

Figure 23.3: Scatter plots between TROPOMI HCHO columns and (a) 1-D MAX-DOAS observations and (b) dual-scan MAX-DOAS observations during one year and a half.

23.2.2 Use of dual-scan MAX-DOAS measurements

Here, the dual-scan MAX-DOAS HCHO VCDs are compared with TROPOMI HCHO columns. HCHO VCDs in every MAX-DOAS azimuthal direction around TROPOMI overpass time (± 1 hour) are averaged and compared to daily-mean TROPOMI HCHO columns (inside a radius of 20km).

Figure 23.3 shows that the agreement between satellite and MAX-DOAS improved when using the dual-scan dataset instead of the MAX-DOAS observations in the main azimuthal direction, with a slope value (± its uncertainty) of 0.85 (± 0.05) instead of 0.76 (± 0.05). The correlation coefficient value (0.74 ± 0.02 instead of 0.72 ± 0.02) is slightly improved. The median relative bias between satellite and 2-D ground-based data is +7 %, which is slightly higher than the median relative bias in section 23.2.1 (in absolute value: 7% instead of 6%). This finding indicates that the amelioration of the spatial coincidence between ground-based and TROPOMI observations improves the agreement between both HCHO VCD column data sets in terms of correlation coefficient and slope values, but increases the bias of the comparison.

Chapter 24

Conclusions

In the present study, one year and a half (May 2018-December 2019) of MAX-DOAS measurements is used to validate TROPOMI HCHO columns above Brussels.

MAX-DOAS HCHO VCDs are retrieved in several azimuthal directions by applying the dual-scan MAX-DOAS retrieval strategy. The adopted experimental set-up allows to better characterize the HCHO horizontal distribution and its variability. Higher HCHO VCDs are observed during summer, because of the high temperature dependency of HCHO. Anthropogenic sources are the main contributors of HCHO emissions during cold months, while during warmer months HCHO is released in the troposphere from both anthropogenic and biogenic sources, which leads to higher HCHO VCDs.

The 1-D and dual-scan MAX-DOAS HCHO VCDs are compared with TROPOMI HCHO columns above the Brussels-Capital Region during the period May 2018-December 2019. The two comparison exercises reveal that the use of the dual-scan MAX-DOAS HCHO measurements improves the TROPOMI HCHO column validation results under urban conditions.

Future steps include a detailed investigation of the remaining TROPOMI HCHO columns underestimation compared to ground-based MAX-DOAS measurements and more precisely, the role of the a priori HCHO profile shape used in the TROPOMI HCHO column retrieval.

General conclusions

This thesis focuses on the retrieval of the horizontal distributions of NO_2, HCHO, and aerosols near-surface concentrations and vertical columns from urban ground-based MAX-DOAS measurements in support to the TROPOMI/S5P air quality satellite validation. Two years (from March 2018 to February 2020) of dual-scan MAX-DOAS measurements performed in Uccle, which is an urban background site located in the south of the Brussels-Capital Region, have been used for this purpose.

The primary objectives given in the General Introduction are again presented here, together with the corresponding main progress, results and outcomes achieved during this thesis:

- **Optimization of the MAX-DOAS instrument's operation mode to enable the retrieval of both vertical and horizontal distribution of NO_2, HCHO, and aerosols around the measurement site with a time resolution representative of these trace gases' and aerosols' natural variabilities.**

  The retrieval of the vertical and horizontal distributions of NO_2, HCHO, and aerosols has been driven by the trade-off between the acquisition time of the spectrum and the horizontal coverage and representativeness of the measurements. To detect weak absorbers, such as HCHO, the acquisition time of the spectrum should be large enough to ensure that the measurements are not too noisy. At the same time, the acquisition time has to be small to complete a full measurement scan at a time resolution appropriate for the detection and monitoring of the NO_2, HCHO, and aerosols' vertical and horizontal natural variabilities. The absence of obstacle in any of the chosen pointing directions should be also ensured.

  Based on the above limitations and trade-off, our investigations have led to the following optimal MAX-DOAS instrument's operation mode: one complete measurement dual-scan is composed of two different sub-modes. First, one azimuthal direction, pointing towards the city center and the national airport, has been selected to perform a vertical scan covering nine different elevation angles from the horizon to the zenith. Secondly, an azimuthal scan is performed in nine azimuthal directions (mainly located in the N, NE, and NW directions) at one low elevation angle (2^o above the horizon). The choice of such a low elevation angle is crucial for the retrieval of near-surface concentrations.

  Onward July 3, 2019, elevation scans have been performed in three additional azimuthal directions once per day (around noon) to complement the already existing measurement set-up. These additional azimuthal directions are the following: 11^o, 105^o, and 262.5^o clockwise with respect to North.

  By adopting this measurement set-up, the retrieval of information about the vertical distribution of NO_2, HCHO, and aerosols is done in one azimuthal direction and the horizontal distributions of the near-surface concentration and vertical column of these pollutants is retrieved from a set of ten different azimuthal directions.

- **Development of new strategies for retrieving vertical and horizontal NO_2 and HCHO near-surface concentrations and tropospheric vertical columns from the collected ground-based multi-azimuthal MAX-DOAS measurements at various wavelengths**

  New retrieval strategies for NO_2 and HCHO near-surface concentrations inside the NO_2 mixing layer height (MLH_{NO_2}) and tropospheric columns from a complete MAX-DOAS dual-scan is developed. In a first step,

two wavelengths have been used, one in the UV (360 nm) and one in the Visible (477 nm) spectral ranges. This first retrieval strategy is an adaptation of the parameterization technique proposed by Sinreich et al. (2013). It consists of a conversion of NO_2, and HCHO dSCDs measured at one low elevation angle (here, the 2^o elevation angle) to near-surface box-averaged mixing ratios and tropospheric columns. As proposed by Sinreich et al. (2013) and Ortega et al. (2015), the use of a realistic MLH_{NO_2} daily variation is crucial for the successful application of the parameterization technique. In the present thesis, we estimated the MLH_{NO_2} by using the vertical NO_2 profiles retrieved using the OEM-technique in the main azimuthal direction. Despite its simplicity, our approach provides more robust estimates of the MLH_{NO_2}, which is an improvement over more empirical approaches previously published. However, an important limitation of this technique is the presence of sufficient aerosols inside the MLH_{NO_2} to ensure that the near-surface NO_2 and HCHO concentration can be approximated by near-surface NO_2 and HCHO box-averaged concentration. Additionally, the use of the vertical distribution of trace gases from one azimuthal direction is based on two assumptions: (1) the homogeneous distribution of NO_2 inside the MLH_{NO_2} and (2) an homogeneous MLH_{NO_2} around the measurement site.

With the exploitation of dual-scan MAX-DOAS NO_2 concentrations and VCDs at two wavelengths, and by using the fact that the horizontal sensitivity of MAX-DOAS measurements depends on the wavelength (the largest the wavelength, the longest the horizontal sensitivity range), the location of the NO_2 concentration and VCD peaks along every azimuthal direction is determined. Generally, maximum NO_2 concentrations are detected during winter in the N, NE, and NW directions, where the city center, the national airport, and the Drogenbos power plant are located. Additionally, NO_2 concentration peaks are associated with the wind blowing from the NE direction. On the contrary, maximum HCHO VCDs are retrieved during summer in the SE direction, where a big forested area is located, indicating the significant contribution of biogenic sources to HCHO emissions in Brussels.

In a second step, the above dual-scan MAX-DOAS inversion algorithm is extended to 6 wavelengths (343 nm, 360 nm, 380 nm, 447 nm, 477 nm, and 530 nm) instead of 2. A new dual-scan multi-wavelength MAX-DOAS parameterization technique is therefore developed where the NO_2 near-surface concentrations and VCDs are retrieved in all the azimuthal directions and for the six selected wavelengths as a function of the MLH_{NO_2}, measured O_4 dSCDs, and measurement geometry. More precisely, for every combination of input parameters, which are the elevation angle, solar zenith angle, relative azimuth angle, AOD, MLH_{NO_2}, NO_2 concentration, and wavelength, a polynomial fit of the NO_2's horizontal sensitivity (L_{NO_2}) as a function of simulated O_4 dSCDs is applied. For each measured O_4 dSCD, a L_{NO_2} value can be therefore estimated by this approach. It should be noted that this new dual-scan parameterization technique enables also the retrieval of the near-surface aerosol extinction.

The wavelength dependency of the horizontal sensitivity is then exploited for developing a new OEM-based horizontal distribution inversion algorithm. By using the six near-surface NO_2 concentrations and aerosol extinction values per azimuthal direction, the NO_2 near-surface concentration and vertical column and aerosol extinction horizontal profiles are retrieved on an output grid of 500 m thickness extending from the instrument's location over a distance corresponding to the maximum horizontal sensitivity range of the measurements, and this, in each azimuthal direction. This novel algorithm enables a more precise allocation of NO_2 peaks around the measurement site than the two-wavelength-based method developed in the first stage of the thesis. Based on these retrieval results, maps of the NO_2 horizontal field have been constructed from ground-based MAX-DOAS measurements for the first time.

- **Validation of the retrieved NO_2 concentration and column horizontal fields by comparing them with collected ancillary data, such as in-situ, airborne and car-doas observations**

  The dual-scan parameterized NO_2 concentrations and VCDs are validated using the following ancillary data: (1) MAX-DOAS OEM-based vertical profiles, and (2) in-situ NO_2 concentrations. Overall, a reasonably good agreement is found between the MAX-DOAS and ancillary data in the two verification tests. In the case of

HCHO, OEM-based vertical profiles are also used to verify the parameterized retrieval and a good agreement is found between retrieval results from the two parameterized and OEM-based approaches. Similarly, the quantities retrieved from the new dual-scan multi-wavelength MAX-DOAS parameterization technique has been verified through comparisons with OEM-based vertical profiles in the main azimuthal direction and three additional azimuthal directions.

The MAX-DOAS NO_2 VCD horizontal profiles, as retrieved by the new OEM-based horizontal distribution inversion algorithm, are validated using airborne and mobile car-DOAS tropospheric NO_2 column measurements during the S5P validation campaign in the Brussels-Capital Region on June 28, 2019, and a good overall consistency is found between the different datasets, especially in terms of correlation coefficient.

- **Use of the ground-based multi-azimuthal MAX-DOAS retrieval results to validate the TROPOMI/S5P observations over Uccle. In particular, we investigate how these new MAX-DOAS data sets can affect the validation of the satellite observations in urban conditions.**

  In urban regions, the validation of high spatial resolution air-quality satellite observations, such as TROPOMI/S5P, requires ground-based measurements that can give information about the horizontal distribution or air pollutants.

  For the first time, one entire year (March 2018-March 2019) of TROPOMI tropospheric NO_2 and HCHO VCD measurements are compared to the retrieved dual-scan MAX-DOAS NO_2 and HCHO VCDs in Uccle, Brussels. This exercise revealed that the use of the derived MAX-DOAS horizontal sensitivity range to define a sampling area around the measurement site for the selection of the co-located TROPOMI pixels leads to an improved agreement (better slope and correlation coefficient values) between MAX-DOAS and satellite data compared to the case where MAX-DOAS VCDs in only one azimuthal direction are used. However, despite the improvement, TROPOMI tropospheric columns are found systematically lower than ground-based observations. Further investigations showed that after recalculating the TROPOMI columns using daily median MAX-DOAS profiles as a priori for the satellite AMF calculations, TROPOMI and MAX-DOAS data have a much better quantitative agreement. This finding suggests that using adequate a priori profiles in the TROPOMI retrieval can considerably improve the performance of high spatial resolution satellite observations over urban regions.

  In a second step, maps of seasonally-averaged NO_2 VCDs around the measurement site are generated using the dual-scan multi-wavelength MAX-DOAS NO_2 horizontal profiles retrieved over the April 2018-February 2020 period by applying the new OEM-based horizontal distribution inversion algorithm. It is the first time that maps of MAX-DOAS NO_2 VCDs are compared to corresponding TROPOMI NO_2 VCD maps. A good overall agreement is found between both datasets in allocating NO_2 peaks and minima over the Brussels-Capital Region. However, it is found that even for a better spatial sampling between TROPOMI and ground-based observations, the underestimation of the MAX-DOAS tropospheric NO_2 columns by TROPOMI still persists, as in the first comparison study. The investigation of the role of the cloud product in the TROPOMI AMF calculations reveals that the use of an improved cloud retrieval reduces the bias with respect to the ground-based NO_2 columns. Similarly as in the first validation exercise, the use of MAX-DOAS a priori profiles in the TROPOMI retrieval is found to have the most considerable effect for bringing satellite and ground-based observations in good agreement in urban conditions.

Perspectives

Based on the work and results achieved during this thesis, we consider that future investigations should focus on the following main aspects:

- The measurement set-up of ground-based MAX-DOAS instruments could be further improved to better sample the NO_2, HCHO, and aerosols horizontal distributions through the selection of a larger number of azimuthal directions throughout the day. Additionally, several ground-based dual-scan MAX-DOAS instruments could be installed in different locations in order to reach a better spatial coverage and also cover common areas as consistency verification purpose. Overall, the deployment of at least two instruments and the development of retrieval methodologies combining the measurements of both instruments could improve our knowledge about the horizontal distribution of pollutants in urban regions.

- By performing vertical scans in multiple azimuthal directions, the dual-scan MAX-DOAS parameterization technique could also take into account the azimuthal dependency of the vertical distribution of NO_2, HCHO, and aerosols, and consequently, of the MLH around the measurement site. By obtaining this information, ground-based MAX-DOAS instruments could potentially provide 3-D distributions of NO_2, HCHO and aerosols around the instrument.

- Additional comparisons are needed between the dual-scan MAX-DOAS NO_2, HCHO, and aerosols measurements and ancillary data. Airborne and mobile car-doas observations were of great importance to validate our new OEM-based horizontal distribution inversion algorithm. It is deemed necessary to have more measurement campaigns above urban regions to verify and potentially improve the quality of ground-based MAX-DOAS measurements in such conditions.

- The improvements mentioned above concerning the ground-based dual-scan MAX-DOAS instruments and the developed retrieval methodologies result in better agreement between ground-based and satellite datasets. However, the main ancillary parameter used for the AMF calculation in the satellite retrievals, i.e. the NO_2 a priori profiles, could be further improved by conducting thorough comparisons between MAX-DOAS vertical profiles and those from the models currently used in the standard satellite retrievals.

- Comparisons between the dual-scan MAX-DOAS NO_2, HCHO, and aerosols and tropospheric chemistry transport models could be also considered as a valuable task to improve the modeled datasets in urban regions.

Bibliography

Aliwell, S., Van Roozendael, M., Johnston, P., Richter, A., Wagner, T., Arlander, D., Burrows, J., Fish, D., Jones, R., Tørnkvist, K., et al. (2002). Analysis for BrO in zenith-sky spectra: An intercomparison exercise for analysis improvement. *Journal of Geophysical Research: Atmospheres*, 107(D14):ACH–10.

Allegre, C. J., Poirier, J.-P., Humler, E., and Hofmann, A. W. (1995). The chemical composition of the Earth. *Earth and Planetary Science Letters*, 134(3-4):515–526.

Barret, B., De Mazière, M., and Demoulin, P. (2002). Retrieval and characterization of ozone profiles from solar infrared spectra at the Jungfraujoch. *Journal of Geophysical Research: Atmospheres*, 107(D24):ACH–19.

Bauer, S. E., Tsigaridis, K., Faluvegi, G., Kelley, M., Lo, K. K., Miller, R. L., Nazarenko, L., Schmidt, G. A., and Wu, J. (2020). Historical (1850–2014) aerosol evolution and role on climate forcing using the GISS ModelE2. 1 contribution to CMIP6. *Journal of Advances in Modeling Earth Systems*, 12(8):e2019MS001978.

Beirle, S., Boersma, K. F., Platt, U., Lawrence, M. G., and Wagner, T. (2011). Megacity emissions and lifetimes of nitrogen oxides probed from space. *Science*, 333(6050):1737–1739.

Beirle, S., Dörner, S., Dönner, S., Remmers, J., Wang, Y., and Wagner, T. (2019). The Mainz profile algorithm (MAPA). *Atmospheric Measurement Techniques*, 12(3):1785–1806.

Bell, M. L., Davis, D. L., and Fletcher, T. (2004). A retrospective assessment of mortality from the London smog episode of 1952: the role of influenza and pollution. *Environmental health perspectives*, 112(1):6–8.

Boersma, K., Eskes, H., and Brinksma, E. (2004). Error analysis for tropospheric NO_2 retrieval from space. *Journal of Geophysical Research: Atmospheres*, 109(D4).

Bösch, T., Rozanov, V., Richter, A., Peters, E., Rozanov, A., Wittrock, F., Merlaud, A., Lampel, J., Schmitt, S., Haij, M. d., et al. (2018). BOREAS–a new MAX-DOAS profile retrieval algorithm for aerosols and trace gases. *Atmospheric Measurement Techniques*, 11(12):6833–6859.

Bovensmann, H., Burrows, J., Buchwitz, M., Frerick, J., Noël, S., Rozanov, V., Chance, K., and Goede, A. (1999). SCIAMACHY: Mission objectives and measurement modes. *Journal of the atmospheric sciences*, 56(2):127–150.

Brimblecombe, P. (1976). Attitudes and responses towards air pollution in medieval England. *Journal of the Air Pollution Control Association*, 26(10):941–945.

Burrows, J. P., Weber, M., Buchwitz, M., Rozanov, V., Ladstätter-Weißenmayer, A., Richter, A., DeBeek, R., Hoogen, R., Bramstedt, K., Eichmann, K.-U., et al. (1999). The global ozone monitoring experiment (GOME): Mission concept and first scientific results. *Journal of the Atmospheric Sciences*, 56(2):151–175.

Celarier, E., Brinksma, E., Gleason, J., Veefkind, J., Cede, A., Herman, J., Ionov, D., Goutail, F., Pommereau, J.-P., Lambert, J.-C., et al. (2008). Validation of Ozone Monitoring Instrument nitrogen dioxide columns. *Journal of Geophysical Research: Atmospheres*, 113(D15).

Chance, K. V. and Spurr, R. J. (1997). Ring effect studies: Rayleigh scattering, including molecular parameters for rotational Raman scattering, and the Fraunhofer spectrum. *Applied optics*, 36(21):5224–5230.

Chen, D., Zhou, B., Beirle, S., Chen, L., and Wagner, T. (2009). Tropospheric NO_2 column densities deduced from zenith-sky DOAS measurements in Shanghai, China, and their application to satellite validation. *Atmospheric Chemistry and Physics*, 9(11):3641–3662.

Clarisse, L., Clerbaux, C., Dentener, F., Hurtmans, D., and Coheur, P.-F. (2009). Global ammonia distribution derived from infrared satellite observations. *Nature Geoscience*, 2(7):479–483.

Clémer, K., Van Roozendael, M., Fayt, C., Hendrick, F., Hermans, C., Pinardi, G., Spurr, R., Wang, P., and Mazière, M. D. (2010). Multiple wavelength retrieval of tropospheric aerosol optical properties from MAXDOAS measurements in Beijing. *Atmospheric Measurement Techniques*, 3(4):863–878.

Compernolle, S., Argyrouli, A., Lutz, R., Sneep, M., Lambert, J.-C., Fjæraa, A. M., Hubert, D., Keppens, A., Loyola, D., O'Connor, E., et al. (2021). Validation of the Sentinel-5 Precursor TROPOMI cloud data with Cloudnet, Aura OMI O_2–O_2, MODIS, and Suomi-NPP VIIRS. *Atmospheric Measurement Techniques*, 14(3):2451–2476.

De Haij, M., Wauben, W., and Baltink, H. K. (2007). *Continuous mixing layer height determination using the LD-40 ceilometer: a feasibility study*. Royal Netherlands Meteorological Institute (KNMI) De Bilt.

De Smedt, I., Pinardi, G., Vigouroux, C., Compernolle, S., Bais, A., Benavent, N., Boersma, F., Chan, K.-L., Dönner, S., Eichmann, K.-U., et al. (2021). Comparative assessment of TROPOMI and OMI formaldehyde observations against MAX-DOAS network column measurements. *Atmospheric Chemistry and Physics Discussions*, pages 1–51.

De Smedt, I., Theys, N., Yu, H., Danckaert, T., Lerot, C., Compernolle, S., Van Roozendael, M., Richter, A., Hilboll, A., Peters, E., et al. (2018). Algorithm theoretical baseline for formaldehyde retrievals from S5P TROPOMI and from the QA4ECV project. *Atmospheric Measurement Techniques*, 11(4):2395–2426.

Delmas, R., Serça, D., and Jambert, C. (1997). Global inventory of NO_x sources. *Nutrient cycling in agroecosystems*, 48(1):51–60.

Deutschmann, T., Beirle, S., Frieß, U., Grzegorski, M., Kern, C., Kritten, L., Platt, U., Prados-Román, C., Puķı, J., Wagner, T., et al. (2011). The Monte Carlo atmospheric radiative transfer model McArtim: Introduction and validation of Jacobians and 3D features. *Journal of Quantitative Spectroscopy and Radiative Transfer*, 112(6):1119–1137.

Deutschmann, T., Wagner, T., and von Friedeburg, C. (2007). TRACY-II manual 0.85. *Institut für Umweltphysik der Universität Heidelberg, Heidelberg*.

Dieudonné, E., Ravetta, F., Pelon, J., Goutail, F., and Pommereau, J.-P. (2013). Linking NO_2 surface concentration and integrated content in the urban developed atmospheric boundary layer. *Geophysical research letters*, 40(6):1247–1251.

Dimitropoulou, E., Assimakopoulos, V. D., Fameli, K. M., Flocas, H. A., Kosmopoulos, P., Kazadzis, S., Lagouvardos, K., and Bossioli, E. (2018). Estimating the biogenic non-methane hydrocarbon emissions over Greece. *Atmosphere*, 9(1):14.

Dimitropoulou, E., Hendrick, F., Pinardi, G., Friedrich, M. M., Merlaud, A., Tack, F., De Longueville, H., Fayt, C., Hermans, C., Laffineur, Q., et al. (2020). Validation of TROPOMI tropospheric NO_2 columns using dual-scan multi-axis differential optical absorption spectroscopy (MAX-DOAS) measurements in Uccle, Brussels. *Atmospheric Measurement Techniques*, 13(10):5165–5191.

Dönner, S., Kuhn, J., Van Roozendael, M., Bais, A., Beirle, S., Bösch, T., Bognar, K., Bruchkouski, I., Chan, K. L., Dörner, S., et al. (2020). Evaluating different methods for elevation calibration of MAX-DOAS (Multi AXis Differential Optical Absorption Spectroscopy) instruments during the CINDI-2 campaign. *Atmospheric Measurement Techniques*, 13(2):685–712.

Dunn, R. J., Stanitski, D. M., Gobron, N., Willett, K. M., Ades, M., Adler, R., Allan, R., Allan, R., Anderson, J., Argüez, A., et al. (2020). Global climate. *Bulletin of the American Meteorological Society*, 101(101 (8)):S9–S127.

Ehhalt, D. H., Rohrer, F., and Wahner, A. (1992). Sources and distribution of NO_x in the upper troposphere at northern mid-latitudes. *Journal of Geophysical Research: Atmospheres*, 97(D4):3725–3738.

Emde, C., Buras, R., and Mayer, B. (2011). ALIS: An efficient method to compute high spectral resolution polarized solar radiances using the Monte Carlo approach. *Journal of Quantitative Spectroscopy and Radiative Transfer*, 112(10):1622–1631.

Eskes, H. and Boersma, K. (2003). Averaging kernels for DOAS total-column satellite retrievals. *Atmospheric Chemistry and Physics*, 3(5):1285–1291.

Fayt, C., De Smedt, I., Letocart, V., Merlaud, A., Pinardi, G., and Van Roozendael, M. (2011). QDOAS Software user manual. *Belgian Institute for Space Aeronomy: Brussels, Belgium*, 1.

Feynman, R. P., Leighton, R. B., and Sands, M. (1965). The Feynman lectures on physics; vol. i. *American Journal of Physics*, 33(9):750–752.

Fleischmann, O. C., Hartmann, M., Burrows, J. P., and Orphal, J. (2004). New ultraviolet absorption cross-sections of BrO at atmospheric temperatures measured by time-windowing Fourier transform spectroscopy. *Journal of Photochemistry and Photobiology A: Chemistry*, 168(1-2):117–132.

Friedeburg, C. v. (2003). *Derivation of trace gas information combining differential optical absorption spectroscopy with radiative transfer modelling*. PhD thesis.

Friedrich, M. M., Rivera, C., Stremme, W., Ojeda, Z., Arellano, J., Bezanilla, A., García-Reynoso, J. A., and Grutter, M. (2019). NO_2 vertical profiles and column densities from MAX-DOAS measurements in Mexico City. *Atmospheric Measurement Techniques*, 12(4):2545–2565.

Frieß, U., Beirle, S., Alvarado Bonilla, L., Bösch, T., Friedrich, M. M., Hendrick, F., Piters, A., Richter, A., Van Roozendael, M., Rozanov, V. V., et al. (2019). Intercomparison of MAX-DOAS vertical profile retrieval algorithms: studies using synthetic data. *Atmospheric Measurement Techniques*, 12(4):2155–2181.

Frieß, U., Monks, P., Remedios, J., Rozanov, A., Sinreich, R., Wagner, T., and Platt, U. (2006). MAX-DOAS O_4 measurements: A new technique to derive information on atmospheric aerosols: 2. Modeling studies. *Journal of Geophysical Research: Atmospheres*, 111(D14).

Geffen, J. v., Boersma, K. F., Eskes, H., Sneep, M., Linden, M. t., Zara, M., and Veefkind, J. P. (2020). S5P TROPOMI NO_2 slant column retrieval: Method, stability, uncertainties and comparisons with OMI. *Atmospheric Measurement Techniques*, 13(3):1315–1335.

Gielen, C., Van Roozendael, M., Hendrick, F., Pinardi, G., Vlemmix, T., De Bock, V., De Backer, H., Fayt, C., Hermans, C., Gillotay, D., et al. (2014). A simple and versatile cloud-screening method for MAX-DOAS retrievals. *Atmospheric Measurement Techniques*, 7(10):3509–3527.

Gilardoni, S. and Fuzzi, S. (2017). Chemical composition of aerosols of different origin. *Atmospheric Aerosols: Life Cycles and Effects on Air Quality and Climate*.

Gillotay, D., Besnard, T., and Zanghi, F. (2001). A systematic approach of the cloud cover by thermic infrared measurements.

Grainger, J. and Ring, J. (1962). Anomalous Fraunhofer line profiles. *Nature*, 193(4817):762–762.

Griffin, D., Zhao, X., McLinden, C. A., Boersma, F., Bourassa, A., Dammers, E., Degenstein, D., Eskes, H., Fehr, L., Fioletov, V., et al. (2019). High-resolution mapping of nitrogen dioxide with TROPOMI: First results and validation over the Canadian oil sands. *Geophysical Research Letters*, 46(2):1049–1060.

Güdel, M. (2007). The Sun in time: Activity and environment. *Living Reviews in Solar Physics*, 4(1):1–137.

Haeffelin, M., Laffineur, Q., Bravo-Aranda, J.-A., Drouin, M.-A., Casquero-Vera, J.-A., Dupont, J.-C., and Backer, H. D. (2016). Radiation fog formation alerts using attenuated backscatter power from automatic lidars and ceilometers. *Atmospheric Measurement Techniques*, 9(11):5347–5365.

Haiducek, J. (2010). Experimental Validation Techniques for the HELEEOS Off-Axis Laser Propagation Model. Technical report, AIR FORCE INST OF TECH WRIGHT-PATTERSON AFB OH SCHOOL OF ENGINEERING AND.

Heckel, A., Kim, S.-W., Frost, G., Richter, A., Trainer, M., and Burrows, J. (2011). Influence of low spatial resolution a priori data on tropospheric NO_2 satellite retrievals. *Atmospheric measurement techniques*, 4(9):1805–1820.

Hendrick, F., Müller, J.-F., Clémer, K., Wang, P., Maziere, M. D., Fayt, C., Gielen, C., Hermans, C., Ma, J., Pinardi, G., et al. (2014). Four years of ground-based MAX-DOAS observations of HONO and NO_2 in the Beijing area. *Atmospheric Chemistry and Physics*, 14(2):765–781.

Henyey, L. G. and Greenstein, J. L. (1941). Diffuse radiation in the galaxy. *The Astrophysical Journal*, 93:70–83.

Hönninger, G., Friedeburg, C. v., and Platt, U. (2004). Multi axis differential optical absorption spectroscopy (MAX-DOAS). *Atmospheric Chemistry and Physics*, 4(1):231–254.

Hooyberghs, J., Mensink, C., Dumont, G., Fierens, F., and Brasseur, O. (2005). A neural network forecast for daily average PM_{10} concentrations in Belgium. *Atmospheric Environment*, 39(18):3279–3289.

Huijnen, V., Eskes, H., Poupkou, A., Elbern, H., Boersma, K., Foret, G., Sofiev, M., Valdebenito, A., Flemming, J., Stein, O., et al. (2010). Comparison of OMI NO_2 tropospheric columns with an ensemble of global and European regional air quality models. *Atmospheric Chemistry and Physics*, 10(7):3273–3296.

Ialongo, I., Virta, H., Eskes, H., Hovila, J., and Douros, J. (2020). Comparison of TROPOMI/Sentinel-5 Precursor NO_2 observations with ground-based measurements in Helsinki. *Atmospheric Measurement Techniques*, 13(1):205–218.

Irie, H., Boersma, K., Kanaya, Y., Takashima, H., Pan, X., and Wang, Z. (2012). Quantitative bias estimates for tropospheric NO_2 columns retrieved from SCIAMACHY, OMI, and GOME-2 using a common standard for East Asia. *Atmospheric Measurement Techniques*, 5(10):2403–2411.

Irie, H., Kanaya, Y., Akimoto, H., Tanimoto, H., Wang, Z., Gleason, J., and Bucsela, E. (2008). Validation of OMI tropospheric NO_2 column data using MAX-DOAS measurements deep inside the North China Plain in June 2006: Mount Tai Experiment 2006. *Atmospheric Chemistry and Physics*, 8(22):6577–6586.

Irie, H., Takashima, H., Kanaya, Y., Boersma, K., Gast, L., Wittrock, F., Brunner, D., Zhou, Y., and Van Roozendael, M. (2011). Eight-component retrievals from ground-based MAX-DOAS observations. *Atmospheric Measurement Techniques*, 4(6):1027–1044.

Jacob, D. J. (1999). *Introduction to atmospheric chemistry*. Princeton University Press.

Janssen, S., Fierens, F., Dumont, G., and Mensink, C. (2008). RIO: a novel approach for air pollution mapping. *Hrvatski meteorološki časopis*, 43(43/1):172–176.

Judd, L. M., Al-Saadi, J. A., Szykman, J. J., Valin, L. C., Janz, S. J., Kowalewski, M. G., Eskes, H. J., Veefkind, J. P., Cede, A., Mueller, M., et al. (2020). Evaluating Sentinel-5P TROPOMI tropospheric NO_2 column densities with airborne and Pandora spectrometers near New York City and Long Island Sound. *Atmospheric Measurement Techniques*, 13(11):6113–6140.

Kanakidou, M., Seinfeld, J., Pandis, S., Barnes, I., Dentener, F. J., Facchini, M. C., Dingenen, R. V., Ervens, B., Nenes, A., Nielsen, C., et al. (2005). Organic aerosol and global climate modelling: a review. *Atmospheric Chemistry and Physics*, 5(4):1053–1123.

Kleipool, Q., Dobber, M., de Haan, J., and Levelt, P. (2008). Earth surface reflectance climatology from 3 years of OMI data. *Journal of Geophysical Research: Atmospheres*, 113(D18).

Koelemeijer, R., Stammes, P., Hovenier, J., and De Haan, J. (2001). A fast method for retrieval of cloud parameters using oxygen A band measurements from the Global Ozone Monitoring Experiment. *Journal of Geophysical Research: Atmospheres*, 106(D4):3475–3490.

Kramer, L. J., Leigh, R. J., Remedios, J. J., and Monks, P. S. (2008). Comparison of OMI and ground-based in situ and MAX-DOAS measurements of tropospheric nitrogen dioxide in an urban area. *Journal of Geophysical Research: Atmospheres*, 113(D16).

Kreher, K., Van Roozendael, M., Hendrick, F., Apituley, A., Dimitropoulou, E., Frieß, U., Richter, A., Wagner, T., Lampel, J., Abuhassan, N., et al. (2020). Intercomparison of NO_2, O_4, O_3 and HCHO slant column measurements by MAX-DOAS and zenith-sky UV–visible spectrometers during CINDI-2. *Atmospheric Measurement Techniques*, 13(5):2169–2208.

Kurucz, R. L. (1984). Solar Flux Atlas from 296 to 1300 nm. *National Solar Observatory Atlas*, 1.

Lamsal, L. N., Krotkov, N. A., Vasilkov, A., Marchenko, S., Qin, W., Yang, E.-S., Fasnacht, Z., Joiner, J., Choi, S., Haffner, D., et al. (2021). Ozone Monitoring Instrument (OMI) Aura nitrogen dioxide standard product version 4.0 with improved surface and cloud treatments. *Atmospheric Measurement Techniques*, 14(1):455–479.

Leighton, P. (1961). Photochemistry of Air Pollution, Acad. *Press, New York*.

Leitão, J., Richter, A., Vrekoussis, M., Kokhanovsky, A., Zhang, Q., Beekmann, M., and Burrows, J. (2010). On the improvement of NO_2 satellite retrievals–aerosol impact on the airmass factors. *Atmospheric Measurement Techniques*, 3(2):475–493.

Levelt, P. F., Van Den Oord, G. H., Dobber, M. R., Malkki, A., Visser, H., De Vries, J., Stammes, P., Lundell, J. O., and Saari, H. (2006). The ozone monitoring instrument. *IEEE Transactions on geoscience and remote sensing*, 44(5):1093–1101.

Liu, S., Valks, P., Pinardi, G., Xu, J., Argyrouli, A., Lutz, R., Tilstra, L. G., Huijnen, V., Hendrick, F., and Van Roozendael, M. (2020). An improved air mass factor calculation for nitrogen dioxide measurements from the Global Ozone Monitoring Experiment-2 (GOME-2). *Atmospheric Measurement Techniques*, 13(2):755–787.

Ma, J., Beirle, S., Jin, J., Shaiganfar, R., Yan, P., and Wagner, T. (2013). Tropospheric NO_2 vertical column densities over Beijing: results of the first three years of ground-based MAX-DOAS measurements (2008–2011) and satellite validation. *Atmospheric Chemistry and Physics*, 13(3):1547–1567.

Mayer, B. and Kylling, A. (2005). The libRadtran software package for radiative transfer calculations-description and examples of use. *Atmospheric Chemistry and Physics*, 5(7):1855–1877.

McLinden, C., Fioletov, V., Boersma, K., Kharol, S., Krotkov, N., Lamsal, L., Makar, P., Martin, R., Veefkind, J., and Yang, K. (2014). Improved satellite retrievals of NO_2 and SO_2 over the Canadian oil sands and comparisons with surface measurements. *Atmospheric Chemistry and Physics*, 14(7):3637–3656.

Meller, R. and Moortgat, G. K. (2000). Temperature dependence of the absorption cross sections of formaldehyde between 223 and 323 K in the wavelength range 225–375 nm. *Journal of Geophysical Research: Atmospheres*, 105(D6):7089–7101.

Menut, L., Flamant, C., Pelon, J., and Flamant, P. H. (1999). Urban boundary-layer height determination from lidar measurements over the Paris area. *Applied Optics*, 38(6):945–954.

Merlaud, A. (2013). *Development and use of compact instruments for tropospheric investigations based on optical spectroscopy from mobile platforms*. Presses univ. de Louvain.

Munro, R., Lang, R., Klaes, D., Poli, G., Retscher, C., Lindstrot, R., Huckle, R., Lacan, A., Grzegorski, M., Holdak, A., et al. (2016). The GOME-2 instrument on the Metop series of satellites: instrument design, calibration, and level 1 data processing–an overview. *Atmospheric Measurement Techniques*, 9(3):1279–1301.

Nan, J., Wang, S., Guo, Y., Xiang, Y., and Zhou, B. (2017). Study on the daytime OH radical and implication for its relationship with fine particles over megacity of Shanghai, China. *Atmospheric Environment*, 154:167–178.

Nicolet, M. (1984). On the molecular scattering in the terrestrial atmosphere: An empirical formula for its calculation in the homosphere. *Planetary and Space Science*, 32(11):1467–1468.

Ortega, I., Koenig, T., Sinreich, R., Thomson, D., and Volkamer, R. (2015). The CU 2-D-MAX-DOAS instrument–Part 1: Retrieval of 3-D distributions of NO_2 and azimuth-dependent OVOC ratios. *Atmospheric Measurement Techniques*, 8(6):2371–2395.

Peters, E., Wittrock, F., Großmann, K., Frieß, U., Richter, A., and Burrows, J. (2012). Formaldehyde and nitrogen dioxide over the remote western Pacific Ocean: SCIAMACHY and GOME-2 validation using ship-based MAX-DOAS observations. *Atmospheric Chemistry and Physics*, 12(22):11179–11197.

Petty, G. W. (2006). *A first course in atmospheric radiation*. Sundog Pub.

Pinardi, G., Hendrick, F., Clémer, K., Lambert, J., Bai, J., and Van Roozendael, M. (2008). On the use of the MAX-DOAS technique for the validation of tropospheric NO_2 column measurements from satellite. In *Proc. Eumetsat Conf.*

Pinardi, G., Van Roozendael, M., Abuhassan, N., Adams, C., Cede, A., Clémer, K., Fayt, C., Frieß, U., Gil, M., Herman, J., et al. (2013). MAX-DOAS formaldehyde slant column measurements during CINDI: intercomparison and analysis improvement. *Atmospheric Measurement Techniques*, 6(1):167–185.

Pinardi, G., Van Roozendael, M., Hendrick, F., Theys, N., Abuhassan, N., Bais, A., Boersma, F., Cede, A., Chong, J., Dönner, S., et al. (2020). Validation of tropospheric NO_2 column measurements of GOME-2A and OMI using MAX-DOAS and direct sun network observations. *Atmospheric Measurement Techniques*, 13(11):6141–6174.

Platt, U. and Perner, D. (1980). Direct measurements of atmospheric CH_2O, HNO_2, O_3, NO_2, and SO_2 by differential optical absorption in the near UV. *Journal of Geophysical Research: Oceans*, 85(C12):7453–7458.

Platt, U. and Stutz, J. (2008). Differential absorption spectroscopy. In *Differential Optical Absorption Spectroscopy*, pages 135–174. Springer.

Pöhler, D., Vogel, L., Frieß, U., and Platt, U. (2010). Atmospheric Chemistry Special Feature: Observation of halogen species in the Amundsen Gulf, Arctic, by active long-path differential optical absorption spectroscopy. In *Proceedings of the National Academy of Science*, volume 107, pages 6582–6587.

Puķīte, J., Kühl, S., Deutschmann, T., Platt, U., and Wagner, T. (2010). Extending differential optical absorption spectroscopy for limb measurements in the UV. *Atmospheric Measurement Techniques*, 3(3):631–653.

Ramanathan, V. and Carmichael, G. (2008). Global and regional climate changes due to black carbon. *Nature geoscience*, 1(4):221–227.

Reay, D. S., Davidson, E. A., Smith, K. A., Smith, P., Melillo, J. M., Dentener, F., and Crutzen, P. J. (2012). Global agriculture and nitrous oxide emissions. *Nature climate change*, 2(6):410–416.

Rodgers, C. D. (2000). *Inverse methods for atmospheric sounding: theory and practice*, volume 2. World scientific.

Rothman, L. S., Gordon, I. E., Barbe, A., Benner, D. C., Bernath, P. F., Birk, M., Boudon, V., Brown, L. R., Campargue, A., Champion, J.-P., et al. (2009). The HITRAN 2008 molecular spectroscopic database. *Journal of Quantitative Spectroscopy and Radiative Transfer*, 110(9-10):533–572.

Rozanov, A., Rozanov, V., Buchwitz, M., Kokhanovsky, A., and Burrows, J. (2005). SCIATRAN 2.0–A new radiative transfer model for geophysical applications in the 175–2400 nm spectral region. *Advances in Space Research*, 36(5):1015–1019.

Rybicki, G. B. and Lightman, A. P. (2008). *Radiative processes in astrophysics*. John Wiley & Sons.

Schreier, S. F., Richter, A., and Burrows, J. P. (2019). Near-surface and path-averaged mixing ratios of NO_2 derived from car DOAS zenith-sky and tower DOAS off-axis measurements in Vienna: A case study. *Atmospheric Chemistry and Physics*, 19(9):5853–5879.

Schreier, S. F., Richter, A., Peters, E., Ostendorf, M., Schmalwieser, A. W., Weihs, P., and Burrows, J. P. (2020). Dual ground-based MAX-DOAS observations in Vienna, Austria: Evaluation of horizontal and temporal NO_2, HCHO, and CHOCHO distributions and comparison with independent data sets. *Atmospheric Environment: X*, 5:100059.

Seinfeld, J. H. and Pandis, S. N. (2016). *Atmospheric chemistry and physics: from air pollution to climate change*. John Wiley & Sons.

Serdyuchenko, A., Gorshelev, V., Weber, M., Chehade, W., and Burrows, J. (2014). High spectral resolution ozone absorption cross-sections–Part 2: Temperature dependence. *Atmospheric Measurement Techniques*, 7(2):625–636.

Seyler, A., Meier, A. C., Wittrock, F., Kattner, L., Mathieu-Üffing, B., Peters, E., Richter, A., Ruhtz, T., Schönhardt, A., Schmolke, S., et al. (2019). Studies of the horizontal inhomogeneities in NO_2 concentrations above a shipping lane using ground-based multi-axis differential optical absorption spectroscopy (MAX-DOAS) measurements and validation with airborne imaging DOAS measurements. *Atmospheric Measurement Techniques*, 12(11):5959–5977.

Sillman, S. (1999). The relation between ozone, NO_x and hydrocarbons in urban and polluted rural environments. *Atmospheric Environment*, 33(12):1821–1845.

Sinreich, R., Merten, A., Molina, L., and Volkamer, R. (2013). Parameterizing radiative transfer to convert MAX-DOAS dSCDs into near-surface box-averaged mixing ratios. *Atmospheric Measurement Techniques*, 6(6):1521–1532.

Sinreich, R., Volkamer, R., Filsinger, F., Frieß, U., Kern, C., Platt, U., Sebastián, O., and Wagner, T. (2007). MAX-DOAS detection of glyoxal during ICARTT 2004. *Atmospheric Chemistry and Physics*, 7(5):1293–1303.

Spurr, R. J. (2006). VLIDORT: A linearized pseudo-spherical vector discrete ordinate radiative transfer code for forward model and retrieval studies in multilayer multiple scattering media. *Journal of Quantitative Spectroscopy and Radiative Transfer*, 102(2):316–342.

Stavrakou, T., Müller, J.-F., De Smedt, I., Van Roozendael, M., Van Der Werf, G., Giglio, L., and Guenther, A. (2009). Global emissions of non-methane hydrocarbons deduced from SCIAMACHY formaldehyde columns through 2003–2006. *Atmospheric Chemistry and Physics*, 9(11):3663–3679.

Stull, R. B. (1988). *An introduction to boundary layer meteorology*, volume 13. Springer Science & Business Media.

Tack, F., Merlaud, A., Iordache, M.-D., Danckaert, T., Yu, H., Fayt, C., Meuleman, K., Deutsch, F., Fierens, F., and Van Roozendael, M. (2017). High-resolution mapping of the NO_2 spatial distribution over Belgian urban areas based on airborne APEX remote sensing. *Atmospheric Measurement Techniques*, 10(5):1665–1688.

Tack, F., Merlaud, A., Iordache, M.-D., Pinardi, G., Dimitropoulou, E., Eskes, H., Bomans, B., Veefkind, P., and Van Roozendael, M. (2021). Assessment of the TROPOMI tropospheric NO_2 product based on airborne APEX observations. *Atmospheric Measurement Techniques*, 14(1):615–646.

Takashima, H., Irie, H., Kanaya, Y., and Syamsudin, F. (2012). NO_2 observations over the western Pacific and Indian Ocean by MAX-DOAS on Kaiyo, a Japanese research vessel. *Atmospheric Measurement Techniques*, 5(10):2351–2360.

Thalman, R. and Volkamer, R. (2013). Temperature dependent absorption cross-sections of O_2–O_2 collision pairs between 340 and 630 nm and at atmospherically relevant pressure. *Physical chemistry chemical physics*, 15(37):15371–15381.

Tirpitz, J.-L., Frieß, U., Hendrick, F., Alberti, C., Allaart, M., Apituley, A., Bais, A., Beirle, S., Berkhout, S., Bognar, K., et al. (2021). Intercomparison of MAX-DOAS vertical profile retrieval algorithms: studies on field data from the CINDI-2 campaign. *Atmospheric Measurement Techniques*, 14(1):1–35.

van Geffen, J., Eskes, H., Boersma, K., Maasakkers, J., and Veefkind, J. (2019). TROPOMI ATBD of the total and tropospheric NO_2 data products, KNMI.

Vandaele, A. C., Hermans, C., Simon, P. C., Carleer, M., Colin, R., Fally, S., Merienne, M.-F., Jenouvrier, A., and Coquart, B. (1998). Measurements of the NO_2 absorption cross-section from 42 000 cm^{-1} to 10 000 cm^{-1} (238–1000 nm) at 220 K and 294 K. *Journal of Quantitative Spectroscopy and Radiative Transfer*, 59(3-5):171–184.

Vardavas, I. and Taylor, F. (2007). Radiation and Climate, vol. 138 of International Series of Monographs on Physics.

Veefkind, J., Boersma, K., Wang, J., Kurosu, T., Krotkov, N., Chance, K., and Levelt, P. (2011). Global satellite analysis of the relation between aerosols and short-lived trace gases. *Atmospheric Chemistry and Physics*, 11(3):1255–1267.

Verhoelst, T., Compernolle, S., Pinardi, G., Lambert, J.-C., Eskes, H. J., Eichmann, K.-U., Fjæraa, A. M., Granville, J., Niemeijer, S., Cede, A., et al. (2021). Ground-based validation of the Copernicus Sentinel-5p TROPOMI NO_2 measurements with the NDACC ZSL-DOAS, MAX-DOAS and Pandonia global networks. *Atmospheric Measurement Techniques*, 14(1):481–510.

Vestreng, V., Ntziachristos, L., Semb, A., Reis, S., Isaksen, I. S., and Tarrason, L. (2009). Evolution of NO_x emissions in Europe with focus on road transport control measures. *Atmospheric Chemistry and Physics*, 9(4):1503–1520.

Villena, G., Wiesen, P., Cantrell, C., Flocke, F., Fried, A., Hall, S., Hornbrook, R., Knapp, D., Kosciuch, E., Mauldin, R., et al. (2011). Nitrous acid (HONO) during polar spring in Barrow, Alaska: A net source of OH radicals? *Journal of Geophysical Research: Atmospheres*, 116(D14).

Volkamer, R., Molina, L. T., Molina, M. J., Shirley, T., and Brune, W. H. (2005). DOAS measurement of glyoxal as an indicator for fast VOC chemistry in urban air. *Geophysical Research Letters*, 32(8).

Wagner, T., Apituley, A., Beirle, S., Dorner, S., Friess, U., Remmers, J., and Shaiganfar, R. (2014). Cloud detection and classification based on MAX-DOAS observations. *Atmospheric Measurement Techniques*, 7(5):1289–1320.

Wagner, T., Beirle, S., Benavent, N., Bösch, T., Chan, K. L., Dönner, S., Dörner, S., Fayt, C., Frieß, U., García-Nieto, D., et al. (2019). Is a scaling factor required to obtain closure between measured and modelled atmospheric O_4 absorptions? An assessment of uncertainties of measurements and radiative transfer simulations for 2 selected days during the MAD-CAT campaign. *Atmospheric Measurement Techniques*, 12(5):2745–2817.

Wagner, T., Beirle, S., Brauers, T., Deutschmann, T., Frieß, U., Hak, C., Halla, J., Heue, K., Junkermann, W., Li, X., et al. (2011). Inversion of tropospheric profiles of aerosol extinction and HCHO and NO_2 mixing ratios from MAX-DOAS observations in Milano during the summer of 2003 and comparison with independent data sets. *Atmospheric Measurement Techniques*, 4(12):2685–2715.

Wagner, T., Burrows, J., Deutschmann, T., Dix, B., Friedeburg, C. v., Frieß, U., Hendrick, F., Heue, K.-P., Irie, H., Iwabuchi, H., et al. (2007). Comparison of box-air-mass-factors and radiances for Multiple-Axis Differential Optical Absorption Spectroscopy (MAX-DOAS) geometries calculated from different UV/visible radiative transfer models. *Atmospheric Chemistry and Physics*, 7(7):1809–1833.

Wagner, T., Deutschmann, T., and Platt, U. (2009). Determination of aerosol properties from MAX-DOAS observations of the Ring effect. *Atmospheric Measurement Techniques*, 2(2):495–512.

Wang, Y., Beirle, S., Lampel, J., Koukouli, M., De Smedt, I., Theys, N., Li, A., Wu, D., Xie, P., Liu, C., et al. (2017). Validation of OMI, GOME-2A and GOME-2B tropospheric NO_2, SO_2 and HCHO products using MAX-DOAS observations from 2011 to 2014 in Wuxi, China: investigation of the effects of priori profiles and aerosols on the satellite products. *Atmospheric Chemistry and Physics*, 17(8):5007–5033.

Wang, Y., Li, A., Xie, P., Wagner, T., Chen, H., Liu, W., and Liu, J. (2014). A rapid method to derive horizontal distributions of trace gases and aerosols near the surface using multi-axis differential optical absorption spectroscopy. *Atmospheric Measurement Techniques*, 7(6):1663–1680.

Wei, C. (2010). Modeling the effects of heterogeneous reactions on atmospheric chemistry and aerosol properties.

Williams, J. E., Boersma, K. F., Sager, P. L., and Verstraeten, W. W. (2017). The high-resolution version of TM5-MP for optimized satellite retrievals: description and validation. *Geoscientific Model Development*, 10(2):721–750.

Wittrock, F., Oetjen, H., Richter, A., Fietkau, S., Medeke, T., Rozanov, A., and Burrows, J. (2004). MAX-DOAS measurements of atmospheric trace gases in Ny-Ålesund-Radiative transfer studies and their application. *Atmospheric Chemistry and Physics*, 4(4):955–966.

Zhao, X., Griffin, D., Fioletov, V., McLinden, C., Cede, A., Tiefengraber, M., Müller, M., Bognar, K., Strong, K., Boersma, F., et al. (2020). Assessment of the quality of TROPOMI high-spatial-resolution NO_2 data products in the Greater Toronto Area. *Atmospheric Measurement Techniques*, 13(4):2131–2159.